Parameter sensitivity of synthetic spectra and light curves of Type Ia supernovae

Dissertation
zur Erlangung des Doktorgrades
an der Fakultät für Mathematik,
Informatik und Naturwissenschaften
Fachbereich Physik
der Universität Hamburg

vorgelegt von

Ernst Rolf Lexen
aus Kronstadt

Hamburg
2014

Gutachter der Dissertation:	Prof. Dr. Peter H. Hauschildt Prof. Dr. Edward A. Baron
Gutachter der Disputation:	Prof. Dr. Robi Banerjee Prof. Dr. Dieter Horns
Datum der Disputation:	24.01.2014
Vorsitzender des Prüfungsausschusses:	Dr. Robert Baade
Vorsitzende des Promotionsausschusses:	Prof. Dr. Daniela Pfannkuche
Dekan der MIN-Fakultät:	Prof. Dr. Heinrich Graener
Leiter des Fachbereichs Physik:	Prof. Dr. Peter H. Hauschildt


SN 2011by

Effulſiße autem Nouam aliquam Stellam, quæ a Mundi primordijs nuſquam antea patuerit, eandemque vltra integrum Annum in eodem Cœli loce perſeueraße, & ſucceßiue tandem diſparuiße, Miraculum eſt, omnium Hominum expectatione atque captu maius, & inter ea, quæ a Mundi primæua Origine in tota rerum Natura extiterunt, Literiſque prodita ſunt admiranda ſpectacula, ſi non maximum, ſaltem illis æquiparandum [...][1]

(T. Brahe, 1602)

To strive, to seek, to find, and not to yield.[2]

(A. Tennyson, 1853)

[...] the Universe is not only queerer than we suppose,
but queerer than we can suppose.[3]

(J. B. S. Haldane, 1927)

[1] Tichonis Brahe, 1602, in *Astronomiae Instavratæ Progymnasmata [...]*, reprinted 1915, *Tychonis Brahe Dani Opera Omnia*, II, 317, 22-28

[2] Alfred Tennyson, 1853, in *The poems of Alfred Tennyson 1830 - 1863*, reprinted 1909,188

[3] J. B. S. Haldane, 1927, in *Possible worlds and other essays*, reprinted 1932, 286

Kurzfassung

In dieser Arbeit werden die Parameter von Typ Ia Supernova Lichtkurven-Simulationen systematisch variiert um die Sensitivität des Modells auf Parameteränderungen zu testen. Als Ausgangsmodell wird das parametrisierte Deflagrationsmodell *W* 7 verwendet. Die atmosphärische Struktur und die synthetischen Spektren werden mit PHOENIX berechnet.
Zuerst wird der Anteil der radioaktiven Energie geändert. Dazu wird die initiale ^{56}Ni-Masse des *W* 7-Modells ($m_{^{56}Ni} \equiv 0,568\,m_\odot$) in 10 %-Schritten von 50 % auf 150 % ^{56}Ni geändert. Während die optische Tiefe sich dabei nicht wesentlich verändert, treten Temperaturunterschiede von bis zu $11 \cdot 10^3$ K auf. Die statistische Analyse der Lichtkurven ergibt keine Ausreißer in den Bändern U, B und V (Johnson), u und g (SDSS), sowie Kp und D51 (Kepler). Für Modelle mit mehr ^{56}Ni verschiebt sich im Infraroten (IR) das zweite Maximum zeitlich weiter nach hinten. Dadurch kommt es teilweise zu einer Inversion der Helligkeiten in den Lichtkurven. Sie ist wellenlängenabhängig, was anhand der Bänder I (Johnson) und i (SDSS) gezeigt wird.
Danach wird die initiale Expansionsgeschwindigkeit ($v_{exp}^{max} \equiv 30 \cdot 10^3$ km s^{-1}) in 10 %-Schritten zwischen 50 % und 150 % v_{exp} variiert. Dabei verschieben sich die optischen Tiefen ($\Delta \log\tau \simeq 1,1$) und es tritt eine Temperaturdifferenz von bis zu $33 \cdot 10^3$ K auf. Modelle mit verringerter v_{exp} sind heißer und erreichen ihr Maximum später.
Verändert man die beiden Parameter simultan, verstärken bzw. kompensieren sich diese Effekte gegenseitig. Das lässt sich gut in den Spektren beobachten. In den Lichtkurven hingegen sind die Effekte nicht immer direkt ersichtlich.
Stabiles Eisen (Fe) wird in Abhängigkeit von der Geschwindigkeit der Schicht partiell durch ^{56}Ni ersetzt. Zuerst wird dazu sämtliches Fe, das örtlich langsamer als $\lesssim 4440$ km s^{-1} ist, in Schritten von 20 % ersetzt. Das bedeutet insgesamt eine Erhöhung des ^{56}Ni um $\simeq 12,8$ %. Die Auswirkungen sind geringer als bei einer globalen Erhöhung des ^{56}Ni-Anteils um 10 %. Bereits damit lässt sich die Phillips Relation auf eine differentielle Weise reproduzieren. Es kommt zu einer zeitlichen Verschiebung des zweiten Maximums und damit zu einer Inversion der Helligkeiten in den IR-Lichtkurven. In einem weiteren Schritt werden 50 % Fe für 7 Geschwindigkeiten an Orten $\lesssim 4440$ km s^{-1} durch ^{56}Ni ersetzt. Die Auswirkungen auf das Spektrum sind gering und können erst in den späten Spektren beobachtet werden.
Der Wert der parametrisierten Linienstreuung (ε_{line}) wird variiert, so dass zwischen 0 und 90 % der Photonen gestreut werden. Starke Streuung hat dabei große Auswirkung auf die Modellspektren, insbesondere im IR, wo die Effekte sehr deutlich zum Vorschein treten. Die Lage der Photosphäre ist wellenlängenabhängig: Im Ultravioletten (UV) verschiebt höhere Streuung die pseudo UV-Photosphäre näher an die Oberfläche und wir erhalten insgesamt eine höhere UV-Leuchtkraft. Im IR passiert das genaue Gegenteil.
Werden die drei Ionisationszustände von Calcium (Ca I, Ca II und Ca III) unter der Annahme von NLTE betrachtet, so ergeben sich deutliche Änderungen gegenüber den reinen LTE-Rechnungen in den Spektren und in den Lichtkurven. Die größten Abweichungen treten in den (Johnson) Bändern U, Ca II H und K, und I, Ca II (8579 Å) IR Triplett auf.

Abstract

In this work, parameters of Type Ia supernova light curve simulations are systematically varied to test the model sensitivity due to parameter changes. As a starting model, the parametrized deflagration model $W7$ is used. The atmospheric structure and the synthetic spectra are calculated with PHOENIX. Variations are done one at a time, first, the content of the radioactive energy is changed. For this purpose, the initial ^{56}Ni mass of the $W7$ model ($m_{^{56}Ni} \equiv 0.568\,m_{\odot}$) is changed in steps of 10 % from 50 % up to 150 % ^{56}Ni. While the optical depth is not changed significantly, temperature differences occur up to $11 \cdot 10^3$ K. The statistical analysis of the light curves shows no outliers in the bands U, B, and V (Johnson), u and g (SDSS), and Kp and D51 (Kepler). The second maximum in the infrared (IR) shifts further back in time for models with higher ^{56}Ni content. This leads to a partial inversion in the brightness of the light curves. The inversion is wavelength dependent and is prominent in the bands I (Johnson) and i (SDSS).
Then, the initial expansion velocity ($v_{exp}^{max} \equiv 30 \cdot 10^3$ km s^{-1}) is varied in steps of 10 % from 50 % up to 150 % v_{exp}. In this case, the total optical depths ($\Delta \log \tau \simeq 1.1$) changes and a temperature difference of up to $33 \cdot 10^3$ K occurs. Models with reduced v_{exp} are hotter and reach maximum later.
Changing these two parameters simultaneously, they amplify or compensate each other. This can be well observed in the spectra. In the light curves, however, the effects are not always immediately apparent.
Stable iron (Fe) is partially replaced by ^{56}Ni, depending on the velocity of the layer. First, the entire Fe, which is at locations slower than $\lesssim 4440$ km s^{-1}, is successively replaced in steps of 20 %. This is a total increase of ^{56}Ni of 12.8 %. The effects are smaller than for the global increase of ^{56}Ni of 10 %. With this the Phillips relation can be reproduced differentially. It leads to a time shift of the second maximum, and thus an inversion of the brightness in the IR light curves. In a next step, 50 % Fe for 7 velocities at locations up to $\lesssim 4440$ km s^{-1} are replaced by ^{56}Ni. The effects in the spectrum are small and can only be observed in the later spectra.
The value of the parametrized line scattering parameter, (ε_{line}) is varied so that between 0 and 90 % of the photons are scattered. Strong scattering has great impact on the model spectra, especially in the IR, where the effects are very clear. The position of the photosphere is wavelength dependent: In the ultraviolet (UV) higher scattering shifts the pseudo UV photosphere closer to the surface and we obtain a higher UV luminosity. In the IR, the exact opposite happens.
Considering the three ionization stages of calcium (Ca I, Ca II, and Ca III) under the assumption of non-local thermodynamic equilibrium (NLTE), significant changes compared to the pure LTE calculations can be observed, both in the spectra and in the light curves. The largest deviations occur in the (Johnson) bands U, Ca II H and K and I, Ca II (8579 Å) IR triplet.

Contents

1 Introduction **1**

2 Supernovae **3**
2.1 Historical approach . . . 3
2.2 Empirical classification and diversity based on spectra and light curves . . . 4
2.3 Progenitors and physical background of Type Ia supernovae . . . 8
2.4 Standardizability and cosmological applications . . . 10
2.5 Definite departure from the canonical behavior . . . 14

3 Parameter sensitivity of Type Ia supernovae simulations from a parameter estimation perspective **17**

4 Modeling spectra and light curves of Type Ia supernovae with PHOENIX **21**
4.1 Radiative transfer . . . 21
4.1.1 Radiative transfer in general . . . 21
4.1.2 The specific intensity and its moments . . . 22
4.1.3 Interaction between radiation and matter . . . 25
4.1.4 The equation of radiative transfer . . . 25
4.2 Thermodynamical approximations . . . 30
4.2.1 Thermodynamic equilibrium and local thermodynamic equilibrium 30
4.2.2 Non-local thermodynamic equilibrium . . . 31
4.3 Hydrodynamics of Type Ia supernova ejecta . . . 33
4.3.1 The carbon deflagration model $W7$ . . . 33
4.3.2 Analytical solver . . . 35
4.4 Time dependent radiative transfer . . . 40
4.4.1 First discretization of the wavelength and time derivative . . . 41
4.4.2 Second discretization of the wavelength and time derivative . . . 42
4.5 Method . . . 44

5 Variation of parameters, the sensitivity, and the model response **55**
5.1 Varying the abundance of ^{56}Ni . . . 58
5.2 Varying the expansion velocity . . . 82
5.3 Simultaneous variation of the expansion velocity and the abundance of ^{56}Ni 91
5.4 Partial replacement of stable iron by ^{56}Ni in the core . . . 94
5.5 Varying the value of the parametrized line scattering parameter . . . 100
5.6 NLTE – taking into account three ionization stages of calcium . . . 108

6 Conclusions and outlook **113**

Bibliography **116**

List of Figures

0.1 Supernova SN 2011by in the north of the center of NGC 3972 iv

2.1 Spectra of SN 2011fe 5
2.2 Light curves of SN 2011fe 7
2.3 Sample of supernovae light curves from the Calán/Tololo Supernova Survey 10
2.4 Template light curves in the bands U, B, V, R, I, J, H, and K 11
2.5 Hubble diagram for supernovae from the Calán/Tololo Supernova Survey and the Supernova Cosmology Project 12
2.6 Bar graphs of the total number of discovered supernovae per year and certainly recognized Type Ia supernovae since 1913 15

4.1 Geometric basis for the definition of the specific intensity 22
4.2 Geometric volume element for the derivation of the radiative transfer equation 26
4.3 Evolution of the temperature as a function of the density of a white dwarf from the $W7$ model 33
4.4 Temperature and density at the deflagration front of the $W7$ model as a function of Lagrangian mass coordinate $M/M_{\odot}$ 34
4.5 Representation of the radioactive decay of ^{56}Ni and ^{56}Co 38
4.6 Time evolving series of spectra 44
4.7 Johnson filter functions U, B, V, R, and I 45
4.8 Johnson filter functions J, H, and K 45
4.9 Filter functions for the photometric systems 2MASS, UKIDSS, SDSSS, and Kepler 46
4.10 Photometric systems and the wavelength range of its passbands 48
4.11 Iteration scheme of PHOENIX 49
4.12 Model light curves for the fiducial model for U, B, V, R, and I (for the Johnson photometric system) and for J, H, K (2MASS) 51
4.13 Same as in Figure 4.12 but for Z, Y, J, H, and K (for UKIDSS) and for Kp (Kepler) 52
4.14 Same as in Figures 4.12 and 4.13 but for u, g, r, i, and z (SDSS) and D51 (Kepler) 53

5.1 Normalized initial composition structure of $W7$ 55
5.2 Entire synthetic spectrum, as well as a section 56
5.3 Particles of ^{56}Ni as a function of speed for models in the range with 50 % reduced ^{56}Ni and 50 % enriched ^{56}Ni 58
5.4 Synthetic spectra for day 20 after the explosion for varying ^{56}Ni 59
5.5 Normalized particle number of ionized iron as a function of the optical depth τ and plotted against temperature for day 20 after the explosion 60

5.6 Same as in Figure 5.5, but for day 40 after the explosion 61
5.7 Synthetic spectra for days 5, 10, 14, 16, 18, 20, 22, 24, 26, 30, 40, and 50 of models for varying ^{56}Ni abundances 63
5.8 Same as in Figure 5.7, but for the wavelength range of the B band 64
5.9 Spatial representation of model light curves in the bands U, B, V, R, I, J, H, and K for varying ^{56}Ni 65
5.10 Model light curves in the bands U, B, V, R, I, J, H, and K for varying ^{56}Ni . 66
5.11 Summarized graphical representation of the statistical analysis of the model light curves from Figure 5.9 in the bands U, B, V, and R. 68
5.12 Summarized graphical representation of the statistical analysis of the model light curves from Figure 5.9 in the bands I, J, H, and K. 69
5.13 Pearson correlation coefficients for the individual days of the light curve of the B band for models with varying ^{56}Ni 70
5.14 Summed absolute values of the differences between two adjacent models for previously discussed bands shown in Figures 5.9 and 5.10 71
5.15 Summarized graphical representation of the statistical analysis of the model light curves from Section 4.5, Figure 4.12 for the Johnson photometric system for the bands U, B, V, R, and I and for 2MASS for the bands J, H, and K 73
5.16 Summarized graphical representation of the statistical analysis of the model light curves from Section 4.5, Figure 4.13 for the UKIDSS photometric system for the bands Z, Y, J, H, and K and for Kepler for the band Kp 74
5.17 Summarized graphical representation of the statistical analysis of the model light curves from Section 4.5, Figure 4.14 for the SDSS photometric system for the bands u, g, r, i, and z and for Kepler for the band D51 75
5.18 Temperature stratifications as a function of the optical depth for the 32 models from which the light curve was calculated for the fiducial model 77
5.19 Temperature stratifications as a function of the optical depth for the 32 models from which the light curve was calculated for the models with 50 % ^{56}Ni and 150 % ^{56}Ni 78
5.20 Temperature profiles in 10^3 K as a function of the optical depth for models with varying ^{56}Ni abundance for days 5, 10, 14, 16, 18, 20, 22, 24, 26, 30, 40, and 50 80
5.21 Discretized velocity model profiles as a function of the layers 82
5.22 Synthetic spectra for day 20 after the explosion for varying v_{exp} 83
5.23 Synthetic spectra for days 5, 10, 14, 16, 18, 20, 22, 24, 26, 30, 40, and 50 of models for varying v_{exp} 84
5.24 Spatial representation of model light curves in the bands U, B, V, R, I, J, H, and K for varying v_{exp} 85
5.25 Model light curves in the bands U, B, V, R, I, J, H, and K for varying v_{exp} . 86
5.26 Summed absolute values of the differences between two adjacent models for bands of models shown in Figures 5.24 and 5.25. 87
5.27 Temperature stratifications as a function of the optical depth for the 32 models from which the light curve was calculated for the models with 50 % v_{exp} and 150 % v_{exp} 89

5.28 Synthetic spectra for the day 20 after the explosion for varying simultaneously ^{56}Ni and v_{exp} . . . 91
5.29 Model light curves in the bands U, B, V, R, I, J, H, and K for varying simultaneously ^{56}Ni and v_{exp} . . . 92
5.30 Mass fractions of Fe and ^{56}Ni as a function of velocity at locations up to $4440\,\mathrm{km\,s^{-1}}$ . . . 94
5.31 Normalized (to the mass of the sun) mass fractions of Fe and ^{56}Ni as a function of velocity . . . 95
5.32 Course of the velocity dependent substitution of Fe by ^{56}Ni . . . 95
5.33 Synthetic spectra for days 5, 20, and 50 after the explosion for replaced Fe in the core. The corresponding models are shown in Figures 5.30 and 5.32 96
5.34 Synthetic spectra for day 20 after the explosion for Fe replaced in the core . 97
5.35 Model light curves in the bands U, B, V, R, I, J, H, and K. Fe was partially replaced by ^{56}Ni at locations up to $\lesssim 4440\,\mathrm{km\,s^{-1}}$ . . . 98
5.36 Synthetic spectra for day 20 after the explosion for varying $\varepsilon_{\mathrm{line}}$ . . . 100
5.37 Synthetic spectra for days 5, 10, 14, 16, 18, 20, 22, 24, 26, 30, 40, and 50 of models for varying $\varepsilon_{\mathrm{line}}$ . . . 101
5.38 Spatial representation of model light curves in the bands U, B, V, R, I, J, H, and K for varying $\varepsilon_{\mathrm{line}}$ . . . 103
5.39 Model light curves in the bands U, B, V, R, I, J, H, and K for varying $\varepsilon_{\mathrm{line}}$. 104
5.40 The summed absolute values of the differences of the models for different $\varepsilon_{\mathrm{line}}$ shown in Figure 5.38. . . . 105
5.41 Temperature stratifications as a function of the optical depth for the 32 models from which the light curve was calculated for the models with $\varepsilon_{\mathrm{line}} = 0.1$ and $\varepsilon_{\mathrm{line}} = 1$ . . . 106
5.42 Synthetic NLTE spectra for day 20 after the explosion . . . 108
5.43 NLTE model light curves in the bands U, B, V, R, I, J, H, and K . . . 109
5.44 Synthetic NLTE spectra within the wavelength region of the I band for day 20 after the explosion . . . 110

List of Tables

4.1 Compilation of passbands used in this work, specifying the filter name, the effective wavelength midpoint, the bandwidth, the specifying region, and the description of the photometric system. 47

5.1 Summarized results for the temperatures and the range of the optical depths for days 5, 20, and 50 for the fiducial model (100 % ^{56}Ni) shown in Figure 5.18 and for the two extreme models with 50 % ^{56}Ni and 150 % ^{56}Ni shown in Figure 5.19 79

5.2 Summarized results for the temperatures and the range of the optical depths for days 5, 20, and 50 for the fiducial model (100 % v_{exp}) shown in Figure 5.18 and for the two extreme models with 50 % v_{exp} and 150 % v_{exp} shown in Figure 5.27 88

5.3 Summarized results for the temperatures and the range of the optical depths for days 5, 20, and 50 for the fiducial model ($\varepsilon_{line} = 0.8$) shown in Figure 5.18 and for the two extreme models with $\varepsilon_{line} = 0.1$ and $\varepsilon_{line} = 1.0$ shown in Figure 5.41 106

Chapter 1

Introduction

Type Ia supernovae are among the brightest single objects in the Universe. It is generally agreed that they arise from the thermonuclear explosion of a white dwarf in a binary system. Due to the high luminosity of these objects and their explosion near a critical mass limit they became important cosmological distance indicators.
A general overview about supernovae is given in Section 2 of this work. We start with a historical overview (Section 2.1), and have a closer look at empirical classification and diversity, based on spectra and light curves (Section 2.2). Thereafter, an overview about progenitors and the physical background of Type Ia supernovae is given (Section 2.3). In Section 2.4 we focus on the standardizability of spectroscopically normal and canonical Type Ia supernovae light curves. Finally, in Section 2.5 definite departure from the canonical behavior based on observational data is shown. The strong increase of observational data since the 1990s (cf. Section 2.5) showed that Type Ia supernovae are not standard candles, but a major part can be transformed in standardizable candles.
However, intrinsic brightness differences are caused by different effects. Nevertheless, the unusual light curve decline of some peculiar supernovae can be explained within the framework of normal supernovae. The objects can be modeled under the assumption of extended individual parameters (cf. Baron et al. (2012) and Section 2.5).
The state of the art method to determine model parameters is parameter estimation based on mathematical methods as proposed by Bock (1981, 1987). These methods are presented in Section 3 especially for the astrophysical problem of parameter estimation. The individual parameters and the parameter sensitivity of Type Ia supernovae are determined.
However, these kinds of inverse problems can only be applied to single objects, where models and parameters are individually adjusted.
The aim of this work is to analyze the behavior of simulation results, e.g., spectra and light curves in different passbands, to change the underlying explosion model by varying the structures systematically. This is important as it helps us to quantify the uncertainties of parameter determinations through light curve simulations. Thus naturally depends on a series of related problems, e.g., requests for parameters which are poorly constrained by the observations and the modeling approach and that can, therefore, not be measured reliably. Additional questions are connected, e.g., effects on the model by changing technical or algorithmic parameters.
It is clear, therefore, that the systematic investigation of these dependencies considered as classical forward problem is truly astronomical. On the other hand, a fundamental obstacle is the fact that we cannot simply "reverse" the simulations based on the solution of integro-differential equations (here: the time dependent radiative transfer equation with scattering),

while linear, cannot be directly reversed.
Therefore, we will use a methodology that instruments the forward simulations with PHOENIX/1D to provide information about the reaction of the simulation results, e.g., synthetic spectra and light curves, to vary the different sets of input parameters directly.
Following, the results will be discussed and the conclusions and the outlook (Section 6) show the necessity of a quantitative understanding of this extensive and complex problem.

Chapter 2

Supernovae

2.1 Historical approach

As one of the brightest events in the Universe, supernovae have great importance and formed, both in the distant and in the recent past, milestones in our understanding of stellar evolution and cosmology. In Europe, the first "new star" (nowadays we call such stars supernovae) was discovered by Tycho Brahe in the constellation Cassiopeia in 1572[1]. He wrote about it "De nova et nullius aevi memoria prius visa stella, [...]"[2]. As the new discovered star did not change its position against the fixed stars, Brahe concluded that the star had to belong to the fixed stars. Thus began a new era, away from Aristotle and dogmatic belief of the Church of the immutability of the heavens. Previously, there had already been more observations of so-called "new stars", such as SN 1054, now known as the Crab Nebula[3], which was only observed outside Europe, but they were simply not known or ignored by European scholars. Clark & Stephenson (1977), Green & Stephenson (2003), and Stephenson & Green (2005) summarized the historical "evolution" of supernovae.

Astronomically a split second later, followed the discovery of the second, and until now, the last supernova in our galaxy in 1604. It was Kepler's supernova, in the constellation Ophiuchius[4]. He wrote about it "De stella nova in pede Serpentari, [...]"[5].

The rate in which Type Ia supernovae occur in a galaxy like the Milky Way is only a few per millennium. Supernova rates and estimates are discussed in, e.g., Cappellaro et al. (1997) and the Type Ia supernovae rates especially in, e.g., Pain et al. (1996, 2002) and Graur & Maoz (2013). Supernova rates are briefly discussed in Section 2.5, where they are shown graphically in Figure 2.6.

But what are supernovae? The term was introduced by Walter Bade and Fritz Zwicky (cf. Osterbrock 2001).

Commonly, supernovae are thought to be exploding stars whose luminosity increase abruptly by several orders of magnitude and cause a burst of radiation that often briefly outshines the entire host galaxy.

[1] It was the supernova SN 1572

[2] Tychonis Brahe, Dani, 1573, in *De nova et nullius aevi memoria prius visa stella, iam pridem anno à nato Christo 1572, mense Novembri primum conspecta, contemplatio mathematica [...]*

[3] M1 in the Messier Catalogue

[4] Formerly known as Serpentarius

[5] Joannis Keppleri, 1606, *De Stella Nova in Pede Serpentarii, et qui sub ejus Exortum de novo iniit, Trigono Igneo*

2.2 Empirical classification and diversity based on spectra and light curves

It took until 1885 until the first spectrum of a supernova was published[6] (Sherman 1885, 1886, and for a summary Gaposchkin (1936)) and almost another 60 years until Popper (1937) noted that there may be more kinds of supernovae.
The two main classes, the Types I and II were "provisionally" established by Minkowski (1941), after he had deviated from his earlier position that all supernovae have similar spectra and only differ in details of minor importance (Minkowski 1939). Of his 14 supernovae, nine spectra were extremely homogeneous, while the remaining five were distinctly different. He took the division and could show that Type I supernovae have, compared to those of Type II, lower expansion velocities and no lines of hydrogen or any other elements (Minkowski 1941). At this time it was very difficult to obtain good spectra of supernovae and some had to be withdrawn because they turned out to be not spectra of supernovae, e.g., Strohmeier (1938). This was caused by the instruments, the absence of linear detectors, but also the very large distances of these objects. Therefore, photometry was mainly used to obtain light curves. From changes in luminosity with time, which is measured as the evolution of the apparent brightness, conclusions can be drawn on the properties of the observed object. Zwicky (1938) and Baade & Zwicky (1938) realized the importance of the light curves for the understanding of supernovae. Today, they are, still, an important tool and also the historical observations can be used today. Branch (1990) gave a historical overview of spectra and Kirshner (1990) of light curves of supernovae.
Despite some additions and corrections to the current taxonomy, such as the subclassification of the Type I supernovae (Bertola 1962) into classical Ia (cf. Elias et al. 1985; Harkness & Wheeler 1990; Wheeler & Harkness 1990; Filippenko 1997; Wheeler & Benetti 2000) and the extension to the physically distinct class Ib, which is characterized by the presence of neutral helium He I (Harkness et al. 1987) and the absence of the strong singly ionized silicon Si II absorption feature at 6150 Å (Pskovskii 1969; Branch & Patchett 1973), and later the branch into another variety with poor He I, Ic (Elias et al. 1985; Wheeler & Levreault 1985; Porter & Filippenko 1987; Harkness & Wheeler 1990; Wheeler & Harkness 1990; Filippenko 1997; Wheeler & Benetti 2000), or the rearrangement of Zwicky's (1965) newly introduced Types III, IV, and V supernovae among Type II supernovae, the present day classification scheme is useful to sort out supernovae according to their characteristics and to look for similarities and differences. Regardless of the achievements in the classification, it is ambiguous and the many peculiar objects make it even more confusing. For example, there are peculiar types as the super-Chandrasekhar mass Type Ia supernovae, or a distinct class within the peculiar supernovae, the Type Iax (Foley et al. 2013).
A review of the supernovae taxonomy is given in, e.g., Harkness & Wheeler (1990), da Silva (1993), Filippenko (1997), and Wheeler & Benetti (2000).
Type Ia supernovae are traditionally defined by their spectra, which contain much information about the ejected matter, such as the composition and the expansion velocities. One of its main features is the total absence of hydrogen in their spectra near maximum light (Minkowski 1941).

[6] S Andromedae / SN 1885A (Hartwig 1885; Ward 1885) the first observed extragalactic supernova

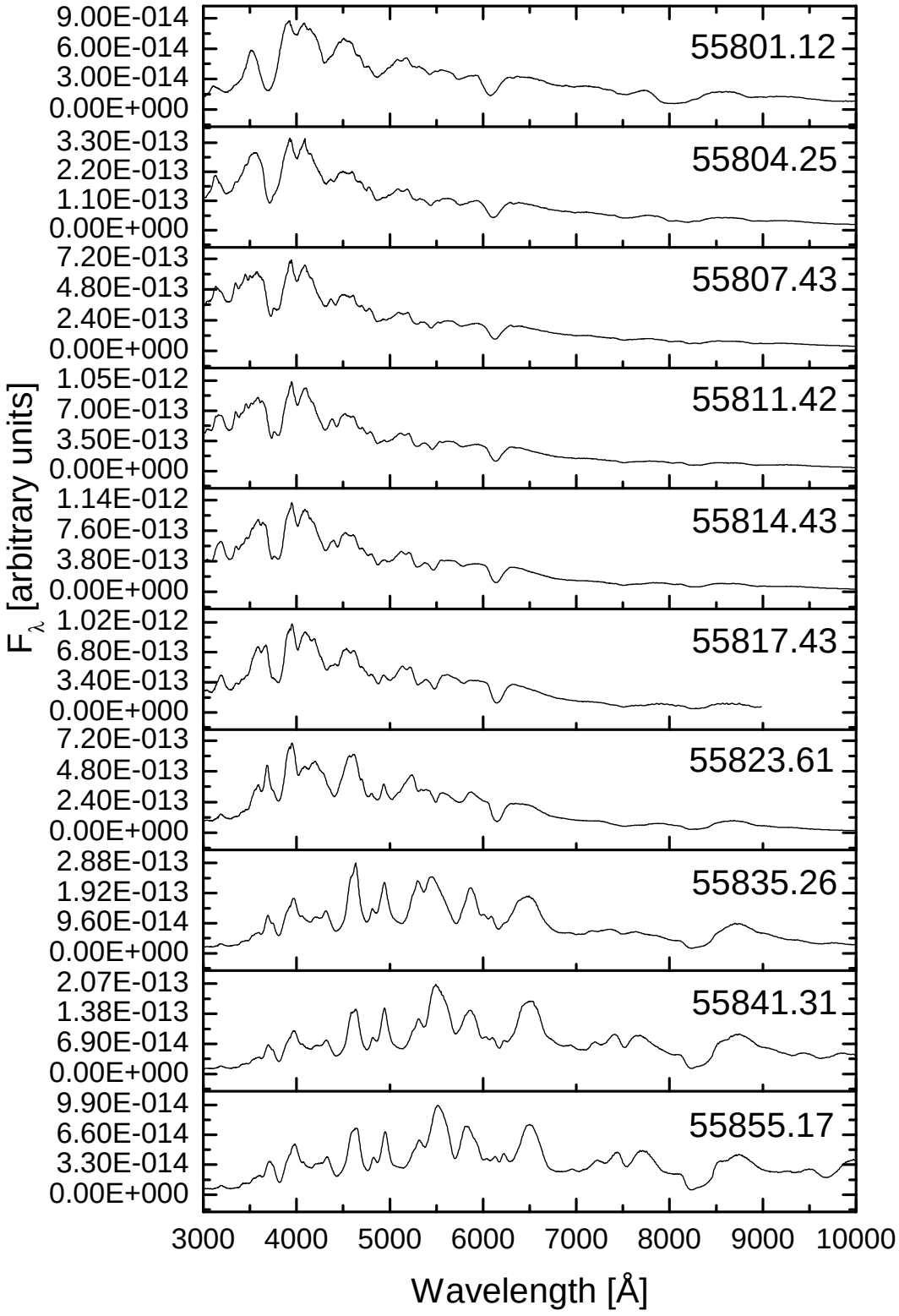

Figure 2.1: Spectral evolution of the Type Ia supernova SN 2011fe from 08-28-2011 (top) to 10-21-2011 (bottom). In the upper right corner of each spectrum is the Modified Julian Date specified. In the early spectra Ca II, Mg II, Fe II, Si II were identified (Parrent et al. 2012). See text for details.

A second characteristic is the empirical subdivision based on features in their spectra, such as the presence of the strong singly ionized silicon (Si II) absorption feature at 6150 Å, produced by blueshifted Si II (6347 Å and 6371 Å) (Pskovskii 1969; Branch & Patchett 1973). Together with the two Fraunhofer lines of singly ionized calcium Ca II, H and K (3968.5 Å and 3933.7 Å) they are the strongest lines in the spectrum. Other prominent lines near maximum light are singly ionized silicon Si II (3858 Å, 4130 Å, 5051 Å, and 5972 Å), singly ionized calcium Ca II (8579 Å), singly ionized magnesium Mg II (4481 Å), singly ionized sulfur S II (5468 Å, 5612 Å, and 5654 Å), and neutral oxygen O I (7773 Å). These features are usually formed by resonant scattering above the photosphere and show strong P Cygni profiles characteristic of expanding atmospheres (Filippenko 1997).
There are some contributions from lowly ionized iron and iron peak elements, which increase after maximum brightness (Mazzali et al. 1997).
In Figure 2.1 the spectra of the supernova PTF11kly/SN 2011fe[7] are shown in the wavelength range $[3000, 10000]$ Å starting from 08-28-2011 to 10-21-2011. In particular, the days specified in Modified Julian Date (MJD) are: 55801.12 (08-28-2011), 55804.25 (08-31-2011), 55807.43 (09-03-2011), 55811.42 (09-07-2011), 55814.43 (09-10-2011), 55817.43 (09-13-2011), 55823.61 (09-19-2011), 55835.26 (10-01-2011), 55841.31 (10-07-2011), and 55855.17 (10-21-2011).
In Figure 2.2 the light curves in the bands B, V, R, and I of the supernova PTF11kly/SN 2011f are shown for the first 350 days.
SN 2011fe was detected by the Palomar Transient Factory (Law et al. 2009; Rau et al. 2009) in the Pinwheel galaxy[8], a spiral galaxy at a distance of 6.4 Mpc (Shappee & Stanek 2011), the closest[9] Type Ia supernova in the past 25 years (Nugent et al. 2011). The onset of the event was established based on models at UT 2011, August 23, 16:29 and Ca II, Mg II, Fe II, Si II were identified in the early spectra (Nugent et al. 2011).
Filippenko (1997) urged caution of uncorrected spectra. The spectra may be contaminated with hydrogen from superimposed H II regions or contain emission lines from circumstellar material. A discussion of the presence or absence of circumstellar material is given in, e.g., Branch et al. (1995). Type Ia supernovae are usually not associated with star formation regions (and, therefore, with H II regions). However, there are exceptions, such as SN 2002ic (Wood-Vasey et al. 2002a; Hamuy et al. 2002), the first observed Type Ia supernova with strong H_α and a weaker H_β emission (Hamuy et al. 2003a) caused by the interaction with hydrogen-rich circumstellar medium (Hamuy et al. 2003b; Wang et al. 2004). However, it is also possible, based on the light curve behavior and the H_α profile, that it is a Type IIn supernova, whereas it was spectroscopically identified as Type Ia (Hamuy et al. 2002, 2003b; Wood-Vasey et al. 2004).
Unlike other supernovae, Type Ia supernovae occur in all morphological types of galaxies and are usually associated with older stellar populations. In spiral galaxies they are concentrated in spiral arms only to the extent where the oldest stars are (Maza & van den Bergh 1976; McMillan & Ciardullo 1996; Wheeler & Benetti 2000). It is now known that there is a relation between the luminosity of Type Ia supernovae and the morphological classifi-

[7] The latter is the official name of the IAU
[8] M101 in the Messier Catalogue
[9] Before SN 2011fe a closer Type I supernova was SN 1986G (Evans et al. 1986) in M83 (specifically NGC 5128 (Centaurus A)) (Feast et al. 1986) and earlier SN 1972E in NGC 5253 (Kowal 1972)

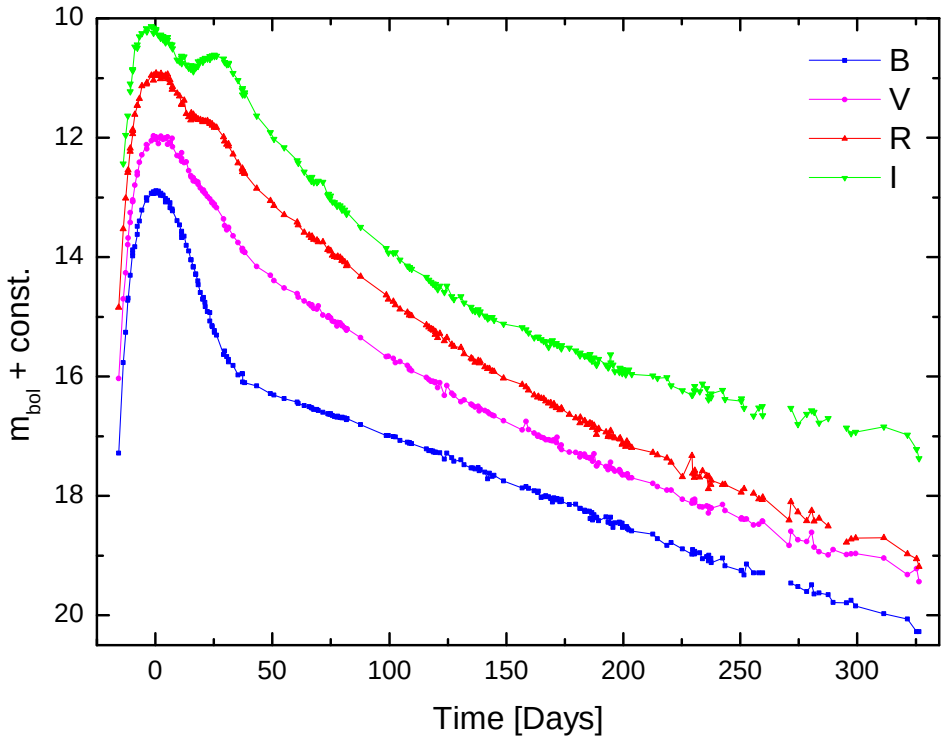

Figure 2.2: Light curves of the Type Ia supernova SN 2011fe in the bands B, V, R, and I. The data for each passband have been offset vertically (Baron et al. forthcoming).

cation of the host galaxy. Hamuy et al. (1995, 1996b) found that the intrinsically brightest Type Ia supernovae occur in late-type galaxies. Likewise, it was found by Howell (2001) that peculiar subluminous Type Ia supernovae come from an old population. Overall, it can be said that the brightness and the width of the light curve are correlated with the mass, the star formation rate, the age, and the metallicity of the host galaxy.

2.3 Progenitors and physical background of Type Ia supernovae

It is thought that Type Ia supernovae are carbon-oxygen white dwarfs that exceed by accretion of mass from a companion in a binary system a critical mass limit (Chandrasekhar 1931, 1939). It was named after its discoverer Chandrasekhar $\mathscr{M}_{Chan}$[10]. As soon as the white dwarf grows (close) to $\mathscr{M}_{Chan}$, carbon is ignited. In the ensuing explosion the white dwarf will completely destroyed (Hoyle & Fowler 1960). The nature of the accretion process and the companion still remain open questions. One of the possibilities is the single-degenerate scenario, where the companion star is a main sequence star or a red giant (Whelan & Iben 1973). In the double-degenerate scenario the companion is another white dwarf (Iben & Tutukov 1984; Webbink 1984). Another option is sub-Chandra, where a helium layer accumulates on a carbon-oxygen white dwarf (Woosley & Weaver 1986). When the pressure exceeds a critical threshold value, helium is ignited and the white dwarf (markedly) below the Chandrasekhar mass detonates due to the inward propagating shock front compressing the carbon-oxygen core which ignites (Nomoto 1980). Other compositions of the white dwarf, such as oxygen-neon-magnesium or helium are possible, but can be excluded for this scenario, because they play only a minor role due to physical and statistical considerations[11]. The identification of the progenitor system remains a major unsolved problem (Maoz & Mannucci 2012). Even the very early discovery of the "nearby" supernova SN 2011fe in the era of modern instruments could not resolve this question, but some scenarios, such as the companion star being a red giant, could be excluded (Nugent et al. 2011; Li et al. 2011; Horesh et al. 2012). Bloom et al. (2012) determined the radius of the progenitor and concluded that it is a compact object. Nugent et al. (2011) concluded from the lack of an early shock that the companion was most likely a main sequence star. Using archive images of the region from the Hubble Space Telescope, Li et al. (2011) ruled out almost all helium stars as companion stars[12]. Using radio data, Chomiuk et al. (2012) placed constraints on the density of medium the progenitor surrounding and interpreted it as ruling out the single degenerate scenario, even limited the double degenerate scenario and did not rule out "exotic" scenarios or the core degenerate scenario.

The explosion of a carbon-oxygen white dwarf itself is the result of a thermonuclear runaway in degenerate carbon burning. This process is poorly understood theoretically, despite some progress. In particular, the conditions of the "simmering", the exact moment until nuclear fusion begins, where it starts, and if it starts possibly several times and ultimately the mechanism that triggers the detonation is vague. It is commonly thought that the nuclear burning "flame" front propagates initially at subsonic speed as a deflagration wave outward. Fusion processes take place and many of the (neutral and singly ionized) intermediate mass elements lighter than iron, such as oxygen, magnesium, silicon, sulfur, and calcium are produced. A closer look on the nucleosynthesis is given in, e.g., Hoyle & Fowler (1960, 1961), Truran et al. (1967), Thielemann et al. (1986), and Travaglio & Hix (2013). At different densi-

[10] $\mathscr{M}_{Chan} = 1.46 \left(\frac{Y_e}{0.5}\right)^2 M_\odot$, where Y_e is the electron mole fraction (Chandrasekhar 1939)

[11] An oxygen-neon-magnesium white dwarf will not end as a Type Ia supernova (cf. Miyaji et al. 1980)

[12] "This directly rules out luminous red giants and the vast majority of helium stars as the mass-donating companion to the exploding white dwarf." Li et al. (2011)

ties, the flame front becomes Rayleigh-Taylor unstable (cf. Chandrasekhar 1961). Rayleigh-Taylor instabilities enlarge and deform the surface of the flame front, as also known from the chemical combustion physics, e.g., Jäger et al. (2007). Turbulence plays a major role in the mixing of unburnt material in the deformed burning front. In the outer layers, ultimately a detonation wave is induced by fast deflagration (cf. Khokhlov et al. 1993; Nomoto et al. 1996). The transition in the unregulated carbon burning from deflagration (subsonic burning wave) to detonation (supersonic) is, still, not well understood but is, in fact, needed, since a pure deflagration would not provide enough power and the flame would fizzle, whereas a pure detonation would lead to an overabundance of iron group elements and not enough of the intermediate mass elements observed in the peak phase. Ultimately, the flame front is accelerated to supersonic speed, and the released nuclear energy is ripping the white dwarf completely apart. It releases a kinetic energy of $\approx 10^{51}$ erg (Khokhlov et al. 1993) often abbreviated "foe" ([ten to the power of] fifty-one ergs)[13]. Here all burnt and unburnt material is ejected into space. Partial trapping and thermalization of β-unstable $^{56}_{28}$Ni (half-life 6.075 d (Junde et al. 2011)) and its daughter nucleus $^{56}_{27}$Co (half-life 77.236 d (Junde et al. 2011)) play an important role. Both isotopes power the heating of the adiabatically cooling shell through gamma ray emission,

$$^{56}_{28}\mathrm{Ni}_{28} \xrightarrow[\mathrm{T}_{1/2}=6.075\,\mathrm{d}]{\mathrm{e}^-\text{capture}} {}^{56}_{27}\mathrm{Co}_{29} \xrightarrow[\mathrm{T}_{1/2}=77.236\,\mathrm{d}]{\mathrm{e}^-\text{capture}\,\&\,\beta^+} {}^{56}_{26}\mathrm{Fe}_{30}.$$

While $^{56}_{28}$Ni decays only by electron capture, $^{56}_{27}$Co decays by both electron capture $(81\,\%)$ and β^+ decay $(19\,\%)$ (Leibundgut 2000).
The idea of nuclear heating through decaying isotopes goes back to Truran et al. (1967) and Colgate & McKee (1969) and has been confirmed by measurements of Kuchner et al. (1994).

[13] 10^{51} erg $\equiv 10^{44}$ Joule

2.4 Standardizability and cosmological applications

Due to the huge luminosity, it becomes possible to see Type Ia supernovae far away in space and, therefore, far back in time. Thus, when the white dwarf reaches the same critical mass, $\mathscr{M}_{Chan}$, before it is fully disrupted by the thermonuclear explosion, it is believed that the explosion energy is nearly the same. All types of supernovae, except for the Type Ia, are very inhomogeneous and can ultimately not be used for inductive statements[14]. Canonical Type Ia supernovae light curves look remarkably similar. Most of them differ only slightly. Especially in the B and V bands, where the majority of the energy of Type Ia supernova is emitted, there are only small deviations around a template behavior.

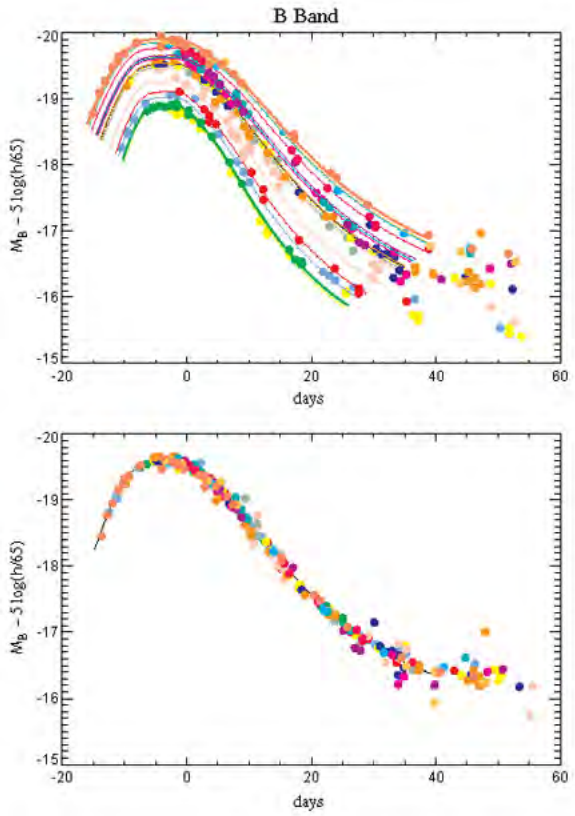

Figure 2.3: In the upper panel a sample of light curves from low redshift Type Ia supernovae from the Calán/Tololo Supernova Survey (Hamuy et al. 1996a) is shown. The brightness in the B band as a function of time is shown before and after maximum (day 0). The light curves of brighter supernovae decline more slowly whereas the decrease of the dimmer is faster (Phillips 1993). In the lower panel the same light curves are shown after calibration. Corrected is the stretch of the timescale and the intrinsic peak of the color. The figure is based on Perlmutter (1999) (and references therein), with modifications.

[14] However, see the expanding photosphere method (Kirshner & Kwan 1974)

This could be shown with the measured Type Ia supernovae from the Calán/Tololo Supernova Survey (Hamuy et al. 1993, 1996a). Light curves of this supernova survey are shown in Figure 2.3, where the Phillips relation (Phillips 1993) can be seen very well. Phillips showed a linear relationship between a defined parameter, Δm_{15}, which describes the decrease of the B magnitude within the first 15 days after the maximum in the B band and the absolute peak luminosity. The light curves of brighter supernovae decline more slowly, whereas the decrease of the dimmer is faster. These results based on the investigation from the Calán/Tololo Supernova Survey and were earlier proposed by Barbon et al. (1973) and Pskovskii (1977, 1984). In the lower panel of Figure 2.3, the standardized profile of the recalibrated light curves is shown. These data were essential to show that supernovae may be standard candles and also provide an important basis for subsequent work. Later, the Phillips relation was further developed and improved (Hamuy et al. 1995, 1996a; Phillips et al. 1999). Other methods based on the initial idea are the multicolor light-curve shape method (Riess et al. 1995, 1996, 1998; Jha et al. 2007) and the stretch correction method (Perlmutter et al. 1997; Goldhaber et al. 2001).
At least since the discovery and observation of supernovae in galaxies with known distances it becomes possible to use Type Ia supernovae as distance indicators in cosmology. Cepheids[15] are used to determine distances (Hubble 1925). However, they are only suitable for (astronomical) nearby galaxies. With the appearance of supernovae in such galaxies[16], direct comparison methods were thus available (Panagia et al. 1992; Sandage et al. 1992, 1994, 1996; Saha et al. 1995, 1996a,b, 1997, 1999, 2001a,b).

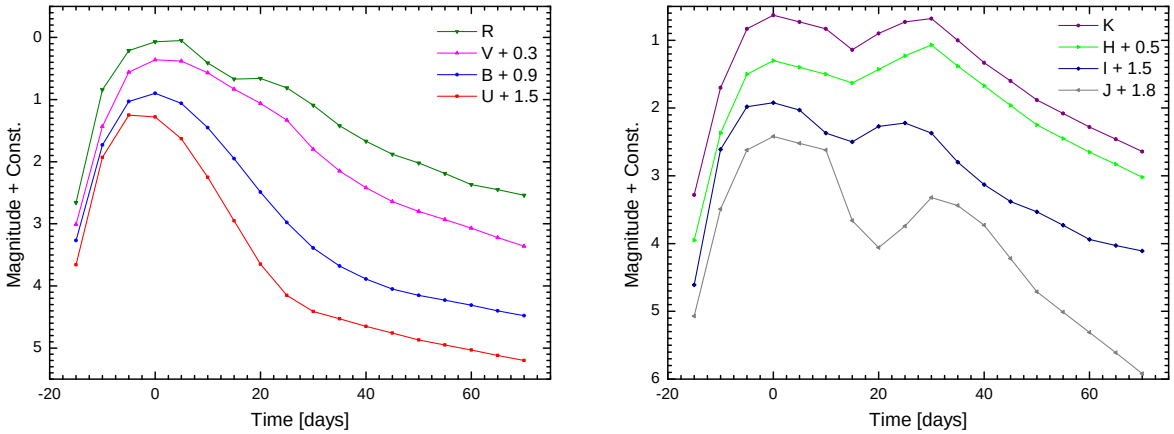

Figure 2.4: Plotted are the magnitudes as a function of time of the template light curves in the bands U + 1.5, B + 0.9, V + 0.3, and R (left panel) and I + 1.5, J + 1.8, H + 0.5, and K (right panel). The legend labels the bands and the added constants. The figure is based on the data of Nugent et al. (2002), with modifications. See text for details.

[15] After the eponymous star Delta Cephei (for classical Cepheids). There is a relationship between their periods and luminosities (Leavitt & Pickering 1912).

[16] Recently SN 1895B (Johnson 1936; Hoffleit 1939) and SN 1937C (Baade & Zwicky 1938; Minkowski 1939) are the first known Type Ia supernovae whose parent galaxies, NGC 5253 and IC 4182, has been reached by Cepheids (Panagia et al. 1992; Sandage et al. 1992, 1994; Saha et al. 1995)

Wilson (1939) suggested as one of the first to use supernovae for the study of nebular redshifts and thus for cosmological distances. It was followed by contributions to the determination of cosmological parameters, e.g., Branch & Patchett (1972), Branch (1977a,b, 1985a), Branch & Tammann (1992), Riess et al. (1998), and Perlmutter et al. (1999). In 1992, Branch & Tammann discussed Type Ia supernovae as standard candles and concluded that with advances in observation and modeling, they are certain to become increasingly valuable as extragalactic distance indicators. Branch et al. (1993) defined from an observational sample spectroscopically normal and peculiar Type Ia supernovae. Ultimately, out of this a template has been developed whose supernovae are commonly called "Branch-normal Type Ia supernovae". Nugent et al. (2002) showed a further development of this scheme for the near-infrared bands. Their data for the template light curves in the bands U, B, V, R, I, J, H, and K are shown in Figure 2.4.

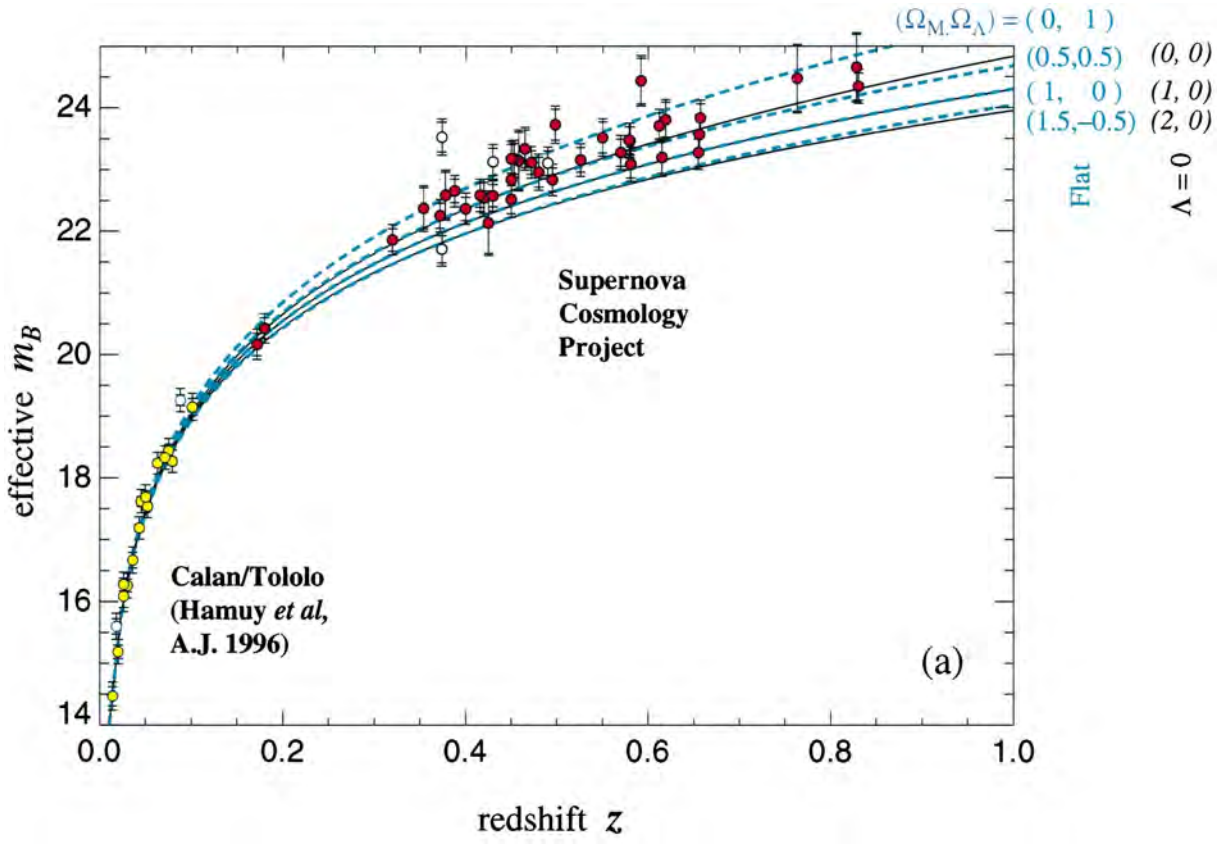

Figure 2.5: The Hubble diagram for 18 low redshift Type Ia supernovae from the Calán/Tololo Supernova Survey and 42 high redshift supernovae from the Supernova Cosmology Project, plotted on a linear redshift scale. The solid curves represent a range of cosmological models with $\Lambda = 0$, $\Omega_\Lambda = 0$, and $\Omega_M = 0, 1$, and 2. The dashed curves show a range of flat cosmological models for $\Omega_M = 0, 0.5, 1$, and 1.5 where $\Omega_M + \Omega_\Lambda = 1$. The unfilled circles indicate not included supernovae. The figure is from Perlmutter et al. (1999), with modifications.

They used the supernovae SN 1981B, SN 1989B, SN 1990N, SN 1990af, SN 1992A, SN 1992P, SN 1992ag, SN 1992al, SN 1992aq, SN 1992bc, SN 1992bh, SN 1992bl, SN 1992bo, SN 1992bp, SN 1992br, SN 1992bs, SN 1992b, SN 1992b, SN 1992b, SN 1993H, SN 1993O, and SN 1994D to create this template.
The near infrared has many advantages, but it is not easy to get good spectra in this region. After all, Marion et al. (2003), still, had claimed that with the release of twelve near infrared spectra, they more than doubled the number of published spectra within three weeks of maximum light. Marion et al. (2009) published 41 near infrared spectra, however, which meant a huge improvement to the relatively few published in the literature at this time.
The first high redshift Type Ia supernovae was observed at $z = 0.31$ (Norgaard-Nielsen et al. 1989), the most distant one at $z = 1.914$ (Jones et al. 2013), corresponding to a lookback time of the order of $\gtrsim 10$ Gy. The most important discovery was that the expansion of the Universe is not slowing down, due to the attractive force of gravity, but is, instead, accelerated (Riess et al. 1998; Perlmutter et al. 1999). The force responsible is called the vacuum energy, often "dark energy", and constitutes $\approx 70\,\%$ ($\Omega_\Lambda = 0.713$) of the content of the Universe (Kowalski et al. 2008). Perlmutter et al. (1999) received from their best fits values of $\Omega_\Lambda = 0.72$ and $\Omega_M = 0.28$. Their data from the measured 42 high redshift Type Ia supernovae from the Supernova Cosmology Project and the data from 18 low redshift ($z \leqslant 0.1$) supernovae from the Calán/Tololo Supernova Survey are shown in Figure 2.5.
The effective rest frame B magnitude corrected for the width luminosity relation, m_B is plotted as a function of redshift z. This is called an observed Hubble diagram. In the original Hubble diagram, the apparent magnitude is plotted as a function of redshift (Hubble 1929, 1936). Sandage (1956) called the "red-shift" speed of recession and plotted it as a function of apparent magnitude. The theoretical curves for mass density $\Omega_M = 0$, 1, and 2 and cosmological constant $\Lambda = 0$ are shown as solid curves (from top to bottom), whereas the dashed curves show a range of flat cosmological models for $\Omega_M = 0$, 0.5, 1, and 1.5 and the total mass energy density $\Omega_\Lambda + \Omega_M = 1$ with $\Omega_\Lambda = \frac{\Lambda}{3H_0^2}$ as the contribution for vacuum energy. It can be seen that models with $\Omega_\Lambda = 0$ are clearly ruled out. However, currently we lack the theoretical understanding of this value, $\Omega_\Lambda \approx 70\,\%$.
"For the discovery of the accelerating expansion of the Universe through observations of distant supernovae"[17], Saul Perlmutter[18], Brian P. Schmidt[19], and Adam G. Riess[19] were awarded with the Nobel Prize in Physics 2011.

[17] "The 2011 Nobel Prize in Physics - Press Release". Nobelprize.org. Nobel Media AB 2013. Web. 12-27-2013. <http://www.nobelprize.org/nobel_prizes/physics/laureates/2011/press.html>
[18] The Supernova Cosmology Project
[19] The High-z Supernova Search Team

2.5 Definite departure from the canonical behavior

Despite of the achievements in cosmology that were achieved by using supernovae, the idea that all Type Ia supernovae are exactly the same is rather simplistic. The accuracy to determine distances using Type Ia supernova is $\approx 10\,\%$. Definite departures from the canonical behavior shows the much brighter SN 1991T (Filippenko et al. 1992b; Phillips et al. 1992; Wheeler & Benetti 2000). At maximum light it was 0.6 mag brighter in V than a typical Type Ia supernova (Wheeler & Benetti 2000) and shows Fe III but not the "classical" Si 6355 Å blend[20] nor sulfur or calcium (Filippenko et al. 1992b). The other extreme is the subluminous SN 1991bg, which was at maximum brightness 1.6 mag subluminous in V and 2.5 mag subluminous in B (Filippenko et al. 1992a; Leibundgut et al. 1993; Turatto et al. 1996; Mazzali et al. 1997; Wheeler & Benetti 2000). Moreover, it shows no evidence for a secondary infrared peak in its light curve. These two supernovae are now eponymous for supernovae with these properties. They are generally called "peculiar". An other exception is the peculiar Type Ia supernova SN 2001ay. It was not overluminous in optical bands at maximum light ($M_B = -19.19$ and $M_V = -19.17$ mag) but showed with $\Delta m_{15}(B) = 0.58 \pm 0.05$ a brightness decline rate as three of the four overluminous super-Chandrasekhar mass candidates (Krisciunas et al. 2011). This makes it the most slowly declining Type Ia supernova. Baron et al. (2012) showed that it consisted of 80 % carbon and that the unusual light curve decline can be explained within the framework of normal supernovae. As final exemption should be mentioned the Type Iax supernovae (Foley et al. 2013). It is characterized by the prototype SN 2002cx (Wood-Vasey et al. 2002b; Li et al. 2003). It was published by Li et al. (2003) as "The most peculiar known Type Ia supernova" with a premaximum spectrum similar to SN 1991T, but a luminosity like that of SN 1991bg, expansion velocities of only $6 \cdot 10^3\,\mathrm{km\,s^{-1}}$, and many spectral peculiarities. Branch (2004), however, showed that SN 2002cx was a good example of a low photospheric velocity Type Ia supernova, a low luminosity SN 1991bg-like event that, in accordance with Marietta et al. (2000) is viewed right down a hole in the ejecta caused by the presence of the secondary star. Jha et al. (2006) considered it as prototype of a new subclass, with spectral characteristics that may be consistent with recent pure deflagration models of Chandrasekhar mass thermonuclear supernovae.

Ultimately, these observations were only possible with extensive monitoring programs and the discovery of a statistically relevant number of supernovae. As mentioned in Section 2.1, the supernova rate of a galaxy is rather small with a few per millennium.

This is recognized in the original IAU designation[21]. In the upper left corner of Figure 2.6 the total number of discovered supernovae per year of the last hundred years (1913 – July 2013) is shown.

The data are taken from the IAU Central Bureau for Astronomical Telegrams[22]. In the lower left corner of Figure 2.6, a cutout of the upper diagram until 1991 is shown, while the ordinate is scaled. Beginning in the 1990s, a larger number of supernovae were discovered. In the upper right corner of Figure 2.6 the supernovae that are certainly recognized as Type Ia

[20] Collective designation for Si II at 6347 Å and 6371 Å

[21] The common name is formed by combining the prefix SN, the year of discovery and an upper case letter from A to Z. So, however, previously were only 26 per year possible.

[22] IAU Central Bureau for Astronomical Telegrams.
Web. 12-27-2013. <http://www.cbat.eps.harvard.edu/lists/Supernovae.html>

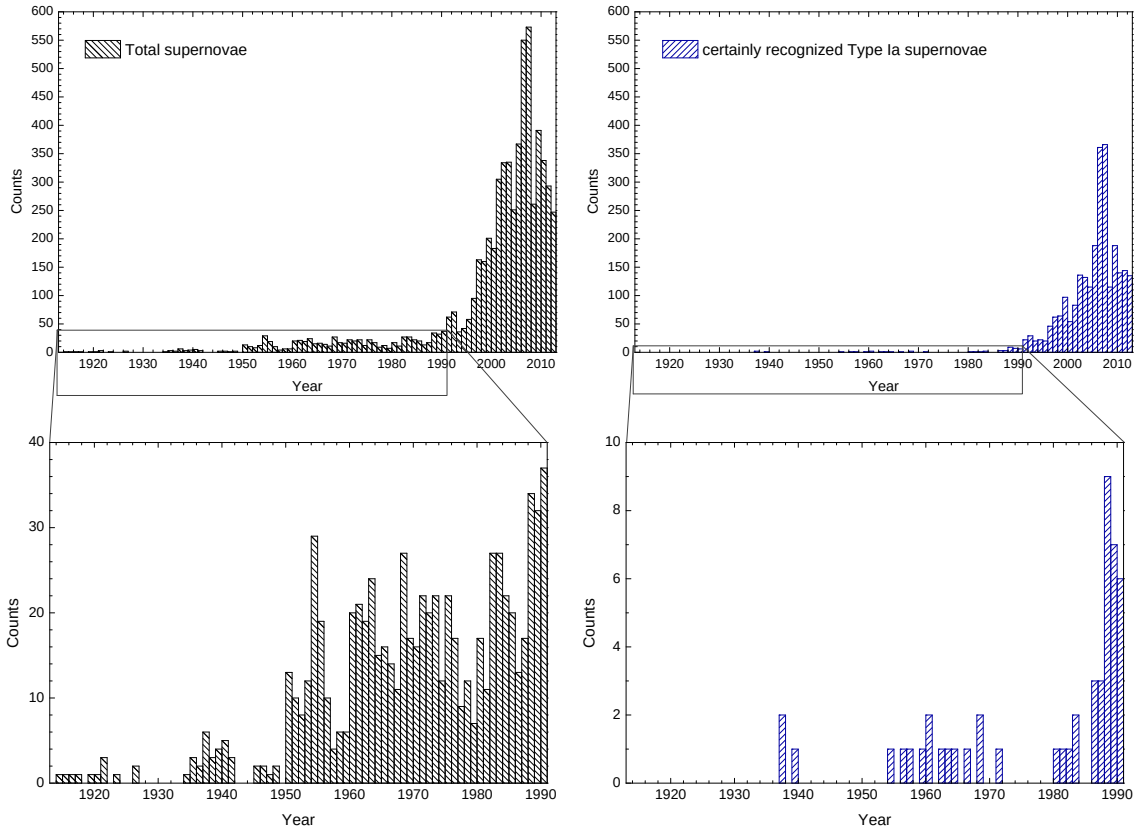

Figure 2.6: Graphical representation of the number of discovered supernovae per year of the last hundred years (1913 – July 2013). In the upper left corner the total number of discovered supernovae per year is shown as bar graph. In the upper right corner the part of supernovae that is certainly recognized as Type Ia supernovae is shown. In the lower part of the diagram cutouts of the upper diagrams until 1991 are shown with a scaled ordinate. The data are taken from the IAU Central Bureau for Astronomical Telegrams. See text for details.

supernovae is shown. In the lower right corner a cutout of the upper diagram until 1991 with a scaled ordinate is shown.
Especially those supernovae that differ somewhat from the canonical behavior are very interesting. They allow for model testing, that is the determination of to what extent the models reproduce a process quantitatively. One of the questions that remains is, whether the mechanisms of these supernovae are really different, or depart only from the ordinary and can finally be explained in the framework of our theoretical understanding.

Chapter 3

Parameter sensitivity of Type Ia supernovae simulations from a parameter estimation perspective

Parameter estimation is a term for mathematical procedures to obtain reasonable values for model parameters based on data. The identification and estimation of parameters is an inverse problem, and thus belongs to a class of mathematical problems that are commonly hard to handle and not always uniquely solvable. However, compared to the classical forward problem, mathematical parameter estimation has many advantages, e.g., several parameters can be determined simultaneously, with distinct error ranges.

On the one hand there are often sets of noisy experimental and observational data. On the other hand there are theoretical models that are supposed to correctly reproduce a given process quantitatively. Although the first fine analysis of a star[1] was performed more than 70 years ago (Unsöld 1942a,b,c, 1944) and much progress has been achieved since, an orderly mathematical corresponding error analysis does not exist. Even today the process of parameter estimation often involves parameter tuning by hand or comparing the observed spectra with a grid of synthetic flux spectra within relatively wide parameter ranges. In astronomy, a well established technique is the minimum distance method (Bailer-Jones 2002). A special case of this method is the well known χ^2 minimization. This approach goes back to A.-M. Legendre [2] and J. C. F. Gauss[3]. J.-L. Lagrange introduced algebraic equations as constraints into the minimization problem[4]. Later inequalities were introduced as constraints (Karush 1939; Kuhn & Tucker 1951), nowadays we know it as Karush-Kuhn-Tucker (KKT) conditions. They form the generalized method of Lagrange multipliers.

Recently, Bock (1981, 1987) developed a boundary value problem approach and applied it, e.g., to the denitrogenation of pyridine[5], where the solution of the boundary value problem and the minimization are performed simultaneously. He used a system of ordinary differential equations as a model for the reaction kinetics.

In astronomy, classically, the problem of determination on the basis of a model grid and unconstrained minimization would in most cases require the calculation of 10^n atmosphere

[1] Tau Scorpii

[2] A. M. Legendre, 1805, *Nouvelles méthodes pour la détermination des orbites des comètes*

[3] Carolo Friderico Gavss, 1809, *Theoria motvs corporvm coelestivm in sectionibvs conicis solem ambientivm*

[4] J.-L. Lagrange, 1788, *Méchanique analitique; par M. de la Grange, [...]*

[5] C_5H_5N, a basic heterocyclic organic compound that can be recycled into the valuable substances ammonia NH_3 and pentane C_5H_{10} under the influence of several catalysts. For more details see Bock (1981, 1987).

models with n being the number of free parameters (cf. Wehrse & Rosenau 1997) and especially for light curves of Type Ia supernovae, Section 5.3). Despite the effort to calculate and store this large number of synthetic spectra this method is much faster than the empirical method of changing parameters until the calculated spectrum converges to the observed one. Even for experienced practitioners, the latter approach takes longer and can be at most randomly objective. Reliable error estimations are hardly available at all. The usual method to estimate the accuracy by comparing analysis from different authors does not necessarily yield good results. The discussion on the first carbon dwarf star (Gass et al. 1988) and on the iron abundance of Vega (Sadakane 1990) illustrates the problem. A detailed discussion of errors in astronomy and particularly in spectroscopy is given in Wehrse (1991).
However, the method developed by Bock (1981, 1987) is now used in many fields, and we plan to apply it directly to the astrophysical problem of parameter sensitivity of Type Ia supernovae.
We describe the parameter estimation problem as a process, which can be modeled by systems of partial differential equations.
From modeling, there are the state variables,

$$\mathrm{y}(t,\tau,\lambda,\mathscr{P}), \tag{3.1}$$

y includes the states, i.e., dependent variables. The states of the model are the solutions of the governing equations, e.g., partial differential equations, such as the time dependent radiative transfer equation (cf. Section 4.4, Eq. (4.66)). The independent variables are, e.g., the time t, a local variable τ_i, and the wavelength λ_i. It is assumed that the object, for which the spectral analysis is carried out, is fully described by the parameter vector for the model

$$\mathscr{P}_m = \left(T_{eff}, g, \epsilon_\mathrm{a}, \xi, \ldots\right). \tag{3.2}$$

It is noted, that the element abundances ϵ_a depend on the number of considered elements.
For the model equations we write in general form

$$\mathrm{F}(\dot{\mathrm{y}},\mathrm{y},\mathscr{P}_m) = 0, \tag{3.3}$$

which contains differential operators, initial conditions, and boundary conditions.
We assume that for given $\mathscr{P}$, F has a unique solution, $\mathrm{y}(t,\tau,\lambda\,\mathscr{P}_m)$.
Adapted to the measurable values, the model response is

$$h\left(t,\lambda,\mathrm{y},\mathscr{P}_h\right). \tag{3.4}$$

The parameter vector $\mathscr{P}$ is composed of the parameter vector of the model (Eq. (3.2)) and the parameter vector of observation $\mathscr{P}_h$

$$\mathscr{P} = \begin{pmatrix}\mathscr{P}_m\\ \mathscr{P}_h\end{pmatrix}. \tag{3.5}$$

From observations we have the measured values η_{ij} at time points t_j, $j = 1,\ldots,N_t$, and wavelengths λ_i with known variances σ_i^2, $i = 1,\ldots,N_\lambda$.
We assume the data obey a nonlinear regression

$$\eta_{ij} = h\left(t_j,\lambda_i,y,\mathscr{P}_h\right) + \varepsilon_{ij} \tag{3.6}$$

with given observation functions h_{ij} and ε_{ij} stochastic errors, that are assumed to be independent and normally distributed,

$$\varepsilon_{ij} \sim \mathcal{N}\left(0, \sigma_i^2\right). \tag{3.7}$$

The ε_{ij} does not depend on the observation epoch.
In parameter estimation the partial differential equation system is treated as an implicit constraint. The parameter estimation problem is given by the minimization of a sum of weighted residuals and can be written for the corresponding norm as (cf. Bock 1987),

$$\min_{y,\mathscr{P}} = \sum_{j=1}^{N_t} \sum_{i=1}^{N_\lambda} \frac{\left(\eta_{ij} - h\left(t_j, \lambda_i, y, \mathscr{P}\right)\right)^2}{\sigma_i^2}. \tag{3.8}$$

The minimizing of Eq. (3.8) is a maximum likelihood estimate. The obtained variables fulfill the model equations, subject to

$$\mathrm{F}(\dot{\mathrm{y}}, \mathrm{y}, \mathscr{P}_m) = 0. \tag{3.9}$$

Since the measured values are random variables, there are also the estimated parameters.
The sensitivities

$$\begin{aligned} \mathscr{J}_{ij,k} &= \frac{\mathrm{d}}{\mathrm{d}\mathscr{P}_k} \frac{1}{\sigma_i} \left(\eta_{ij} - h\left(t_j, \lambda_i, y, \mathscr{P}_h\right)\right) \\ &= -\frac{1}{\sigma_i} \left(\frac{\partial h}{\partial \mathrm{y}} \frac{\partial \mathrm{y}}{\partial \mathscr{P}_k} + \frac{\partial h}{\partial \mathscr{P}_k} \right) \Bigg|_{\substack{\lambda=\lambda_i \\ t=t_j}} \end{aligned} \tag{3.10}$$

form the entries of the Jacobian $\mathscr{J} \in \mathbb{R}^{N_t \cdot N_\lambda \times n_{\mathscr{P}}}$ of the residuals with respect to the parameters. The number of the parameter is denoted by k.
From $\mathscr{J}$, the variance-covariance matrix of the parameter estimate can be calculated by

$$\mathscr{C}(\hat{\mathscr{P}}) = \mathscr{J}^+ \left(\mathscr{J}^+\right)^T = \left(\mathscr{J}^T \mathscr{J}\right)^{-1}, \tag{3.11}$$

where $\hat{\mathscr{P}}$ denotes the estimated parameters and $\mathscr{J}^+$ the solution operator,

$$\mathscr{J}^+ = \left(\mathscr{J}^T \mathscr{J}\right)^{-1} \mathscr{J}^T, \tag{3.12}$$

which is a generalized inverse of $\mathscr{J}$.
$\mathscr{J}$ and $\mathscr{C}$ do not depend on the observational data. The diagonal elements of $\mathscr{C}$ can be interpreted as variances of the particular parameters. The off-diagonal elements are their covariances and describe their correlation.
In order to enforce model validity during the parameter estimation computations, constraints can be considered, e.g., box constraints to the parameters

$$\mathscr{P}_k^l < \mathscr{P}_k < \mathscr{P}_k^u. \tag{3.13}$$

$\mathscr{P}_k$ (cf. Eqs. (3.5) and (3.2)) may represent, e.g., element abundances, temperature, or the parametrized line scattering scattering fraction. The latter can be set for line scattering $\varepsilon_{\text{line}}$

to be in a range close to 0, which means that almost 100 % of photons are scattered via line scattering, and 1, which means that no photons are scattered,

$$\varepsilon_{\text{line}} \in]0,1]\,. \tag{3.14}$$

Normally $\varepsilon_{\text{line}}$ is computed and not used as a parameter. For test and special cases it can be used as a parameter (cf. Sections 5.5 and 5.6).
The parameters are obtained by least squares minimization constrained by a boundary value problem.
An approximation for the $100 \cdot (1-\alpha)\%$ confidence region of the estimated parameters $\hat{\mathscr{P}}$ is described by the linearized confidence range

$$\begin{aligned} G(\alpha, \hat{\mathscr{P}}) &= \left\{ \hat{\mathscr{P}} + \delta\mathscr{P} \;\middle|\; \delta\mathscr{P}^T \mathscr{J}^T \mathscr{J}\, \delta\mathscr{P} \leqslant \gamma^2(\alpha) \right\} \\ &= \left\{ \hat{\mathscr{P}} + \delta\mathscr{P} \;\middle|\; \delta\mathscr{P}^T \mathscr{C}^{-1}\, \delta\mathscr{P} \leqslant \gamma^2(\alpha) \right\} \\ &= \left\{ \hat{\mathscr{P}} + \delta\mathscr{P} \;\middle|\; \left\| \mathscr{C}^{-\frac{1}{2}}\, \delta\mathscr{P} \right\|_2^2 \leqslant \gamma^2(\alpha) \right\}, \end{aligned} \tag{3.15}$$

$\| \quad \|_2^2$ is the square of the Euclidean norm, and $\gamma(\alpha)$ the quantile for the value α of the chosen distribution. In this case, it is the χ^2 distribution[6].
The confidence ellipsoid of the parameter estimate is described by $\mathscr{C}^{-1}$.

[6] Because we assume that we know the variances σ_i^2

Chapter 4

Modeling spectra and light curves of Type Ia supernovae with PHOENIX

4.1 Radiative transfer

4.1.1 Radiative transfer in general

Radiative transfer describes the energy transfer in the form of electromagnetic radiation. If crossing material, radiation is influenced by absorption, emission, and scattering. Many of these effects can not be explained classically, but must be considered quantum mechanically. Lord Rayleigh (1871) was the first who considered scattering effects. He developed a mathematical boundary value problem, with many assumptions, often not accurately stated and demonstrated that the sky is blue due to the stronger scattering of light at shorter wavelengths. Next, Mie (1908) extended this theory by looking at additional absorption. Mathematically, it is again a boundary value problem and now even more complex. The first person who considered multiple scattering was Schuster (1903, 1905), more than a century ago. He assumed that the light passes through a plane in two directions, both perpendicular to the plane. Mathematically, Schuster's differential equations depend only on the depth of penetration. Schwarzschild (1914) integrated over all directions in the forward and in the backward hemisphere, so that his equations in addition to the depth of penetration take into account the angle of incidence θ, i.e., for the forward direction $0 < \theta \leqslant \frac{1}{2}\pi$ and for the backward direction $\frac{1}{2}\pi < \theta \leqslant \pi$. His equations are more general than in the original formulation.
Today, we can derive the radiative transfer equation in several ways, e.g., from the Boltzmann equation by linearization (Oxenius 1986), from quantum field theory (Sapar 1978; Landi Degl'Innocenti 1996), by means of a stochastic model (von Waldenfels 2009; von Waldenfels et al. 2011), or, as shortly introduced here, phenomenologically. Wehrse & Kalkofen (2006) summarized the progress in radiative transfer together since 1985.
Radiative transfer is important in all areas where light is used as diagnostic or modeling tool, e.g., in medicine, combustion engine design, environmental and plasma physics, and in astrophysics, where photons are by far the most important source of information. Therefore, especially for an astronomer, the modeling of the formation of the radiation field and its propagation is of particular interest. The radiation field links microscopic effects from the interaction of photons with matter to the observable macroscopic effects. Unfortunately, the computational effort is enormous, despite the progress in recent years in computer technology. In addition to the mathematical and numerical challenges, such as the strong variability (a few dex) of the extinction coefficient entering the radiative transfer equation and the enor-

mous number of atomic lines that have to be included. Nevertheless, in astrophysics, it is one of the most important equations that allows to examine the conditions in the Universe, a stellar atmosphere, or, as here in this work, the atmosphere of a Type Ia supernova.
In this chapter, the description of the radiation field and the basics of radiative transfer are introduced and briefly discussed.

4.1.2 The specific intensity and its moments

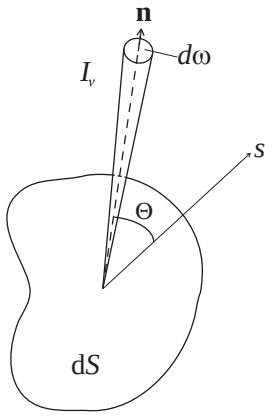

Figure 4.1: Geometric basis for the definition of the specific intensity I_ν (based on Unsöld (1968) and Mihalas (1978), with modifications). See text for details.

The radiation field of unpolarized or natural light is described by the specific intensity $I_\nu(\mathbf{r},\mathbf{s},\nu,t)$, which is in general a function of the position in space $\mathbf{r}$, the propagation direction $\mathbf{n} = (\cos\phi\sin\theta, \sin\phi\sin\theta, \cos\theta)^{\mathrm{t}}$, frequency ν, and the time variable t. The subscript refers to a normalized frequency interval (cf. Unsöld 1968). As can be seen in Figure 4.1, θ is the angle between the direction of the propagation of radiation $\mathbf{n}$ and the outward normal $\mathbf{s}$ to the plane dS. The radiation is filling a truncated cone $\mathrm{d}\omega = \sin\theta\,\mathrm{d}\theta\,\mathrm{d}\phi$ around the direction $\mathbf{n}$, through a point $\mathbf{P}$ of dS in a time interval dt, and a frequency range $\nu\ldots\nu+\mathrm{d}\nu$. This amount of energy d$\mathscr{E}$ is in astrophysics traditionally written as,

$$\mathrm{d}\mathscr{E} = I_\nu(\mathbf{r},\mathbf{n},\nu,t)\cos\theta\,\mathrm{d}\sigma\,\mathrm{d}t\,\mathrm{d}\omega\,\mathrm{d}\nu, \tag{4.1}$$

and goes back to Unsöld (1938) and Chandrasekhar (1950).
Alternatively, dealing with light in the particle picture, the specific intensity can be written by its relation to the photon distribution function $\phi(\mathbf{r},\mathbf{n},\mathbf{p},t)$ normalized in a particular way,

$$I_\nu(\mathbf{r},\mathbf{n},\nu,t) = \frac{h^4\nu^3}{c^2}\phi(\mathbf{r},\mathbf{n},\mathbf{p},t), \tag{4.2}$$

where h is the Planck constant[1], c the speed of light[2], and $\mathbf{p} = \frac{h\nu}{c}\mathbf{n}$ the photon momentum (Oxenius 1986).

[1] $h = 62606957(29)\cdot 10^{-34}$ J s
[2] $c = 2.99792458\cdot 10^{8}$ m s^{-1} (in vacuum)

In the wave picture, we have to use the more complex definition from quantum field theory (cf. Wehrse & Kalkofen 2006; Kanschat et al. 2009). The radiation field is given in terms of the electric and magnetic fields $\mathbf{E}(\mathbf{r},t)$ and $\mathbf{B}(\mathbf{r},t)$. Since these two fields are linked to each other through Maxwell's equations and special relativity, it is sufficient to use only one of the variables. Here we have chosen the electric field $\mathbf{E}(\mathbf{r},t)$, which is in a plane perpendicular to the propagation direction and oscillates in phase with $\mathbf{B}(\mathbf{r},t)$. It is given by Maxwell's equation $\mathbf{E} = -\nabla\Phi - \frac{\partial \mathbf{A}}{\partial t}$, which is reformulated in terms of (magnetic) vector potential $\mathbf{A}$ and (electric) scalar potential Φ (Stenflo 1994),

$$\mathbf{E}(\mathbf{r},t) = -\frac{\partial \mathbf{A}}{\partial t} = \mathbf{E}^{+}(\mathbf{r},t) + \mathbf{E}^{-}(\mathbf{r},t), \tag{4.3}$$

with the two field vectors $\mathbf{E}^{+}(\mathbf{r},t)$ and $\mathbf{E}^{-}(\mathbf{r},t)$ at the space-time point $(\mathbf{r},t)$ (Mandel & Wolf 1995; Vogel & Welsch 2006),

$$\mathbf{E}^{+}(\mathbf{r},t) = \frac{1}{\sqrt{V}} \sum_{\mathbf{k},\sigma} l(\omega)\hat{\mathbf{a}}_{\mathbf{k}\sigma}\mathbf{e}_{\mathbf{k}\sigma} \exp(i(\mathbf{k}\cdot\mathbf{r} - \omega t)), \tag{4.4}$$

$$\mathbf{E}^{-}(\mathbf{r},t) = \left(\mathbf{E}^{+}(\mathbf{r},t)\right)^{\dagger}, \tag{4.5}$$

where V is the quantization volume, $l(\omega)$ a function of ω, e.g., $\sqrt{\frac{\hbar}{2\omega\epsilon_0}}$ for the vector potential, $\hbar$ the Dirac constant[3], ϵ_0 the vacuum permittivity[4], $\hat{\mathbf{a}}_{\mathbf{k}\sigma}$ an operator, $\mathbf{e}_{\mathbf{k}\sigma}$ is an unit polarization vector orthogonal to the wave vector $\mathbf{k} = k\mathbf{n}$, and ω the corresponding frequency. We assume that the field is in a mixed state and summing over all final states $\langle\psi_j|$ and thereafter over all initial states $\langle\psi_i|$,

$$\begin{aligned}
\mathbf{I}(\mathbf{r},t) &= \sum_{\psi_j}\sum_{\psi_i} \langle\psi_i|\mathbf{E}^{-}(\mathbf{r},t)|\psi_j\rangle \langle\psi_j|\mathbf{E}^{+}(\mathbf{r},t)|\psi_i\rangle \\
&= \sum_{\psi_i} \langle\psi_i|\mathbf{E}^{-}(\mathbf{r},t)\mathbf{E}^{+}(\mathbf{r},t)|\psi_i\rangle \\
&= \mathrm{Tr}\left(\hat{\rho}(\mathbf{r},t)\mathbf{E}^{-}(\mathbf{r},t)\mathbf{E}^{+}(\mathbf{r},t)\right).
\end{aligned} \tag{4.6}$$

The details with the density operator $\hat{\rho}(\mathbf{r},t)$ defined by

$$\hat{\rho}(\mathbf{r},t) = \sum_i P_i |\psi_i\rangle \langle\psi_i| \tag{4.7}$$

and characterizes an ensemble of states $\langle\psi_i|$ where P_i is the probability that a randomly selected particle of the ensemble is in the state, which is described by the wave function ψ_i (Cohen-Tannoudji et al. 1999).
The Stokes vector may be expressed as

$$\mathbf{I} = \begin{pmatrix} I \\ Q \\ U \\ V \end{pmatrix} = \begin{pmatrix} G_{11}^{(1)} + G_{22}^{(1)} \\ G_{12}^{(1)} + G_{21}^{(1)} \\ i\left(G_{12}^{(1)} - G_{21}^{(1)}\right) \\ G_{11}^{(1)} - G_{22}^{(1)} \end{pmatrix}, \tag{4.8}$$

[3] $\hbar = \frac{h}{2\pi} = 1.054571726(47)\cdot 10^{-34}$ J s
[4] $\epsilon_0 = 8.854187817[\ldots]\cdot 10^{-12}$ F m^{-1}

by the generalized n-th order correlation tensor $\mathbf{G}^{(n)}$ (Stenflo 1994; Wehrse & Kalkofen 2006),

$$G^{(n)}_{i_1\ldots i_{2n}}(\mathbf{r}_1,t_1,\ldots,\mathbf{r}_{2n},t_{2n}) \\ = \mathrm{Tr}\left(\rho \mathbf{E}^-_{i_1}(\mathbf{r}_1,t_1)\ldots\mathbf{E}^-_{i_n}(\mathbf{r}_n,t_n)\mathbf{E}^+_{i_{n+1}}(\mathbf{r}_{n+1},t_{n+1})\ldots\mathbf{E}^+_{i_{2n}}(\mathbf{r}_{2n},t_{2n})\right). \tag{4.9}$$

Of particular interest are angle averages of the specific intensity.
The mean intensity or zeroth angle moment (J) is obtained by integrating the specific intensity (I) over the solid angle (ω),

$$J_\nu(\mathbf{r},\nu,t) = \frac{1}{4\pi}\oint_{4\pi} I_\nu(\mathbf{r},\mathbf{n},\nu,t)\,\mathrm{d}\omega. \tag{4.10}$$

The index ν refers to an interval $\mathrm{d}\nu$ around ν and provides information about the transformation behavior (cf. Unsöld 1968).
Using $\mathrm{d}\omega = sin\theta\,\mathrm{d}\theta\,\mathrm{d}\phi = -\mathrm{d}\mu\,\mathrm{d}\phi$, with $\mu = \cos\theta$ and assuming that the specific intensity is independent of the azimuth angle (ϕ), we obtain for the 1D case (from Eq. (4.10)),

$$\begin{aligned} J_\nu(r,\nu,t) &= \frac{1}{4\pi}\int_0^{2\pi}\mathrm{d}\phi\int_{-1}^{1} I_\nu(r,\mu,\nu,t)\,\mathrm{d}\mu \\ &= \frac{1}{2}\int_{-1}^{1} I_\nu(r,\mu,\nu,t)\,\mathrm{d}\mu. \end{aligned} \tag{4.11}$$

Chandrasekhar (1939, 1950) and Unsöld (1938, 1968) denote this quantity with J, while Schwarzschild and Kourganoff (1952) denote it with $\bar{I}$. Its physical meaning is that it is a direct measure of the energy density of radiation (Unsöld 1968),

$$u_\nu(\mathbf{r},\nu,t) = \frac{4\pi}{c} J_\nu(\mathbf{r},\nu,t). \tag{4.12}$$

The first moment of I is the monochromatic flux,

$$\begin{aligned} \mathbf{F}_\nu(\mathbf{r},\nu,t) &= \oint_{4\pi}\mathbf{n} I_\nu(\mathbf{r},\mathbf{n},\nu,t)\,\mathrm{d}\omega \\ &= \int_0^{2\pi} d\phi\int_{-1}^{1}\begin{pmatrix}\cos\phi\sin\theta\\ \sin\phi\sin\theta\\ \cos\theta\end{pmatrix} I_\nu(\mathbf{r},\mathbf{n},\nu,t)\sin\theta\,\mathrm{d}\theta. \end{aligned} \tag{4.13}$$

The monochromatic flux defines the rate of flow of radiant energy across dS per unit area and per unit frequency interval. In spherical 1D media $\mathbf{F}_\nu(\mathbf{r},\nu,t) = (0,0,F_\nu(r,\nu,t))^t$ is a scalar,

$$F_\nu(r,\nu,t) = 2\pi\int_{-1}^{1} I_\nu(r,\mu,\nu,t)\mu\,\mathrm{d}\mu. \tag{4.14}$$

This yields, by definition, the first moment of the specific intensity or the Eddington flux,

$$H_\nu(r,\nu,t) = \frac{1}{2}\int_{-1}^{1} I_\nu(r,\mu,\nu,t)\mu\,\mathrm{d}\mu, \tag{4.15}$$

it refers to the vertical or radial component of the flux divided by 4π.
The second moment of the specific intensity is,

$$K_\nu(r,\nu,t) = \frac{1}{2}\int_{-1}^{1} I_\nu(r,\mu,\nu,t)\mu^2 \,\mathrm{d}\mu. \tag{4.16}$$

There are also higher moments, but they only play a role in mathematics and theoretical considerations.

4.1.3 Interaction between radiation and matter

Further variables to phenomenologically describe the interaction between radiation and matter are emission, described by the function η_ν, absorption, described by the absorption coefficient κ_ν, and scattering, described by the scattering coefficient σ_ν. They depend on frequency, ionization and excitation level, element of solid angle $\mathrm{d}\omega$, as well as the chemical composition of the matter.
The change of the intensity of an uncollimated ray along the direction $\mathbf{n}$, along a path $\mathrm{d}\mathbf{r}$ can be described by extinction and emission. If we assume the intensity is independent of the azimuth angle (ϕ) (cf. Eq. (4.11)) the decrease or attenuation by extinction along a path length $\mathrm{d}s$ (and an infinitesimal surface $\mathrm{d}S$) can be written as,

$$\mathrm{d}I_\nu(r,\mu,\nu,t)_- = -\chi_\nu(r,\mu,\nu,t)\, I_\nu(r,\mu,\nu,t)\,\mathrm{d}s, \tag{4.17}$$

where the extinction includes absorption and scattering,

$$\chi_\nu(r,\mu,\nu,t) = \kappa_\nu(r,\mu,\nu,t) + \sigma_\nu(r,\mu,\nu,t). \tag{4.18}$$

Physically, the two quantities, absorption and scattering, are different in the energy exchange, which is carried out by absorption on matter in scattering over the radiation field.
The increase by emission can be written as,

$$\mathrm{d}I_\nu(r,\mu,\nu,t)_+ = \eta_\nu(r,\mu,\nu,t)\,\mathrm{d}s. \tag{4.19}$$

The ratio of the absorption coefficient κ_ν and extinction coefficient χ_ν is called thermal coupling or deexcitation coefficient ε_ν,

$$\varepsilon_\nu(r,\mu,\nu,t) = \frac{\kappa_\nu(r,\mu,\nu,t)}{\chi_\nu(r,\mu,\nu,t)}. \tag{4.20}$$

4.1.4 The equation of radiative transfer

Radiation transport is the connection between the microscopic interaction of photons with atoms and molecules and the macroscopic quantities, e.g., the radiation flux. It is the link between the evolutionary and hydrodynamical calculations, which are used for the calculations of realistic model atmospheres, which can be compared to real observational data. For the calculation of model atmospheres, radiative transfer is required, described by the radiative transfer equation, a linearized Boltzmann equation, which is a (partial) first order integro-differential equation.

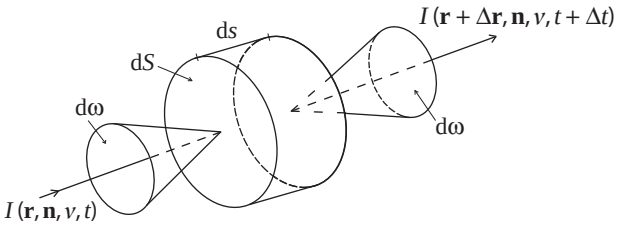

Figure 4.2: Geometric volume element for the derivation of the radiative transfer equation (based on Mihalas (1978) and Mihalas & Weibel Mihalas (1984), with modifications). See text for details.

Mihalas (1978) and Mihalas & Weibel Mihalas (1984) gave an introduction to radiative transfer used for the modeling of stellar atmospheres.
If one considers a system to change the energy of the radiation field through a volume element of length ds and surface dS in a solid angle dω in the direction $\mathbf{n}$ normal to dS, in the frequency interval dν, at time interval dt, the amount of the difference of the energy emanating from the volume element at the place $\mathbf{r}+\Delta\mathbf{r}$ at time $t+\Delta t$ of the energy entering the volume element at the place $\mathbf{r}$ at time t to be equal to the difference of the amount that is generated by emission and destroyed by absorption (Figure 4.2),

$$\begin{aligned}[I(\mathbf{r}+\Delta\mathbf{r},\mathbf{n},\nu,t+\Delta t)-I(\mathbf{r},\mathbf{n},\nu,t)]\,\mathrm{d}S\,\mathrm{d}\omega\,\mathrm{d}\nu\,\mathrm{d}t = \\ [\eta(\mathbf{r},\mathbf{n},\nu,t)-\chi(\mathbf{r},\mathbf{n},\nu,t)I(\mathbf{r},\mathbf{n},\nu,t)]\,\mathrm{d}s\,\mathrm{d}S\,\mathrm{d}\omega\,\mathrm{d}\nu\,\mathrm{d}t.\end{aligned} \tag{4.21}$$

In the limit $s\to 0$ of the path length s along the ray and $\Delta t=\frac{\mathrm{d}s}{c}$, there is,

$$\left[\frac{1}{c}\left(\frac{\partial}{\partial t}\right)+\left(\frac{\partial}{\partial s}\right)\right]I_\nu(\mathbf{r},\mathbf{n},\nu,t)=\eta_\nu(\mathbf{r},\mathbf{n},\nu,t)-\chi_\nu(\mathbf{r},\mathbf{n},\nu,t)I_\nu(\mathbf{r},\mathbf{n},\nu,t). \tag{4.22}$$

Here, c is the velocity of light, I_ν the monochromatic specific intensity of radiation, η_ν the emission coefficient, and χ_ν the extinction coefficient. The mathematical expression for $\frac{\partial}{\partial s}$ depends on geometry. For curvilinear coordinate systems:

$$\frac{\partial}{\partial s}=\mathbf{n}\nabla+\left(\frac{\mathrm{d}\mathbf{n}}{\mathrm{d}s}\right)\nabla_{\mathbf{n}}, \tag{4.23}$$

$\mathbf{n}\nabla$ stands for the directional derivative, $\left(\frac{\mathrm{d}\mathbf{n}}{\mathrm{d}s}\right)\nabla_{\mathbf{n}}$ stands for the shift of the reference point $\mathbf{r}$ along the path d$s\mathbf{n}$ in the direction of the propagation vector $\mathbf{n}$, with $\nabla_{\mathbf{n}}$ the gradient with respect to the direction cosines of $\mathbf{n}$.
For the consideration of this type of linear differential equation it is common to change the independent variable. Therefore, we introduce the optical depth; it is a measure of the decay of the intensity from $\mathbf{r}$ to $\mathbf{r}+s\,\mathbf{n}$ and given by,

$$\tau(\mathbf{r},\mathbf{r}+s\,\mathbf{n},\nu,t)=\int_0^s\chi_\nu(\mathbf{r}+s'\,\mathbf{n},\mathbf{n},\nu,t)\,\mathrm{d}s'=\int_0^s\frac{\mathrm{d}s'}{\tilde{\lambda}(\mathbf{r}+s'\,\mathbf{n},\mathbf{n},\nu,t)}, \tag{4.24}$$

where $s = |(\mathbf{r} + s\,\mathbf{n}) - \mathbf{r}|$, $\mathrm{d}s'$ is the path length increment, and $\mathbf{n}$ is the unit vector pointing from $\mathbf{r}$ to $\mathbf{r} + s\,\mathbf{n}$. The second form indicates that $\tau(\mathbf{r}, \mathbf{r} + s\,\mathbf{n}, \nu, t)$ is measured in number of photon mean free paths $\tilde{\lambda}$ between $\mathbf{r}$ and $\mathbf{r} + s\,\mathbf{n}$.
Dividing Eq. (4.22) by the term of the extinction, χ_ν, we get on the left side of the equation the concept of optical depth and on the right side, by definition, the source function[5],

$$S_\nu(\mathbf{r}, \mathbf{n}, \nu, t) = \frac{\eta_\nu(\mathbf{r}, \mathbf{n}, \nu, t)}{\chi_\nu(\mathbf{r}, \mathbf{n}, \nu, t)}. \tag{4.25}$$

The radiative transfer equation can than be written in the general form, containing the optical depth and the source function.
Eq. (4.22) can be solved analytically only for very special cases (Chandrasekhar 1950; Kourganoff 1952; Kalkofen & Wehrse 1982; Cannon 1985; Efimov et al. 1995; Baschek et al. 1997; Dittmann 1997; Efimov et al. 2001). One of the assumptions to obtain an analytical solution is that of a constant deexcitation coefficient ε, or ε approximated by a piecewise constant function (Kryzhevoi et al. 2001). Leaving trivial examples, such as no absorption and no emission, or the source function is already known the radiative transfer equation becomes an integro-differential equation, because emission into solid angles $\mathrm{d}\omega$ depends on the intensity in solid angles $\mathrm{d}\omega'$, integrated over the latter due to scattering from $\mathrm{d}\omega'$ into $\mathrm{d}\omega$.
However, the availability of ever-faster computers and parallelization has ensured that the radiative transfer equation can be usually solved numerically and also more focused effort in this direction. The calculation of the radiation field from a given source function is called the "formal solution" and denoted symbolically by the (linear) Λ operator, or rather a Λ matrix (e.g., Mihalas 1978; Baschek et al. 1996),

$$S = \Lambda S + S_{bc}, \tag{4.26}$$

where S_{bc} represents the boundary condition, with the solution

$$S = (1 - \Lambda)^{-1} S_{bc}. \tag{4.27}$$

The discretization of Eq. (4.26) taking into account dependent variables, depth, angle, and frequency, leads to a very large system of linear equations whose inversion would be extremely costly and time consuming.
By simply extending the Λ operator by operator splitting, by a new approximate Λ^* operator,

$$\Lambda = \Lambda^* + (\Lambda - \Lambda^*), \tag{4.28}$$

this method is faster and provides better convergence behavior than the classic iteration that is intolerably slow, especially in optically thick media and small ε[6].
In astrophysics, the operator splitting method, mathematically it belongs to the same family as Jacobi or Gauss-Seidel iteration (Golub & Van Loan 1996), is called accelerated (or approximate) lambda iteration (Cannon 1973a; Scharmer 1984; Peraiah 1984, 2001) often abbreviated to "ALI".

[5] In German "Ergiebigkeit" (Unsöld 1968)

[6] For optically thick media and small ε the largest eigenvalue of the amplification matrix is very close to unity and, therefore, the convergence rate of the Λ-iteration is very poor (cf. Hauschildt 1992).

Because of its importance the formalism is shown here shortly, following Hamann (1985, 1986, 1987). The mean intensity J_ν is calculated from a given source function S_ν, the formal solution, and denoted symbolically by the linear operator Λ,

$$J_\nu = \Lambda_\nu S_\nu. \tag{4.29}$$

The averaged mean intensity is given by

$$\overline{J} = \int_{-\infty}^{\infty} \phi(\nu) J_\nu \, \mathrm{d}\nu, \tag{4.30}$$

where $\phi(\nu)$ is the normalized profile function. We rewrite Eq. (4.29)

$$\overline{J} = \Lambda S, \tag{4.31}$$

where $\Lambda = \int_{-\infty}^{\infty} \phi(\nu)\Lambda_\nu \, \mathrm{d}\nu$ is given by definition. In the case of a two-level atom, the source function is given by $S = (1-\varepsilon)\overline{J} + \varepsilon B$. The first term describes the scattering process, and the second containing the Planck function B [7], denotes the thermal sources. From Eq. (4.30) and the source function S we get

$$\overline{J} = \Lambda \left[(1-\varepsilon)\overline{J} + \varepsilon B \right]. \tag{4.32}$$

The solution is found iteratively by Λ iteration (Cannon 1973a,b; Scharmer 1981)

$$\overline{J}_{\mathrm{new}} = \Lambda \left[(1-\varepsilon)\overline{J}_{\mathrm{old}} + \varepsilon B \right], \tag{4.33}$$

respectively, from Eq. (4.31)

$$\overline{J}_{\mathrm{new}} = \Lambda S_{\mathrm{old}}, \tag{4.34}$$

and

$$S_{\mathrm{new}} = (1-\varepsilon)\overline{J}_{\mathrm{new}} + \varepsilon B. \tag{4.35}$$

The following equations are used for an iteration scheme in order to obtain the solution of the radiative transfer: As mentioned above, for large optical depths and small ε, this iteration scheme converges extremely slowly (Mihalas et al. 1975). Therefore, an operator splitting method is used, Eq. (4.28), with a new approximate operator Λ^*, similar to the original Λ operator. Thus, the Eqs. (4.34) and (4.35) can be written

$$\overline{J}_{\mathrm{new}} = \Lambda^* S_{\mathrm{new}} + (\Lambda - \Lambda^*) S_{\mathrm{old}}. \tag{4.36}$$

As noted by Hamann (1987), $\Lambda - \Lambda^*$ does not yield contributions from optically thick line cores so that the convergence problems from the conventional Λ iteration are avoided, although that this term acts on the old source function. We set ΛS_{old} equal to $\overline{J}_{\mathrm{fs}}$ and assume that Λ^* can be easily converted, so that substituting the source function of a two-level atom in Eq. (4.36) we get

[7] $B_\nu(\nu,T) = \frac{2h\nu^3}{c^2} \frac{1}{exp(\frac{h\nu}{kT})-1}$ respectively, as a function of wavelength (witht $c = \lambda\nu$) $B_\lambda(\lambda,T) = \frac{2hc^2}{\lambda^5} \frac{1}{exp(\frac{hc}{k\lambda T})-1}$

$$\overline{J}_{\rm new} = \left[1 - \Lambda^*(1-\varepsilon)\right]^{-1} \left[\overline{J}_{\rm fs} - \Lambda^*(1-\varepsilon)\overline{J}_{\rm old}\right]. \tag{4.37}$$

This equation is used to obtain the new value for $J_{\rm new}$, which is a formal solution. The choice of a reasonable $\Lambda^\star$ is important. Hauschildt & Baron (1999) described the construction of the $\Lambda^\star$ matrix based on Olson & Kunasz (1987). The application of this method leads to an unprecedented reduction of computation time and thus allows first the calculation of complex radiation transport problems.
Other methods that accelerate the convergence behavior are conjugate gradient algorithm (Auer 1987), or multigrid method (Steiner 1991, 2003).

4.2 Thermodynamical approximations

4.2.1 Thermodynamic equilibrium and local thermodynamic equilibrium

The simplest approach to describe gas in an excited state is the assumption of thermodynamic equilibrium (TE). In TE the radiation field is given by Planck's formula for blackbody radiation[8] (Unsöld 1968),

$$I_\nu(\nu,T) = B_\nu(\nu,T) \equiv S_\nu(\nu,T). \tag{4.38}$$

In TE the intensity $I_\nu(\nu,T)$ is given, according to Kirchhoff's theorem, by a universal function that depends only on the frequency and temperature.
For a stellar atmosphere the requirement of TE means that the optical depth must be infinitely large. The state of the gas[9] is given by two thermodynamic variables. These are, e.g., the absolute temperature T and the total number density n.
In TE at temperature T, the atoms are distributed over their bound levels according to the Boltzmann excitation equation, so the relative population density of a state s above the ground state for the (ideal) gas in TE is given by the ratio of

$$\frac{n_{r,s}}{n_{r,0}} = \frac{g_{r,s}}{g_{r,0}} \exp\left(-\frac{\chi_{r,s}}{k_B T}\right) \tag{4.39}$$

(Unsöld 1968), where $n_{r,s}$ is the number density of atoms in excited level s of ionization state r, $n_{r,0}$ is the number density of atoms in excited level 0 of ionization state, that is the ground level, $g_{r,s}$ and $g_{r,0}$ are statistical weights assigned to the corresponding quantum state, $\chi_{r,s}$ is the excitation energy, k_B is the Boltzmann constant[10], and $\tilde{\chi}$ is the excitation potential in eV.
Applying the approximation for TE locally, one speaks of local thermodynamic equilibrium (LTE). Under this assumption, it is allowed to use the local values of n and T.
If we extend Eq. (4.39), we get the Saha ionization equation, which describes the ratio of the number of atoms in the ground states of the $r+1$, resp. r-times ionized atoms

$$\frac{n_{r+1,0}}{n_{r,0}} P_e = \frac{g_{r+1,0}}{g_{r,0}} 2 \frac{(2\pi m)^{\frac{3}{2}} (k_B T)^{\frac{5}{2}}}{h^3} \exp\left(-\frac{\chi_r}{k_B T}\right) \tag{4.40}$$

(Unsöld 1968), where $n_{r+1,0}$ and $n_{r,0}$ are the population densities of the two ground states of the successive ionization stages r and $r+1$, P_e is the partial pressure of the free electrons[11], $g_{r+1,0}$ and $g_{r,0}$ are the statistical weights of the two ground levels, m the electron mass, h the Planck constant[12], and χ_r the ionization energy of stage r. However, these two equations can be written combined. Rewriting Eq. (4.39)

$$\frac{n_{r,s}}{n_r} = \frac{g_{r,s}}{u_r} \exp\left(-\frac{\chi_{r,s}}{k_B T}\right) \tag{4.41}$$

[8] $B_\nu(\nu,T) = \frac{2h\nu^3}{c^2} \frac{1}{exp(\frac{h\nu}{k_B T})-1}$
[9] The distribution of atoms over bound and free states
[10] $k_B = 1.3806488(13) \cdot 10^{-23}$ J K^{-1}
[11] $P_e = n_e \cdot k_B T$
[12] $h = 62606957(29) \cdot 10^{-34}$ J s

with the partition function

$$u_r(T) = \sum_{s=0}^{\infty} g_{r,s} \exp\left(-\frac{\chi_{r,s}}{k_B T}\right), \tag{4.42}$$

which is the sum over the states. From the Eqs. (4.40) and (4.41) we obtain the Saha-Boltzmann ionization equation

$$\frac{n_{r+1}}{n_r} P_e = \frac{u_{r+1}}{u_r} 2 \frac{(2\pi m)^{\frac{3}{2}} (k_B T)^{\frac{5}{2}}}{h^3} \exp\left(-\frac{\chi_r}{k_B T}\right), \tag{4.43}$$

it is the distribution of ion species for a plasma in LTE.
Using LTE, this means the same local temperature is used in the velocity distribution for all atoms and electrons. The (thermal) velocity distribution for the number of gas particles per unit volume having speeds between u and $u + \mathrm{d}u$ is Maxwellian and given by the Maxwell-Boltzmann (velocity) distribution

$$n(u)\,\mathrm{d}u = n\left(\frac{m}{2\pi k_B T}\right)^{\frac{3}{2}} \exp\left(-\frac{1}{2}\frac{mu^2}{k_B T}\right) 4\pi u^2\,\mathrm{d}u, \tag{4.44}$$

where n is the total number density, so number of particles per unit volume, $n(u) \equiv \frac{\partial n}{\partial u}$ is the number of particles with a velocity u, m is a particle's mass, k_B is the Boltzmann constant, T is the temperature of the gas in Kelvin, $\frac{1}{2}mu^2$ is the exponent of the distribution function is the kinetic energy of a gas particle, and $k_B T$ the characteristic thermal energy.
If a majority of the particles energy is equal to the thermal energy, the distribution has a peak at a most probable speed of

$$u_{\mathrm{mp}} = \sqrt{\frac{2k_B T}{m}}. \tag{4.45}$$

The high-speed exponential tail of the distribution function is the result of the root mean square speed

$$u_{\mathrm{rms}} = < u > = \sqrt{u^2} = \sqrt{\frac{3k_B T}{m}}. \tag{4.46}$$

4.2.2 Non-local thermodynamic equilibrium

Although LTE in a non isolated system, such as a star, strictly speaking, can not exist, it is a good approximation and well fulfilled at a high gas pressure. Near the surface of the atmosphere, or for atoms, molecules and ions with a simple level scheme there are significant deviations and a strong departure from the LTE situation. For such situations, one must consider a non-local thermodynamic equilibrium (non-LTE or NLTE). Equilibrium states must now be statistically considered. These equations of statistical equilibrium or rate equations must be solved. In the case of a static atmosphere we have the general form

$$n_{ik} \sum_{j \neq i} P_{ij}^k - \sum_{j \neq i} n_{jk} P_{ji}^k = 0 \tag{4.47}$$

(Mihalas 1978; Mihalas & Weibel Mihalas 1984), where n_{ik} is the number density of atoms in (excitation) state i of chemical species k, P_{ij}^{k} is the total transition radiative and collisional rate from level j to level i, and j is the ionization stage.
Taking into account certain processes, such as radiative rates with bound-bound and bound-free transitions, collisional rates, autoionization, and recombination we obtain a rate equation for the NLTE population n_i for each bound level L (Mihalas 1978; Mihalas & Weibel Mihalas 1984),

$$\sum_{j<i} n_j(R_{ji}+C_{ji}) - n_i\left[\sum_{j<i}\left(\frac{n_j}{n_i}\right)^*(R_{ij}+C_{ji}) + \sum_{j>i}^{k}(R_{ij}+C_{ij})\right] + \sum_{j>i}^{k} n_j\left(\frac{n_i}{n_j}\right)^*(R_{ji}+C_{ij}) = 0$$

$$(i = 1,\ldots,L), \tag{4.48}$$

where R_{ij} denotes the radiative upward rates $(i \to j)$ bound or free, as $n_i R_{ij}$ where

$$R_{ij} \equiv 4\pi \int_{\nu_0}^{\infty} \alpha_{ij}(\nu)\,\frac{1}{h\nu}\,J_\nu\,\mathrm{d}\nu, \tag{4.49}$$

R_{ji} the radiative downward rates $(j \to i)$ as $n_i\left(\frac{n_j}{n_i}\right)^* R_{ji}$ where

$$R_{ji} \equiv 4\pi \int_{\nu_0}^{\infty} \alpha_{ij}(\nu)\,\frac{1}{h\nu}\left(\frac{2h\nu^3}{c^2}+J_\nu\right)\exp\left(-\frac{h\nu}{kT}\right)\mathrm{d}\nu, \tag{4.50}$$

n_{ij}^* the LTE population density of any excitation level i of ion j in terms of the temperature T, the number density of free electrons n_e, and ground state population $n_{0,j+1}$ of ion $j+1$,

$$n_{ij}^* = C_I\, n_{0,j+1}\, n_e \frac{g_{ij}}{g_{0,j+1}} T^{-\frac{3}{2}} \exp\left(-\frac{\varepsilon_{Ij}-\varepsilon_{ij}}{kT}\right) \equiv n_{0,j+1}\, n_e \Phi_{ij}(T) \tag{4.51}$$

with the numerical constant $C_I = 2.07 \cdot 10^{-16}$ (in cgs units), and finally the total number of collision transition $(i \to j)$ rates

$$n_i C_{ij} = n_i n_e \int_{\nu_0}^{\infty} \sigma_{ij}(v)\, f(v)\, v\,\mathrm{d}v, \tag{4.52}$$

where $\sigma_{ij}(v)$ is the cross section for the transition, $f(v)$ is the Maxwellian velocity distribution, and v_0 is the is the velocity corresponding to the threshold energy E_{ij} of the transition. Always, unless electrons are non maxwellian, we have $n_i^* C_{ij} = n_i^* C_{ji}$.

4.3 Hydrodynamics of Type Ia supernova ejecta

4.3.1 The carbon deflagration model *W 7*

We use the 1D and well established carbon deflagration model *W 7* (Nomoto et al. 1984; Thielemann et al. 1986). Among the hydrodynamical models of carbon deflagration supernovae, it is considered as one of the standard models and confirmed in numerous calculations, e.g., Branch (1985b), Branch et al. (1985), and Baron et al. (2006).
The *W 7* model originates from a series of calculated models from Nomoto et al. (1984) and achieved the best fits to the observations. The *W 7* model assumes a white dwarf with initially $\approx 1M_{\odot}$, composed of $X(^{12}\mathrm{C} = 0.475)$, $X(^{16}\mathrm{O} = 0.5)$, and $X(^{22}\mathrm{Ne} = 0.025)$, which has cooled down for $5.8 \cdot 10^8$ yr. The white dwarf accretes mass in a binary system at a rate of $\dot{M} = 4 \cdot 10^{-8} M_{\odot}\,\mathrm{yr}^{-1}$. At the high mass transfer rate the white dwarf grows to nearly $\mathscr{M}_{Chan}$ ($M/M_{\odot} = 1.378$), its radius shrinks accordingly, whereas the temperature at the center ($T_c = 1 \cdot 10^7$ K) steadily rises. This is accomplished by compression, just as the increase in density at the center ρ_c from $3.4 \cdot 10^7 \mathrm{g\,cm}^{-3}$ (initial model) to $2.6 \cdot 10^9 \mathrm{g\,cm}^{-3}$ (ignition model). Another factor for the rise in the interior temperature can be the flow of heat by conduction from the outside inwards, caused by the higher temperature of the helium burning shell.

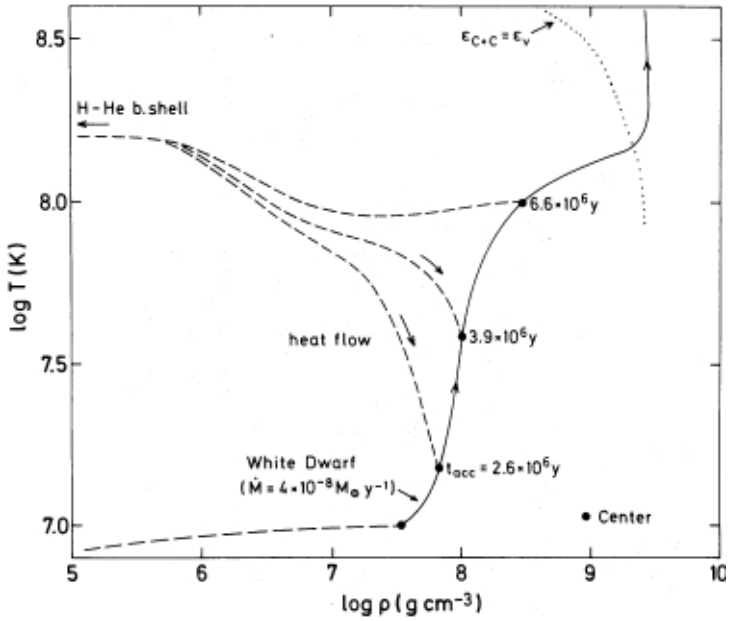

Figure 4.3: Shown is the evolution of the temperature as a function of the density of a white dwarf (solid lines), on which matter is accreted at a rate of $\dot{M} = 4 \cdot 10^{-8} M_{\odot}\,\mathrm{yr}^{-1}$ for the *W 7* model. The dashed lines represent the structure lines of the white dwarf where heat flows from the surface into the interior. The dotted line represents the ignition line of carbon burning. See text for details. The figure is from Nomoto et al. (1984), with modifications.

The temperature depends on the mass transfer rate, and is here, under the assumption of a steadily burning hydrogen-helium shell, roughly $1.5 \cdot 10^8$ K. With increasing $\dot{M}$ faster compression ignites the carbon at higher T_c and lower ρ_c, while smaller $\dot{M}$ T_c is lower and thus ρ_c ignition higher (Nomoto et al. 1984). In Figure 4.3 the evolution of the temperature as a function of the density of a white dwarf (solid lines) is shown, on which matter is accreted at a rate of $\dot{M} = 4 \cdot 10^{-8} M_\odot \, \mathrm{yr}^{-1}$ for the $W7$ model. The dashed lines represent the structure lines of the white dwarf where heat flows from the surface into the interior. The dotted line represents the ignition line of carbon burning defined by the nuclear energy generation rate and the neutrino loss rate $\epsilon_{C+C} = \epsilon_\nu$. Nomoto (1985) argued, that an accretion rate of $\dot{M} \gtrsim 4 \cdot 10^{-8} M_\odot \, \mathrm{yr}^{-1}$ produces only "relatively weak" shell flashes of hydrogen and helium and thus increases the mass of the white dwarf. Therefore, it is assumed that the accreted material is processed into carbon and oxygen at the same rate as the accretion.
Under these strongly degenerate conditions, carbon is ignited at the center. At these high central densities, the nuclear energy release is only $\sim 20\,\%$ of the Fermi energy of degenerate electrons (Nomoto 1985; Nomoto et al. 1996). Therefore, a (supersonic) detonation wave arises not directly. The acceleration of the flame speed is essentially performed by Rayleigh-Taylor instabilities, caused by density differences and the deformation of the burning front. During carbon burning, a thermonuclear runaway occurs. During this phase iron peak elements, such as nickel and cobalt are generated in the interior of the white dwarf. The peak temperatures of the explosive carbon burning front become smaller for lower densities because of larger heat capacity. Ultimately, the speed of the carbon burning front is slowed down to zero so that in the outer layers much unburnt carbon and oxygen remains. This can be seen in Figure 5.1 of Section 5, where the relative abundance is plotted against the expansion velocity for the $W7$ model. Inside are the iron peak elements, then in the transition region the intermediate mass elements and in the outer layers the unburnt matter.

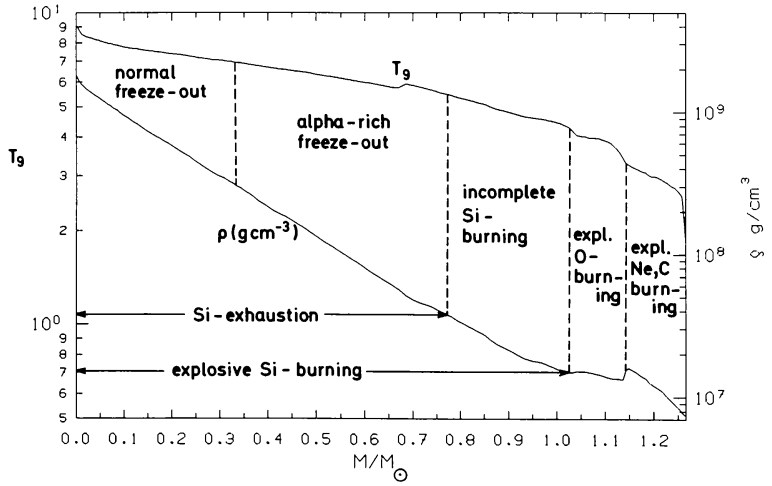

Figure 4.4: Temperature and density at the deflagration front of the $W7$ model as a function of Lagrangian mass coordinate $M/M_\odot$. See text for details. The figure is from Thielemann et al. (1986), with modifications.

In Figure 4.4 various modes of nuclear burning are shown with the dependence of the temperature and density at the deflagration front of the $W7$ model, shown as a function of the Lagrangian mass coordinate $M/M_\odot$.
For the convective energy transport in the $W7$ model the time dependent mixing length theory (Unno 1967) was used. The resulting mixing length parameter α, which is the ratio of the mixing length l to the pressure scale height H_p was set to $\alpha = 0.7$ in the hydrodynamical calculations. From this the name of the model $W7$ was derived, because it produces better fits for white dwarfs as the models $W6$ with $\alpha = 0.6$ and $W8$ with $\alpha = 0.8$. Thielemann et al. (1986) noted that in the model with the values described here, the ignition time scale is longer than the heat conduction time scale and solidified white dwarfs would melt before central ignition, thus avoiding ignition in a solid.
As successful as this very highly parametrized deflagration model may be it still leaves many open questions. One of the most important issues will be, to what extent this artificial model $W7$ can be used to make safe physical and mathematical statements. Open problems of this model are, e.g., the question why at the high mass transfer rate of hydrogen, helium or even heavier elements, the mass can actually rise and is not repelled back again. More general common problems are, e.g., the details of the possible progenitor system.

4.3.2 Analytical solver

To calculate the structure of a certain point of time after the explosion of the white dwarf, the analytical solver was used, implemented in `PHOENIX` by Jack et al. (2009).
The change of the energy density of the material considering absorption and emission and additional energy sources is given by Mihalas & Weibel Mihalas (1984, Eq. 96.7)

$$\rho_0 \left[\frac{\mathrm{D}e}{\mathrm{D}\tau} + p_0 \frac{\mathrm{D}}{\mathrm{D}\tau} \left(\frac{1}{\rho_0} \right) \right] = \int_0^\infty \left[c\chi_0(\nu_0) E_0(\nu_0) - 4\pi\eta_0(\nu_0) \right] \mathrm{d}\nu_0 + \rho\varepsilon. \tag{4.53}$$

It is the first law of thermodynamics for the material and describes the rate of change of the material energy density plus the rate of work done by the material pressure. We rewrite Eq. (4.53) as a function of λ

$$\rho \left[\frac{\mathrm{d}e}{\mathrm{d}t} + p \frac{\mathrm{d}}{\mathrm{d}t} \left(\frac{1}{\rho} \right) \right] = \int_0^\infty \left(c\chi E - 4\pi\eta \right) \mathrm{d}\lambda + \rho\varepsilon, \tag{4.54}$$

where ρ is the density, p the pressure, e is the internal energy density, χ the absorption coefficient, η the emission coefficient, $E = \frac{4\pi}{c} J$ the radiation energy density, J the mean intensity, and ε containing all additional energy sources.
We rewrite Eq. (4.54), divided by ρ and obtain for the derivative of the energy with respect to time

$$\frac{\mathrm{d}e}{\mathrm{d}t} = \underbrace{-p \frac{\mathrm{d}}{\mathrm{d}t} \left(\frac{1}{\rho} \right)}_{W} + \frac{4\pi}{\rho} \int_0^\infty \chi (J - S) \, \mathrm{d}\lambda + \varepsilon, \tag{4.55}$$

where W is the work and $S = \frac{\eta}{\chi}$ the source function (cf. Eq. (4.25)).

After a time step dt we get (from Eq. (4.55)) for the new energy density e_n

$$e_n = e_o - \underbrace{p\left(\frac{1}{\rho_n} - \frac{1}{\rho_o}\right)}_{\mathrm{d}W} + \frac{4\pi}{\rho}\,\mathrm{d}t \underbrace{\int_0^\infty \chi(J-S)\,\mathrm{d}\lambda}_{Q} + \varepsilon\,\mathrm{d}t, \tag{4.56}$$

where e_o is the old energy density, W the work done by adiabatic expansion, and Q the change of the energy density by radiation.
Assuming homologous expansion, the new density ρ_n is calculated according a time step dt

$$\rho_n = \rho_o \left(\frac{r_o}{r_n}\right)^3, \tag{4.57}$$

the associated new radius of a layer after a time step dt is

$$r_n = r_o + u\,\mathrm{d}t, \tag{4.58}$$

where u is the velocity.
To obtain the change of energy density by radiation (Q from Eq. (4.56)), the source function is rewritten as defined in Eq. (4.25) and then solved the time dependent spherically symmetric 1D radiative transfer equation (cf. Section 4.4, Eq. (4.66)) with PHOENIX taking into account all the special relativistic effects and frequency dependence, by using the atomic line database[13] of Kurucz & Bell (1995) and Kurucz (2010). By solving the equation of state we get the total energy density of the material by summing the ionization energy e_i and translational energy e_t

$$e = e_i + e_t. \tag{4.59}$$

The translational energy

$$e_t = \frac{3}{2}\frac{p}{\rho} = \frac{3}{2}\frac{R}{M}T = \frac{3}{2}\frac{N_A k_B}{M}T \tag{4.60}$$

contributes to the internal energy density of the material. There is p the gas pressure, ρ the density, R the gas constant[14], M the mean molecular weight, T the temperature, N_A the Avogadro constant[15], and k_B the Boltzmann constant[16].
In summary, the atmosphere is affected by the free expansion, the transport of energy by radiation, and the energy deposition by gamma ray emission, the latter is represented by ε in Eq. (4.53). While we assume in our model that the abundance of elements except ^{56}Ni, ^{56}Co, and ^{56}Fe, do not change during the free expansion phase one must consider separately the decay chain of radioactive ^{56}Ni.
Partial trapping and thermalization of β-unstable ^{56}Ni (half-life 6.075 d (Junde et al. 2011)) and its daughter nucleus ^{56}Co (half-life 77.236 d (Junde et al. 2011)) play an important role.

[13] "Kurucz/Atoms". Robert L. Kurucz. Web. 12-27-2013. <http://kurucz.harvard.edu/atoms.html>
[14] $R = 8.3144621(75)$ J mol^{-1} K^{-1}
[15] $N_A = 6.02214129(27)\cdot 10^{23}$ mol^{-1}
[16] $k_B = 1.3806488(13)\cdot 10^{-23}$ J K^{-1}

Both nuclei heat by gamma rays, the light curve, giving it the characteristic appearance (Truran et al. 1967; Colgate & McKee 1969). The typical course of radioactive decay is shown in Figure 4.5. The normalized abundance of ^{56}Ni is shown as a function of time for the first 150 days. We start at $t = 0$ only with a normalized to one content of ^{56}Ni. It decays by electron capture with a half-life of 6.075 d (Junde et al. 2011) to its daughter nuclide ^{56}Co. The radioactive decay itself is described by an exponential law ($N(t) = N_0 e^{-\lambda t}$), in the case of nickel by

$$\mathrm{Ni}(t) = \mathrm{Ni}(t_0) \cdot e^{-\lambda_{\mathrm{Ni}} t}, \tag{4.61}$$

where $\mathrm{Ni}(t_0)$ is the amount of radioactive nickel at time zero and λ_{Ni} is the decay constant of nickel. The reciprocal of λ is the mean lifetime τ directly linked to the half-life $\mathrm{T}_{\frac{1}{2}}$ by

$$\mathrm{T}_{\frac{1}{2}} = \ln 2 \cdot \tau = \frac{\ln 2}{\lambda}. \tag{4.62}$$

As can be seen in Figure 4.5 the abundance of ^{56}Ni approaches asymptotically to zero and is already less than 10 % on day 21, respectively after another 20 days less than 1 % (on day 41).
While ^{56}Ni decays only by electron capture, ^{56}Co decays by both electron capture (81 %) and β^+ decay (19 %) (Leibundgut 2000), to stable ^{56}Fe

$$^{56}_{28}\mathrm{Ni}_{28} \xrightarrow[\mathrm{T}_{1/2}=6.075\,\mathrm{d}]{\mathrm{e}^- \text{capture}} {}^{56}_{27}\mathrm{Co}_{29} \xrightarrow[\mathrm{T}_{1/2}=77.236\,\mathrm{d}]{\mathrm{e}^- \text{capture} \,\&\, \beta^+} {}^{56}_{26}\mathrm{Fe}_{30}.$$

The radioactive decay of cobalt obeys the decay law (Stöcker 1994)

$$\mathrm{Co}(t) = \mathrm{Ni}(t_0) \cdot \frac{\lambda_{\mathrm{Ni}}}{\lambda_{\mathrm{Co}} - \lambda_{\mathrm{Ni}}} \cdot \left(e^{\lambda_{\mathrm{Ni}} \cdot t} - e^{-\lambda_{\mathrm{Co}} \cdot t} \right) + \mathrm{Co}(t_0) \cdot e^{-\lambda_{\mathrm{Co}} \cdot t}, \tag{4.63}$$

where $\mathrm{Co}(t)$ is the amount of ^{56}Co at time t, λ_{Co} is the decay constant of cobalt, and $\mathrm{Co}(t_0)$ the initial amount of cobalt, which we assumed in the illustrative consideration of Figure 4.5 to be zero. In the model, this proportion is of course considered itself as cobalt is produced simultaneously with nickel in the supernova explosion. This amount will again be described by an exponential law $\mathrm{Co}(t_0) \cdot e^{-\lambda_{\mathrm{Co}} \cdot t}$.
If only cobalt is considered, because of the longer half-life, the abundance of ^{56}Co is less than 10 % on day 267, respectively after another 257 days less than 1 % (on day 524), as indicated in Figure 4.5.
For stable iron (^{56}Fe) must be taken into account the amount of cobalt from the decay of nickel, the amount of cobalt initially present, and the initial iron content. The amount of ^{56}Fe is given by

$$\begin{aligned} \mathrm{Fe}(t) \;=\; & \mathrm{Ni}(t_0) \cdot \left(1 + \frac{\lambda_{\mathrm{Ni}}}{\lambda_{\mathrm{Ni}} - \lambda_{\mathrm{Co}}} \cdot e^{-\lambda_{\mathrm{Co}} \cdot t} - \frac{\lambda_{\mathrm{Co}}}{\lambda_{\mathrm{Ni}} - \lambda_{\mathrm{Co}}} \cdot e^{-\lambda_{\mathrm{Ni}} \cdot t} \right) + \\ & + \mathrm{Co}(t_0) \cdot \left(1 - e^{-\frac{t}{\lambda_{\mathrm{Co}}}} \right) + \mathrm{Fe}(t_0), \end{aligned} \tag{4.64}$$

where $\mathrm{Fe}(t)$ is similar to the preceding example of cobalt, the time dependent iron content, and $\mathrm{Fe}(t = 0\mathrm{s})$ the initial amount of iron.

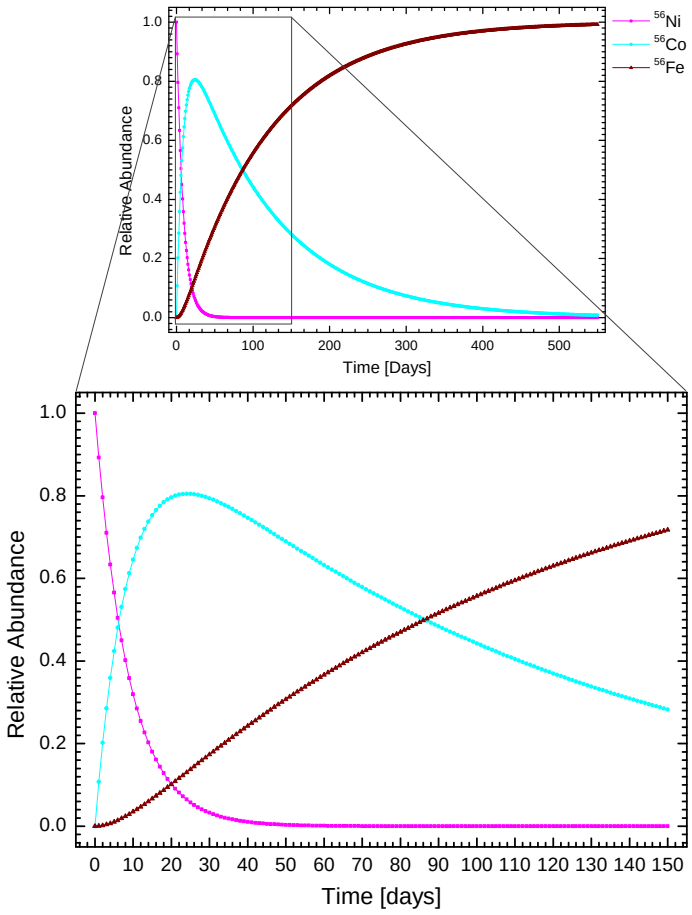

Figure 4.5: Schematic representation of the radioactive decay of ^{56}Ni (magenta) in its daughter nuclide ^{56}Co (cyan) and in turn its decay into stable ^{56}Fe (russet). We start with a normalized to one content of ^{56}Ni and assumes in this representation that we initially have no ^{56}Co and ^{56}Fe. Note, the maximum of cobalt at day 25 and the similarity of the decay curve of ^{56}Co and the light curve of a Type Ia supernova. See text for details.

With the Eqs. (4.61), (4.63), and (4.64) the abundances can thus be determined time dependent and considered in calculating the radiation field. As suggested by Jeffery (1998), the radiative transfer equation is solved for the emitted gamma rays frequency independent, by using a mean opacity $\kappa_\gamma = \frac{0.06}{\mu_e}\,\mathrm{cm^2\,g^{-1}}$, from which it is assumed to be only in pure absorption. The mean atomic mass per electron μ_e takes into account the main composition, i.e., for hydrogen dominated matter $\mu_e \approx 1$. Thus we obtain for the energy contribution of gamma rays, denoted as ε in Eq. (4.53)

$$\varepsilon = 4\pi\frac{\chi}{\rho}J. \tag{4.65}$$

However, this is an approximation. Clearly, the γ rays are scattered down to lower energies and this process is complex. There are also other approaches that assume pure resonance scattering (Branch et al. 1982).

This additional energy deposition is then taken into account in PHOENIX for the frequency dependent calculation of the total energy change.

4.4 Time dependent radiative transfer

In the case of supernovae, the time dependent spherically symmetric radiative transfer equation in the comoving frame, henceforth SSRTE, is given by (Mihalas & Weibel Mihalas 1984),

$$\begin{aligned}
&\gamma(1+\beta\mu)\frac{\partial I_\nu}{\partial t}+\gamma(\mu+\beta)\frac{\partial I_\nu}{\partial r}\\
&+\frac{\partial}{\partial\mu}\left\{\gamma(1-\mu^2)\left[\frac{1+\beta\mu}{r}-\gamma^2(\mu+\beta)\frac{\partial\beta}{\partial r}-\frac{\gamma^2}{c}(1+\beta\mu)\frac{\partial\beta}{\partial t}\right]I_\nu\right\}\\
&-\frac{\partial}{\partial\nu}\left\{\gamma\nu\left[\frac{\beta(1-\mu^2)}{r}+\gamma^2\mu(\mu+\beta)\frac{\partial\beta}{\partial r}+\frac{\gamma^2}{c}\mu(1+\beta\mu)\frac{\partial\beta}{\partial t}\right]I_\nu\right\}\\
&+\gamma\left\{\frac{2\mu+\beta(3-\mu^2)}{r}+\gamma^2(1+\mu^2+2\beta\mu)\frac{\partial\beta}{\partial r}+\frac{\gamma^2}{c}\left[2\mu+\beta(1+\mu^2)\right]\frac{\partial\beta}{\partial t}\right\}I_\nu\\
&=\eta_\nu-\chi_\nu I_\nu,
\end{aligned}\tag{4.66}$$

where $\beta = v/c$ is the speed normalized to the speed of light, c and $\gamma = (1-\beta^2)^{-1/2}$ the Lorentz factor, and $\mu = \cos\theta$ is the cosine of the angle describing the propagation direction. I_ν is, as before, the intensity, η_ν the emission, and χ_ν the extinction coefficients.
Eq. (4.66) is a (partial) integro-differential equation, since the mean intensity J_ν (4.11) is included in the emissivity η_ν, which is given by,

$$\eta_\nu = \kappa_\nu S_\nu + \sigma_\nu J_\nu + \sum_{\text{lines}} \sigma_l(\nu)\int \phi_l J_\nu\, d\nu. \tag{4.67}$$

Hauschildt (1992) and Hauschildt & Baron (2004) considered Eq. (4.66) time independent $\left(\frac{\partial}{\partial t}\equiv 0\right)$, and wrote it as,

$$a_r\frac{\partial I}{\partial r}+a_\mu\frac{\partial I}{\partial\mu}+a_\lambda\frac{\partial\lambda I}{\partial\lambda}+4a_\lambda I=\eta-\chi I, \tag{4.68}$$

with

$$a_r = \gamma(\mu+\beta), \tag{4.69}$$

$$a_\mu = \gamma(1-\mu^2)\left[\frac{1+\beta\mu}{r}-\gamma^2(\mu+\beta)\frac{\partial\beta}{\partial r}\right], \tag{4.70}$$

$$a_\lambda = \gamma\left[\frac{\beta(1-\mu^2)}{r}+\gamma^2\mu(\mu+\beta)\frac{\partial\beta}{\partial r}\right]. \tag{4.71}$$

Jack et al. (2009) considered an additional time dependent part a_t,

$$a_t = \frac{\gamma}{c}(1+\beta\mu)\frac{\partial I}{\partial t}, \tag{4.72}$$

and extended Eq. (4.68), respectively Eq. (4.66), to

$$a_t\frac{\partial I}{\partial t}+a_r\frac{\partial I}{\partial r}+a_\mu\frac{\partial I}{\partial\mu}+a_\lambda\frac{\partial\lambda I}{\partial\lambda}+4a_\lambda I=\eta-\chi I. \tag{4.73}$$

Along the characteristics, Eq. (4.68) has the form (Mihalas 1980; Hauschildt & Baron 2004; Jack et al. 2009)

$$\frac{\mathrm{d}I_l}{\mathrm{d}s} + a_t \frac{\partial I}{\partial t} + a_l \frac{\partial \lambda I}{\partial \lambda} = \eta_l - (\chi_l + 4a_l) I_l, \tag{4.74}$$

where ds is a line element along a (curved) characteristic, $I_l(s)$ is the specific intensity along the characteristic at point $s \geqslant 0$ ($s = 0$ denotes the beginning of the characteristic), and wavelength point λ_l. The coefficient a_l is given by (Hauschildt & Baron 2004),

$$a_l = \gamma \left[\frac{\beta(1-\mu^2)}{r} + \gamma^2 \mu \left(\mu + \beta\right) \frac{\partial \beta}{\partial r} \right], \tag{4.75}$$

where r is the radius.

4.4.1 First discretization of the wavelength and time derivative

In order to ensure stability, Hauschildt & Baron (2004) discretize the wavelength derivative in the SSRTE in the comoving frame with a fully implicit method,

$$\left.\frac{\partial I}{\partial \lambda}\right|_{\lambda=\lambda_j} = \frac{I_{\lambda_j} - I_{\lambda_{j-1}}}{\lambda_j - \lambda_{j-1}}. \tag{4.76}$$

Jack et al. (2009) extended it by a time dependent term,

$$\left.\frac{\partial I}{\partial t}\right|_{t=t_j} = \frac{I_{t_j} - I_{t_{j-1}}}{t_j - t_{j-1}}. \tag{4.77}$$

The wavelength discretized and time discretized SSRTE becomes

$$\frac{\mathrm{d}I}{\mathrm{d}s} + a_\lambda \frac{\lambda_l I_{\lambda_l} - \lambda_{l-1} I_{\lambda_{l-1}}}{\lambda_l - \lambda_{l-1}} + a_t \frac{I_{t_j} - I_{t_{j-1}}}{t_j - t_{j-1}} = \eta_{\lambda_l} - (\chi_{\lambda_l} + 4a_\lambda) I, \tag{4.78}$$

where I is the intensity at wavelength point λ_l and time point t_j. With the definition of the optical depth scale along the ray as,

$$\mathrm{d}\tau \equiv \chi + a_\lambda \left(4 + \frac{\lambda_l}{\lambda_l - \lambda_{l-1}}\right) + \frac{a_t}{t_j - t_{j-1}} \equiv \hat{\chi}\, \mathrm{d}s, \tag{4.79}$$

where $t_j - t_{j-1}$ is the time step. Together with the source function (Eq. (4.25)) $S = \eta/\chi$, we get

$$\frac{\mathrm{d}I}{\mathrm{d}\tau} = \frac{\chi}{\hat{\chi}} \left(S + \frac{a_\lambda}{\chi} \frac{\lambda_{l-1}}{\lambda_l - \lambda_{l-1}} I_{\lambda_{l-1}} + \frac{a_t}{\chi} \frac{1}{t_j - t_{j-1}} I_{t_{j-1}} \right) - I \equiv I - \hat{S}, \tag{4.80}$$

where $\hat{S}$ is the modified source function.
The formal solution can be written in a localized form (Olson & Kunasz 1987; Hauschildt & Baron 2004)

$$I(\tau_i) = I(\tau_{i-1}) \exp\left(\tau_{i-1} - \tau_i\right) + \int_{\tau_{i-1}}^{\tau_i} \hat{S}(\tau) \exp\left(\tau_{i-1} - \tau_i\right) \mathrm{d}\tau, \tag{4.81}$$

$$I(\tau_i) \equiv I_{i-1} \exp(-\Delta\tau_{i-1}) + \Delta I_i. \tag{4.82}$$

The optical depth along the ray is denoted by τ_i with $\tau_i \equiv 0$ and $\tau_{i-1} \leqslant \tau_i$

$$I(\tau_i) \equiv I_{i-1} \exp(-\Delta\tau_{i-1}) + \Delta I_i. \tag{4.83}$$

The intensity increments ΔI_i are given by

$$\Delta I_i = \alpha_i \hat{S}_{i-1} + \beta_i \hat{S}_i + \gamma_i \hat{S}_{i+1}. \tag{4.84}$$

The spatial variation of the source function $\hat{S}_i$ along a characteristic is interpolated by linear or parabolic polynomials. The coefficients α_i, β_i, and γ_i are dependent on the used interpolation method and are given in Olson & Kunasz (1987).

4.4.2 Second discretization of the wavelength and time derivative

Hauschildt & Baron (2004) noted that the discretization of the $\partial I/\partial\lambda$ derivative, as shown in the previous subsection, can be deferred. Eq. (4.78) of the SSRTE in characteristics form is rewritten to (Hauschildt & Baron 2004; Jack et al. 2009),

$$\frac{\mathrm{d}I_l}{\mathrm{d}\tau} - \frac{a_l}{\hat{\chi}_l}\frac{\partial\lambda I}{\partial\lambda} - \frac{a_t}{\hat{\chi}_l}\frac{\partial I}{\partial t} = I - \frac{\eta_l}{\hat{\chi}_l}, \tag{4.85}$$

contains now the time dependent part and with

$$\hat{\chi}_l = \chi_l + 4a_l \tag{4.86}$$

and the definition of the comoving frame optical depth along the characteristic

$$\mathrm{d}\tau \equiv -\hat{\chi}_l \mathrm{d}s. \tag{4.87}$$

By rewriting Eq. (4.85), we get

$$\frac{\mathrm{d}I}{\mathrm{d}\tau} = I - \hat{S} - \tilde{S} - \breve{S}, \tag{4.88}$$

with

$$\hat{S} = \frac{\chi}{\hat{\chi}_l} S = \frac{\eta_l}{\hat{\chi}_l}, \tag{4.89}$$

$$\tilde{S} = -\frac{a_l}{\hat{\chi}}\frac{\partial\lambda I}{\partial\lambda}, \tag{4.90}$$

and the time dependent source coefficient

$$\breve{S} = -\frac{a_t}{\hat{\chi}_l}\frac{\partial I}{\partial t}. \tag{4.91}$$

The following expression for the formal solution is given by (Hauschildt 1992; Hauschildt & Baron 2004),

$$I_{i,l} = I_{i-1,l} \exp(-\Delta\tau_{i-1}) + \delta\hat{I}_{i,l} + \delta\tilde{I}_{i,l} + \delta\breve{I}_{i,l}, \tag{4.92}$$

with the definitions

$$\delta\hat{I}_{i,l} = \alpha_{i,l}\hat{S}_{i-1,l} + \beta_{i,l}\hat{S}_{i,l} + \gamma_{i,l}\hat{S}_{i+1,l}, \tag{4.93}$$

$$\delta\tilde{I}_{i,l} = \tilde{\alpha}_{i,l}\tilde{S}_{i-1,l} + \tilde{\beta}_{i,l}\tilde{S}_{i,l}, \tag{4.94}$$

and the time derivative part (Jack et al. 2009)

$$\delta\breve{I}_{i,l} = \breve{\alpha}_{i,l}\breve{S}_{i-1,l} + \breve{\beta}_{i,l}\breve{S}_{i,l}. \tag{4.95}$$

The source functions include the discretization of the time derivative and are given by

$$\breve{S}_{i-1,t} = -\frac{a_{i-1,t}}{\hat{\chi}_{i-1,t}}\left(\frac{I_{i-1,t}}{\Delta t} - \frac{I_{i-1,t-1}}{\Delta t}\right) \tag{4.96}$$

and

$$\breve{S}_{i,t} = -\frac{a_{i,t}}{\hat{\chi}_{i,t}}\left(\frac{I_{i,t}}{\Delta t} - \frac{I_{i,t-1}}{\Delta t}\right). \tag{4.97}$$

Together with Eq. (4.88) the formal solution can be written in the form

$$\delta\breve{I}_{i,t} = \breve{\alpha}_{i,t}(p_{i-1,t}I_{i-1,t} - p_{i-1,t-1}I_{i-1,t-1}) + \breve{\beta}_{i,t}(p_{i,t}I_{i,t} - p_{i,t-1}I_{i,t-1}), \tag{4.98}$$

with the new coefficients

$$p_{i-1,t} = -\frac{a_{i-1,t}}{\hat{\chi}_{i-1,t}}\frac{1}{\Delta t} = p_{i-1,t-1} \tag{4.99}$$

and

$$p_{i,t} = -\frac{a_{i,t}}{\hat{\chi}_{i,t}}\frac{1}{\Delta t} = p_{i,t-1}. \tag{4.100}$$

The formal solution can then be written as

$$\begin{aligned}(1-\tilde{\beta}_{i,l}p_{i,l} - \breve{\beta}_{i,t}p_{i,t})I_{i,l,t} =& (\tilde{\alpha}p_{i-1,l} + \breve{\alpha}p_{i-1,t} + \exp(-\Delta\tau_{i-1}))I_{i-1,l,t} \\ &- \tilde{\alpha}p_{i-1,l-1}I_{i-1,l-1} - \breve{\alpha}p_{i-1,t-1}I_{i-1,t-1} \\ &- \tilde{\beta}p_{i,l-1}I_{i,l-1} - \breve{\beta}p_{i,t-1}I_{i,t-1} + \delta\tilde{I}.\end{aligned} \tag{4.101}$$

The discretization schemes are not only used individually, but in a mixed form. The parameter ξ is used, in accordance with Hauschildt & Baron (2004).

4.5 Method

In order to test the sensitivity of Type Ia light curves and spectra, we use PHOENIX version 16 (Baron et al. 2006) in the dynamical model mode. In this mode PHOENIX solves the radiative transfer for a given, fixed atmosphere structure, which we calculate with the standard fiducial model for Type Ia supernovae, $W7$ (Nomoto et al. 1984; Thielemann et al. 1986).
The details of PHOENIX are described in Hauschildt (1992, 1993), Allard & Hauschildt (1995), Hauschildt et al. (1995), Hauschildt & Baron (1995, 1999), and Baron et al. (1996). This version allows not only to calculate atmospheres of supernovae, but also of main sequence stars, cool stars, brown dwarfs, and extrasolar planets.
We start with the highly parametrized hydrodynamical model $W7$ of a white dwarf, which explodes by means of a carbon deflagration (Nomoto et al. 1984; Thielemann et al. 1986). The structure and resulting spectra will be calculated with the time dependent version of PHOENIX/1D.
As input the results of the carbon deflagration model $W7$ were used. In all of our models the abundances were taken from the $W7$ model. It was prepared by homologous expansion, i.e., $v(r) = \frac{v_0}{R_0} r$.
For this work, it is important to accurately take into account the effects of special relativity, which become important in rapidly expanding atmospheres, such as Type Ia supernovae,

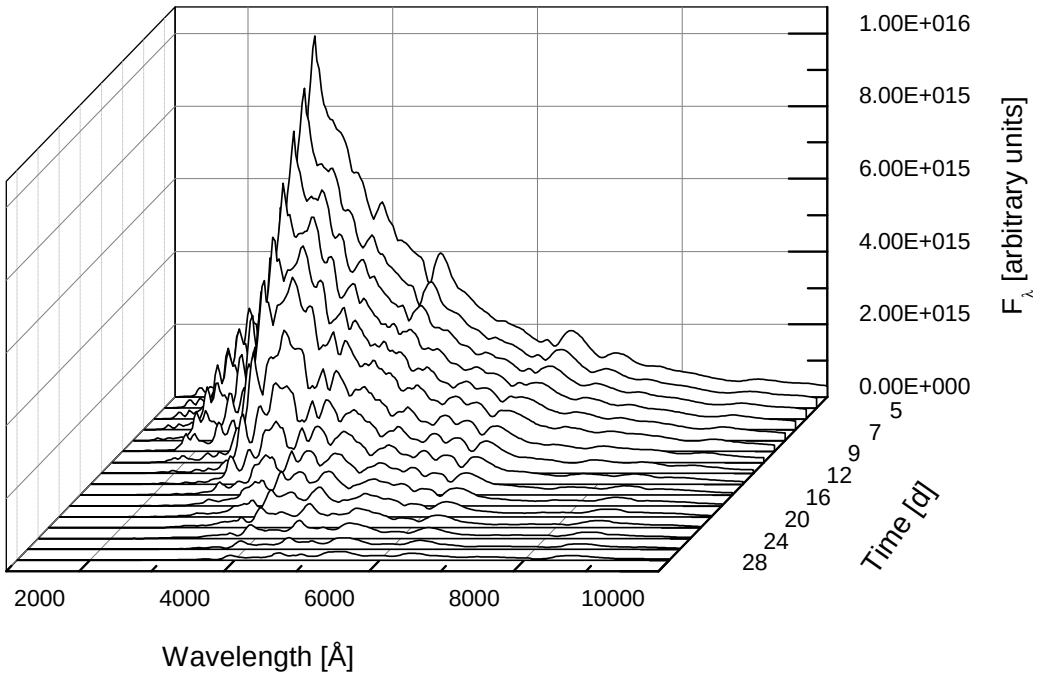

Figure 4.6: Time evolving series of spectra with captured parameters for a particular chemical composition. Plotted is the flux in arbitrary units as a function of the wavelength. The early spectra are shown further back, starting with day 5. The time sequence of the spectra is shown from back to front up to complete fading. See text for details.

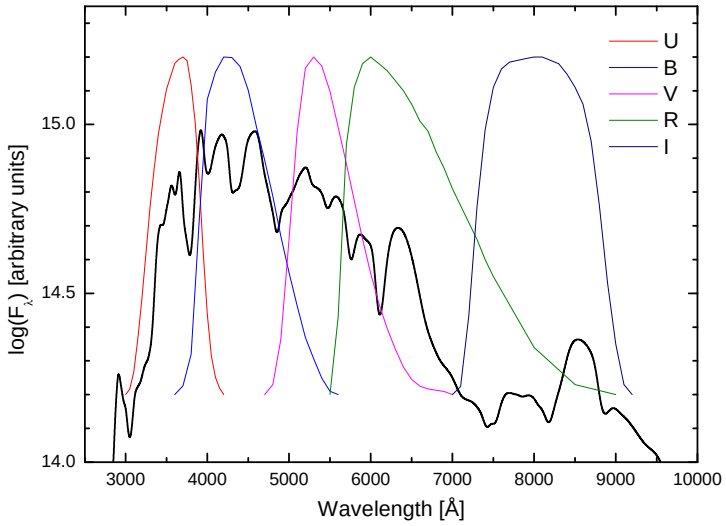

Figure 4.7: Synthetic spectrum for day 20 after the explosion together with filter functions. Plotted is the flux against the wavelength in the range $[2500, 10000]$ Å. Additionally, the Johnson filter functions U, B, V, R, and I are plotted which have been used to calculate the light curves of the respective passbands. See text for details.

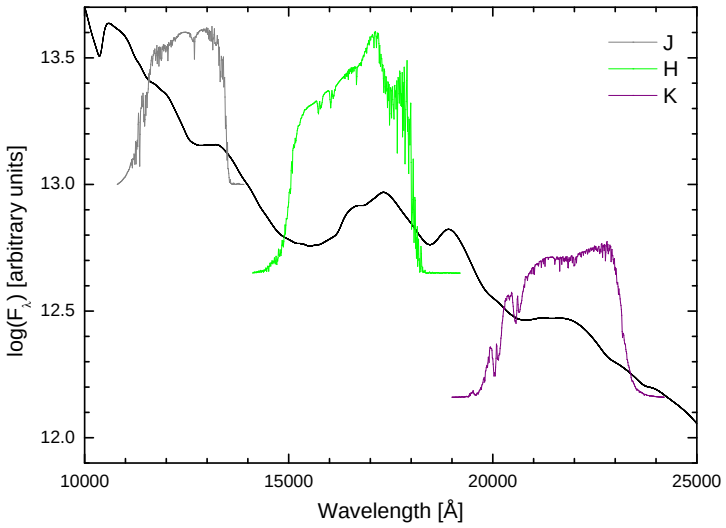

Figure 4.8: Synthetic spectrum for day 20 after the explosion together with filter functions. Plotted is the flux against the wavelength in the range $[7900, 25100]$ Å. Additionally, the Johnson filter functions J, H, and K are plotted which have been used to calculate the light curves of the respective passbands. See text for details.

and to know that the numerical methods are stable and have been checked. The results of PHOENIX with these input parameters are considered for our purposes as established and reviewed in numerous calculations, e.g., Nugent (1997), Nugent et al. (1997), Lentz et al. (2000, 2001a,b), Baron et al. (2006), and Jack et al. (2009, 2011, 2012).
All spectra and the associated light curves for different bands are calculated in LTE, except NLTE calculations which are discussed in Section 5.6. Scattering is considered, and if not stated otherwise, e.g., Sections 5.5 and 5.6, considered as a parameter. In our parameter vector $\mathscr{P}$ (cf. Section 3) we consider the elements H, He, Li, Be, B, C, N, O, F, Ne, Na, Mg, Al, Si, P, S, Cl, Ar, K, Ca, Sc, Ti, V, Cr, Mn, Fe, Co, Ni, Cu, Zn, Ga, Kr, Rb, Sr, Y, Zr, Nb, Ba, La, Cs, and the electrons. For each model, we start with the calculation of the hydrodynamical model, solve the radiative transfer problem and finally calculate with the obtained atmospheric structure, a spectrum for comparison.

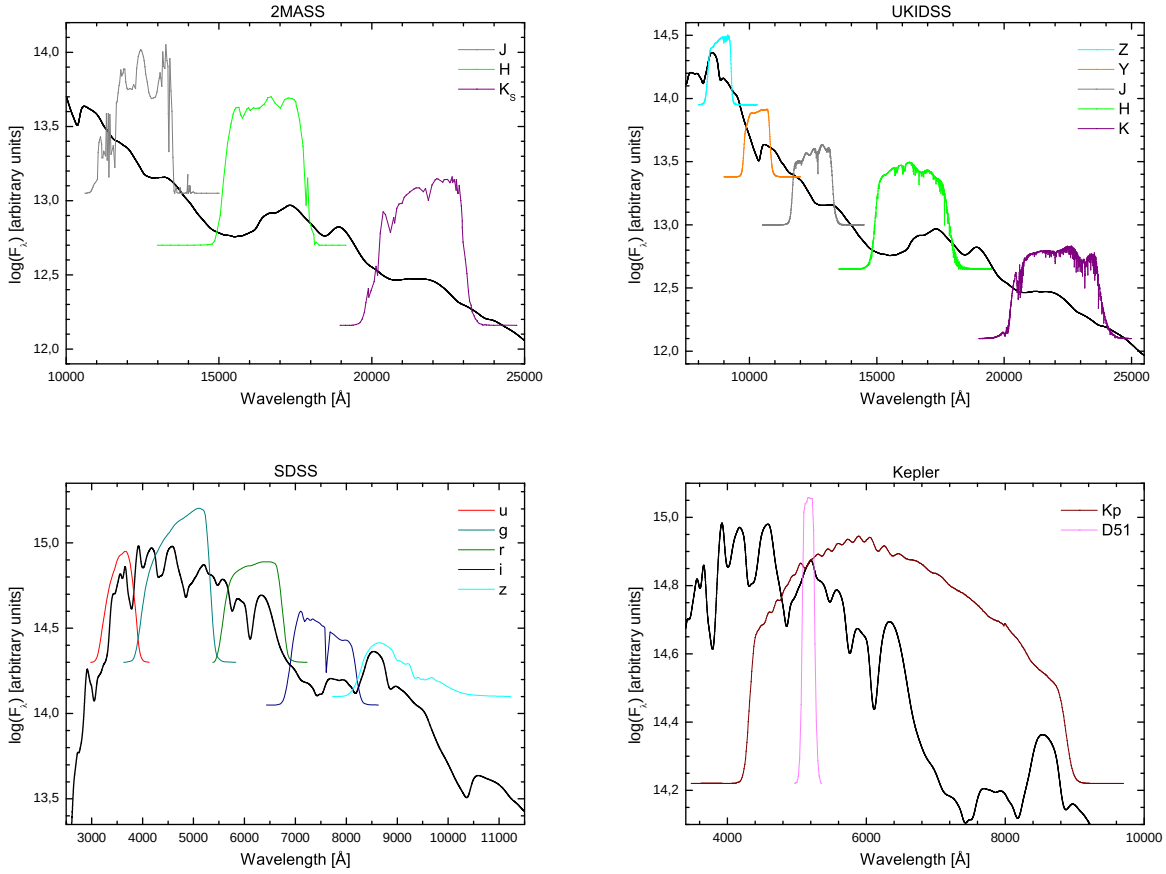

Figure 4.9: Shown are the corresponding filter functions for the photometric systems 2MASS, UKIDSS, SDSSS, and Kepler together with the synthetic spectrum for day 20 after the explosion. In particular, for 2MASS J, H, and K (top left), for UKIDSS Z, Y, J, H, and K (top right), for SDSS u, g, r, i, and z (bottom left), and for Kepler Kp and D51 (bottom right). See text for details.

The first 50 days after the explosion were considered. In total we calculate models for 33 different time steps. The comparison of the spectra is mainly focused on days around maximum. Light curves for different photometric systems in the corresponding passbands were calculated from the spectra. A time evolving series of spectra for a particular chemical composition is shown in Figure 4.6. The first spectrum was calculated for day 5 after the explosion. At this time, the outer layers contain mostly unburnt material, moving with high speed. Deeper layers which have been burnt mainly to intermediate mass elements can be seen around maximum light.
For comparisons in different wavelength ranges, appropriate filter functions have been implemented. In Figure 4.7 a typical spectrum during the maximum brightness together with the Johnson (1966) filter functions U, B, V, R, and I is shown. As can be seen, these filters cover the areas in the ultraviolet to ≈ 4000 Å (passband U), the visible in the range $[3900, 7000]$ Å (passbands B, V, and R), and the connected near infrared (passband I) as well.

Table 4.1: Compilation of passbands used in this work, specifying the filter name, the effective wavelength midpoint λ_{eff}, the bandwidth $\Delta\lambda$, the specifying region, and the description of the photometric system.

Filter	$\boldsymbol{\lambda_{\text{eff}}}$ **[Å]**	$\boldsymbol{\Delta\lambda}$ **[Å]**	**Region**	**Description**
U	$\simeq 3650$	$\simeq 1200$	ultraviolet	ultraviolet, Johnson
B	$\simeq 4450$	$\simeq 2000$	visible	blue, Johnson
V	$\simeq 5510$	$\simeq 2700$	visible	visual, Johnson
R	$\simeq 6850$	$\simeq 3600$	visible	red, Johnson
I	$\simeq 8060$	$\simeq 2200$	near infrared	infrared, Johnson
J	$\simeq 12200$	$\simeq 3100$	near infrared	Johnson
H	$\simeq 16300$	$\simeq 5080$	near infrared	Johnson
K	$\simeq 21900$	$\simeq 5200$	near infrared	Johnson
J	$\simeq 12500$	$\simeq 4380$	near infrared	2MASS
H	$\simeq 16500$	$\simeq 6150$	near infrared	2MASS
K_S	$\simeq 21500$	$\simeq 5770$	near infrared	2MASS
Z	$\simeq 8820$	$\simeq 2300$	near infrared	UKIDSS
Y	$\simeq 10310$	$\simeq 2895$	near infrared	UKIDSS
J	$\simeq 12480$	$\simeq 3985$	near infrared	UKIDSS
H	$\simeq 16310$	$\simeq 5990$	near infrared	UKIDSS
K	$\simeq 22010$	$\simeq 5985$	near infrared	UKIDSS
u	$\simeq 3450$	$\simeq 1150$	ultraviolet	SDSS
g	$\simeq 4750$	$\simeq 2200$	visible	SDSS
r	$\simeq 6220$	$\simeq 1850$	visible	SDSS
i	$\simeq 7630$	$\simeq 2200$	near infrared	SDSS
z	$\simeq 9050$	$\simeq 3500$	near infrared	SDSS
Kp		$\simeq 6220$	visible & near infrared	Kepler
D51		$\simeq 380$	visible	Kepler

Additionally, the Johnson filters J, H, and K are used to extend the range in the near infrared to ≈ 24000 Å. These filter functions are shown in Figure 4.8, together with the synthetic spectrum for day 20 in the corresponding wavelength region.
The individual filters cover different long wavelength and energy ranges. This is difficult for comparisons that are based on statistics.

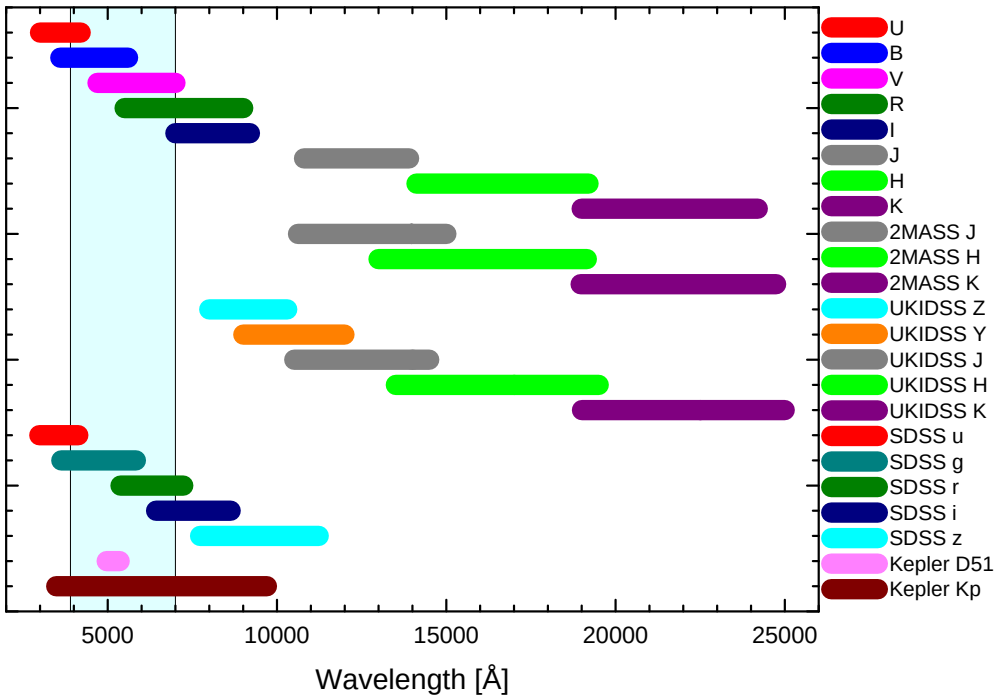

Figure 4.10: Photometric systems and the wavelength range of its passbands. In particular, there are (from top to bottom) the Johnson photometric system with filters U, B, V, R, I, J, H, and K, the Two Mycron All Sky Survey (2MASS) with J, H, and K, the UKIRT Infrared Deep Sky Survey (UKIDSS) with Z, Y, J, H, and K, the Sloan Digital Sky Survey (SDSS) with u, g, r, i, and z, and Kepler with D51 and Kp. The visible region is marked ($[3900, 7000]$ Å). The legend labels the passbands. A summary of the photometric system, their passbands and the respective wavelength ranges are given in Table 4.1. See text for details.

Therefore, other passbands for different photometric systems, such as Two Mycron All Sky Survey (2MASS) for the passbands J, H, and K_S (Skrutskie et al. 2006), UKIRT Infrared Deep Sky Survey (UKIDSS) for the passbands Z, Y[17], J, H, and K (Dye et al. 2006; Hewett et al. 2006; Lawrence et al. 2007), Sloan Digital Sky Survey (SDSS) for the passbands u, g, r, i, and z (Frieman et al. 2008; Sako et al. 2008), and Kepler for the passbands D51 and Kp (Borucki et al. 2010) were used to calculate the corresponding light curves. These filter functions are shown together in Figure 4.9 again with the synthetic spectrum for day 20 in the corresponding wavelength region. All photometric systems used are shown together with

[17] This filter at $[0.97, 1.07]\,\mu$m is for surveys for hypothetical Y dwarfs and for quasars of $z > 6.4$ (Hewett et al. 2006)

the respective passbands in Table 4.1, specifying the filter name, the effective wavelength midpoint λ_{eff}, the bandwidth $\Delta\lambda$, and the specifying region. To graphically emphasize the different bandwidths and the corresponding wavelength range, the filter functions are summarized and shown in Figure 4.10.
SDSS has an extra supernova project within, also known as SDSS Supernova Survey.
The two Kepler bands are taken only for mathematical reasons, e.g., D51 is considered as infinitesimal small band. The mission itself has nothing to do with supernovae. Kp used herein complementary to D51, is a band that includes almost the entire visual, and also extends into the infrared region (cf. Figure 4.9).
The passbands of the Johnson photometric system cover the entire wavelength range, but the length of the wavelength ranges are very different. For example, the passband R $[5500, 9100]$ Å extends far into the range of the passband I $[7000, 9300]$ Å, even if it is weighted (cf. Figure 4.7).

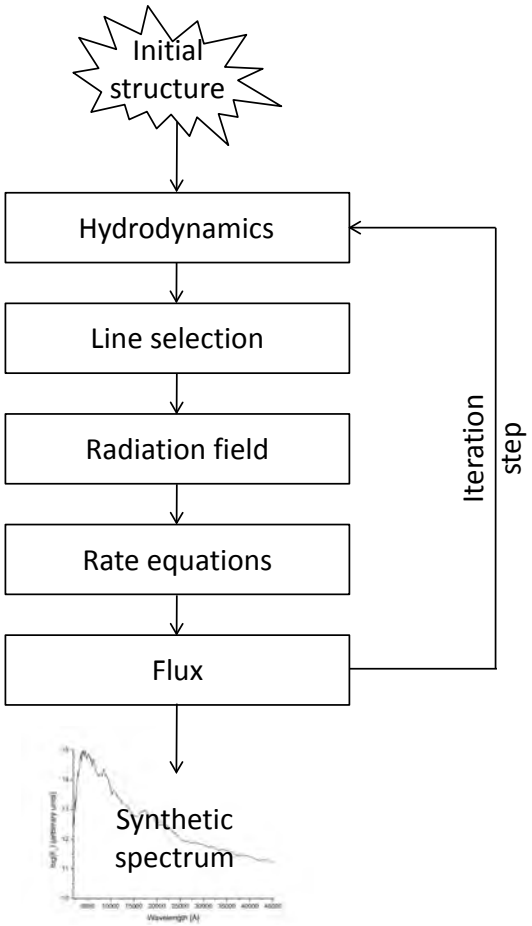

Figure 4.11: Iteration scheme of PHOENIX. See text for details.

The range of R is 1.6 times greater than that of I (cf. Table 4.1). The areas covered in the infrared, appear much larger, whereas in the bands B and V is the most energy transported. The photometric system SDSS covers with the passbands u, g, r i, and z, a much smaller range $[2980, 11230]$ Å than the Johnson photometric system, which goes up to a wavelength range of 24200 Å (cf. Table 4.1 and Figure 4.10).
The Kepler photometric system one can see is the most obvious. The range of the passband D51 is completely enclosed by the bandwidth of Kp, which is $\approx$16.4 times greater[18]. This is shown here to illustrate the different bandwidths. They can be used interchangeably in the formation of the Jacobian matrix (cf. Section 3). The radiative transfer is solved using the dynamical model mode of PHOENIX for the atmosphere taken from the $W7$ model, that is an initial guess of the temperature, density, and pressure structure. The structure of the atmosphere is discretized into 128 layers. For the next time step the hydrodynamic solver calculates the changes of the atmosphere, such as the new radii, the expansion of the layers, and the corresponding density.
Thereafter, the atomic lines are selected and loaded. PHOENIX use the atomic line database[19] of Kurucz & Bell (1995) and Kurucz (2010) as atomic opacity source. It follows the calculation of the radiation field. The radiative transfer equation is solved by accelerated lambda iteration for each wavelength point during the wavelength loop. This part of PHOENIX is parallelized. In this step, the wavelength dependent quantities are calculated, such as the opacities, source functions, and hereafter the intensities. If non-local thermodynamic equilibrium (NLTE, cf. Section 4.2.2) is selected, the radiative rates have to be integrated. Hereafter the rate equations have to be solved with the assumption of statistical equilibrium. For this, all departure coefficients for all levels of the NLTE species must be updated. In the last step, we obtain a synthetic spectrum by solving the radiation field. A flow chart illustrating the iteration scheme, for both LTE and NLTE, is shown in Figure 4.11.
A selection of light curves for the fiducial model is shown in Figure 4.12 for the Johnson photometric system for the bands U, B, V, R, and I and for 2MASS for J, H, and K. We start on day 5 after the explosion and have 32 spectra calculated for the first 50 days. The same has been done for the bands Z, Y, J, H, and K in UKIDSS and Kp in Kepler. The results are shown in Figure 4.13.
The K band from UKIDSS should not be confused with the Kp band from Kepler. They cover very different areas and have different lengths (cf. Table 4.1 and Figures 4.10 and 4.9).
Finally, we have calculated light curves for the Sloan Digital Sky Survey (SDSS) for the bands u, g, r, i, and z and for the Kepler band D51. As mentioned above, D51 is considered the narrowest passband and was originally only calibrated for comparison with Castelli's & Kurucz's (2004) ATLAS9 model atmospheres (Brown et al. 2011).
It was included here because we want to consider it as an infinitesimally narrow filter band in the visible region. The results of this filters are shown in Figure 4.14.
A review of standard photometric systems is given in, e.g., Bessell (2005).

[18] However, these filters are used for different purposes and are only shown here to illustrate the discrepancy
[19] "Kurucz/Atoms". Robert L. Kurucz. Web. 12-27-2013. <http://kurucz.harvard.edu/atoms.html>

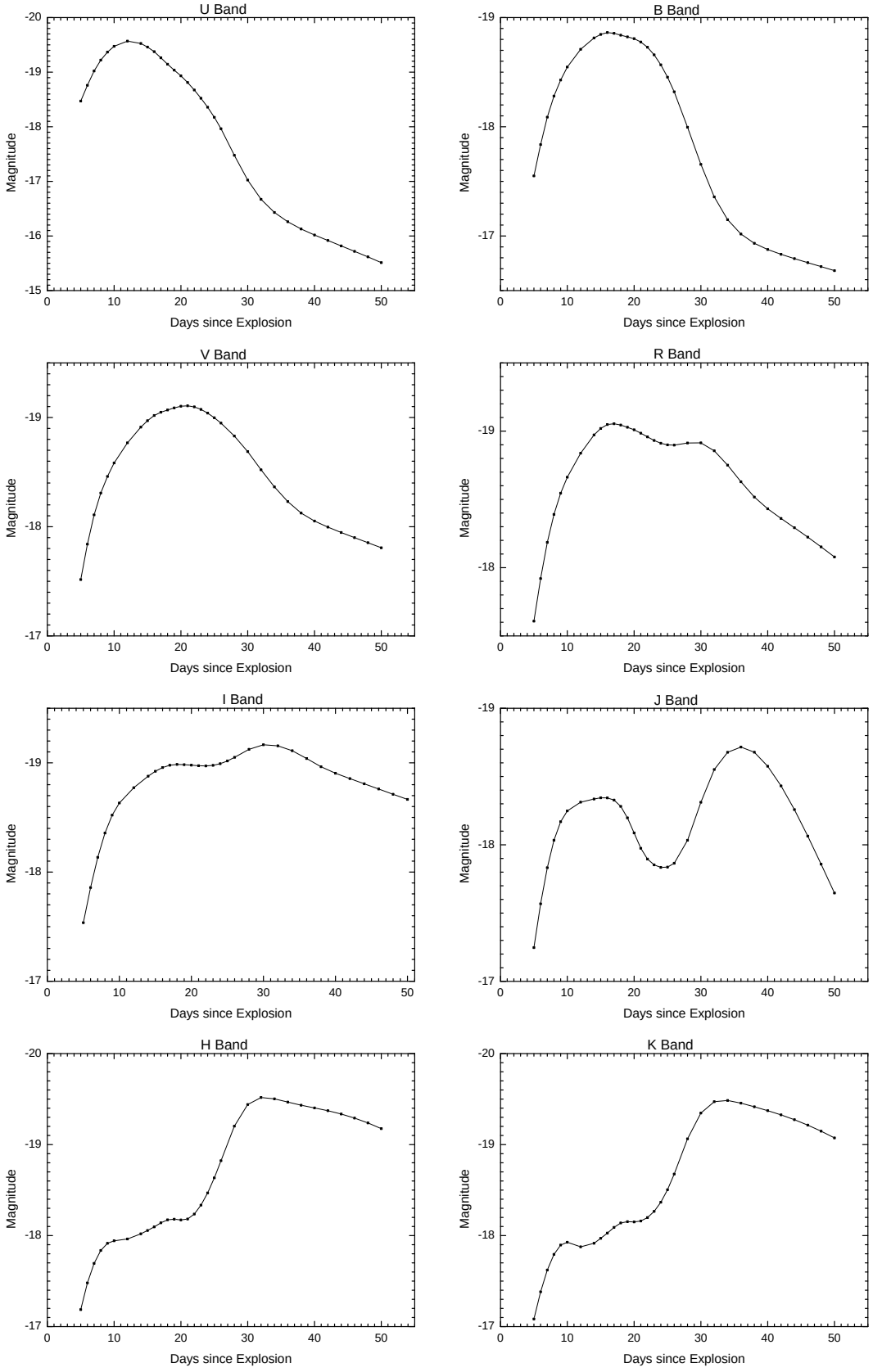

Figure 4.12: Model light curves for the Johnson photometric system for the bands U, B, V, R, and I and for 2MASS for the bands J, H, and K. See text for details.

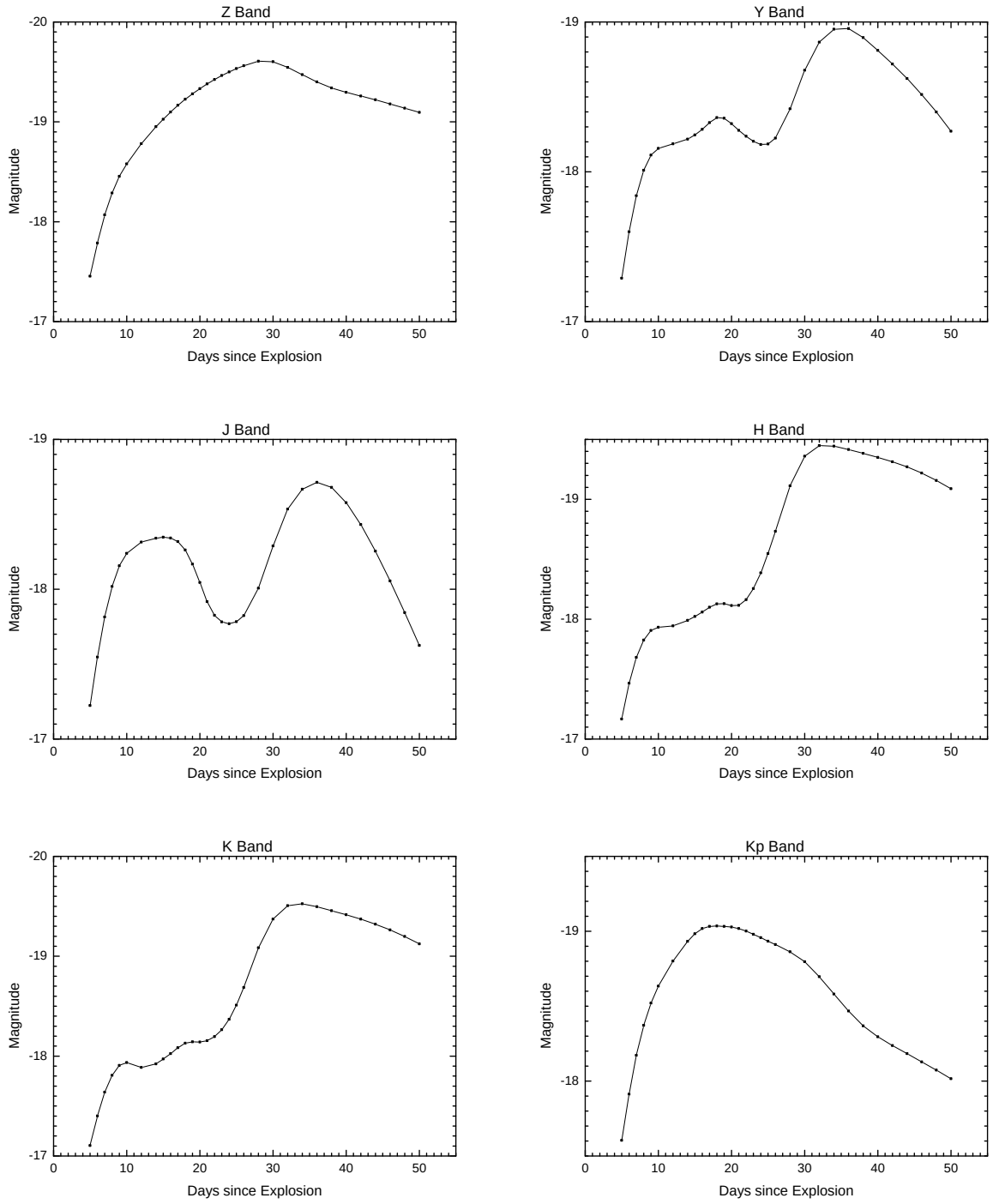

Figure 4.13: The same as in Figure 4.12, but now for light curves for UKIRT Infrared Deep Sky Survey (UKIDSS) for the bands Z, Y, J, H, and K and for Kepler for the band Kp. Plotted is the magnitude as a function of time after the explosion, starting with day 5. See text for details.

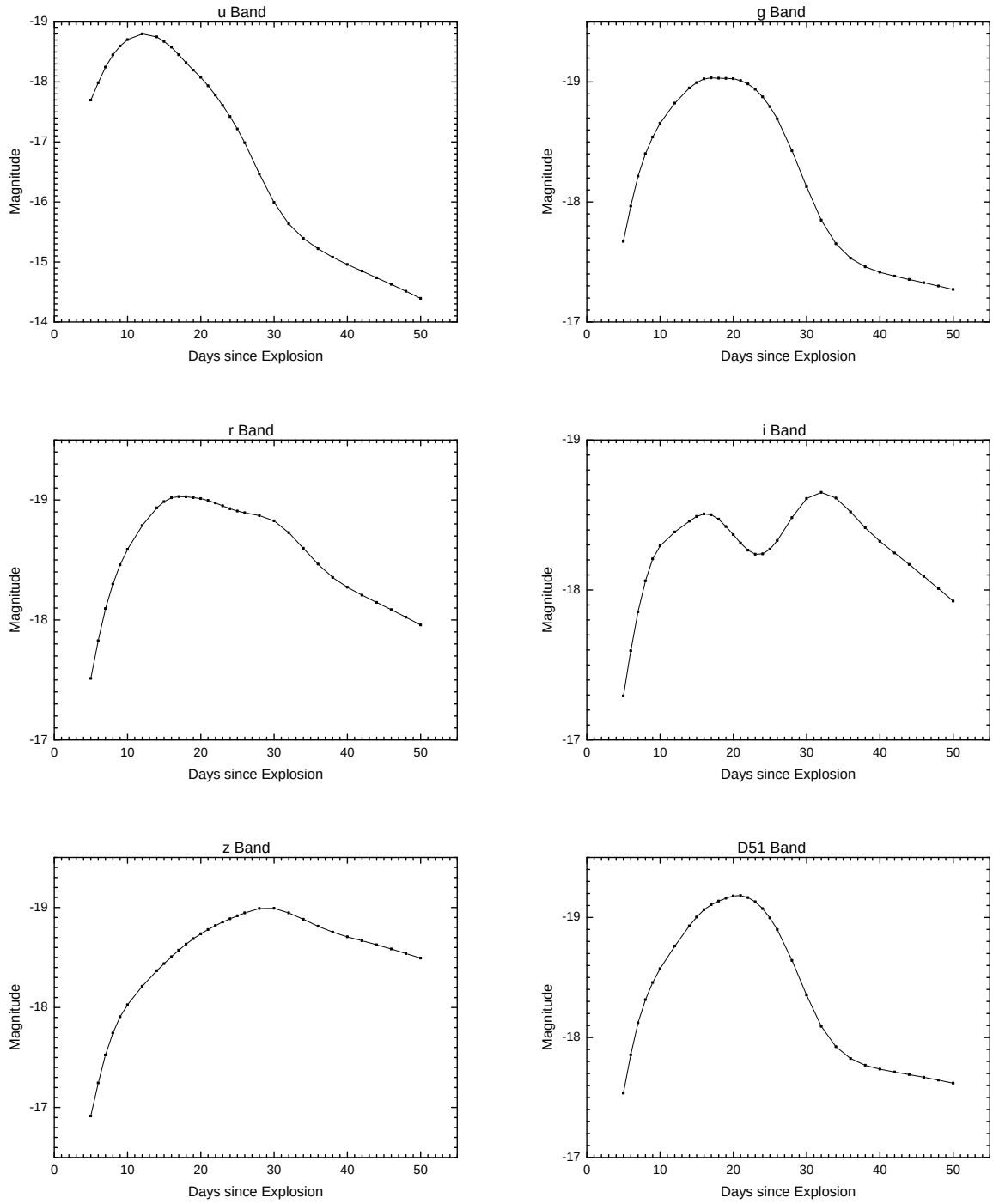

Figure 4.14: The same as in Figures 4.12 and 4.13, but now for light curves for Sloan Digital Sky Survey (SDSS) for the bands u, g, r, i, and z and for Kepler for the band D51. Plotted is the magnitude as a function of time after the explosion, starting with day 5. See text for details.

Chapter 5

Variation of parameters, the sensitivity, and the model response

The purpose of this work is to check the sensitivity of our models to changes of physical and algorithmic parameters. Therefore, parameters were varied systematically and the model response observed. The basic idea is to follow the gradient based method of an inverse problem. In the mathematical parameter estimation differential quotients are formed. Due to the partial integro-differential equations the problem is complex. The derivatives can not be created automatically, e.g, by internal numerical differentiation (cf. Bock 1987). Therefore, difference quotients are formulated. However, they can not easily be generated automatically, the step size must be determined and tested.

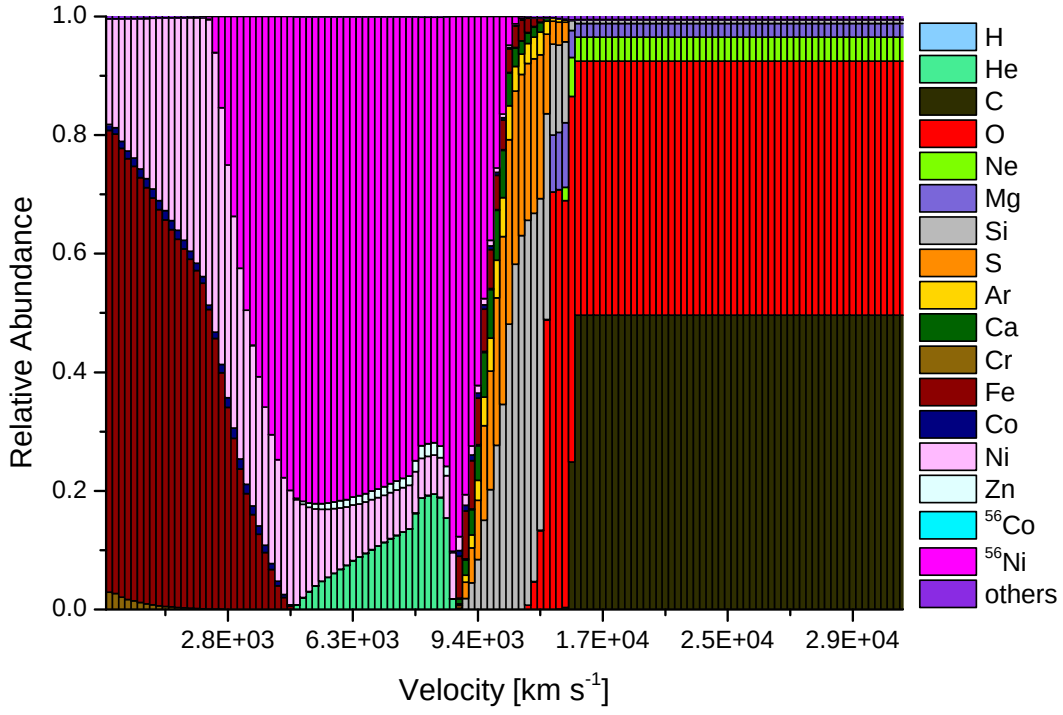

Figure 5.1: Normalized initial composition structure of the *W* 7 model. The relative abundances are plotted as a function of the expansion velocity. The legend labels the most important elements. Low abundance elements are summarized and referred as "others". See text for details.

A fundamental obstacle is the fact that we cannot simply "reverse" the simulations as they are based on the solution of integro-differential equations (here: the time dependent radiative transfer equation with scattering) that, while linear, cannot be directly reversed.
The time dependent version of PHOENIX/1D is used, considering spherical symmetry and special relativistic effects.
The results of the carbon deflagration model $W7$ were used as input for the simulations. As mentioned in Section 4.5, in all of our models the abundances were taken from the $W7$ model.
In Figure 5.1 the normalized initial composition structure of $W7$, which was used as input to PHOENIX is shown. Time zero is right after explosion before the composition begins to change via radioactive decay. Close to the center iron peak elements are found. With increasing radius (here as expansion velocities) the intermediate mass elements turn up. Outside, at high expansion velocities, are unburnt carbon and oxygen, and a small amount of other elements.

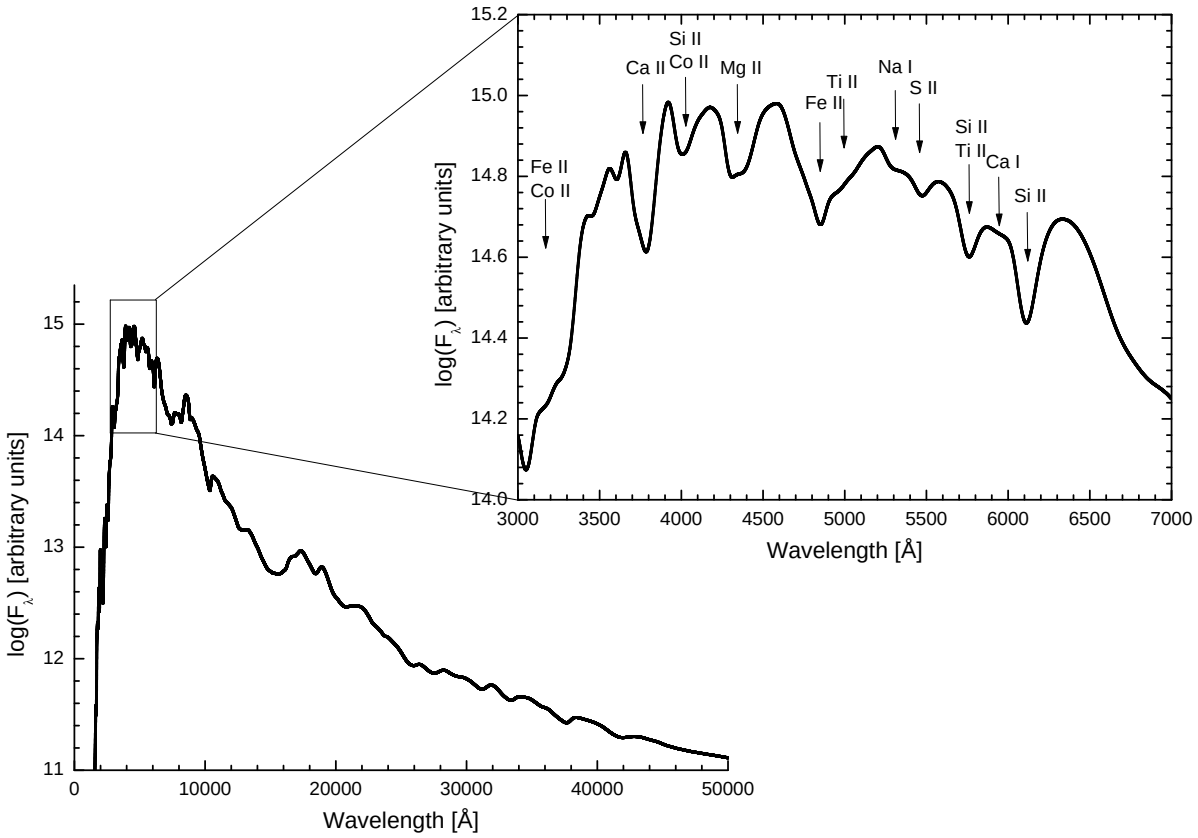

Figure 5.2: Entire synthetic spectrum to 5 μm, as well as a section in the range $[3000, 7000]$ Å from the fiducial model for day 20. Plotted is the logarithmic flux in arbitrary units as a function of wavelength. Important elements that are causing the absorption troughs at the time are specified. See text for details.

As mentioned in Section 4.5, the results of PHOENIX with these input parameters are considered for our purposes as established. All spectra and the associated light curves for different bands are calculated in LTE, except for the explicit NLTE calculations which are discussed in Section 5.6. Line scattering is considered with $\varepsilon_{\text{line}} = 0.8$, i.e., 20 % of the photons are scattered.
An entire synthetic spectrum from 0 to 5 μm is shown in Figure 5.2, and an enlarged section of it in the range $[3000, 7000]$ Å, which we will look at more closely in the following sections. The first 50 days since the explosion started are considered. We choose the individual days 5, 6, 7, 8, 9, 10 , 12, 14, 15, 16, 17, 18, 19, 20, 21, 22, 23, 24, 25, 26, 28, 30, 32, 34, 36, 38, 40, 42, 44, 46, 48, and 50 because they form a compromise between computing time and cover the entire range.
Thus, models for 32 different time steps were calculated. The focus lies on days around the maximum. From the calculated spectra, light curves for different passbands were computed and compared for different parameters. We varied these parameters: the abundance of ^{56}Ni (Section 5.1), the expansion velocity (Section 5.2), simultaneous by the expansion velocity and the abundance of ^{56}Ni (Section 5.3), the position of the iron core, in addition parts of the core were replaced piecewise by ^{56}Ni (Section 5.4), the parametrized line scattering parameter $\varepsilon_{\text{line}}$ (Section 5.5), and finally the three ionization stages of calcium (Ca I, Ca II, and Ca III) under consideration of NLTE (Section 5.6).

5.1 Varying the abundance of ^{56}Ni

It is well known that in first order the brightness depends on the amount of radioactive ^{56}Ni synthesized during the explosion, which decays to ^{56}Co and finally to ^{56}Fe (cf. Section 2.3). Meanwhile, it is also clear that not all Type Ia supernovae produce the same amount of ^{56}Ni in the explosion. This can clearly be seen, e.g., by the significantly growing number of clearly subluminous objects, which is in first order a signature that very little ^{56}Ni was produced. An extreme example is the mentioned SN 1991bg (Turatto et al. 1996; Mazzali et al. 1997) (cf. Section 2.5), or the exact opposite, the luminous SN 1991T (cf. Section 2.5), which is an example, that a lot of ^{56}Ni was synthesized during the explosion (Filippenko et al. 1992b).
In order to study the behavior and the sensitivity of the modeled light curves, the abundance of ^{56}Ni was gradually varied. And thus, by renormalization also the abundance of other elements. Thus we not only observe the first order effects caused by ^{56}Ni, but also second order effects caused by varying abundances of other elements. The decisive factors controlling the fraction of synthesized ^{56}Ni are not well understood, although it is known that there are many factors, which are correlated. It is quite clear that the intrinsic luminosity variation depends in first order on the amount of ^{56}Ni, as well as the Phillips relation with the defined parameter Δm_{15}, which describes the decrease of the B magnitude within the first 15 days after the maximum in the B band and the absolute peak luminosity (Phillips 1993; Hamuy et al. 1995, 1996a; Phillips et al. 1999, cf. Section 2.4). Höflich et al. (1995) concluded that models with a large nickel production produce light curves comparable to those of typical Type Ia supernovae, whereas subluminous supernovae can be explained by models with a low nickel production.
These are obvious examples, which do not deal with second order effects, such as, e.g., the correlation with the mass, the star formation rate, the age, and the metallicity of the host galaxy.

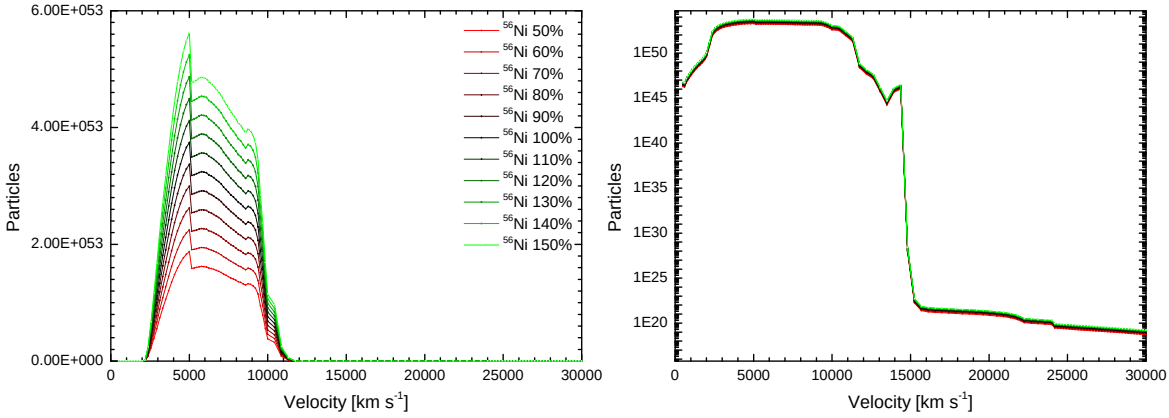

Figure 5.3: Particles of ^{56}Ni as a function of speed for models in the range with 50 % reduced ^{56}Ni (red) and 50 % enriched ^{56}Ni (green). The two plots are identical and differ only in the presentation of their ordinates. The legend in the left plot labels the amount of ^{56}Ni. See text for details.

Therefore, we start by systematically vary the amount of ^{56}Ni. We begin with the fiducial model and change the initial abundance of $^{56}\text{Ni} \equiv 0.568\,m_\odot$ in steps of 10 % from 50 % $\equiv$ $0.284\,m_\odot$ to 150 % $\equiv 0.852\,m_\odot$.
In Figure 5.3 the profile behavior of the amount of ^{56}Ni is shown as a function of the expansion velocity. As can be seen in the logarithmic representation of Figure 5.3, we start with $\approx 10^{46}$ particles of ^{56}Ni. The number of ^{56}Ni particles increases in the velocity range $[2937, 9843]\,\text{km}\,\text{s}^{-1}$ rapidly to $\approx 10^{53}$. As speed increases, the number of particles decreases and is $\approx 10^{21}$, in the range of $15.7 \cdot 10^3\,\text{km}\,\text{s}^{-1}$ and ultimately $\approx 10^{19}$ particles in the outer regions.
The visible region in the range of $[3000, 7000]$ Å of the corresponding spectra for day 20 is shown in Figure 5.4. The colors are again correlated with the corresponding abundances of ^{56}Ni. The red line show the model with 50 % reduced ^{56}Ni, while green shows the model with 50 % enriched ^{56}Ni (150 %). In the spectra, the occurrence of the absorption troughs of the individual features can be well observed. The observational characteristics of normal supernovae are well reproduced, such as the conspicuous absorption features near 6150 Å due to Si II and near 3750 Å due to Ca II. Other absorption features appear near 4000 Å due to Si II and Co II, near 4300 Å due to Mg II, near 4900 Å due to Si II and S II, near 5300 Å due to S II, near 5700 Å due to S II, as well as numerous hidden lines.

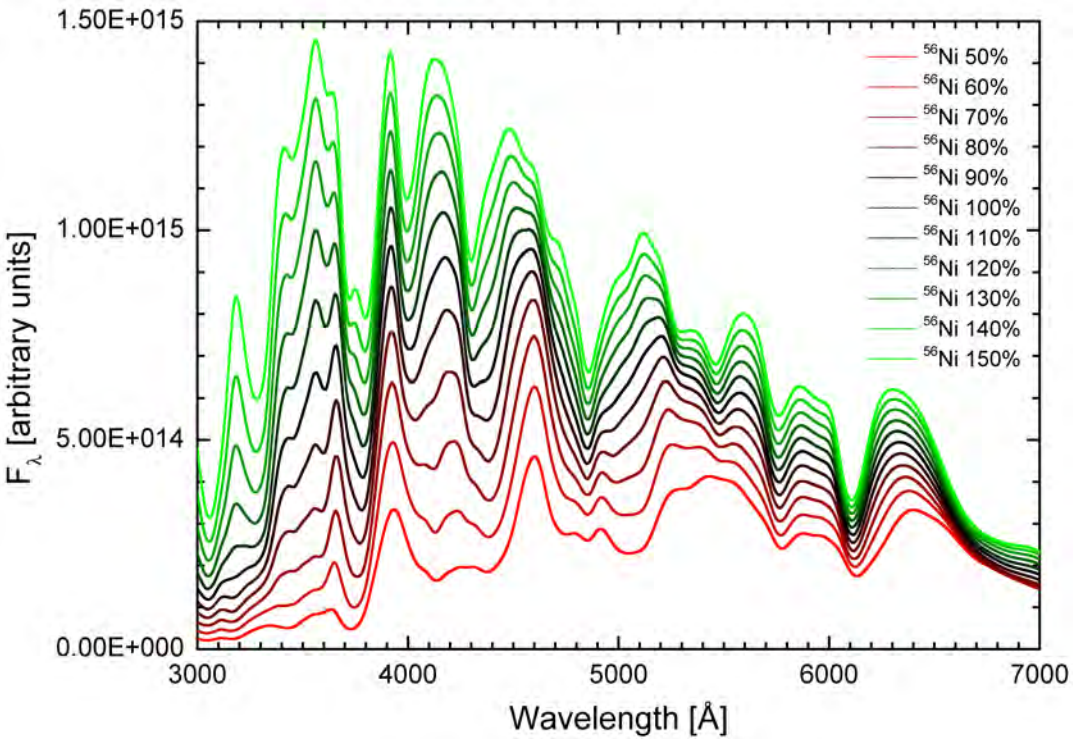

Figure 5.4: Synthetic spectra around the maximum brightness (for day 20 after the explosion) for varying ^{56}Ni. Plotted is the flux in arbitrary units as a function of the wavelength in the range $[3000, 7000]$ Å. The abundance of ^{56}Ni was changed in steps of 10 % from 50 % (red line) to 150 % (green line). The legend labels the amount of ^{56}Ni of each model. See text for details.

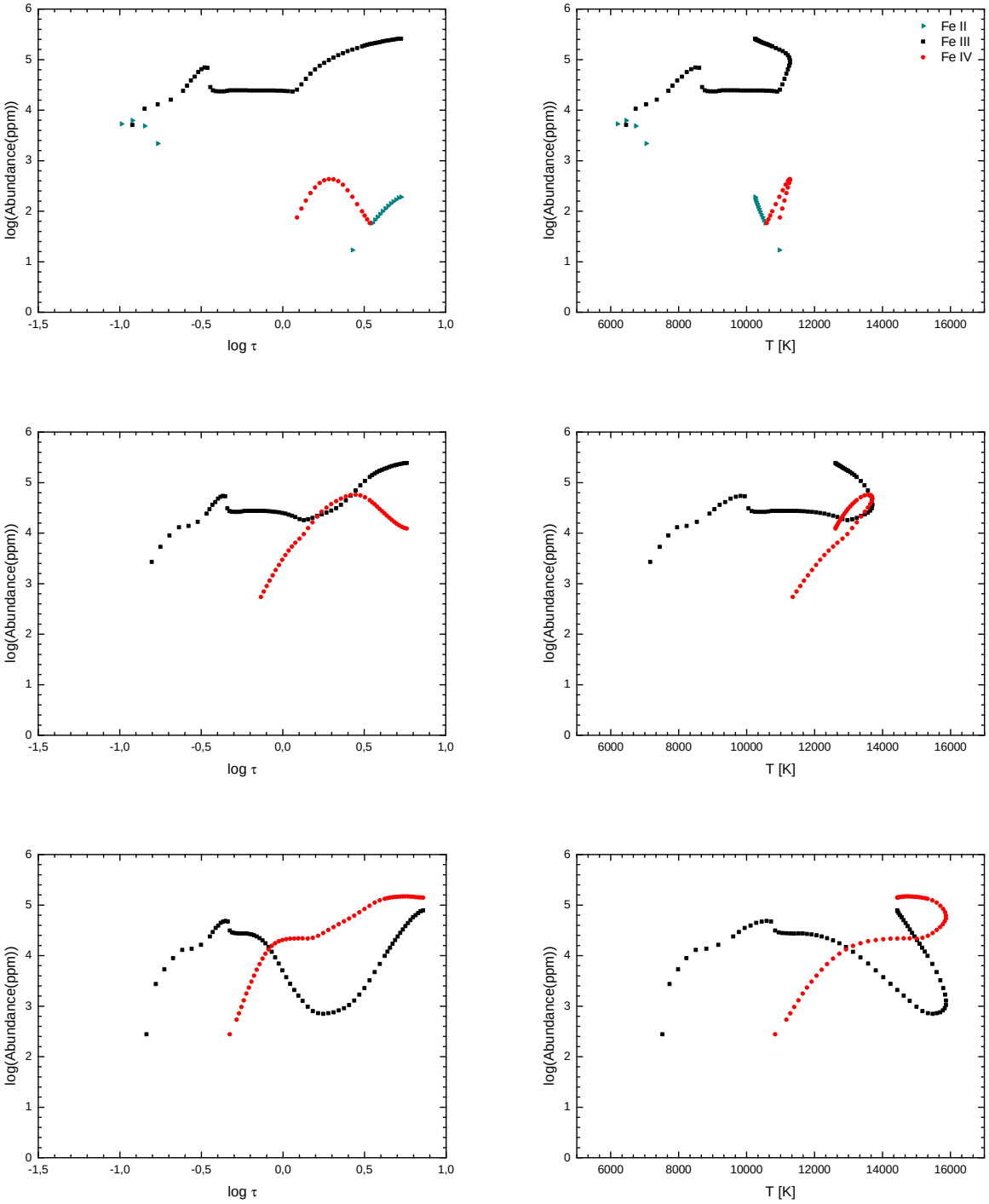

Figure 5.5: For the models with 50 %, 100 %, and 150 % of ^{56}Ni (from top to bottom) the normalized (to 10^6) particle number of ionized iron as a function of the optical depth τ (left side) is shown and plotted against temperature (right side) for day 20 after the explosion. The legend labels the ionization of iron, which occurs as Fe II, Fe III, and Fe IV. See text for details.

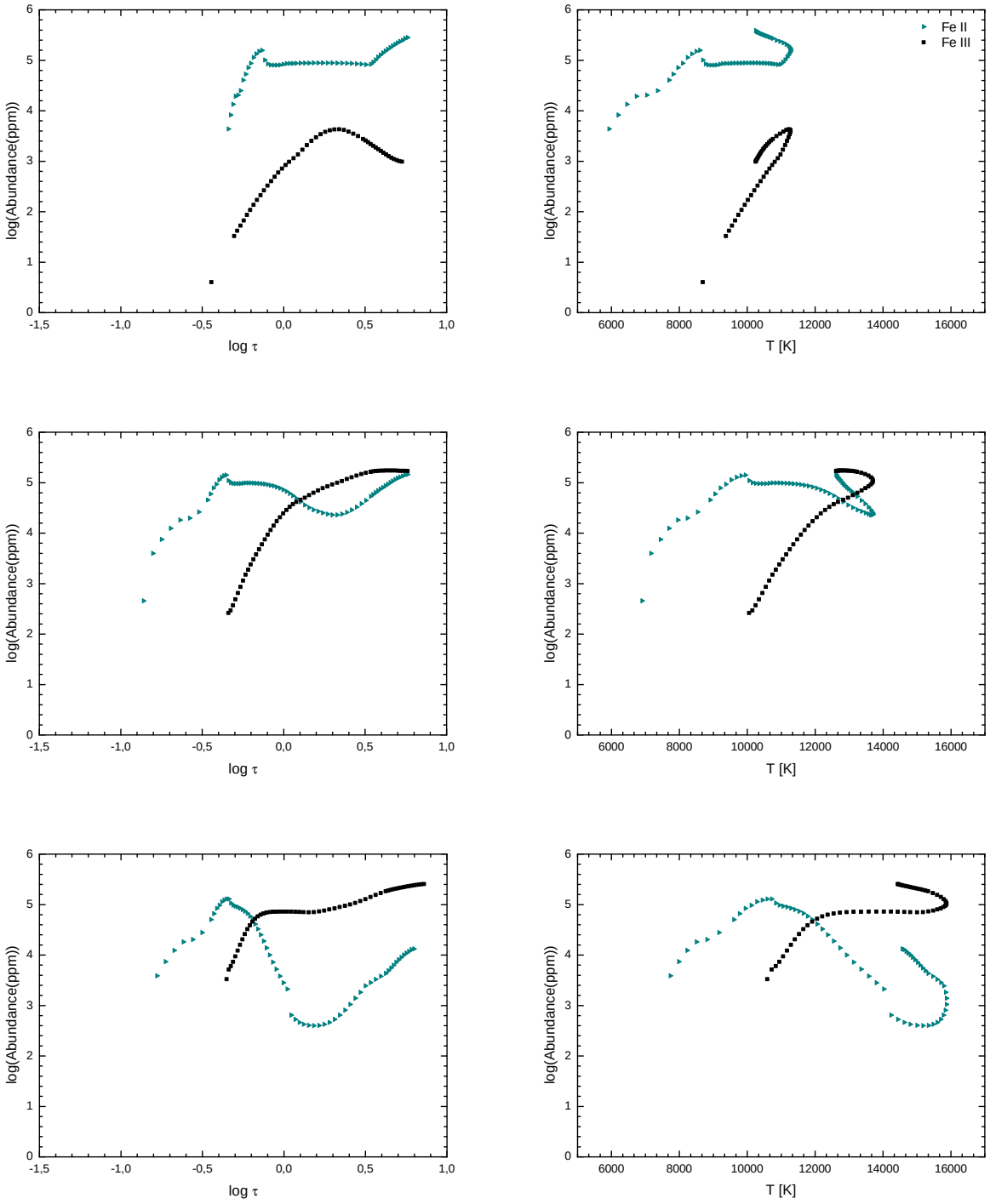

Figure 5.6: Same as in Figure 5.5, but for day 40 after the explosion. For the models with 50 %, 100 %, and 150 % of ^{56}Ni (from top to bottom) the normalized (to 10^6) particle number of ionized iron as a function of the optical depth τ (left side) is shown and plotted against temperature (right side). The legend labels the ionization of iron, which occurs as Fe II and Fe III. See text for details.

For models with more ^{56}Ni these features are more pronounced. The reason is that these models are hotter and the individual features are more pronounced, although the abundance of the other elements is reduced by the renormalization. Calcium, for example, occurs in these models mainly as Ca III, the layers in which it resides are not opaque.

In normal Type Ia supernovae the P Cygni features are found in the lines of O I[1], Mg II, Si II, S II, and Ca II around the time of maximum brightness.

Iron can be seen shortly thereafter, it is one of the lines, which strongly influences the later spectra. The transitions of the different ionization are energy-dependent and thus depend on the temperature. The ionization itself influenced the opacity, e.g., via the number of different line transitions. In Figures 5.5 and 5.6 (left side) the normalized (to 10^6) particle number of ionized iron (Fe II, Fe III, and Fe IV) is shown as a function of the optical depth τ for the models with 50 %, 100 %, and 150 % of ^{56}Ni and plotted against temperature for days 20 (Figure 5.5) and 40 (Figure 5.6) after the explosion. For day 20, in the model with 50 % ^{56}Ni Fe II occurs, in the other two models there occur only Fe III and Fe IV (cf. Figure 5.5). For day 40, only Fe II and Fe III occur (cf. Figure 5.6). However, Fe II is essentially observed everywhere. Increasing energy, which is equivalent to the amount of ^{56}Ni, increases the ionization of iron. Plotting the normalized (to 10^6) particle number of ionized iron to temperature (Figures 5.5 and 5.6 (right side)), one sees the shift for models with larger amount of ^{56}Ni to higher temperatures. Note that the bow of the individual ionization has nothing to do with the temperature dependence. Here, the ionization is only plotted against temperature to show the complex behavior. For illustration we will discuss the temperature stratification at the end of this chapter.

We now take a look at the spectra of selected individual days before we discuss the light curves, which are calculated from these spectra. In Figure 5.7 the spectra for days 5, 10, 14, 16, 18, 20, 22, 24, 26, 30, 40, and 50 are shown in the wavelength range $[3000, 24740]$ Å of the models for varying ^{56}Ni abundances. Thus, all filters are included. In the spectra can be seen clearly, despite the logarithmic representation and the large wavelength range, the temporal evolution. From a physical point of view, one can see in the early spectra high velocity layers, containing mainly unburnt material. During maximum light, around day 20, we see deeper high-velocity layers, mostly burnt to intermediate mass elements, such as oxygen, magnesium, silicon, sulfur, calcium, and cobalt. The later spectra are formed in even deeper and slower layers and contain mainly iron-peak elements. In the last two spectra, days 40 and 50 after the explosion, the strong absorption lines of Si II around 6150 Å and Ca II near 3750 Å and 8300 Å can be seen clearly. The strong absorption, caused by doublet Ca II H and K, can also be seen clearly in Figure 5.8, as well as the weaker features mainly caused by Fe II around 4100, 4400, 4850, 5050, and 5400 Å. In Figure 5.8 the same as in Figure 5.7 is shown, but now focused on the wavelength region of the B band ($[3600, 5600]$ Å). Thus can be seen clearly in the difference below the energy-rich (those with more ^{56}Ni) and the low-energy models. The spectra from the former are more luminous. However, it has to be proved whether it is a hint of the Phillips relation.

In the next step we have calculated from the 32 spectra per model sequence, light curves for the Johnson photometric system for the bands U, B, V, R, I, J, H, and K. The light curves in Figure 5.9 are shown in a spatial representation.

[1] Absorption feature around 7500 Å

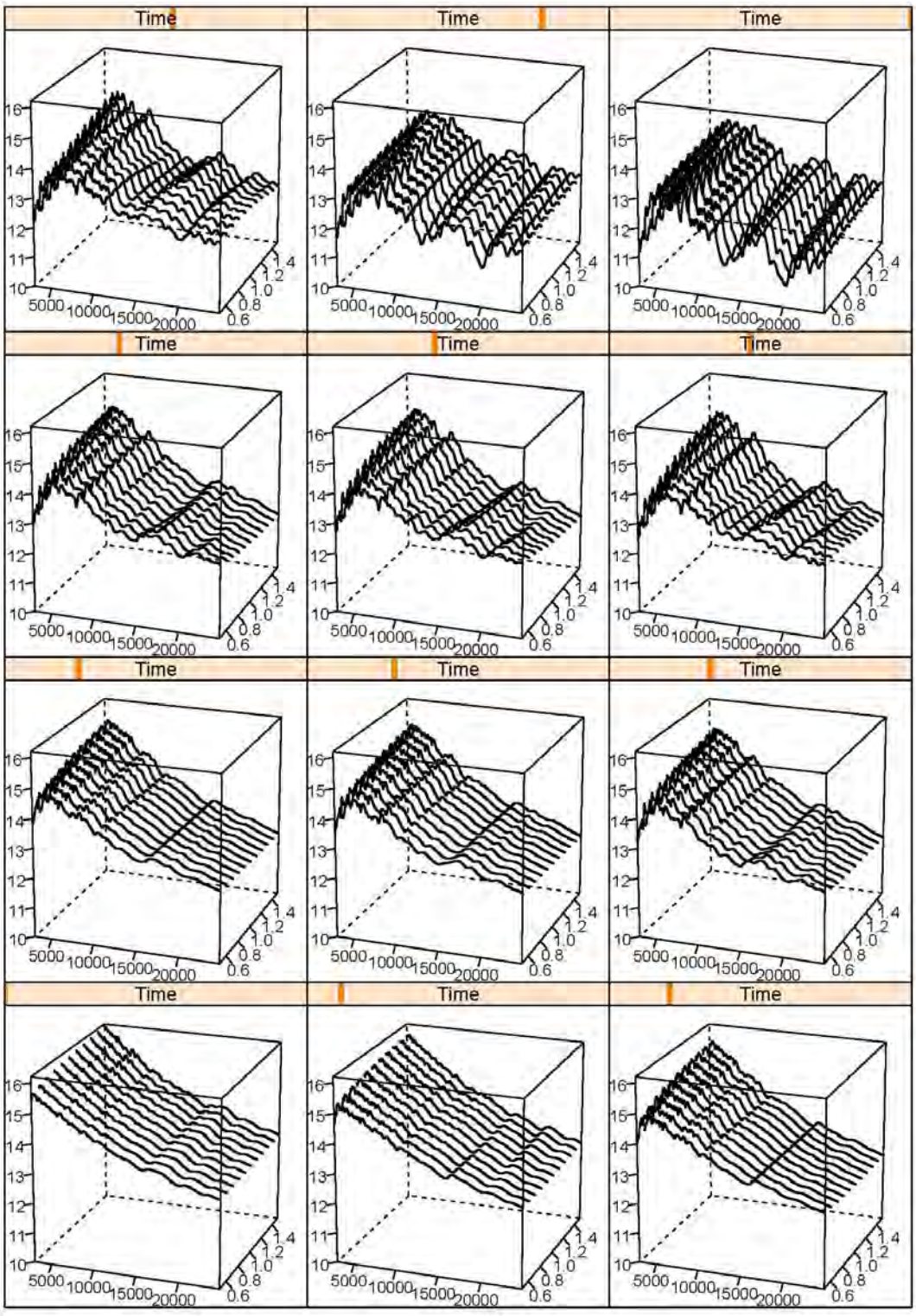

Figure 5.7: Starting in the lower left corner and ending in the upper right corner, synthetic spectra for days 5, 10, 14, 16, 18, 20, 22, 24, 26, 30, 40, and 50 of models for varying ^{56}Ni abundances are shown. Plotted is the logarithmic flux as a function of wavelength in the range $[3000, 24740]$ Å. The depth axis shows the ^{56}Ni abundance. See text for details.

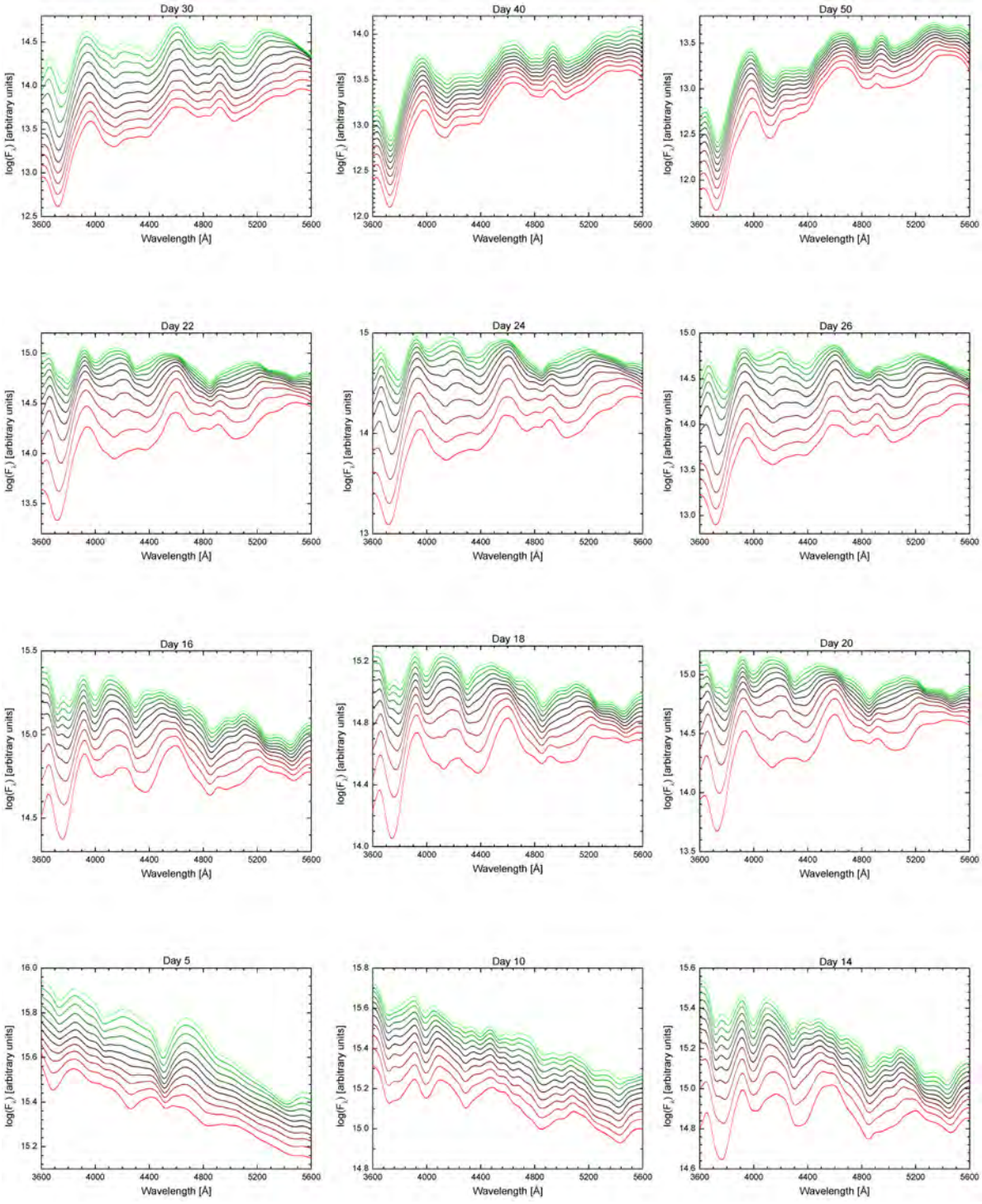

Figure 5.8: The same as in Figure 5.7, but for the wavelength range of the B band ($[3600, 5600]$ Å). See text for details.

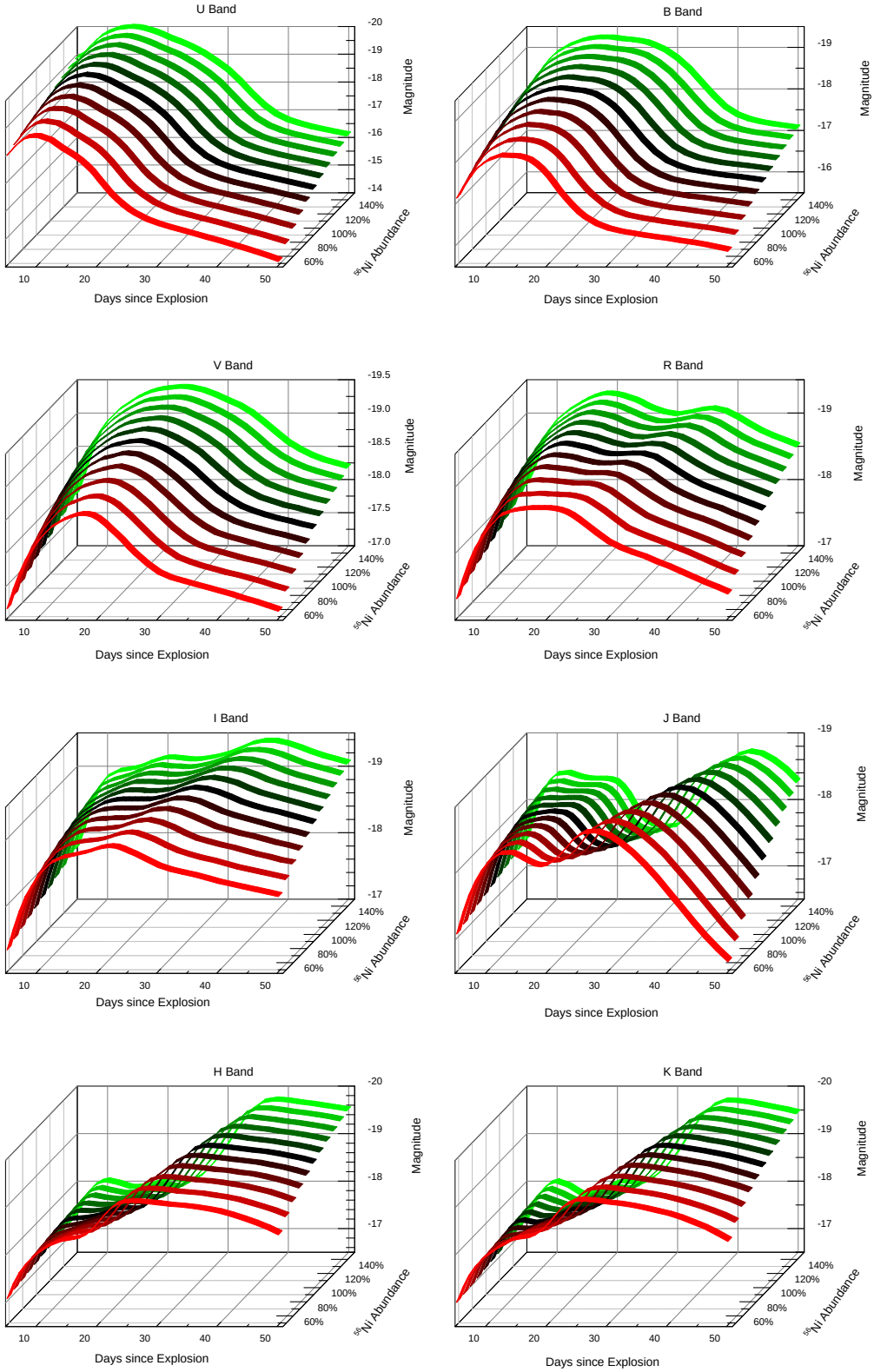

Figure 5.9: Spatial representation of model light curves in the bands U, B, V, R, I, J, H, and K as calculated from synthetic spectra for day 5 until 50 days after the explosion. The abundance of ^{56}Ni was changed in steps of 10 % from 50 % (red curve) to 150 % (green curve). See text for details.

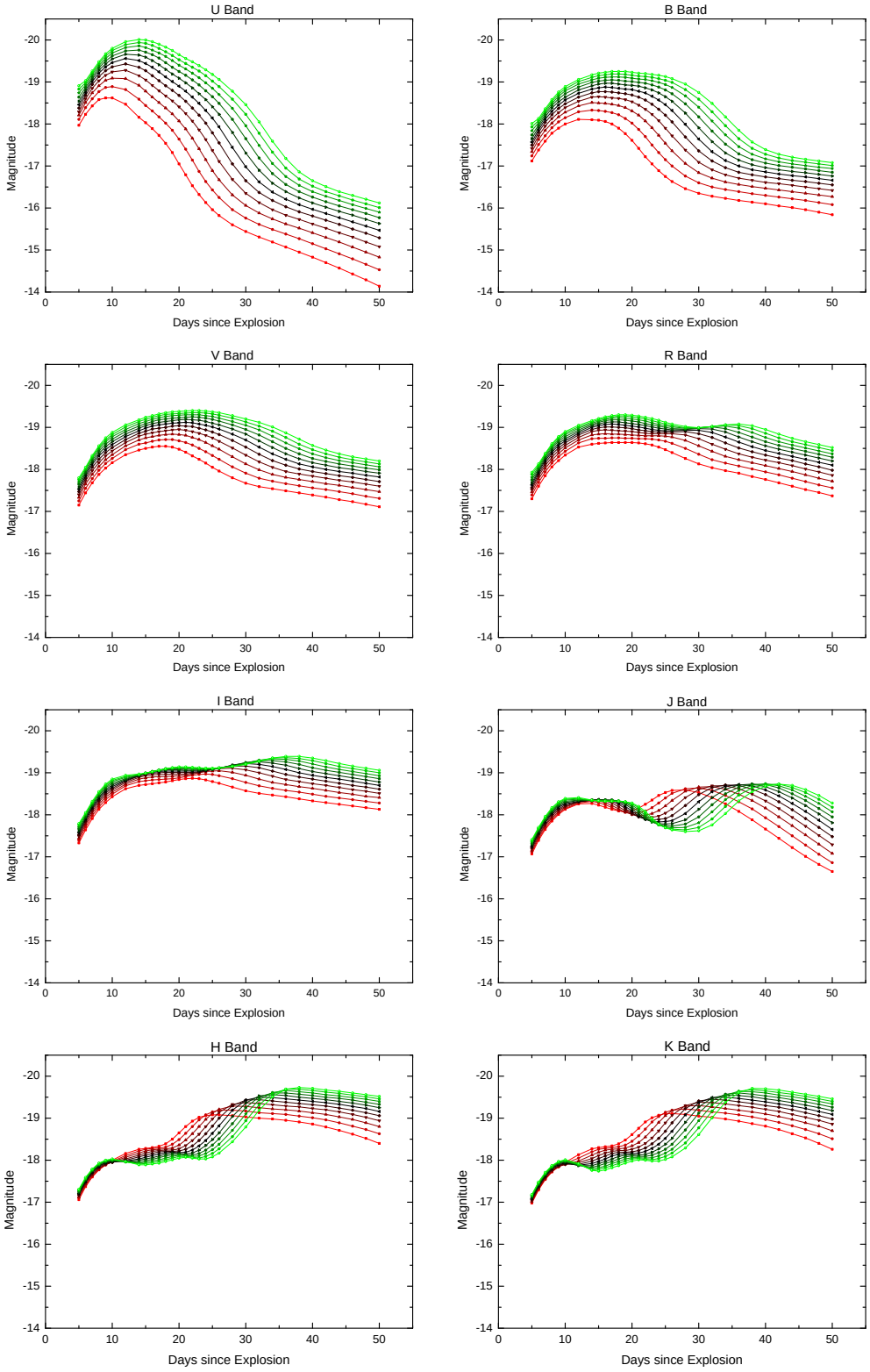

Figure 5.10: The same light curves as shown in Figure 5.9, but in a different presentation. Note the scale of the ordinate is now the same for all bands. The abundance of ^{56}Ni was changed in steps of 10 % from 50 % (red curve) to 150 % (green curve). See text for details.

The same light curves are shown in Figure 5.10 in a different presentation. Note that the scale of the ordinate in Figure 5.10 is the same for all bands. The abundance of ^{56}Ni was changed in steps of 10 % from 50 % (red curve) to 150 % (green curve). As expected, the Phillips relation can be seen in the bands U, B, and V reproduced differentially. The light curves of brighter supernovae decline in these bands more slowly.
In the R band the formation of a second maximum can be seen, which depends on the amount of ^{56}Ni. While in the model with 50 % ^{56}Ni this maximum is not seen, or coinciding with the first maximum, it moves with increasing ^{56}Ni content further back in time, for the model with 150 % ^{56}Ni to day 36 after the explosion.
Models close to the fiducial model are in good agreement with the model templates shown in Section 2.4, Figure 2.4. The trend that the second maximum migrates farther back on the time scale with increasing content of ^{56}Ni, can be seen very well in the near infrared in the bands I, J, H, and K. This effect is so great in these bands so the brightness of the model with 50 % (red curve) ^{56}Ni is locally greater than that of 150 % (green curve) ^{56}Ni, and it leads to a temporary inversion of the brightnesses.
In the next step, the data from the light curves shown in Figures 5.9 and 5.10 were evaluated statistically. The timeline is used as explanatory variable. It is usually a continuous variable. However, we discretize it into 32 time steps, which corresponds exactly to the days for which spectra were calculated. Therefore, we use the timeline for days after the explosion as categorical explanatory variables[2] and the corresponding magnitudes as the response variables and summarize this large amount of information graphically combined in the two Figures 5.11 (for the bands U, B, V, and R) and 5.12 (for the bands I, J, H, and K). The horizontal lines in the constricted boxes, the notches, show the respective median of the magnitudes of the corresponding categorical variables. The upper and lower margin of the yellow box show the first and third quartile. Points more than 1.5 times the interquartile range[3] ($\gtrsim 2\sigma$) above the third quartile, marked by the upper whisker, and points more than 1.5 times the interquartile range below the first quartile, marked by the lower whisker, are defined as outliers and individually plotted as red asterisks. For the bands U, B, and V in Figure 5.11 we have no outliers, the whiskers show the maximum and minimum values of the magnitudes. The margins are formed by the curves of the two models with 50 % (red curve) and 150 % (green curve) ^{56}Ni. Nevertheless, we can see that the response variables spread differently and have skewness, which shows up as asymmetry in the sizes of the upper and lower parts of the box. This can be seen especially well for days 30 and 32 in Figure 5.11 in the R band. The notches of these two days are clearly extended above the 75th percentile. On other days, just around the maximum brightness in the B band, we have the same results. This indicates that within the sample the variance is high. In the R band, we also have outliers for days 25, 26, 28, and 30, the lower whiskers end at these days in the values of the model with 60 % ^{56}Ni. Overall, we have in the bands U, B, V, and R, represented in Figure 5.11, without exception overlapping adjacent boxes. These bands are almost entirely in the visible, except the R band, whose tail extends in the infrared (cf. Section 4.5, Table 4.1 & Figure 4.10).

[2]For more details on the statistical terms used here, e.g., Crawley (2007)
[3]The difference in the response variable between its first and third quartile

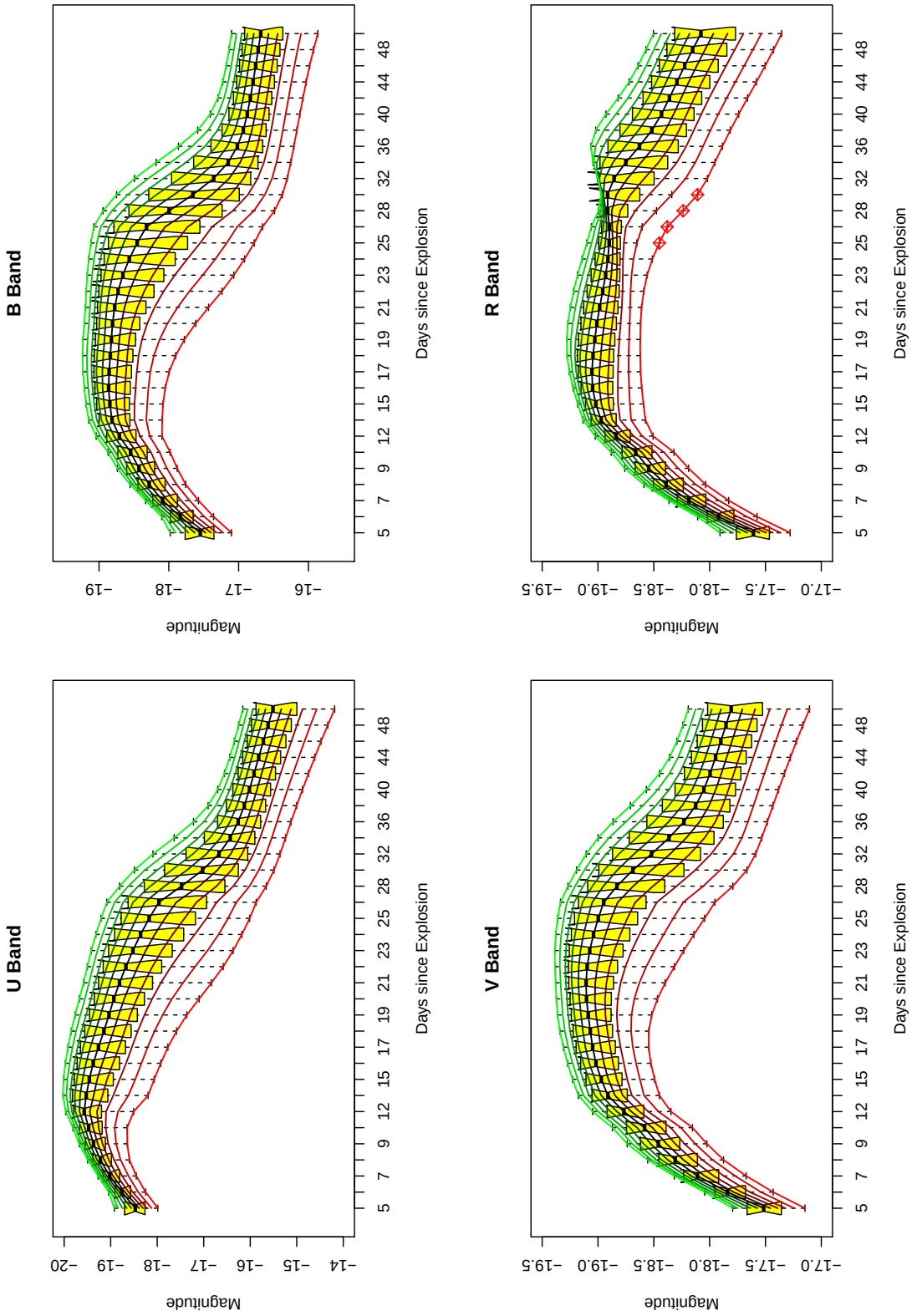

Figure 5.11: Summarized graphical representation of the statistical analysis of the model light curves from Figure 5.9 in the bands U, B, V, and R. See text for details.

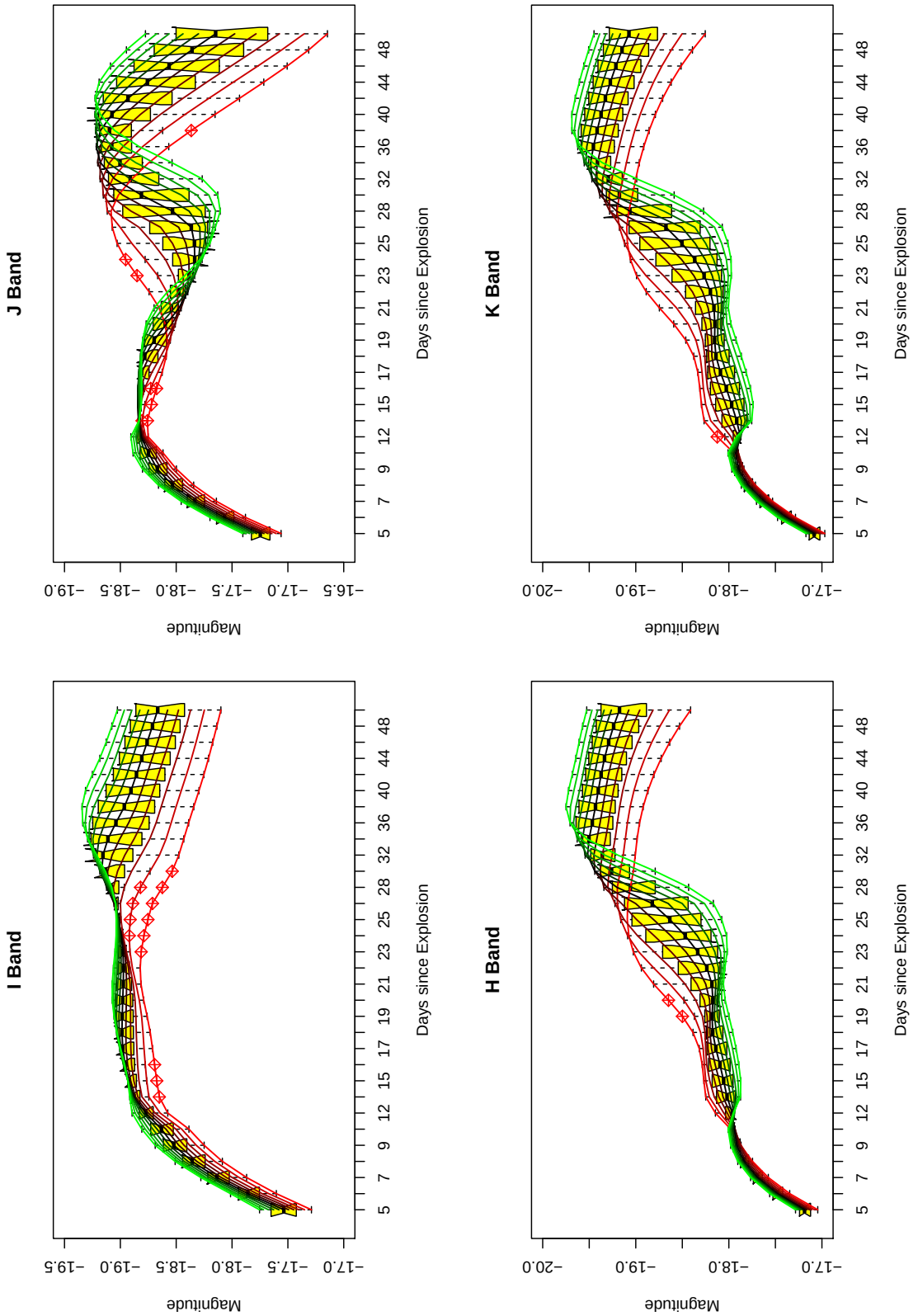

Figure 5.12: Summarized graphical representation of the statistical analysis of the model light curves from Figure 5.9 in the bands I, J, H, and K. See text for details.

Note that the statistical evaluation, summarized and shown in Figures 5.11 and 5.12, based entirely on the calculated data themselves, there are no estimated parameters like means or standard deviations.
Now the statistical evaluation of the data for the bands I, J, H, and K in the region of the near infrared is considered. The results are summarized in Figure 5.12. The situation in this region is now much more challenging. As mentioned above, there is an inversion of the brightnesses of the two marginal models, due to the delayed shift of the second maximum for models containing more ^{56}Ni. The shifted second maximum distorts the statistical analysis in these bands.
However, reliable statements can only be made by statistics. As summarized in Figure 5.12, for the I band one can see that the margins are formed by curves of the two models with 50 % (red curve) and 150 % (green curve) ^{56}Ni. We have again, as in the visible region, that the energy-poor model (50 % ^{56}Ni) forms the bottom line of brightness, whereas the energy-rich model forms the top line of brightness in this band. The response variables spread widely and varying degrees. Again there is skewness. The ^{56}Ni enhanced models, represented by the green curves, are squeezed in the region between days $23-26$ and 28. The notches for days $30-34$ are clearly extended above the 75th percentile. In this band the model with 50 % ^{56}Ni shows outliers for days $14-16$, $23-26$, 28, and 30. The model with 60 % ^{56}Ni shows outliers for days $24-26$ and 28. In the last part of the timeline it is striking that the response variable in the R and J bands spread widely. In addition, we have now in the J band the situation that the low energy model with 50 % ^{56}Ni becomes brighter, because of its second maximum.

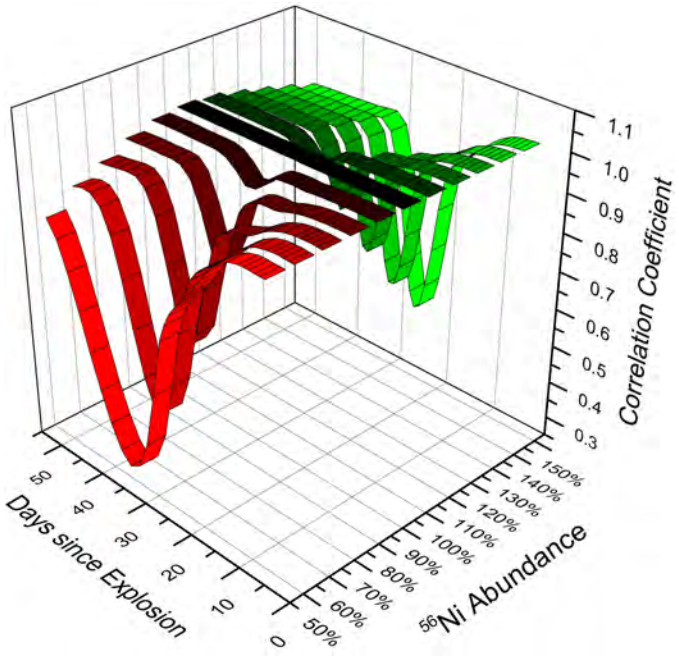

Figure 5.13: Pearson correlation coefficients for the individual days of the light curve of the B band for this model series. Colors, abundances, and days are the same as used previously. See text for details.

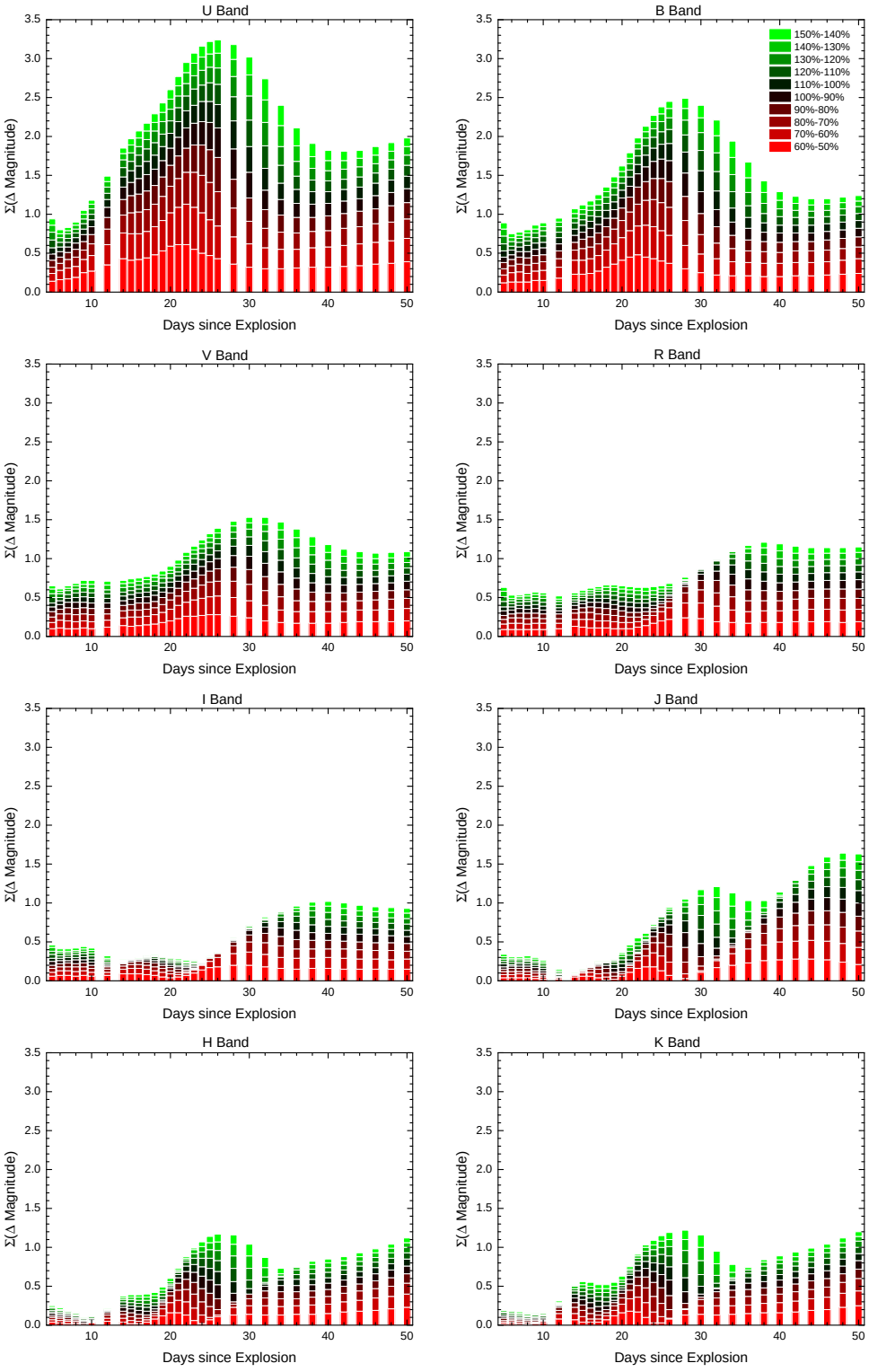

Figure 5.14: Summed absolute values of the differences between two adjacent models for previously discussed bands shown in Figures 5.9 and 5.10. The lower energy model is subtracted from the neighboring model with more ^{56}Ni. The colors are inspired by the colors used so far and given in the legend. Note that the scale of the ordinate is the same for all bands. See text for details.

For day 18, it is just as bright as the model with 60 % ^{56}Ni and in the period between days 22 and 28, it is even the brightest model, even brighter than the model with 150 % ^{56}Ni. In the model with 50 % ^{56}Ni, the magnitudes for days $14-16$, 23, 24, and 38 are statistically considered as outliers. From day 38 this band spreads the largest of the infrared bands. The bands H and K look very similar to J. In the H band, we have the same model outliers for days 19 and 20 and in the K band only one statistical outlier for day 12.
Based on the statistical outliers, but also on the course and behavior of the light curves, the two models with 50 % ^{56}Ni and 60 % ^{56}Ni can be definitely ruled out as valid models. They form extreme margin values and show the limits of the highly parametrized hydrodynamic explosion model.
For the individual days of the light curves, the Pearson correlation coefficients[4] for this model series were calculated and shown in Figure 5.13. The colors, abundances, and days are the same as previously used.
Correlation refers to the fiducial model and is, therefore, for the model with 100 % ^{56}Ni, as expected, one. The poorest correlation shows the model with 50 % ^{56}Ni, also as expected.
One of the questions is, what it means when the model response of the individual models, the magnitudes of the individual days, spread open on certain days and more are squeezed on others.
First, we look at the absolute values between the magnitudes of the individual days of the models. Differences between two adjacent models were computed, usually so that,

$$|X| = \sqrt{\left(X_{\text{upper}} - X_{\text{lower}}\right)^2}, \tag{5.1}$$

with X as the magnitude of the corresponding band. The summed results of these data are shown for the considered bands in Figure 5.14. The biggest differences are, as already indicated in the Figures 5.9, 5.10, 5.11, and 5.12, in the bands U and B in which most of the energy is transported. The V band shows a rather uniform picture with a maximum around day 30. The situation in the R band is similar, but here the maximum is later, the rise starts on day 28 and becomes maximal on day 38 and the following days. In the infrared, the J band shows the largest spread, as indicated in Figure 5.12, starting from day 38. Otherwise, the bands J, H, and K look very much alike in this picture. The summed differences form a maximum on day 30, then fall back and finally rise relatively steadily.
If the model answers are far apart, this is an indication that it is ideal to measure on these days. On other days, when the light curves are squeezed, such as to name only extreme examples of this model the days $5-10$ in the H and K band, the days around the day 25 in the I band, or, at least, the days around the day 14 in the J band, one needs no measurement (containing errors) from a theoretical point of view, because definitely no statements about the abundance of ^{56}Ni can be made with this model during these days in these bands. In general it can be said that for measurements, the days are ideal at which the model answers are far apart. Days on which that is not the case, since the model response is not much different, are less suitable to make statements about the respective parameter.

[4] $r := \frac{\sum_{i=1}^{n}(X_i-\bar{X})\sum_{i=1}^{n}(Y_i-\bar{Y})}{\sqrt{\left(\sum_{i=1}^{n}(X_i-\bar{X})^2\sum_{i=1}^{n}(Y_i-\bar{Y})^2\right)}}$, with $\bar{X} = \frac{1}{n}\sum_{i=1}^{n}X_i$ and $\bar{Y} = \frac{1}{n}\sum_{i=1}^{n}Y_i$, e.g., Rodgers & Nicewander (1988)

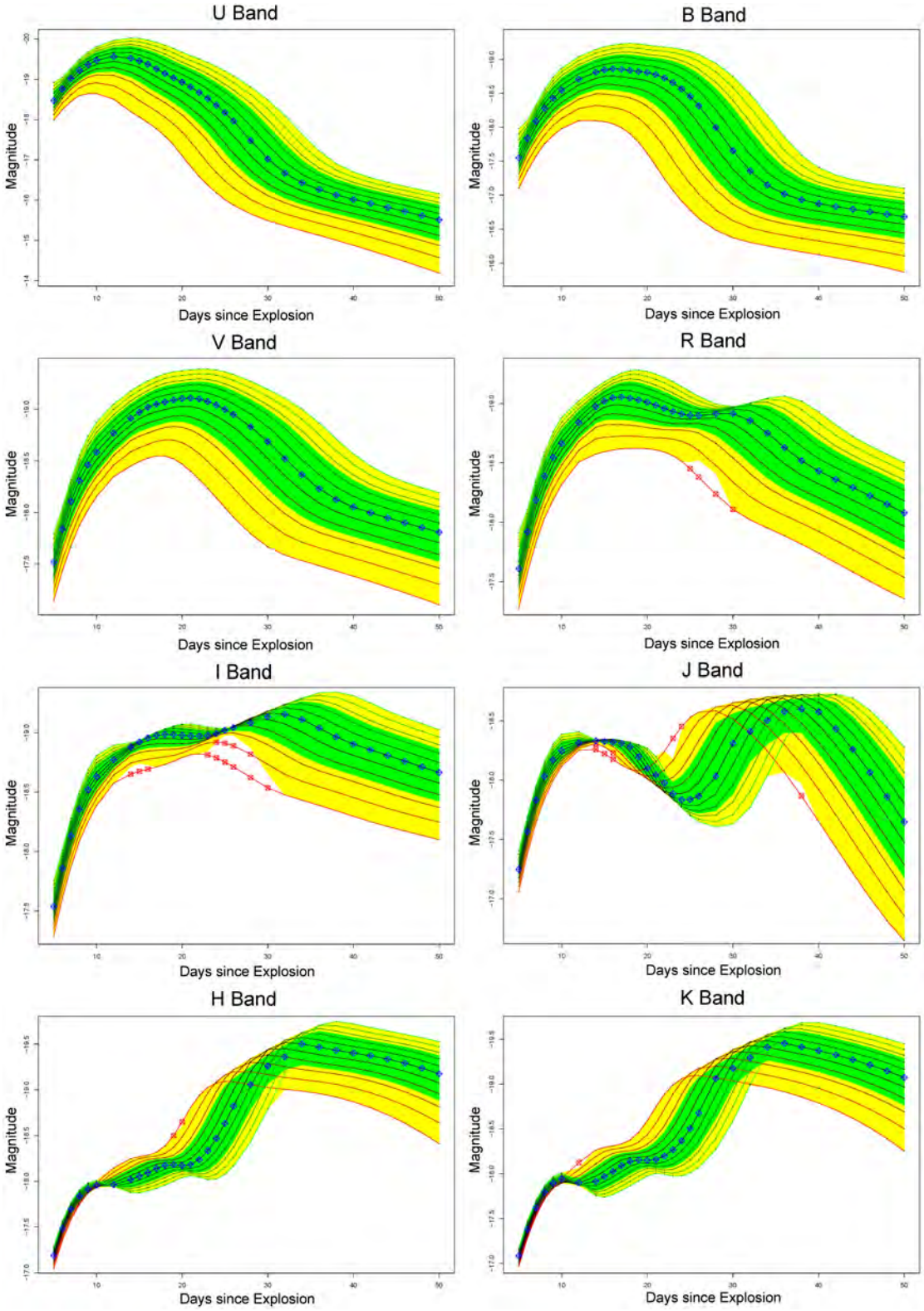

Figure 5.15: Summarized graphical representation of the statistical analysis of the model light curves from Section 4.5, Figure 4.12. The midspread is marked green, 1.5 times the interquartile range above and below the corresponding quartile is marked yellow, outliers are plotted as red asterisks, and the medians are plotted as blue asterisks connected by a dotted line. See text for details.

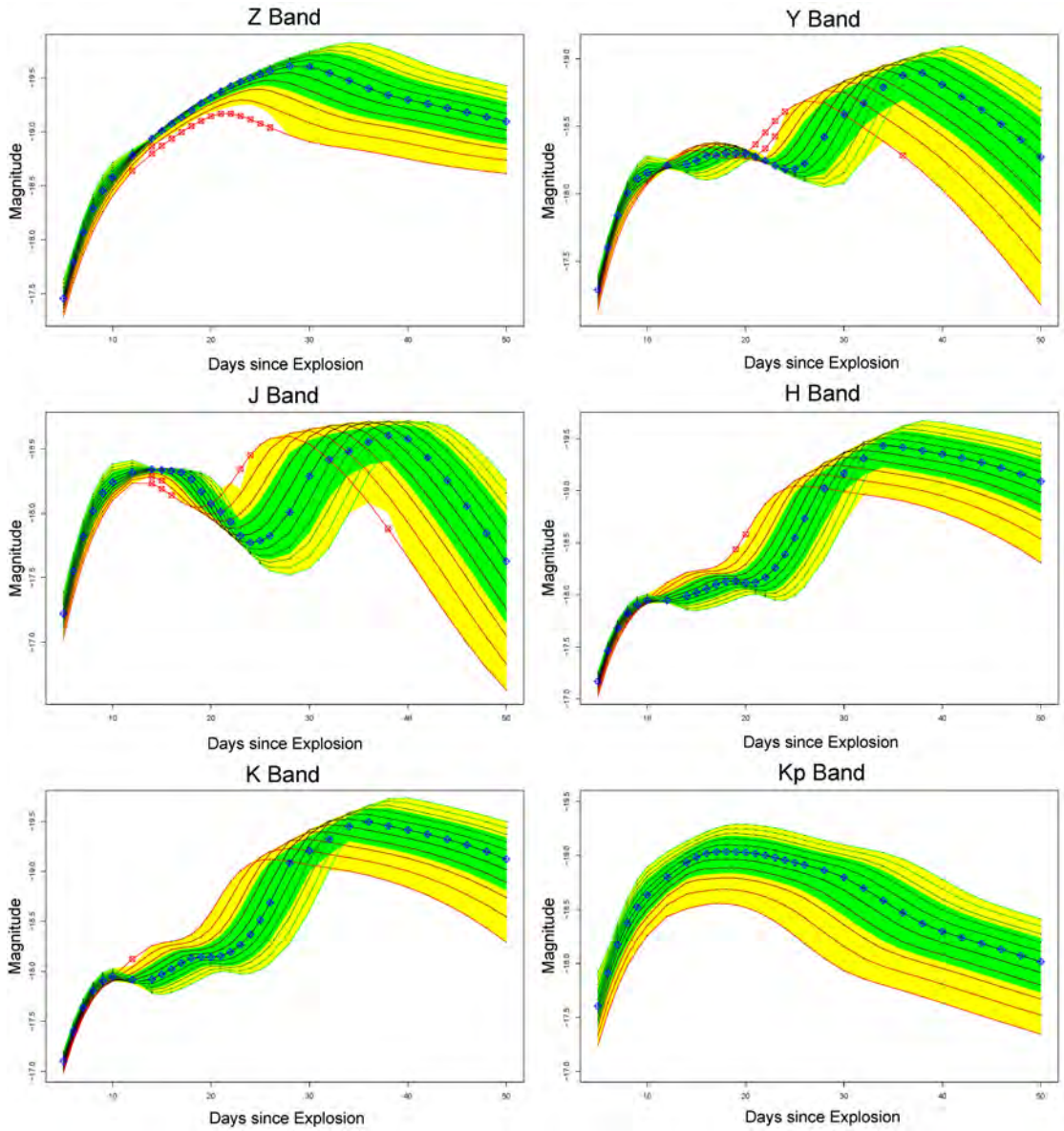

Figure 5.16: Summarized graphical representation of the statistical analysis of the model light curves from Section 4.5, Figure 4.13 for the UKIDSS photometric system for the bands Z, Y, J, H, and K and for Kepler for the band Kp. The midspread is marked green, 1.5 times the interquartile range above and below the corresponding quartile is marked yellow, outliers are plotted as red asterisks, and the medians are plotted as blue asterisks connected by a dotted line. See text for details.

Before we want to consider the possible causes why the model response exhibits this behavior on these days, we briefly look at the statistical evaluation of the other bands, introduced in Section 4.5, Figure 4.9.

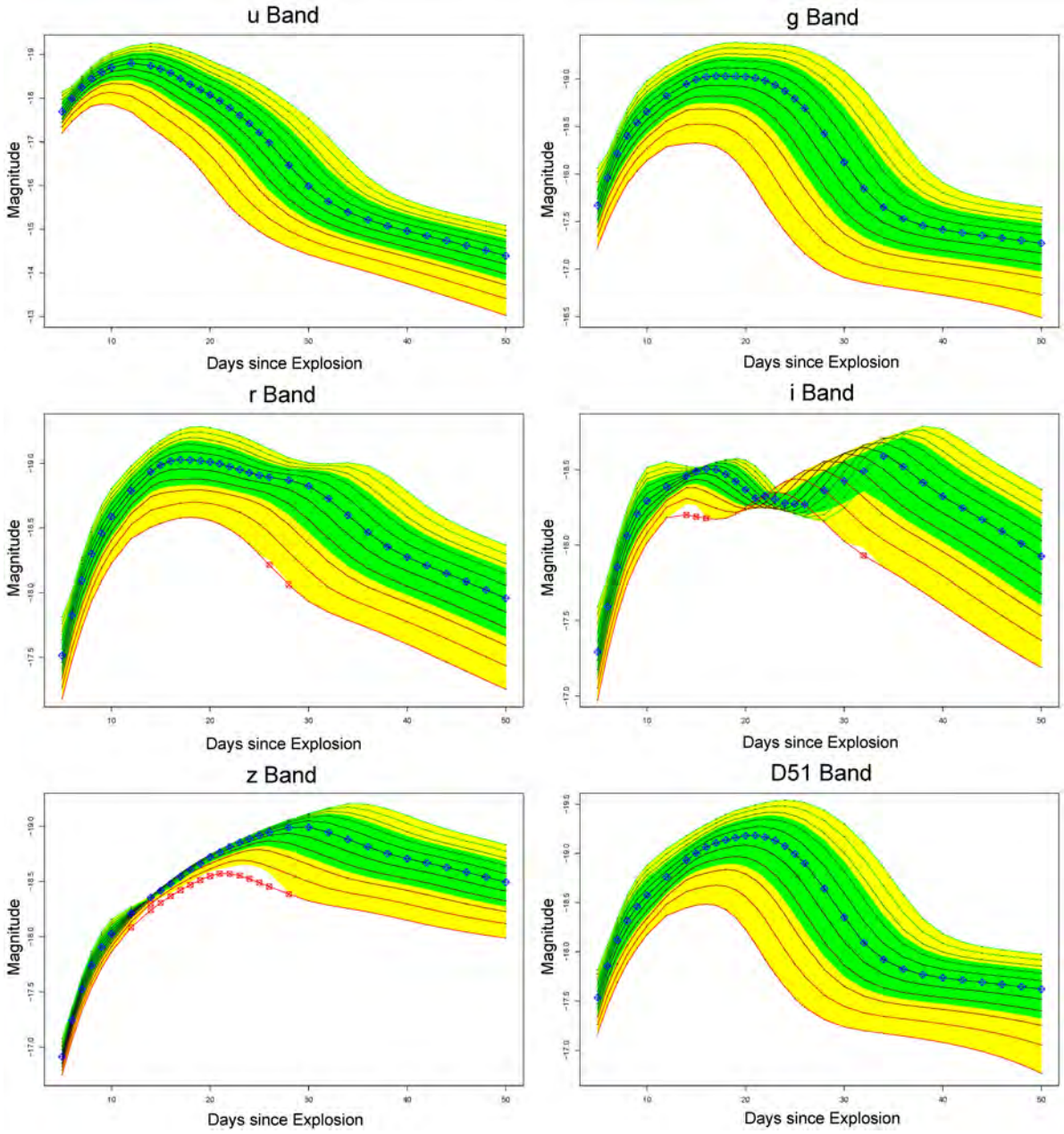

Figure 5.17: Summarized graphical representation of the statistical analysis of the model light curves from Section 4.5, Figure 4.14 for the SDSS photometric system for the bands u, g, r, i, and z and for Kepler for the band D51. The midspread is marked green, 1.5 times the interquartile range above and below the corresponding quartile is marked yellow, outliers are plotted as red asterisks, and the medians are plotted as blue asterisks connected by a dotted line. See text for details.

As shown in Section 4.5, Table 4.1 and mentioned above, from a statistical point of view it is difficult to compare the bands, because they cover very different regions that behave very differently from the perspective of energy and radiation transport.

These models are calculated in LTE. However, it is quite clear that in the infrared NLTE effects become important, whereas LTE seems a good approximation in the visible region.
We calculated the bands of the models shown in Section 4.5, Figures 4.12, 4.13, and 4.14 and evaluated the results statistically. We draw on the method to calculate quartiles, interquartile ranges, whiskers, and outliers, as shown already in Figures 5.11 and 5.12. In Figure 5.15 the model light curves for the bands U, B, V, R, and I for the Johnson photometric system and J, H, and K for 2MASS are shown. As before, we changed the abundance of ^{56}Ni in steps of 10 %. Since we have these light curves analyzed statistically, the median and the confidence limits are additionally drawn in.
The midspread is marked green, the medians are individually plotted by blue asterisks. These two values are estimators, the median is a level estimator, the interquartile range is a trimmed estimator and is the most significant basic robust measure of scale. The yellow area marks the region 1.5 times the interquartile range below the first quartile and above the third quartile. Note that the confidence limits of this range are for a probability density function of a normal $N(0, 1\sigma^2)$ population, already outside $\gtrsim 2.7\sigma$.
The plots of the light curves in the bands U, B, V, R, and I, shown in Figure 5.15, have already been discussed. For the light curves in the bands J, H, and K in 2MASS is the situation very similar as for the same bands in the Johnson system, despite slightly different wavelength ranges and different λ_{eff} (cf. Section 4.5, Table 4.1 and Figure 4.10). Points outside these confidence limits are considered as outliers and plotted as red asterisks. Note the inversion of the light curves in the bands J (for days 25 to 34), H (for days 14 to 30), and K (for days 14 to 32). The faintest light curves in these bands are from the model with 150 % ^{56}Ni.
Note the deviation of the medians in the bands J (for days 14 to 18, 19 to 24, and 30 to 40), H (for days 9 to 12 and 26 to 34), and K (for days 9 to 14 and 28 to 36). This means between days 9 and 38 for this model, that no reliable measurement of the abundance of ^{56}Ni can be made in the H band. The same applies to the band J between days 12 and 44, as well as to the K band between days 9 and 40. The brightness of the light curves of the early days does not even differ by half a magnitude.
In Figure 5.16 is shown the statistical evaluation of the model light curves for the UKIDSS photometric system for the bands Z, Y, J, H, and K and for Kepler for the band Kp. The bands J, H, and K have been already discussed for the Johnson system, as well as for 2MASS. The behavior of these bands in the system UKIDSS is completely analogous to the situation described above. In the Z band of this system, we have statistical outliers for the model with 60 % ^{56}Ni for day 14 and for the model with 50 % ^{56}Ni for days 12, 14, and 15 to 26.
For days around the maximum brightness, the light curves of the models in this band are very close to each other, so that there the abundance of ^{56}Ni can hardly be determined. From day 30 the light curves spread out.
In the Y band of this system, we have statistical outliers for the model with 60 % ^{56}Ni for days 22 and 23 and for the model with 50 % ^{56}Ni for days 21 to 24, 14, and 36. The light curves are compressed and look pinched for days 12 and 22. The light curve of the model with 50 % ^{56}Ni increases, however, it becomes not the brightest curve, falls and then rises again to the brightest curve between days 21 and 26. The medians differ by inversion of the brightness. This can be seen on days when the light curves are pinched off and between days 28 and 38.
We achieve clear results in the Kp band of the Kepler system. This band completely encloses the optical region and extends into the infrared (cf. Section 4.5, Table 4.1 and Figure 4.10).

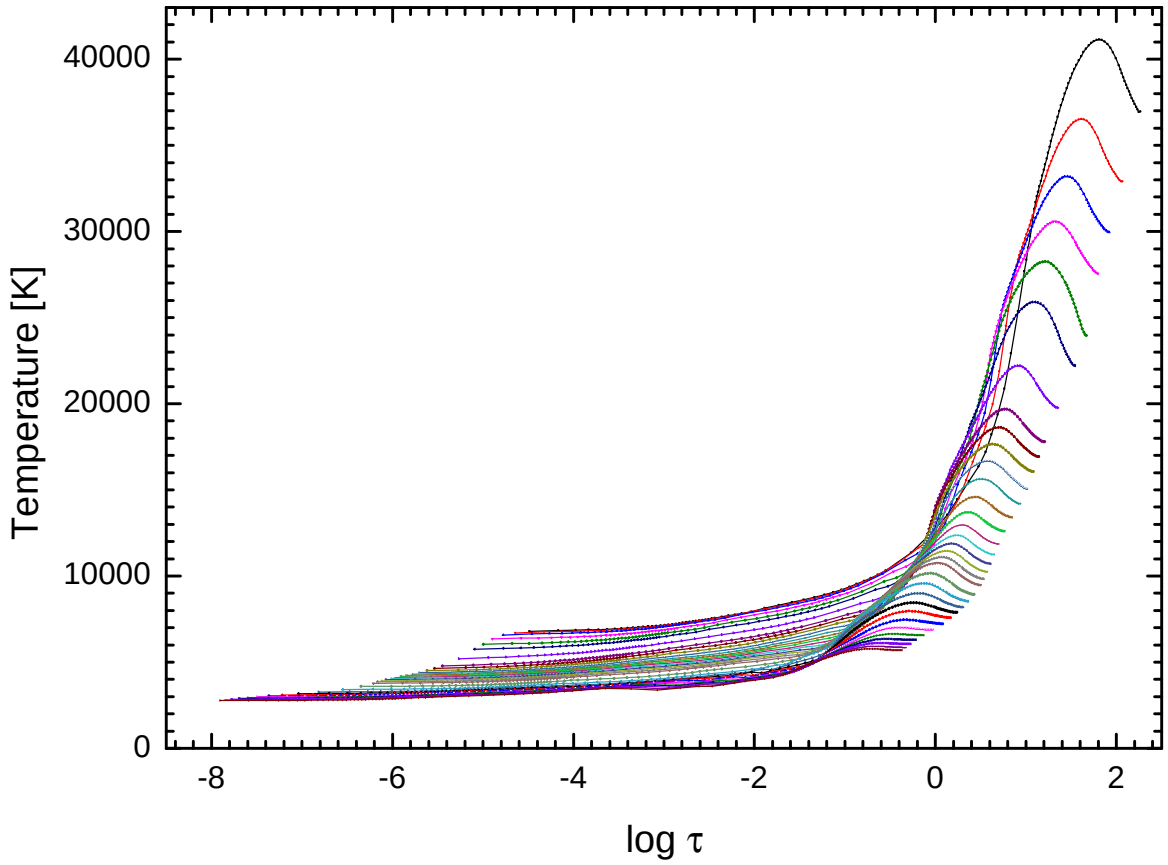

Figure 5.18: Temperature stratifications as a function of the optical depth for the 32 models, representing the time points from which the light curve was calculated for the fiducial model. The hottest models are opaque. Starting with day 5 after explosion, we have $T \simeq 41150\,K$ and $\log\tau \simeq 2.3$. With progress of time, the model atmospheres become cooler and more transparent. For day 50 we have $T \simeq 5750\,K$ and $\log\tau$ in the range $[-7.9, -0.4]$. See text for details.

There are no statistical outliers, the light curves of the models are clearly spread apart.

The last thing we want to have a closer look to are the properties of the light curves SDSS photometric system in the bands u, g, r, i, and z and for Kepler the band D51. The statistical evaluation for the bands u, g, r, i, and z (SDSS) and D52 (Kepler) is shown in Figure 5.17. These bands are very interesting. They cover the range $[2980, 11230]$ Å. As already mentioned, there was a separate supernova project within SDSS. The bands u and g (SDSS) behave similarly as already described for the bands U and B for the Johnson system. There are no statistical outliers in these bands, the median is congruent with our fiducial model.

The situation is similar in the r band (SDSS). Here can clearly be seen the similarity to the R band of the Johnson system. However, compared to the R band, the behavior is not as strong and we have less statistical outliers (only for days 26 and 28, cf. Figures 5.15 and 5.17). However, this band comprises a shorter wavelength range than the R band (cf. Section 4.5, Table 4.1 and Figure 4.10).

The enclosed wavelength range of the i band (SDSS) is a little shorter than that of the I band (Johnson) and extends a little more in to the visible region (cf. Section 4.5, Table 4.1 and Figure 4.10). We have, unlike in the I band, an inversion of the light curves in the i band. Models with less ^{56}Ni are, therefore, temporarily brighter than the ^{56}Ni enriched models (cf. Figures 5.15 and 5.17).
The situation in the z band (SDSS) is similar. However, here it is the other way around, Z (UKIDSS) comprises a shorter wavelength range than the z band (cf. Section 4.5, Table 4.1 and Figure 4.10). In addition, z has a statistical outlier for day 28 for the model with 50 % ^{56}Ni (cf. Figures 5.16 and 5.17).
Both of these bands show impressively that the problem of parameter determination can not be solved only by pure statistics. After day 20, which represents roughly reaching maximum brightness we have in this band merely one statistical outlier (day 32) in contrast to the ten statistical outliers in the I band. However, the outliers are only suppressed by the inversion of the brightness.
In plain text this means that in all bands, where we have such an inversion, no statistical statements can be made for the questionable days, and thus around these days the abundance of ^{56}Ni can not be measured reliably.
The last band considered, is the D51 band from Kepler. This band has, as expected due to the "infinitesimal" covered wavelength range in the visible, no special features. There are no statistical outliers, the median is congruent with our model.

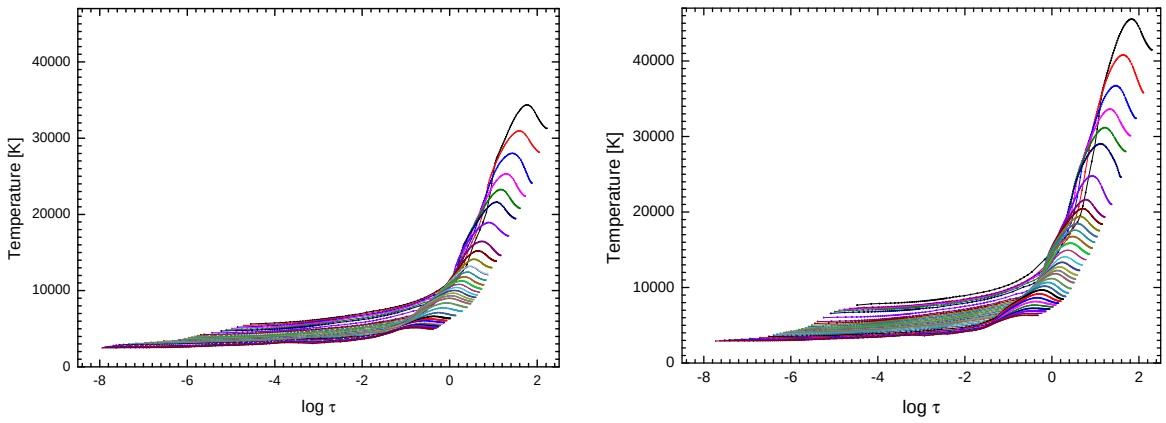

Figure 5.19: Temperature stratifications as a function of the optical depth for the 32 models, representing the time points from which the light curve was calculated for the models with 50 % ^{56}Ni (left side) and 150 % ^{56}Ni (right side). The hottest models are opaque. Starting with day 5 after explosion, we have T $\simeq$ 34350 K and $\log\tau \simeq 2.2$ for the model with 50 % ^{56}Ni and T $\simeq$ 45550 K and $\log\tau \simeq 2.3$ for the model with 150 % ^{56}Ni. With progress of time, the model atmospheres become cooler and more transparent. For day 50 we have T $\simeq$ 5150 K and $\log\tau$ in the range $[-7.9, -0.4]$ for the model with 50 % ^{56}Ni and T $\simeq$ 6350 K and $\log\tau$ in the range $[-7.7, -0.3]$ for the model with 150 % ^{56}Ni. See text for details.

One of the questions is, what causes these changes. Since we vary the amount of ^{56}Ni, we vary the energy and thus the temperature. Higher temperatures mean higher opacity. Therefore, we take a closer look at the temperature stratification as a function of the opacity. We start with the fiducial model. In Figure 5.18 the temperature stratifications as a function of the optical depth for the 32 models are plotted. The starting model (day 5) is at $\simeq 41150$ K the hottest and with an optical depth of $\log\tau \simeq 2.3$ mostly opaque. For the outer layers, we obtain $\log\tau \simeq -4.5$. This also means that we can look at this time only up to an optical depth of $\tau \approx 1$ into the expanding atmosphere. For day 20, the atmosphere with a peak temperature T $\simeq 13700$ K cooled down considerably and is with an optical depth $\log\tau \simeq 0.8$ already nearly transparent. Finally, for day 50 we have T $\simeq 5750$ K and the optical depth in the range $\log\tau \simeq [-7.9, -0.4]$. We consider also the temperature stratification as a function of the optical depth for the two extreme models with 50 % ^{56}Ni and 150 % ^{56}Ni. The results are shown in Figure 5.19. For day 5, we have T $\simeq 34350$ K and $\log\tau \simeq 2.2$ for the model with 50 % ^{56}Ni and T $\simeq 45550$ K and $\log\tau \simeq 2.3$ for the model with 150 % ^{56}Ni. With progress of time, the model atmospheres become cooler and more transparent. For day 50, we have T $\simeq 5150$ K and $\log\tau$ in the range $[-7.9, -0.4]$ for the model with 50 % ^{56}Ni and T $\simeq 6350$ K and $\log\tau$ in the range $[-7.7, -0.3]$ for the model with 150 % ^{56}Ni.
A summary of the temperatures and the optical depths for days 5, 20, and 50 for the fiducial model (100 % ^{56}Ni) and for the two extreme models with 50 % ^{56}Ni and 150 % ^{56}Ni is given in Table 5.1.

Table 5.1: Summarized results for the temperatures and the range of the optical depths for days 5, 20, and 50 for the fiducial model (100 % ^{56}Ni) shown in Figure 5.18 and for the two extreme models with 50 % ^{56}Ni and 150 % ^{56}Ni shown in Figure 5.19.

Model	**Day**	**T [K]**	**log (τ_{min})**	**log (τ_{max})**
^{56}Ni 50 % $\equiv 0.284\,m_\odot$	5	$\simeq 34350$	$\simeq -4.6$	$\simeq 2.2$
^{56}Ni 100 % $\equiv 0.568\,m_\odot$	5	$\simeq 41150$	$\simeq -4.5$	$\simeq 2.3$
^{56}Ni 150 % $\equiv 0.852\,m_\odot$	5	$\simeq 45550$	$\simeq -4.5$	$\simeq 2.3$
^{56}Ni 50 % $\equiv 0.284\,m_\odot$	20	$\simeq 11300$	$\simeq -6.1$	$\simeq 0.7$
^{56}Ni 100 % $\equiv 0.568\,m_\odot$	20	$\simeq 13700$	$\simeq -5.9$	$\simeq 0.8$
^{56}Ni 150 % $\equiv 0.852\,m_\odot$	20	$\simeq 15850$	$\simeq -5.8$	$\simeq 0.9$
^{56}Ni 50 % $\equiv 0.284\,m_\odot$	50	$\simeq 5150$	$\simeq -7.9$	$\simeq -0.4$
^{56}Ni 100 % $\equiv 0.568\,m_\odot$	50	$\simeq 5750$	$\simeq -7.9$	$\simeq -0,4$
^{56}Ni 150 % $\equiv 0.852\,m_\odot$	50	$\simeq 6350$	$\simeq -7.7$	$\simeq -0.3$

Summarized it can be said that throughout the entire evolution, models with more ^{56}Ni have higher temperatures and optical depths.
This can also be clearly seen in Figure 5.20, where the temperature profiles are plotted in 10^3 K as a function of the optical depth for days 5, 10, 14, 16, 18, 20, 22, 24, 26, 30, 40, and 50, whose spectra for varying ^{56}Ni abundances were already shown in Figures 5.7 and 5.8. We start on day 5 with a peak temperature of 45550 K (model with 150 % ^{56}Ni) and have after 45 days for the same model 6350 K.

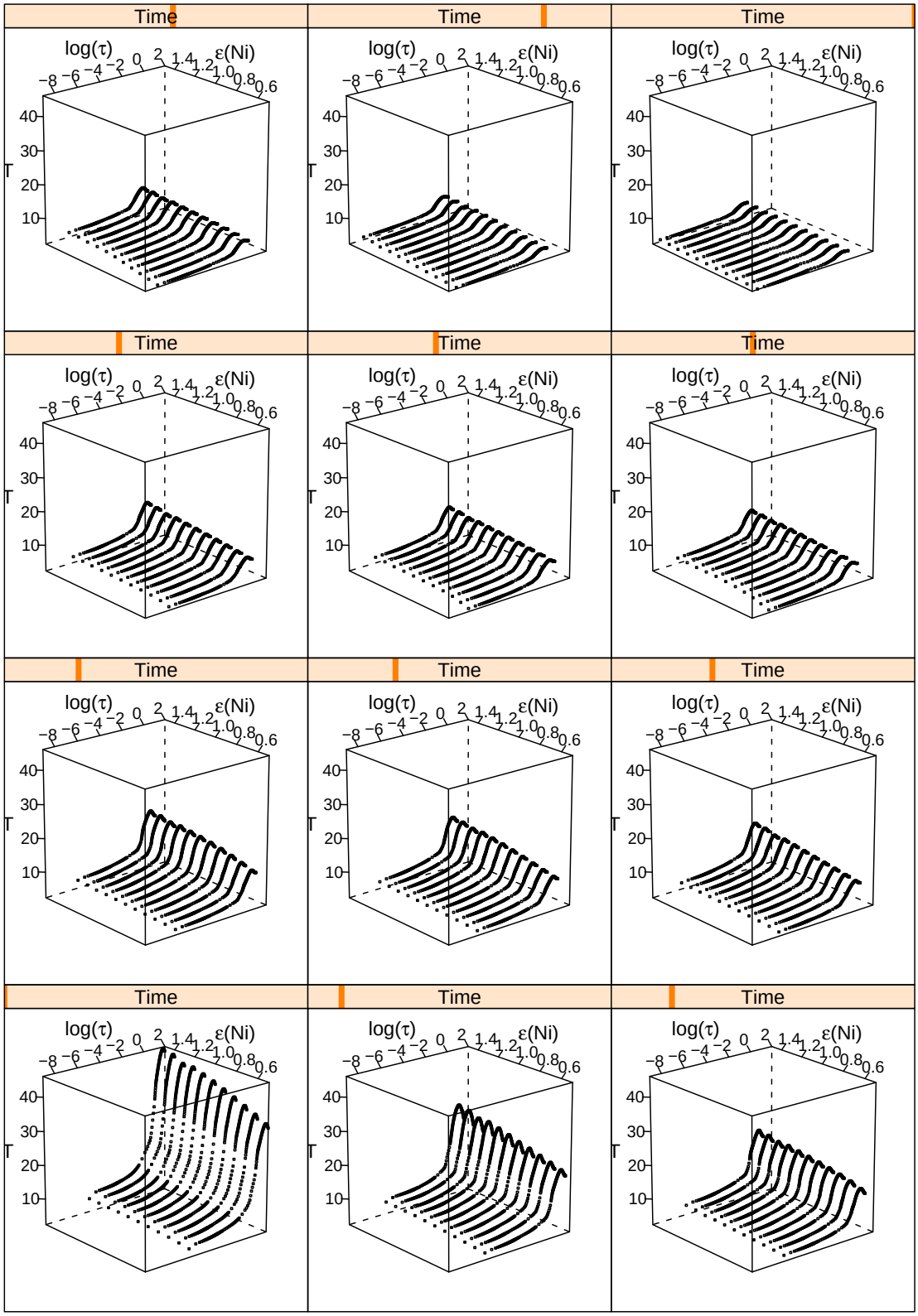

Figure 5.20: Temperature profiles in 10^3 K as a function of the optical depth for days 5, 10, 14, 16, 18, 20, 22, 24, 26, 30, 40, and 50. See text for details.

In summary, one can see in Figure 5.20 clearly the temperature gradient along the time and along the (declining) ^{56}Ni abundance. Otherwise, neither discontinuities nor jumps in the temperature profiles are recorded. Note that the initial rise of the temperature and the fall after reaching a maximum is attributable to the position of the radioactive ^{56}Ni and the iron core.
Finally, it can definitely be said for this highly parametrized model from a statistical perspective that variations of ^{56}Ni within 20 % are within the midspread and thus in a valid range of the trimmed estimator.

5.2 Varying the expansion velocity

The explosion of the white dwarf takes a few seconds. Afterward the envelope expands. While Leibundgut (1988) noted, that the claim of Branch (1987), Schneider et al. (1987), and Branch et al. (1988) that supernovae have different expansion velocities, was based only on two observations[5], this finding is now well established. However, there were at this time not only two supernovae with these characteristics (cf. Branch et al. 1988).
The expansion velocity (v_{exp}) is an important parameter. The physical meaning of v_{exp} is the kinetic energy of the explosion. It is assumed that in the model the expansion should be homologous, which means that the speed in the layers is equal also. We vary v_{exp} systematically, starting in steps of 10 % of the fiducial model. Varying v_{exp} is equivalent to the variation of the kinetic energy of the explosion. The modified velocity profiles are shown as a function of the layers in Figure 5.21. The layer index increases from outside to inside. The fiducial model is shown in black and has an expansion velocity in the outermost layer of $v_{exp} \simeq 30 \cdot 10^3\,\mathrm{km\,s^{-1}}$. The red line represents the velocity distribution of the slowest model, it is compared to the fiducial model 50 % slower, whereas the blue line shows the model that is 50 % faster. The spectra of the models with the velocity profiles shown in Figure 5.21 for day 20 are shown for comparison in Figure 5.22.

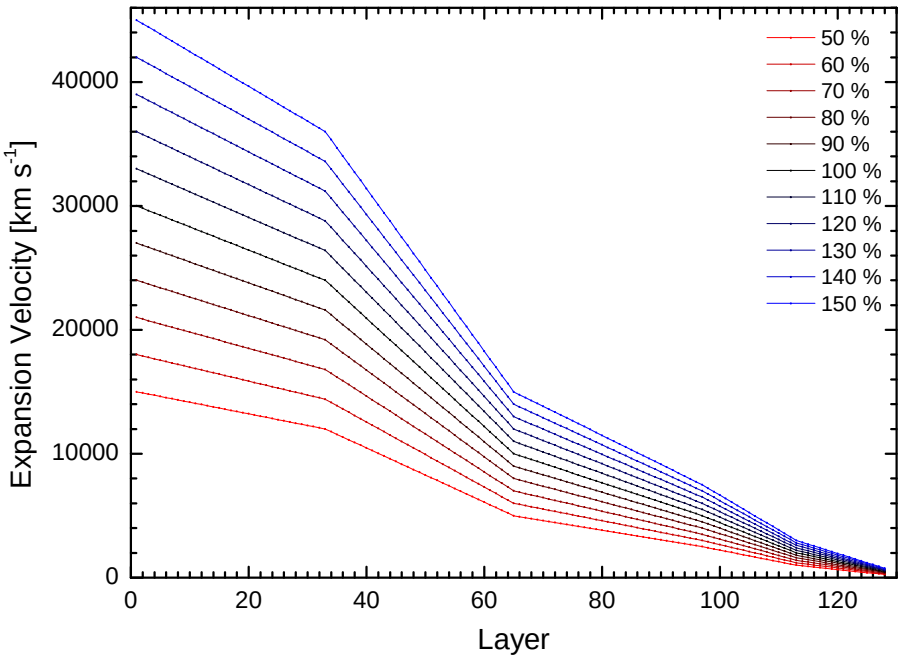

Figure 5.21: Discretized velocity model profiles as a function of the layers. The layers are shown from the outside inwards. The black line represents the fiducial model with $v_{exp} \simeq 30 \cdot 10^3\,\mathrm{km\,s^{-1}}$ in the outer layers. v_{exp} was changed in steps of 10 % from 50 % (red line) to 150 % (blue line). See text for details.

[5]These are the two supernovae SN 1984A and SN 1987D

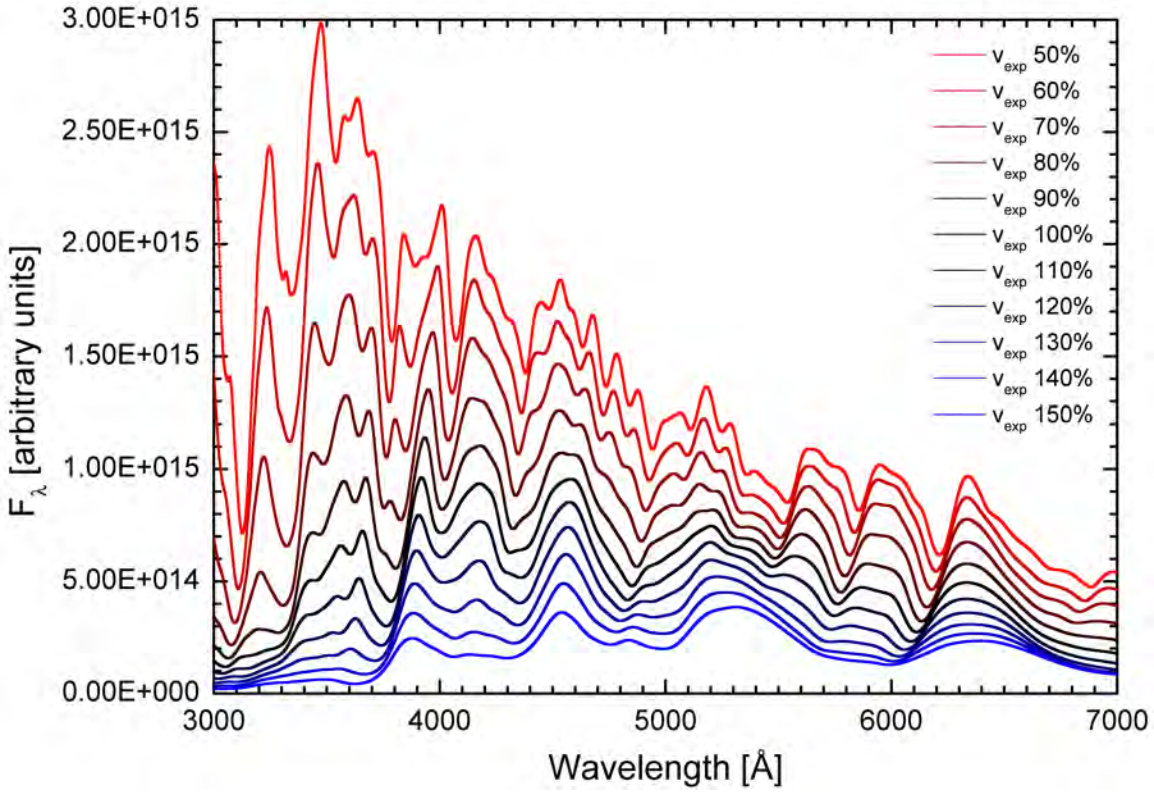

Figure 5.22: Synthetic spectra for day 20 after the explosion for varying expansion velocities. Plotted is the flux in arbitrary units as a function of the wavelength in the range $[3000, 7000]$ Å. The expansion velocity was changed in steps of 10 % from 50 % (red line) to 150 % (blue line). The legend labels the percentage expansion velocities of the models. See text for details.

Note that the slower the expansion velocity is, the more luminous and structured the spectra appear. The velocity field smears out the spectrum, which is seen particularly well, for example, in the lines near 6150 Å due to Si II and near 3750 Å due to Ca II. The spectra for day 20 show different layers, as we see in different optical depths. The changes of the velocity fields have a dramatic effect on the model. The model with the slowest expansion velocity ($v_{exp} \simeq 15 \cdot 10^3\,\mathrm{km\,s^{-1}}$) is overall brighter than the model with 150 % ^{56}Ni.
In summary, the spectra for days 5, 10, 14, 16, 18, 20, 22, 24, 26, 30, 40, and 50 in the wavelength range $[3000, 24740]$ Å of models for varying v_{exp} are shown in Figure 5.23. One can clearly see the spectral evolution over the entire filter. In the visual region it can be seen that the models with higher v_{exp} are less luminous. This is exactly what one expects, but it can be seen for days 20, 22, 24, 26 to 30 that the models with high expansion velocities are brighter in the infrared than those with lower expansion velocities.
Some of the features are more pronounced in the near infrared. Usually these effects are related to the temperature. However, we have no jumps or discontinuities in the temperature profile, which depends, in turn, to the optical depth. Thus, it may be that the radius is bigger and we look deeper into the atmosphere.

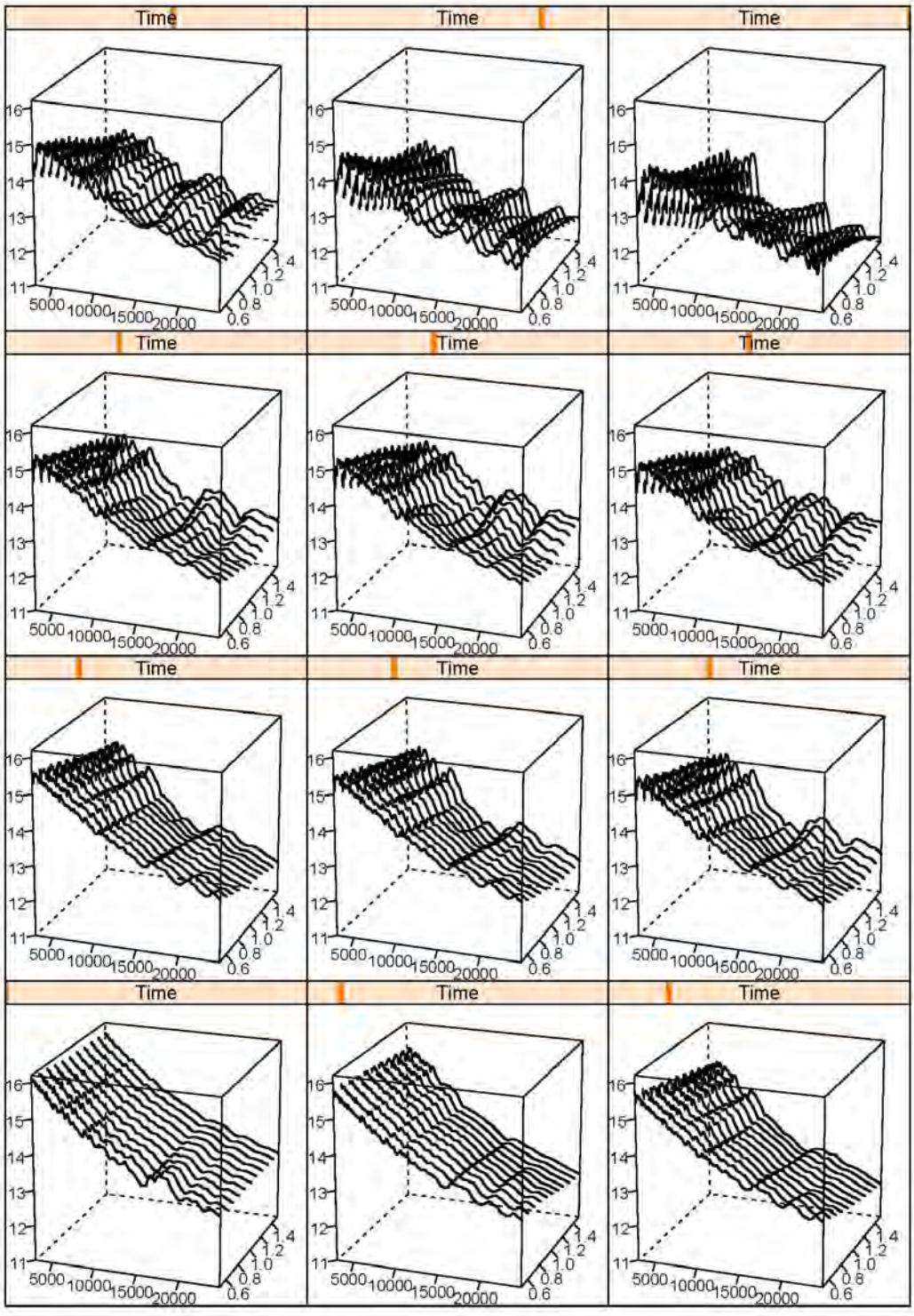

Figure 5.23: Starting in the lower left corner and ending in the upper right corner, synthetic spectra for days 5, 10, 14, 16, 18, 20, 22, 24, 26, 30, 40, and 50 of models for varying v_{exp} are shown. Plotted is the logarithmic flux as a function of wavelength in the range $[3000, 24740]$ Å. The depth axis shows the scaling factor of the velocity field. See text for details.

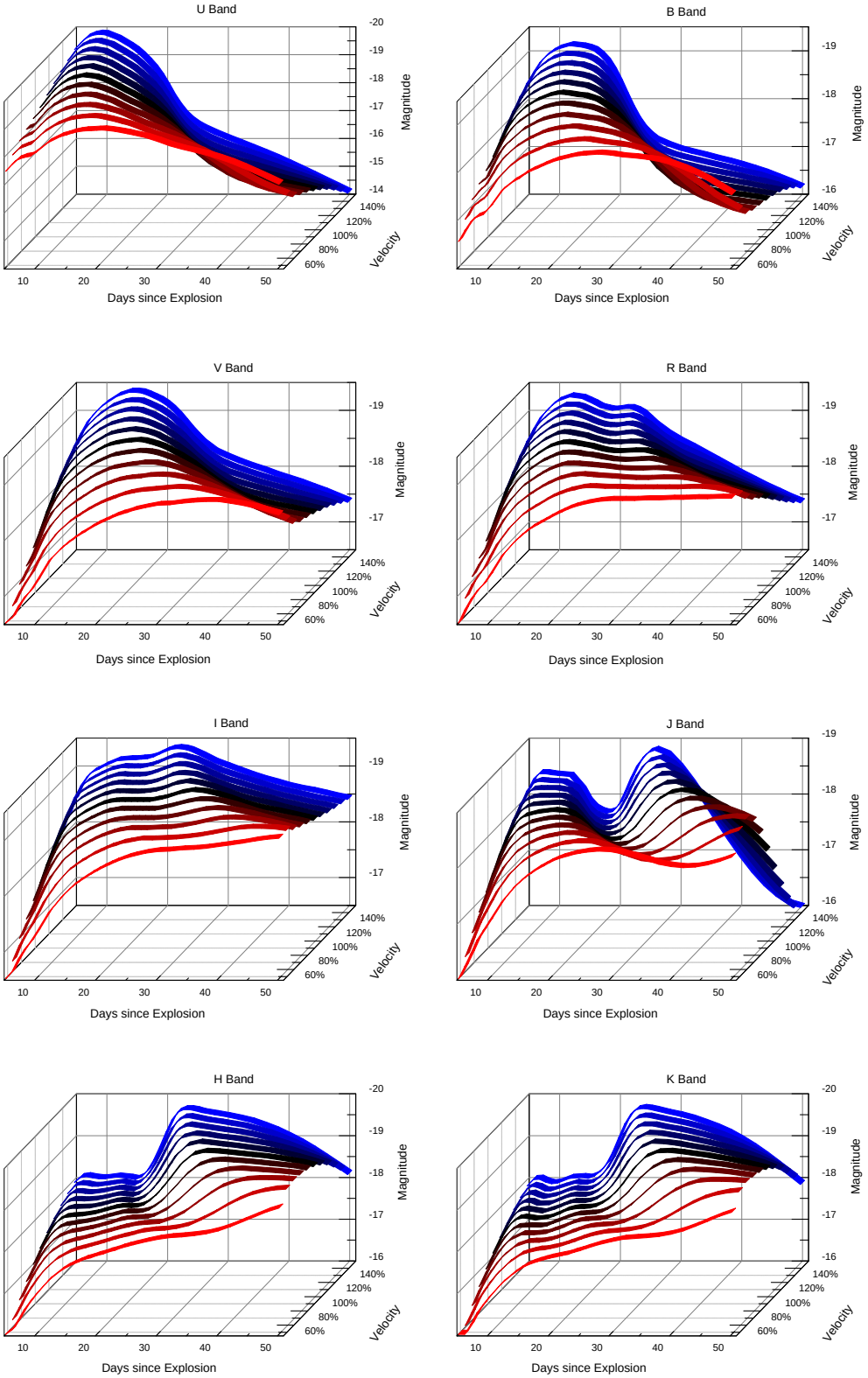

Figure 5.24: Spatial representation of model light curves in the bands U, B, V, R, I, J, H, and K as calculated from synthetic spectra for day 5 until 50 days after the explosion. v_{exp} was changed in steps of 10 % from 50 % (red curve) to 150 % (blue curve). See text for details.

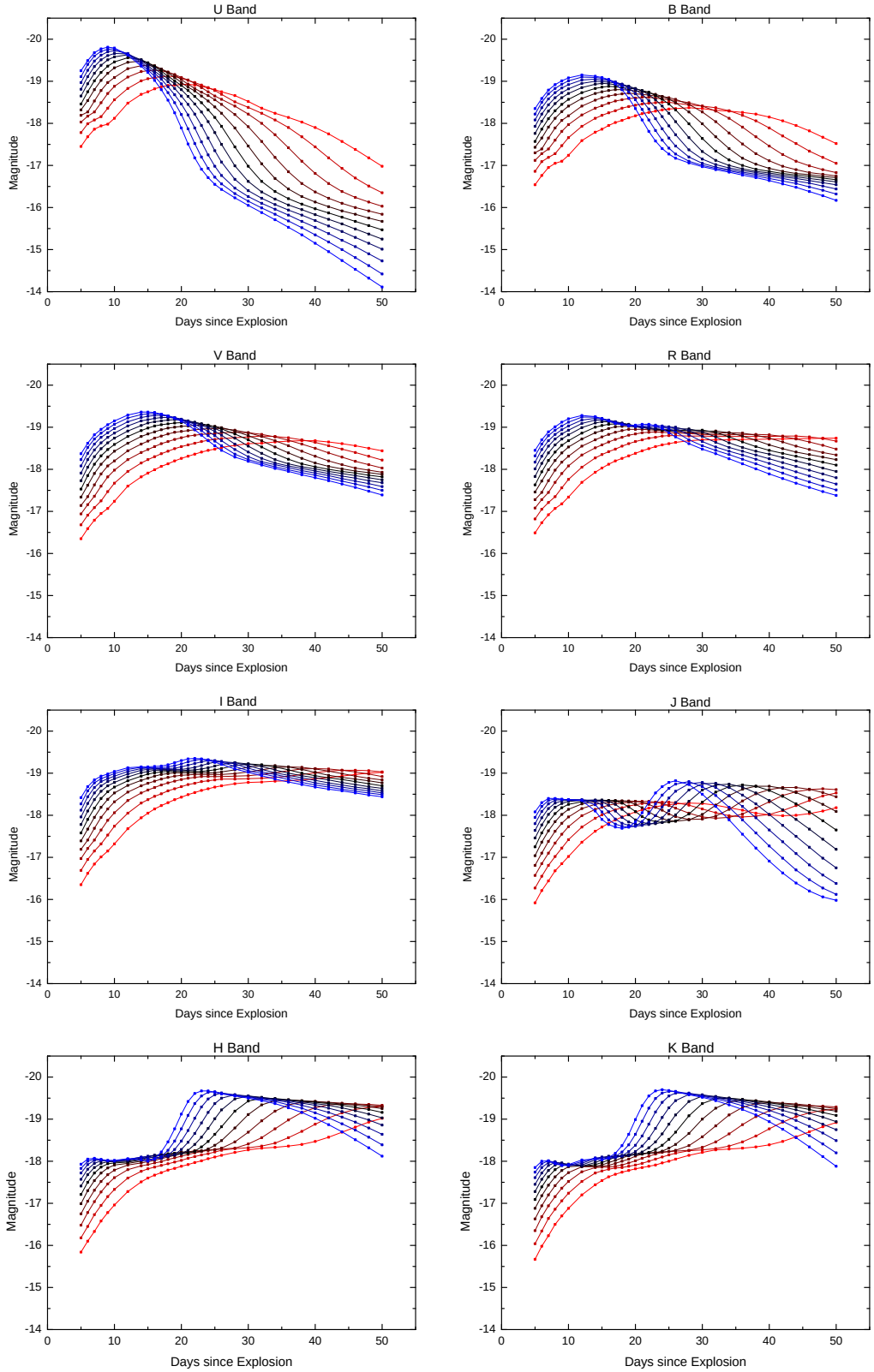

Figure 5.25: The same light curves as shown in Figure 5.24, but in a different presentation. Note that the scale of the ordinate is now the same for all bands. See text for details.

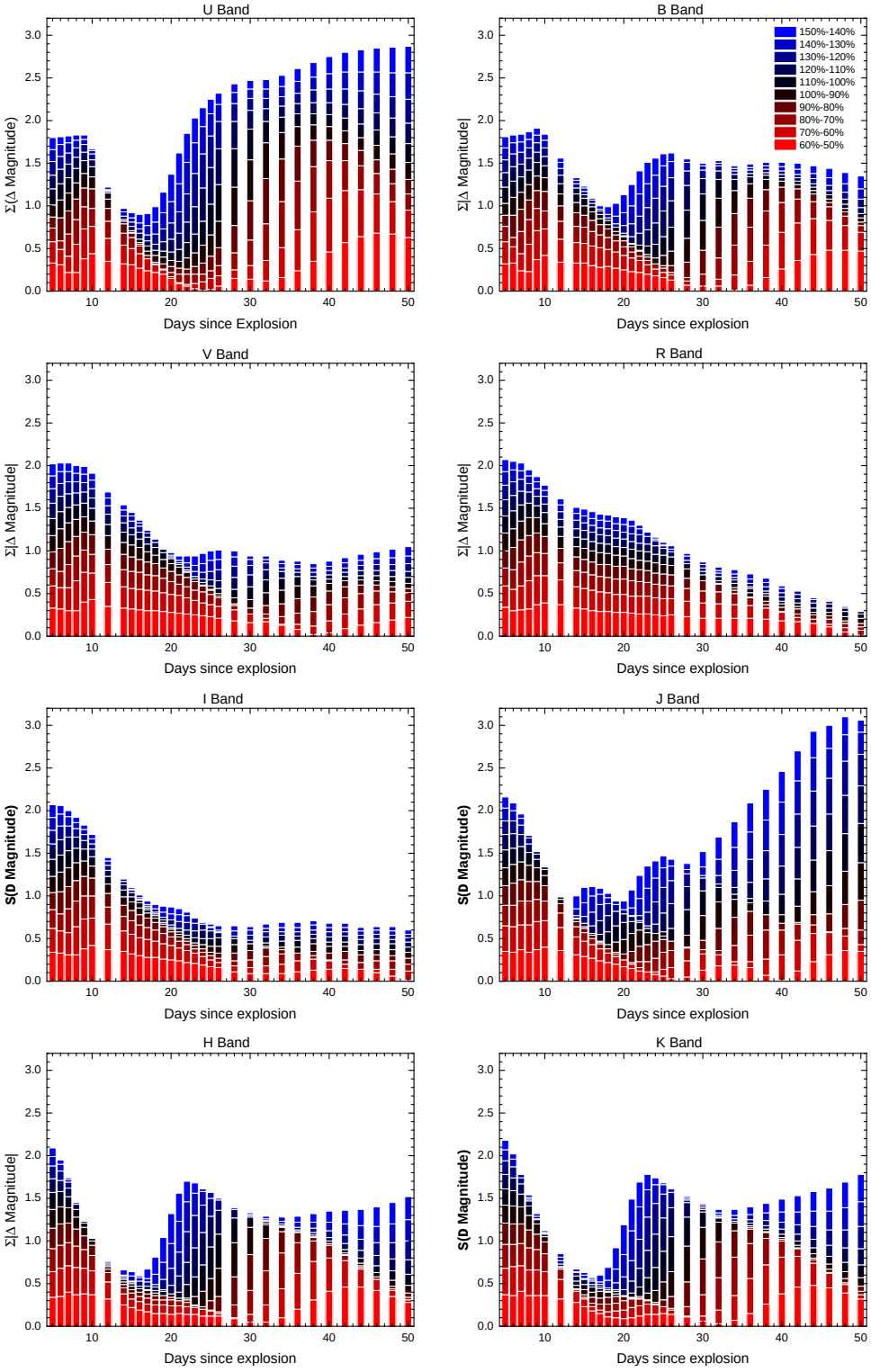

Figure 5.26: Summed absolute values of the differences between two adjacent models for previously discussed bands shown in Figures 5.24 and 5.25. The slower v_{exp} model is subtracted from the neighboring model with higher v_{exp}. The colors are inspired by the colors used so far and given in the legend. Note that the scale of the ordinate is the same for all bands. See text for details.

However, it must be considered that some effects, such as scattering and NLTE, become more important in the near infrared region and that the LTE approximation in these areas is invalid. From a mathematical point of view it must be said clearly, that under such conditions it is really hard to estimate parameters for an extended region of the spectrum without optimum experimental design. Different regions of the spectrum, such as in the ultraviolet, the visible, and the near infrared show very different behavioral characteristics.

In the next step, we have calculated, similar to before, from the 32 spectra sequence light curves for the Johnson bands U, B, V, R, I, J, H, and K. The light curves are shown in Figure 5.24 in a spatial representation. The same light curves are shown in Figure 5.25 in a different presentation. Note that the scale of the ordinate in Figure 5.25 is the same for all bands. The expansion velocity was changed in steps of 10 % from 50 % (red curve) to 150 % (blue curve). For the initial model an expansion velocity of $v_{exp} \simeq 30 \cdot 10^3 \,km\,s^{-1}$ was assumed in the outermost layer. As can be seen in Figures 5.24 and 5.25, the model response is dramatical with changing expansion velocity. In the bands U, B, and V, one can see an inverse Phillips relation. For high expansion velocities a maximum is formed, which again drops faster compared to the slower models. The drop is caused by the adiabatic cooling, which is very well seen in the models with high velocities. The brightness of the low velocity models rises and then declines very flat in these bands. In the R band, especially for the model with $v_{exp} \simeq 15 \cdot 10^3 \,km\,s^{-1}$ no decline is observed. In the near infrared bands I, H, and K, the brightness of this model increases only during the first 50 days. In the I band there is a slight decrease in brightness and then another rise to the second maximum. The formation of a secondary maximum in the R band is obvious for models with high expansion velocities. However, the models show in the bands I, J, H, and K again a second maximum, which is brighter than the primary maximum.

A second maximum, which is brighter than the first maximum was never observed. This can also be seen from the comparison with the template from Section 2.4, Figure 2.4. There, the two secondary maxima in the bands R and I are clearly visible, exactly as shown in Section 2.2, Figure 2.2 from the observation of SN 2011fe.

Table 5.2: Summarized results for the temperatures and the range of the optical depths for days 5, 20, and 50 for the fiducial model (100 % v_{exp}) shown in Figure 5.18 and for the two extreme models with 50 % v_{exp} and 150 % v_{exp} shown in Figure 5.27.

Model	**Day**	**T [K]**	**log (τ_{min})**	**log (τ_{max})**
v_{exp} 50 %	5	$\simeq 64150$	$\simeq -3.9$	$\simeq 3$
v_{exp} 100 %	5	$\simeq 41150$	$\simeq -4.5$	$\simeq 2.3$
v_{exp} 150 %	5	$\simeq 31200$	$\simeq -4.8$	$\simeq 1.9$
v_{exp} 50 %	20	$\simeq 24200$	$\simeq -5.1$	$\simeq 1.5$
v_{exp} 100 %	20	$\simeq 13700$	$\simeq -5.9$	$\simeq 0.8$
v_{exp} 150 %	20	$\simeq 10200$	$\simeq -6.4$	$\simeq 0.4$
v_{exp} 50 %	50	$\simeq 10250$	$\simeq -6.2$	$\simeq 0.5$
v_{exp} 100 %	50	$\simeq 5750$	$\simeq -7.9$	$\simeq -0,4$
v_{exp} 150 %	50	$\simeq 4800$	$\simeq -8.3$	$\simeq -0.7$

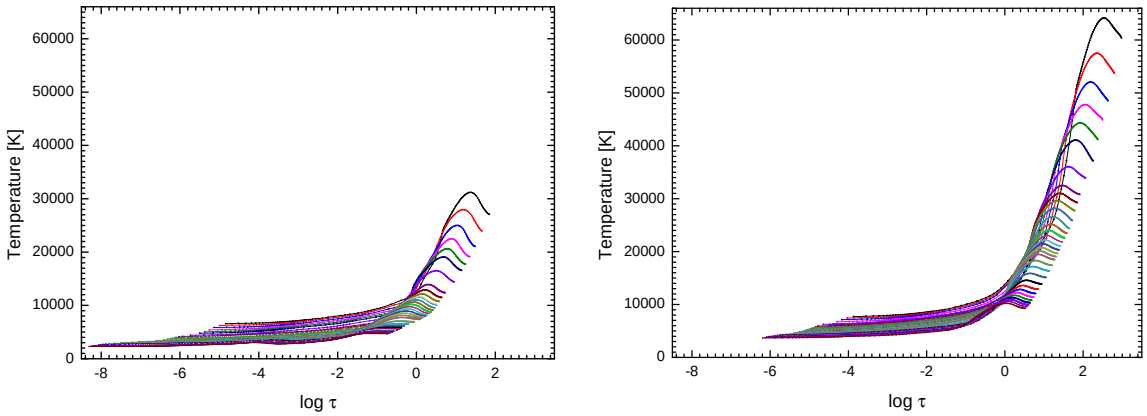

Figure 5.27: Temperature stratifications as a function of the optical depth for the 32 models, representing the time points from which the light curve was calculated for the models with 150 % v_{exp} (left side) and 50 % v_{exp} (right side). The starting models (day 5) have the highest temperature and optical depth of the sequence. We have $T \simeq 31200\,K$ and $\log\tau \simeq 1.9$ for the model with 150 % v_{exp} and $T \simeq 64150\,K$ and $\log\tau \simeq 3$ for the model with 50 % v_{exp}. With progress of time, the model atmospheres become cooler and more transparent. For day 50, we have $T \simeq 4800\,K$ and $\log\tau$ in the range $[-8.3,-0.7]$ for the model with 150 % ^{56}Ni and $T \simeq 10250\,K$ and $\log\tau$ in the range $[-6.2,0.5]$ for the model with 150 % v_{exp}. See text for details.

In our models with varied v_{exp}, a second secondary maximum is only in the R band. In the bands J, H, and K we find a second maximum, which is much too high.

The exact differences between the individual days of two adjacent models were computed. The results are shown for the considered bands in Figure 5.26. In direct comparison with the results of the ^{56}Ni models, shown in Section 5.1, Figure 5.14, the differences are considerably larger. In the early days there are in all bands an almost equidistant spreading. Probably, these models can be used to make specific statements. Models with reduced expansion velocities show the maximum brightness later as models with higher expansion velocities. The latter models adiabatically cool faster. There is an inversion in the brightness of the models. This in turn destorts the statistics, as already discussed in the case of the ^{56}Ni models (cf. Section 5.1).

From the temperature stratification of the models we see that there is a larger temperature range compared to the models of Section 5.1, Figure 5.19 and Table 5.1. For example, for day 5 there is a difference of $\Delta T \approx 33 \cdot 10^3\,K$ in the outer layers of the two extreme models with 50 % v_{exp} and 150 % v_{exp}.

The temperature stratifications of these two models are shown as a function of the optical depth in Figure 5.27. For day 5, we have $T \simeq 31200\,K$ and $\log\tau \simeq 1.9$ for the model with 150 % v_{exp} and $T \simeq 64150\,K$ and $\log\tau \simeq 3$ for the model with 50 % v_{exp}. With progress of time, the model atmospheres expand at different rates, adiabatic cooling, and total optical depths. For day 50, we have $T \simeq 4800\,K$ and $\log\tau$ in the range $[-8.3,-0.7]$ for the model with 150 % v_{exp} and $T \simeq 10250\,K$ and $\log\tau$ in the range $[-6.2,0.5]$ for the model with

50 % v_{exp}.
A summary of the temperatures and the optical depths for days 5, 20, and 50 for the fiducial model (100 % v_{exp}) and for the two extreme models with 50 % v_{exp} and 150 % v_{exp} is given in Table 5.2.
Overall, the comparison is very difficult for these models. With the significantly different expansion velocities we look at different depths in the atmosphere at layers with different temperatures and burnt and unburnt material. As an example, if we compare the spectra for day 20 after the explosion (Figure 5.22), then the spectra are either well before or well after the maximum. Nevertheless, the expansion velocity is an important parameter that is from a theoretical view confined to narrow confidence regions.

5.3 Simultaneous variation of the expansion velocity and the abundance of ^{56}Ni

On the one hand additionally deposited energy, such as by increasing the amount of ^{56}Ni, heating the atmosphere, on the other hand an increased expansion velocity adiabatically cools the atmosphere faster, or vice versa. Therefore, it is important to change these two parameters simultaneously and to analyze the correlations. The questions that arise are if the effects cancel each other or reinforce each other, and if the effects are continuous and linear. However, the computational effort is enormous. If we use, for example, five discrete values of a parameter, such as v_{exp} the values then for 32 time points per light curve 160 model atmospheres have to be calculated.

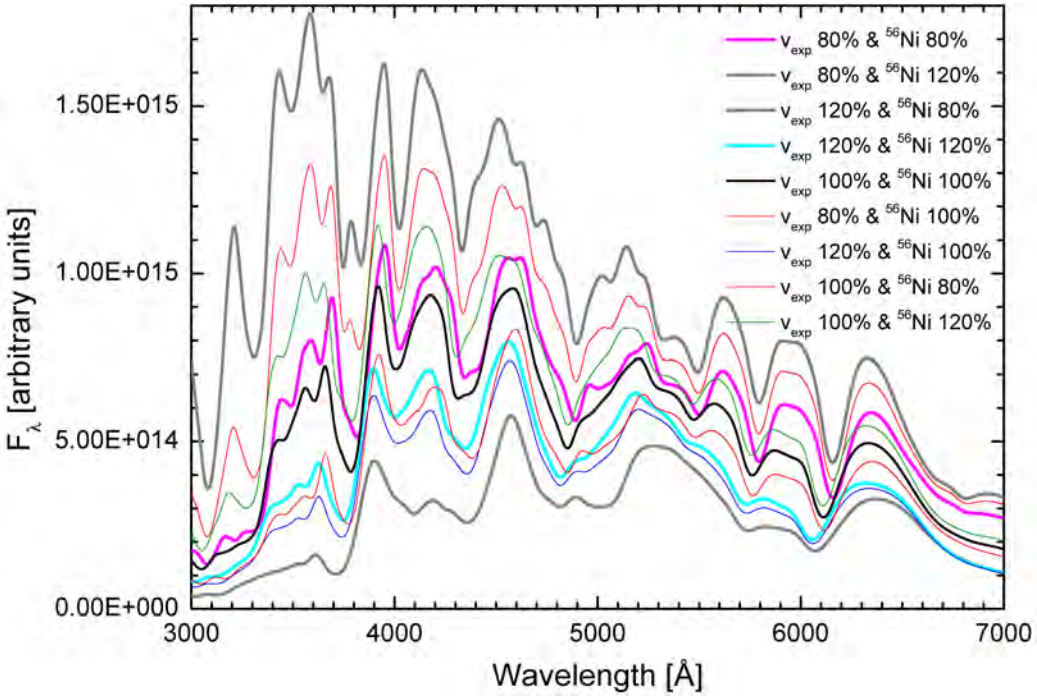

Figure 5.28: Synthetic spectra around the maximum brightness (for day 20 after the explosion) for varying simultaneously ^{56}Ni and v_{exp}. Plotted is the flux in arbitrary units as a function of the wavelength in the range $[3000, 7000]$ Å. The two models with 80 % v_{exp} & 120 % ^{56}Ni and 120 % v_{exp} & 80 % ^{56}Ni are extreme models and represented by the two thick gray lines. The thick magenta line shows the spectrum of the model with 80 % v_{exp} & 80 % ^{56}Ni, it is more luminous than that of the fiducial model (thick black line). The spectrum of the model, with 120 % v_{exp} & 120 % ^{56}Ni (thick cyan line) is then compared to less luminous. In addition, the models with 80 % v_{exp} & 100 % ^{56}Ni (upper thin red line), 120 % v_{exp} & 100 % ^{56}Ni (thin blue line), 100 % v_{exp} & 80 % ^{56}Ni (lower thin red line), and 100 % v_{exp} & 120 % ^{56}Ni (thin green line) are shown. The legend labels the amount of ^{56}Ni and the v_{exp} of each model. See text for details.

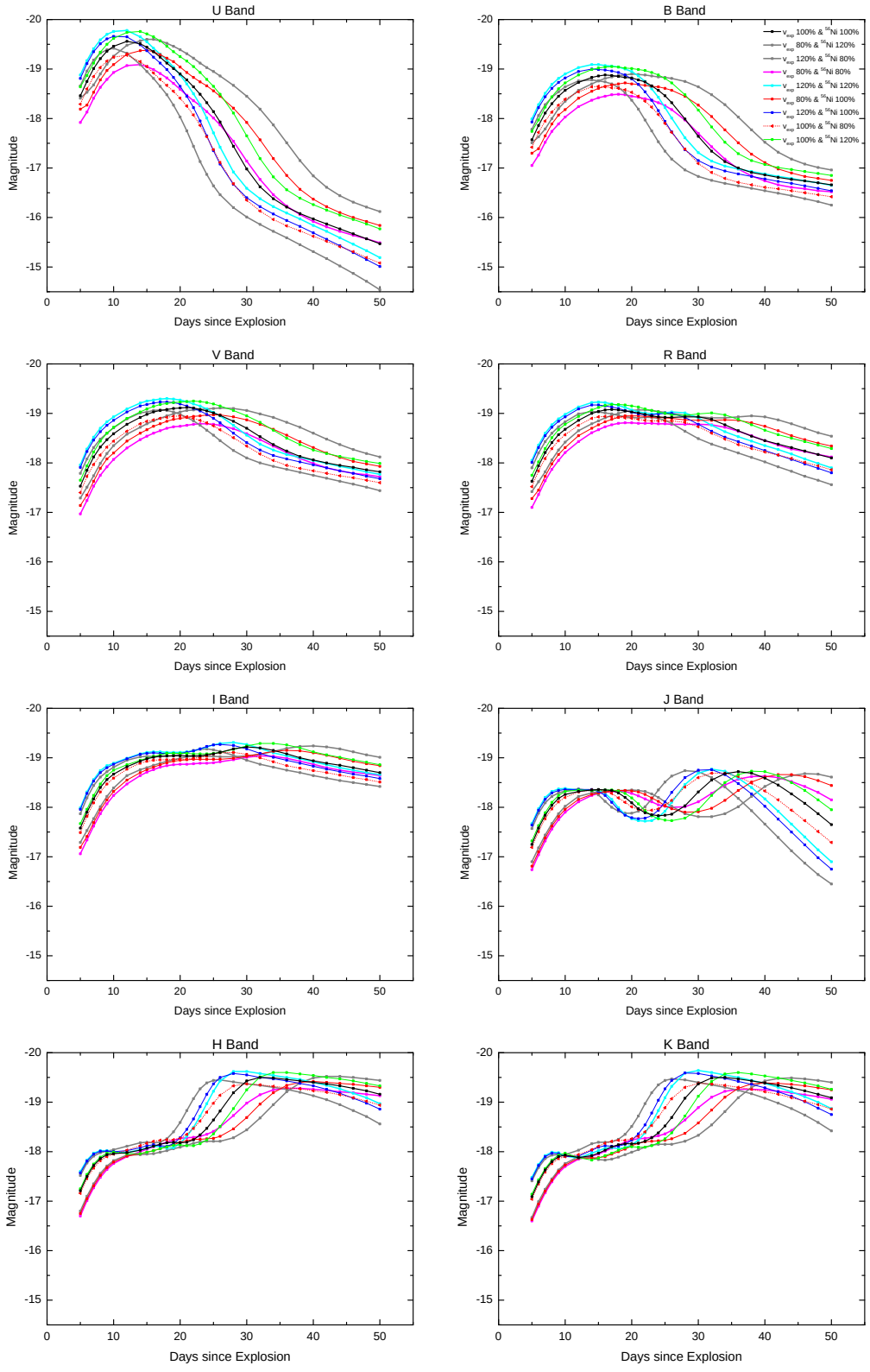

Figure 5.29: Model light curves in the bands U, B, V, R, I, J, H, and K as calculated from synthetic spectra for day 5 until 50 days after the explosion. The legend labels the percentage v_{exp} and ^{56}Ni abundance of the models. The colors of the models correspond to those in Figure 5.28. See text for details.

This means that the problem scale has to be considered as a classical forward problem, with $n \cdot m^X$, where n is the number of time points per light curve, m is the number of discrete values of the parameter space, and X is the number of parameters to be varied. For this purpose $n = 32$, $m = 5$, and $X = 2$ were used and the corresponding model atmospheres computed. The spectra are shown in Figure 5.28, however, the spectra with selected intermediate values (90 % v_{exp} & 90 % ^{56}Ni, 90 % v_{exp} & 110 % ^{56}Ni, 110 % v_{exp} & 90 % ^{56}Ni, and 110 % v_{exp} & 110 % ^{56}Ni) have been omitted for clarity. As expected and obvious in Figure 5.28, the effects are mutually reinforcing. The two models with 80 % v_{exp} & 120 % ^{56}Ni and 120 % v_{exp} & 80 % ^{56}Ni (thick gray lines) are extreme models. The spectrum of the model with 120 % v_{exp} & 80 % ^{56}Ni (thick magenta line) is more luminous than that of the fiducial model (thick black line). The lower v_{exp} compensates the effects of reduced ^{56}Ni content. The other case is similar. The spectrum of the model with 80 % v_{exp} & 120 % ^{56}Ni (thick cyan line) is less luminous than that of the fiducial model. The increased v_{exp} compensates the effect caused by the enhancement of ^{56}Ni. Essentially, these are precisely the effects that were expected. For the same percentage change of v_{exp} and ^{56}Ni one can see that the temperature changes were greater for the former. In addition, in Figure 5.28 models are shown with 80 % v_{exp} & 100 % ^{56}Ni (upper thin red line), 120 % v_{exp} & 100 % ^{56}Ni (thin blue line), 100 % v_{exp} & 80 % ^{56}Ni (lower thin red line), and 100 % v_{exp} & 120 % ^{56}Ni (thin green line). These models were already discussed in the previous two subsections. It can clearly be seen how difficult it is to predict these kinds of effects. There is a vector of parameters and two are varied simultaneously. Especially in the case of destructive interference, it is difficult to make reliable predictions.

Furthermore, we look through the different v_{exp} at different points in time (based on the maximum) at different depths in the atmosphere at layers with different temperatures and burnt and unburnt material.

The corresponding light curves in the Johnson bands U, B, V, R, I, J, H, and K are shown in Figure 5.29. Note that the scale of the ordinate is the same everywhere. While one can understand the model response relatively well in the spectra, the behavior of the light curves is more difficult to interpret. It is not immediately obvious why, for example, the models 80 % v_{exp} & 80 % ^{56}Ni and 120 % v_{exp} & 120 % ^{56}Ni are in the early days in the ultra violet and the blue part of the visual spectrum border models. These examples here show how difficult the individual fitting of the models to observed data is.

5.4 Partial replacement of stable iron by ^{56}Ni in the core

Finally, in the core stable iron (Fe) was partially replaced by ^{56}Ni. Thereby, the diffusion time of the energy is changed. This is done in two ways. First, Fe which is at locations slower than $4440\,\mathrm{km\,s^{-1}}$ will be successively replaced. This is done in steps of 20 %. Mass fractions of the two elements as a function of velocity are shown in Figure 5.30. The initial abundances are represented by the two thick lines. The dashed line shows Fe. The initial content of ^{56}Ni in this area is $\simeq 10.55 \cdot 10^{-2}\,\mathrm{m_{^{56}Ni}/m_\odot}$ corresponding to $\simeq 18.6\,\%$ of the total amount of ^{56}Ni. The green line shows a model in which Fe has been completely superseded by ^{56}Ni. Overall, these are around $\simeq 7.25 \cdot 10^{-2}\,\mathrm{m_{Fe}/m_\odot}$ corresponding to $\simeq 78.9\,\%$ of the total amount of Fe. This means the total of ^{56}Ni is increased by $\simeq 12.8\,\%$.
Second, 50 % of Fe is replaced by ^{56}Ni, depending on the velocity. The replacement, starts very close to the core (at locations $\lesssim 900\ \mathrm{km\,s^{-1}}$) and is ultimately done in seven discrete velocity increments from $\lesssim 900\ \mathrm{km\,s^{-1}}$, $\lesssim 1300\ \mathrm{km\,s^{-1}}$, $\lesssim 1700\ \mathrm{km\,s^{-1}}$, $\lesssim 2190\ \mathrm{km\,s^{-1}}$, $\lesssim 2940\ \mathrm{km\,s^{-1}}$, $\lesssim 3690\ \mathrm{km\,s^{-1}}$, up to $\lesssim 4440\ \mathrm{km\,s^{-1}}$. In each case starting from the inner core 50 % of Fe is piecewise replaced by ^{56}Ni at these points. The proportion of Fe to be replaced, and the new content of ^{56}Ni is shown in Figure 5.31. The proportions were normalized to the mass of the sun. In addition, the initial proportions of Fe and ^{56}Ni are shown. The new proportions of ^{56}Ni in $\mathrm{m_{^{56}Ni}/m_\odot}$ are (from inside to outside, matching the velocity increments) $2.19 \cdot 10^{-3}$, $5.58 \cdot 10^{-3}$, $10.44 \cdot 10^{-3}$, $17.71 \cdot 10^{-3}$, $39.56 \cdot 10^{-3}$, $82.45 \cdot 10^{-3}$, and $14.17 \cdot 10^{-2}$. The course of the substitution is shown in Figure 5.32. The initial abundances are represented by the two thick lines. The dashed line shows Fe.

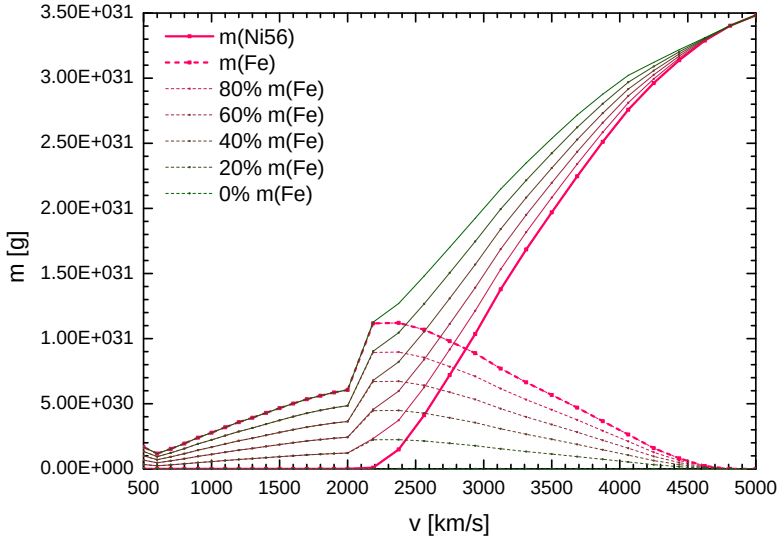

Figure 5.30: Mass fractions of Fe and ^{56}Ni as a function of velocity at locations up to $4440\,\mathrm{km\,s^{-1}}$. The initial abundances are represented by the two thick lines. The dashed line shows Fe. The amount of Fe was partially replaced by ^{56}Ni in steps of 20 %. The green line shows a model in which Fe has been completely superseded by ^{56}Ni. See text for details.

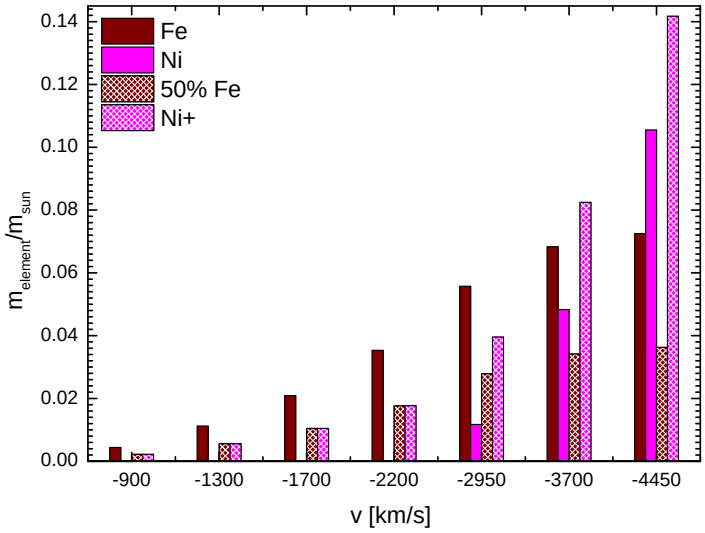

Figure 5.31: Normalized (to the mass of the sun) mass fractions of Fe and ^{56}Ni as a function of velocity. The initial abundances are represented by the two bars of the left side. The russet bar shows Fe, the magenta one ^{56}Ni. The same color checkered bars on the right side show the new mass fractions. Fe was reduced by 50 %, while ^{56}Ni increased by this amount. See text for details.

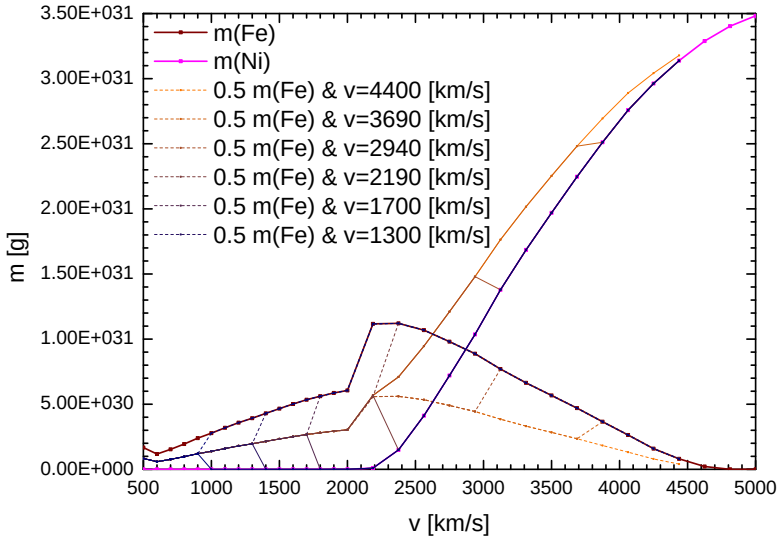

Figure 5.32: Course of the velocity dependent substitution of Fe by ^{56}Ni. The initial mass fraction are represented by the two thick lines. The full magenta line shows ^{56}Ni, the dashed russet line shows Fe. The thin line above the initial ^{56}Ni line indicates the new content of ^{56}Ni. The thin line below the initial Fe line shows the reduced Fe content. The lines connecting the initial lines with the new abundances, indicate the respective reference points. See text for details.

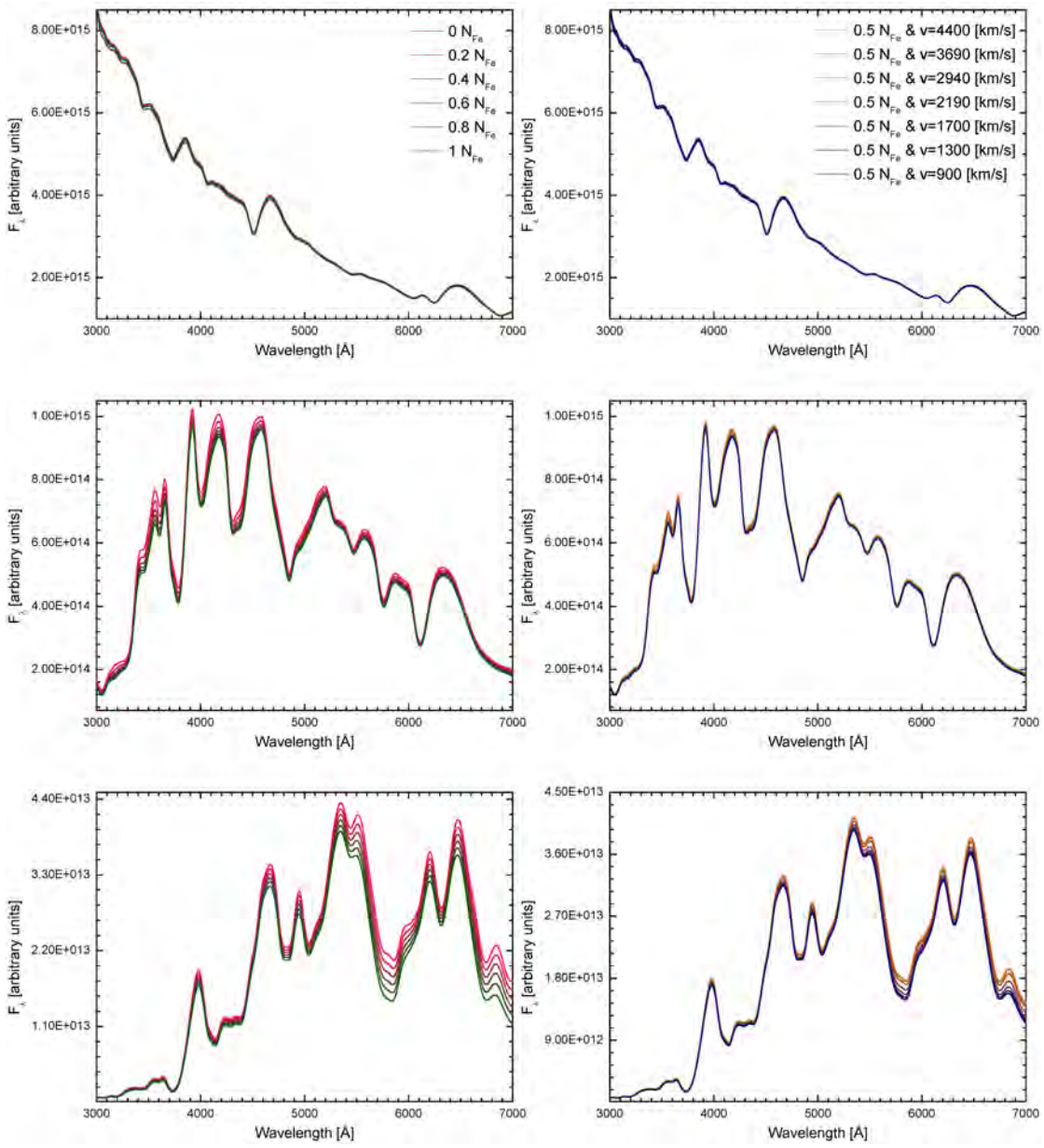

Figure 5.33: Synthetic spectra for days 5, 20, and 50 after the explosion (from top to bottom). On the left side spectra are shown in which Fe is partially replaced by ^{56}Ni in the core in steps of 20 % (models in Figure 5.30). The red line shows models, the Fe was completely replaced at locations up to a speed of $\lesssim 4440\,\mathrm{km\,s^{-1}}$. On the right side spectra are shown in which 50 % Fe is replaced in dependence of the velocity (models in Figure 5.32). The dark blue lines show the spectra of the models Fe was replaced up to $\lesssim 900\,\mathrm{km\,s^{-1}}$. The lighter lines show models in which the replacement took place gradually at locations up to $\lesssim 4440\,\mathrm{km\,s^{-1}}$. The proportion of substitution and the discretized velocities of these models are shown in Figure 5.31. See text for details.

The colors of the two elements are the same as in Figure 5.1. Fe is shown russet, ^{56}Ni in magenta. The thin line above the initial ^{56}Ni line indicates the new content of ^{56}Ni. The thin line below the initial Fe line shows the reduced Fe content. The lines connecting the initial lines with the new abundances, indicate the respective reference points. The spectra for days 5, 20, and 50 are shown in Figure 5.33 for both cases. The wavelength range is limited to the visible region. The colors are correlated with the corresponding models shown in Figures 5.30 and 5.32. On the left side spectra of the models shown in Figure 5.30 can be seen, on the right side those of Figures 5.32. On the left side, the red line shows the spectra of the model, whose Fe is completely replaced by ^{56}Ni in the core. On the right side, the blue line shows the spectra of the model where the Fe was replaced in the innermost core by 50 % ^{56}Ni. For day 5 the spectra do not differ. The individual models produce no difference. The spectra for days 20 and 50 show differences. In the spectra, in which the amount of Fe was replaced by ^{56}Ni at locations up to $\lesssim 4440$ km s^{-1} the changes in the spectra are more noticeable. However, they are weak. The spectra with more ^{56}Ni are brighter. This is best seen on day 50, these spectra are less luminous than the spectra for days 5 and 20. The difference from the additional ^{56}Ni discussed in Section 5.1 is that here, however, only Fe at locations up to a speed of $\lesssim 4440$ km s^{-1} has been completely replaced by ^{56}Ni. Overall, the amount of additional ^{56}Ni in the core is 12.77 %.

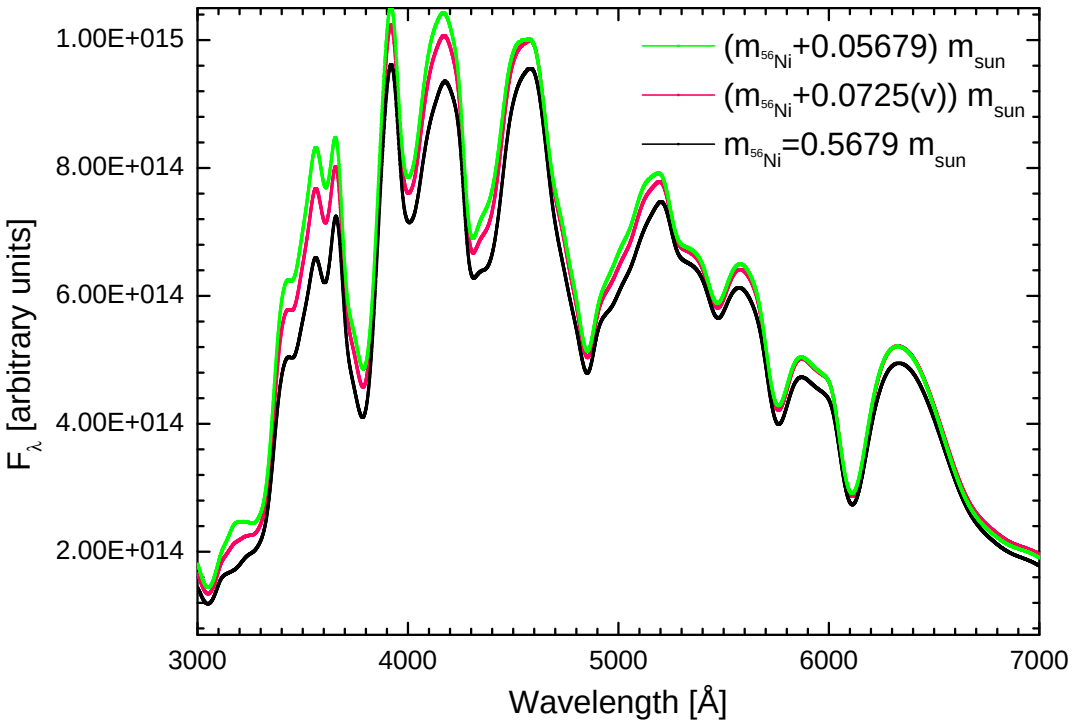

Figure 5.34: Synthetic spectra for day 20 after the explosion. The black line shows the fiducial model. The green line shows a model of the ^{56}Ni content was increased by 10 %. The red line shows a model, the Fe was completely replaced by ^{56}Ni at locations up to a speed of $\lesssim 4440$ km s^{-1}. See text for details.

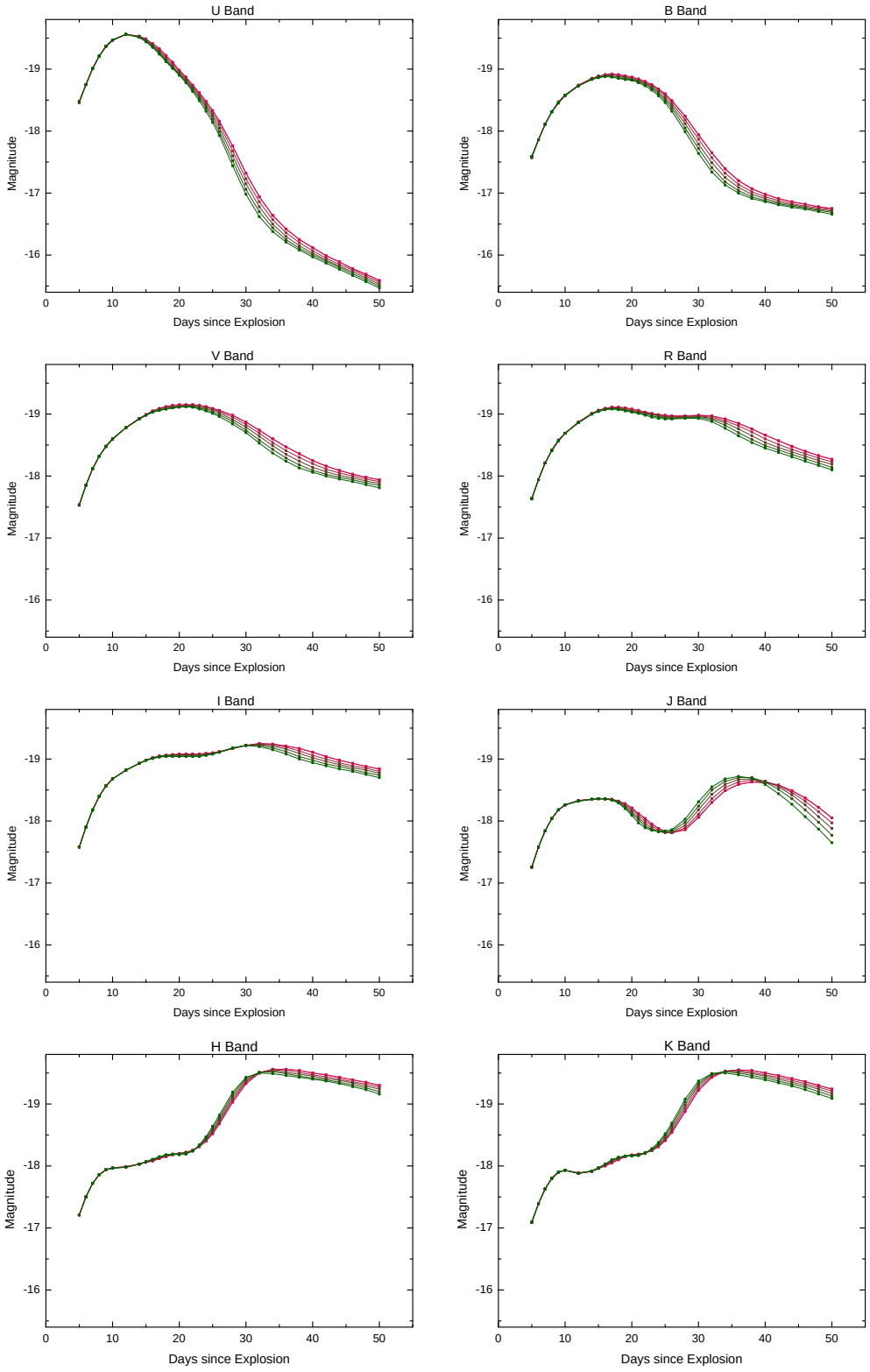

Figure 5.35: Model light curves in the bands U, B, V, R, I, J, H, and K. The colors of the models correspond to those in Figure 5.33. Fe was partially replaced by ^{56}Ni in steps of 20 % at locations up to $\lesssim 4440\ \mathrm{km\,s^{-1}}$. The green line shows a model in which Fe has been completely superseded by ^{56}Ni. See text for details.

In Figure 5.34, the spectra for day 20 are shown for the fiducial model, the model with 10 % additional ^{56}Ni (Figure 5.4), and the model with 12.77 % additional ^{56}Ni in the core (Figure 5.33). In Figure 5.34, it can be seen that not only the additional amount of added ^{56}Ni is important, but also that the place where it is added is important. Therefore, the higher energy model (with 2.77 % more ^{56}Ni) is now less luminous since the diffusion time of the energy was increased. Therefore, it is also crucial where the additional ^{56}Ni is added.
In Figure 5.35, the corresponding light curves in the Johnson bands U, B, V, R, I, J, H, and K are shown for the models, in which Fe was replaced by ^{56}Ni at locations up to $\lesssim 4440\,\mathrm{km\,s^{-1}}$. Note that the scale of the ordinate is the same everywhere. The behavior of the light curves is similar to the light curves discussed in Section 5.1 (cf. Figure 5.10). In both cases, additional energy was added (by adding ^{56}Ni). The difference is that here the diffusion time of the energy has been increased. Furthermore, much less ^{56}Ni was added. No differences can be observed in all bands until day 15. As the column density of the early days is high, the energy changes are not sufficient to induce changes in the light curves. In the I band the light curves are very close together for days 26, 28, and 30. In the bands J, H, and K we observe an inversion. Models with more energy are less luminous on certain days than models with less ^{56}Ni. For example, in J the days $25-40$, in H the days $23-32$, and in K the days $24-36$ are less luminous. For days earlier differences are very small in the H and K bands. Overall, the behavior of the bands is analogous to the bands of the models with parametrized ^{56}Ni (Section 5.1). It is noteworthy that even this small amount of additional ^{56}Ni in the core induces changes in the light curves.

5.5 Varying the value of the parametrized line scattering parameter

The next parameter considered is the fraction of parametrized line scattering parameter, $\varepsilon_{\text{line}}$. As mentioned in Section 3, $\varepsilon_{\text{line}}$ is normally computed and not used as a parameter. For test and special cases it can be used as a parameter. However, Jack et al. (2011, 2012) found that a change in the ratio of line scattering to absorption in the LTE case improves the fits to the I band light curve. To produce a good match they "hand tuned" line scattering. Scattering results occur in both physical and mathematical effects. Physically, these effects are obvious. Mathematically, scattering causes the radiative transfer equation to become an integro-differential equation. The radiation transport problem itself is non-local due to photon scattering, which is very important in the low density environment of Type Ia supernovae, both in spectral lines and via scattering of free electrons in the Thompson limit. In this work, the scattering fraction is parametrized by the line scattering parameter $\varepsilon_{\text{line}}$, via the source function $S = (1-\varepsilon_{\text{line}})J + \varepsilon_{\text{line}}B$. $\varepsilon_{\text{line}}$ is in a range between $]0,1]$, which means that close to $\varepsilon_{\text{line}} = 0$ almost 100 % of interacting photons are scattered via line scattering and $\varepsilon_{\text{line}} = 1$, which means that all photons are absorbed, neither which of course matches physical reality.

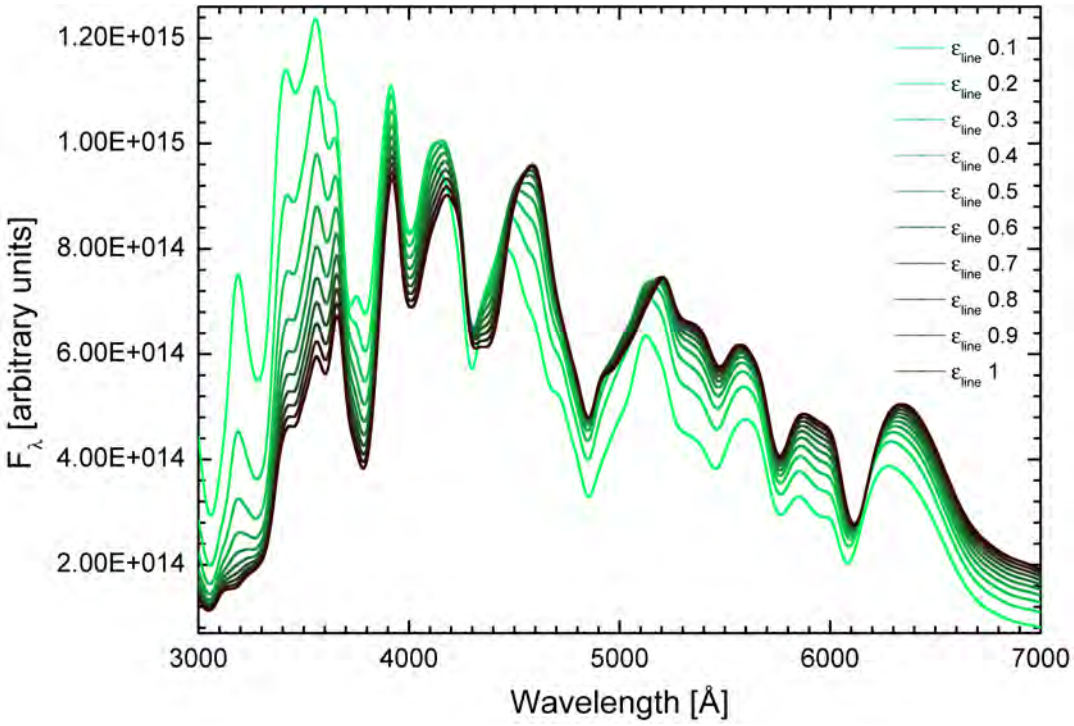

Figure 5.36: Synthetic spectra around the maximum brightness (for day 20 after the explosion) for varying $\varepsilon_{\text{line}}$. Plotted is the flux in arbitrary units as a function of the wavelength in the range $[3000, 7000]$ Å. $\varepsilon_{\text{line}}$ was changed in steps of 0.1 from 0.1 (green line) to 1 (black line). The legend labels the $\varepsilon_{\text{line}}$ of each model. Note, the behavior of the spectra in the ultraviolet and blue visible region. See text for details.

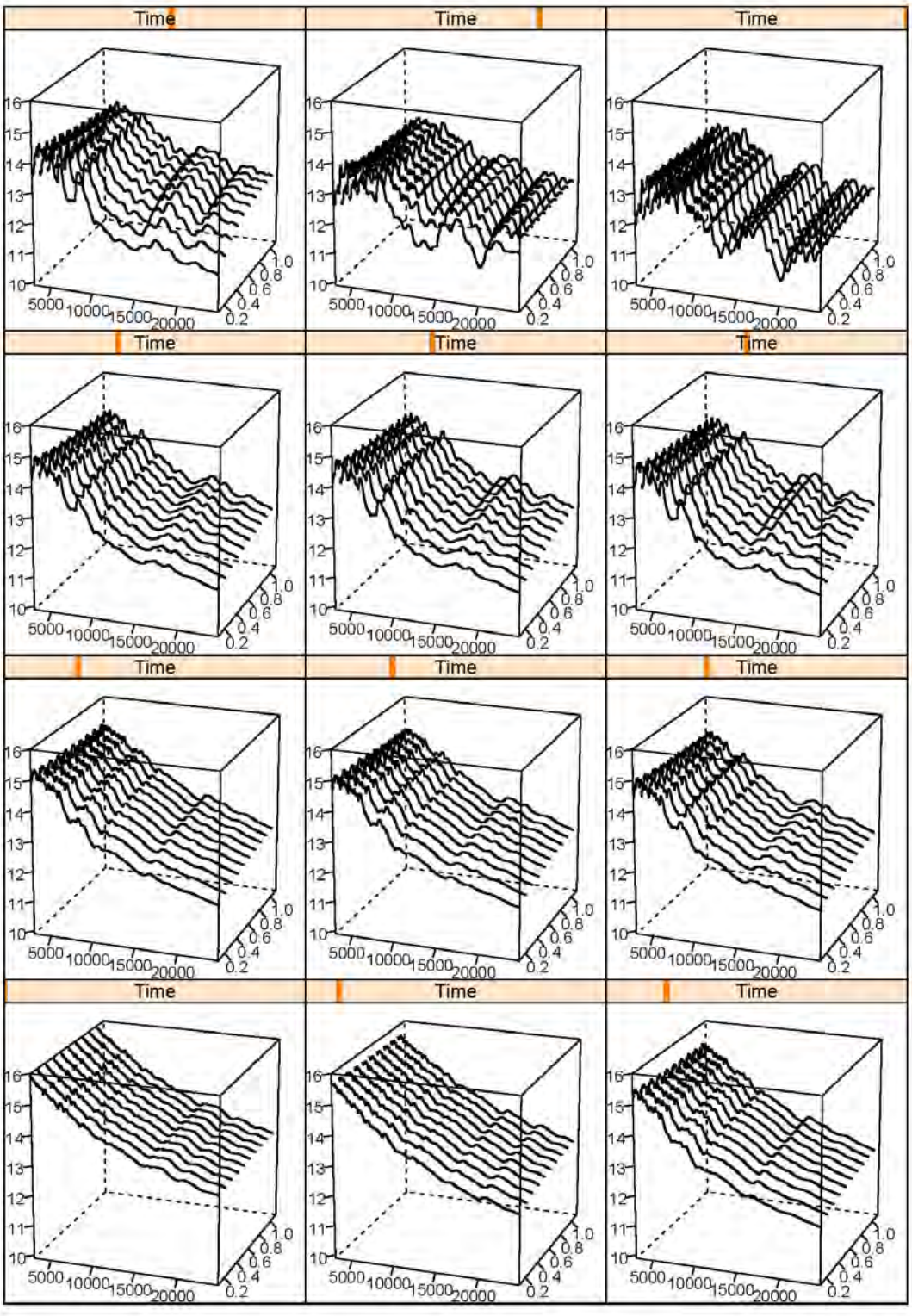

Figure 5.37: Starting in the lower left corner and ending in the upper right corner, synthetic spectra for days 5, 10, 14, 16, 18, 20, 22, 24, 26, 30, 40, and 50 of models for varying v_{exp} are shown. Plotted is the logarithmic flux as a function of wavelength in the range $[3000, 24740]$ Å. The depth axis shows the scaling factor of the velocity field. See text for details.

However, $\varepsilon_{\text{line}}$ is varied between 0.1 (90 % of photons are scattered), and 1 (100 % of photons are absorbed) in steps of 0.1. The visible region in the range $[3000, 7000]$ Å of the corresponding spectra for day 20 is shown in Figure 5.36. The colors are correlated with the corresponding $\varepsilon_{\text{line}}$.
The green line shows models with $\varepsilon_{\text{line}} = 0.1$, while black show models without line scattering ($\varepsilon_{\text{line}} = 1$). In the spectra, the absorption troughs of the individual features and the impact of scattering can be seen.
While scattering attenuates the brightness of the spectra in the red of the visible region, the brightness rises in the ultraviolet and blue visible region. The attenuation can be observed in the conspicuous absorption features near 6150 Å due to Si II and near 4900 Å due to Si II and S II, while a rise can be seen in the region of the Fraunhofer Ca H and K lines (near 3750 Å). It is now of course the question, where this originates, because something like this is not expected in the visible region. However, it is just a change in the photosphere with wavelength. In LTE the ultraviolet photosphere is deeper and the infrared photosphere is further out. The wavelength dependence of the photosphere is small. But with high line scattering the pseudo ultraviolet photosphere essentially moves out to the surface and we get high luminosity there, whereas the pseudo infrared photosphere moves in, so we get low luminosity there. In addition, there is energy conservation since the total bolometric flux is constant. But this is just due to the fact that in the ultraviolet region is intense line blanketing and so the scattering ultraviolet the pseudo photosphere moves nearly to the surface and there are much more separated lines in the infrared so the pseudo photosphere moves in.
In summary, the spectra for days 5, 10, 14, 16, 18, 20, 22, 24, 26, 30, 40, and 50 in the wavelength range $[3000, 24740]$ Å of models for varying $\varepsilon_{\text{line}}$ are shown in Figure 5.37. One can clearly see over the entire filter range the spectral evolution and the previously described effects of the pseudo photosphere moving to different depths. The scattering effects are known to be most obvious in the infrared. This can be also seen very well in the spectra, scattering "scatters away" entire absorption lines, or weakens these (absorption) features dramatically. For day 50, the differences in the spectra are no longer large. In the infrared they always recovers to very high values. However, it must be said that the atmosphere of the supernova is now far extended and completely transparent at this time (cf. Figure 5.41 for the optical depths).
In the next step model light curves were calculated from the spectra, in the Johnson bands U, B, V, R, I, J, H, and K. The light curves are shown in Figure 5.38 in a spatial representation. The same light curves are shown in Figure 5.39 in a different presentation. Note that the scale of the ordinate in Figure 5.39 is the same for all bands and for comparisons also the same as in Figures 5.10 (for ^{56}Ni) and 5.25 (for v_{exp}). Clearly the effects of line scattering on the light curves can be seen, in particular in the ultraviolet and the infrared region. Here the differences are most clear. This model parameter has very strong effects on the model, greater even than the variation of the expansion velocity. In the ultraviolet and the blue part of the visible region the same phenomenon can be seen that has been discussed in the spectra. At large line scattering the light curves become brighter. The exact opposite is the near infrared, most clearly seen in the bands J, H, and K.
The exact differences between the individual days of two adjacent models were computed. In Figure 5.40 the summed absolute values of the differences of the individual days are shown in the different bands of light of the models for different $\varepsilon_{\text{line}}$ as shown in Figure 5.38.

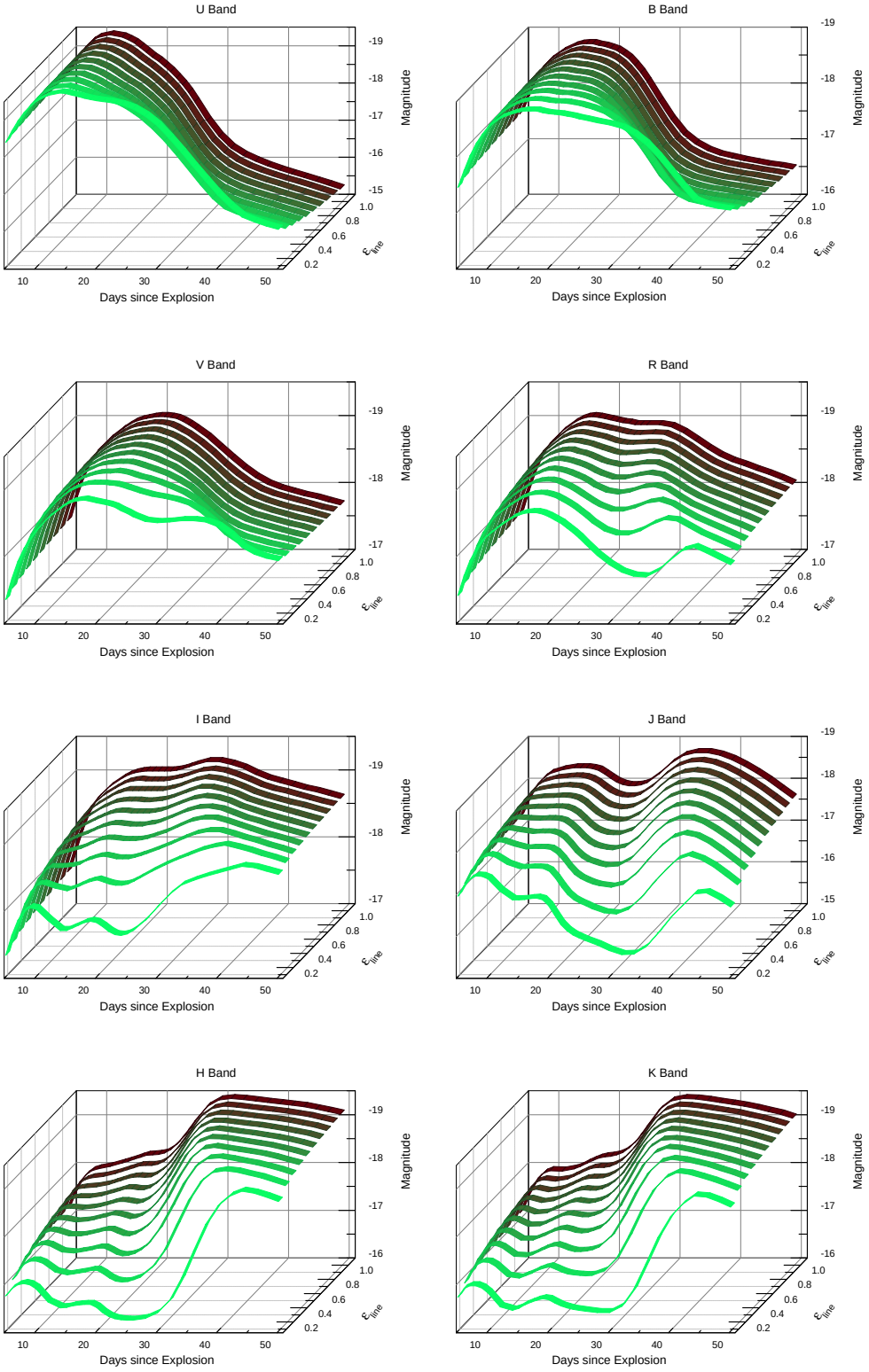

Figure 5.38: Spatial representation of model light curves in the bands U, B, V, R, I, J, H, and K as calculated from synthetic spectra for day 5 until 50 days after the explosion. The line scattering was changed in steps of 0.1 from $\varepsilon_{\mathrm{line}} = 0.1$ (green curve), which means 90% of photons are scattered, to $\varepsilon_{\mathrm{line}} = 1$ (black curve), which means that all photons are absorbed. See text for details.

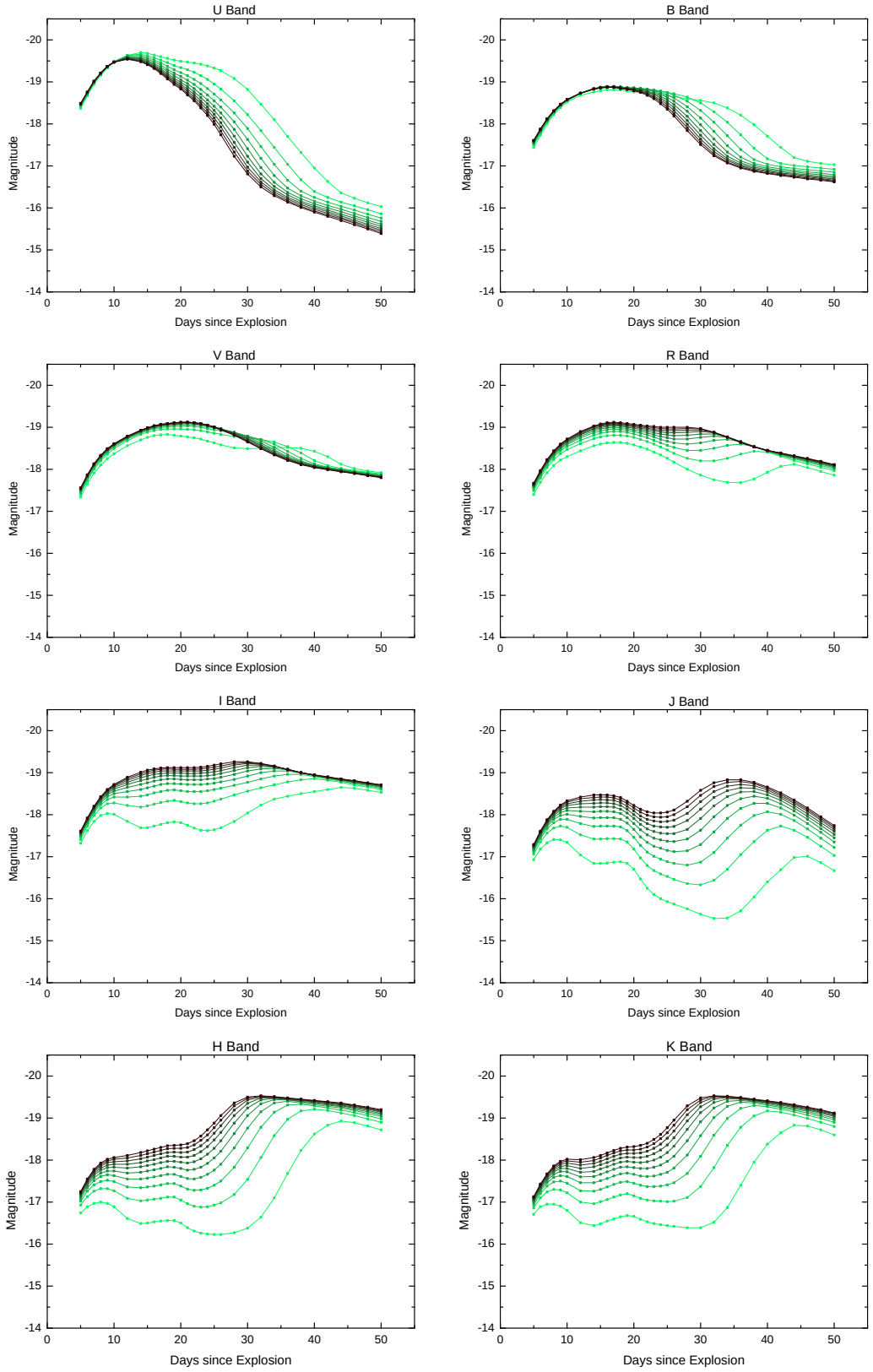

Figure 5.39: The same light curves as shown in Figure 5.24, but in a different presentation. Note that the scale of the ordinate is now the same for all bands. See text for details.

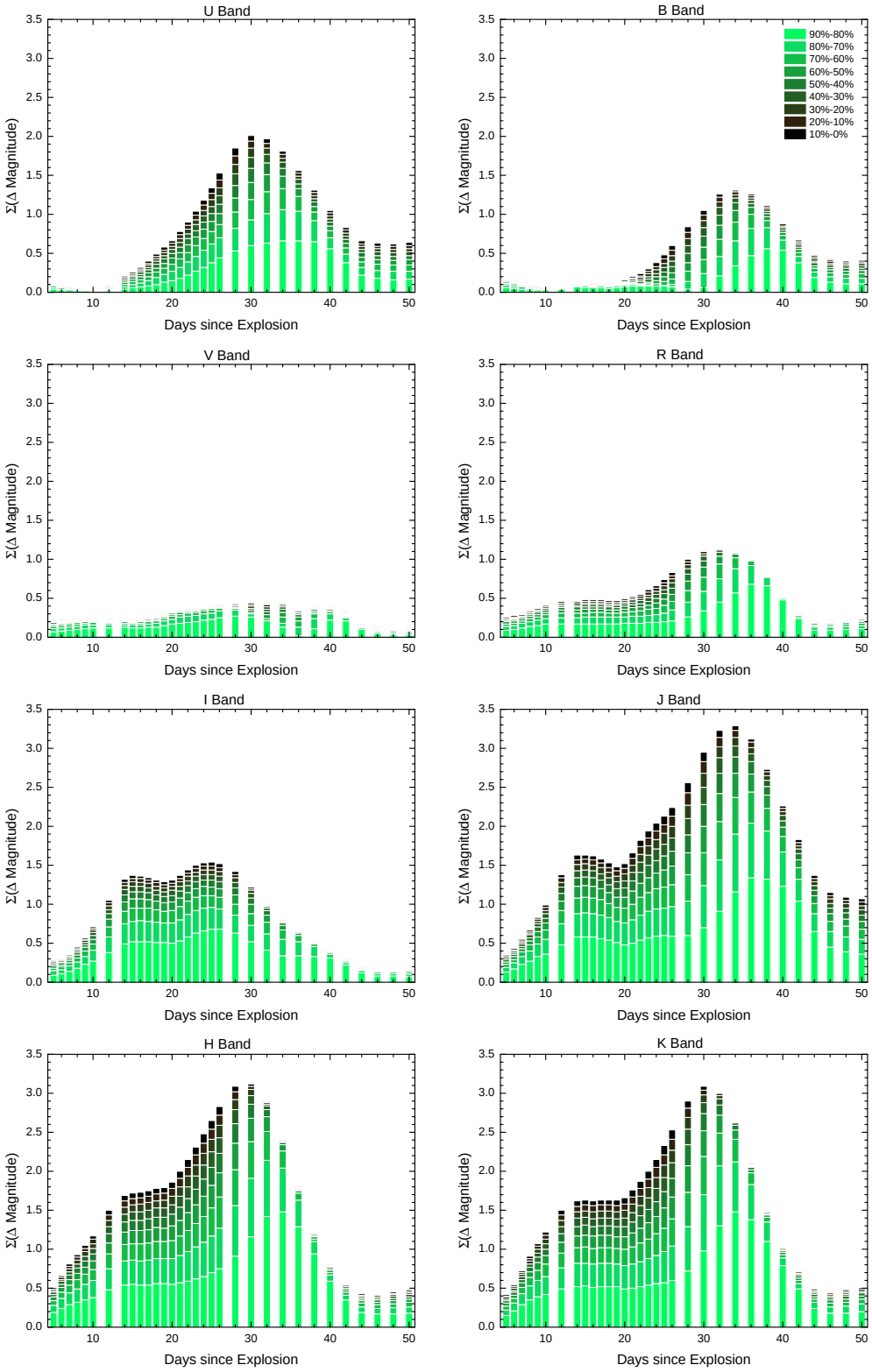

Figure 5.40: The summed absolute values of the differences of the individual days in the different bands of light of the models for different $\varepsilon_{\text{line}}$ shown in Figure 5.38. The legend labels the respective models. See text for details.

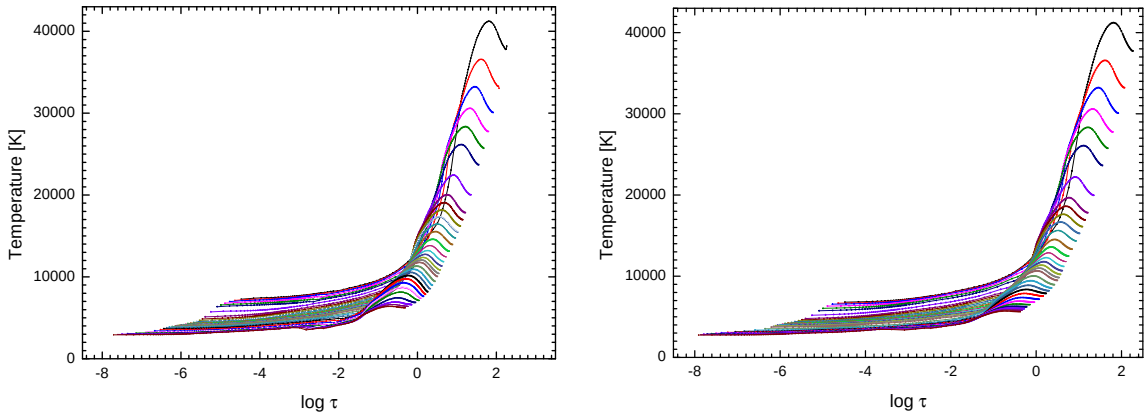

Figure 5.41: Temperature stratifications as a function of the optical depth for the 32 models, representing the time points from which the light curve was calculated for the models with $\varepsilon_{\rm line} = 0.1$ (left side) and $\varepsilon_{\rm line} = 1$ (right side). The starting model (day 5) has the highest temperature and optical depth. The two starting models have the same temperature T $\simeq 41250$ K and $\log\tau \simeq 2.3$. With progress of time, the model atmospheres become cooler and more transparent. For day 50, we have T $\simeq 5700$ K and $\log\tau$ in the range $[-7.7, -0.3]$ for the model with $\varepsilon_{\rm line} = 0.1$ and T $\simeq 6400$ K and $\log\tau$ in the range $[-7.9, -0.4]$ for the model with $\varepsilon_{\rm line} = 1$. See text for details.

Table 5.3: Summarized results for the temperatures and the range of the optical depths for days 5, 20, and 50 for the fiducial model ($\varepsilon_{\rm line} = 0.8$) shown in Figure 5.18 and for the two extreme models with $\varepsilon_{\rm line} = 0.1$ and $\varepsilon_{\rm line} = 1.0$ shown in Figure 5.41.

Model	**Day**	**T [K]**	**log ($\tau_{\rm min}$)**	**log ($\tau_{\rm max}$)**
$\varepsilon_{\rm line} = 0.1$	5	$\simeq 41250$	$\simeq -4.5$	$\simeq 2.3$
$\varepsilon_{\rm line} = 0.8$	5	$\simeq 41150$	$\simeq -4.5$	$\simeq 2.3$
$\varepsilon_{\rm line} = 1.0$	5	$\simeq 41250$	$\simeq -4.5$	$\simeq 2.3$
$\varepsilon_{\rm line} = 0.1$	20	$\simeq 14600$	$\simeq -5.8$	$\simeq 0.7$
$\varepsilon_{\rm line} = 0.8$	20	$\simeq 13700$	$\simeq -5.9$	$\simeq 0.8$
$\varepsilon_{\rm line} = 1.0$	20	$\simeq 13600$	$\simeq -5.9$	$\simeq 0.8$
$\varepsilon_{\rm line} = 0.1$	50	$\simeq 5700$	$\simeq -7.7$	$\simeq -0.3$
$\varepsilon_{\rm line} = 0.8$	50	$\simeq 5750$	$\simeq -7.9$	$\simeq -0,4$
$\varepsilon_{\rm line} = 1.0$	50	$\simeq 6400$	$\simeq -7.9$	$\simeq -0.4$

Direct comparison with the results of the ^{56}Ni models shown in Section 5.1, Figure 5.14 and even with the $v_{\rm exp}$ models shown in Section 5.2, Figure 5.26 show considerably larger differences. If line scattering is considered NLTE effects become more important.
The differences in these models do not originate from the model temperature stratification. The temperatures and the associated optical depths of the two models with $\varepsilon_{\rm line} = 0.1$ and

$\varepsilon_{\rm line} = 1.0$ are shown in Figure 5.41. The starting model (day 5) has the highest temperature and optical depth. The two starting models with $\varepsilon_{\rm line} = 0.1$ and $\varepsilon_{\rm line} = 1.0$ have, as expected, the same temperature T $\simeq 41250\,$K and $\log\tau \simeq 2.3$. With progress of time, the model atmospheres become cooler and more transparent. For day 50, we have T $\simeq 5700\,$K and $\log\tau$ in the range $[-7.7, -0.3]$ for the model with $\varepsilon_{\rm line} = 0.1$ and T $\simeq 6400\,$K and $\log\tau$ in the range $[-7.9, -0.4]$ for the model with $\varepsilon_{\rm line} = 1$. A summary of the temperatures and the optical depths for days 5, 20, and 50 for the fiducial model ($\varepsilon_{\rm line} = 0.8$) and for the two extreme models with $\varepsilon_{\rm line} = 0.1$ and $\varepsilon_{\rm line} = 1$ is given in Table 5.3. It can be seen that the temperatures and optical depths of the models barely differ from each other.

5.6 NLTE – taking into account three ionization stages of calcium

NLTE and scattering effects (cf. Section 5.5) become increasingly important in the ultra violet and infrared regions. Therefore, the model structure[6] of a converged LTE model was used to calculate an NLTE model. Because the computation times increase dramatically, only the three ionization stages of calcium (Ca I, Ca II, and Ca III) were considered. For an average LTE model, for one wavelength point (λ) per time line, with 16 processors (Intel Xeon Harpertown E5472) $\simeq 11 \cdot 10^3$ s are needed, in NLTE taking into account Ca I, Ca II, and Ca III the computation time increases (doubling the processors per node) to $\simeq 43 \cdot 10^3$ s.

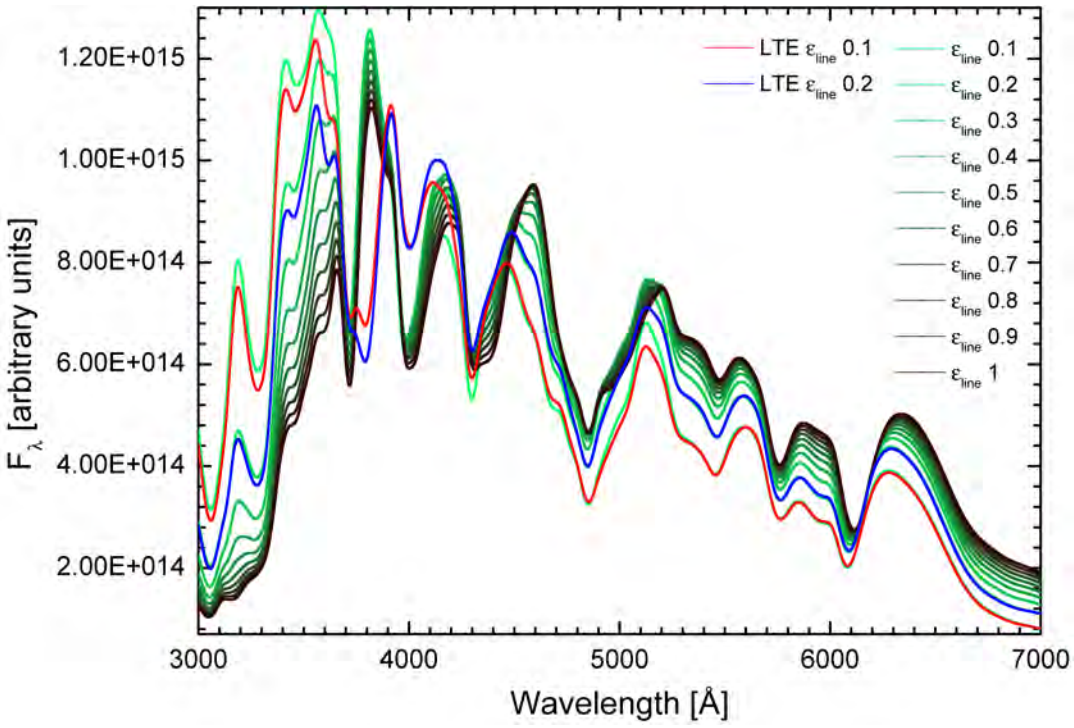

Figure 5.42: Synthetic NLTE spectra around the maximum brightness (for day 20 after the explosion) taking into account of Ca I, Ca II, and Ca III. All other elements were treated with different $\varepsilon_{\text{line}}$. Plotted is the flux in arbitrary units as a function of the wavelength in the range $[3000, 7000]$ Å. The amount of $\varepsilon_{\text{line}}$ was changed in steps of 0.1 from 0.1 (green line) to 1 (black line). Additionally, LTE spectra with $\varepsilon_{\text{line}}^{LTE} = 0.1$ (red line) and $\varepsilon_{\text{line}}^{LTE} = 0.2$ (blue line) are shown. See text for details.

[6] Radiative equilibrium LTE temperature structure of the deflagration model *W* 7

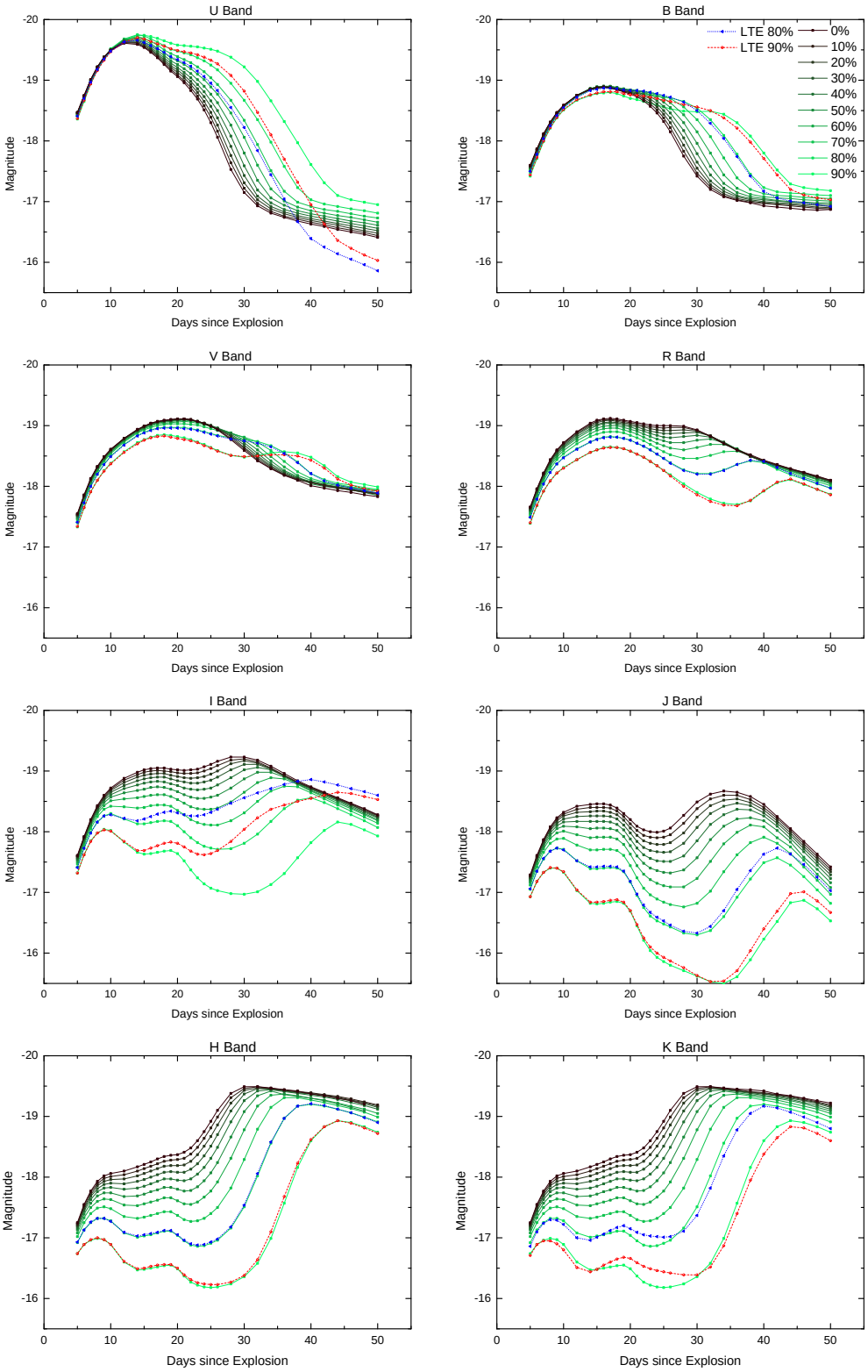

Figure 5.43: NLTE model light curves taking into account the ionization stages Ca I, Ca II, and Ca III in the bands U, B, V, R, I, J, H, and K as calculated from synthetic spectra for day 5 until 50 days after the explosion. Additionally, light curves of the pure LTE models with $\varepsilon_{\text{line}}^{LTE} = 0.1$ (red dashed line) and $\varepsilon_{\text{line}}^{LTE} = 0.2$ (blue dotted line) are shown. The colors of the models correspond to those in Figure 5.42. See text for details.

Taking into account a "full"[7] NLTE model and increasing the number of nodes to 128, each having eight processors (Intel Xeon Gainestown X5570) the computation time increases again dramatically.
However, NLTE models are calculated, taking into account Ca I, Ca II, and Ca III. All other elements were treated in LTE with different $\varepsilon_{\text{line}}$. The visible region in the range of $[3000, 7000]$ Å of the corresponding spectra for day 20 is shown in Figure 5.42. The colors correspond to the corresponding $\varepsilon_{\text{line}}$. Green lines show models with $\varepsilon_{\text{line}} = 0.1$, while black shows models without line scattering ($\varepsilon_{\text{line}} = 1$). Additionally, the two spectra of the LTE models with $\varepsilon_{\text{line}}^{LTE} = 0.1$ (red line) and $\varepsilon_{\text{line}}^{LTE} = 0.2$ (blue line) are shown. In the NLTE spectra, the occurrence of the absorption troughs of the individual features and the impact of scattering can be observed. At first glance the spectra look very similar to the LTE spectra. In particular, the absorption lines are completely congruent around 4800 Å and 6100 Å.

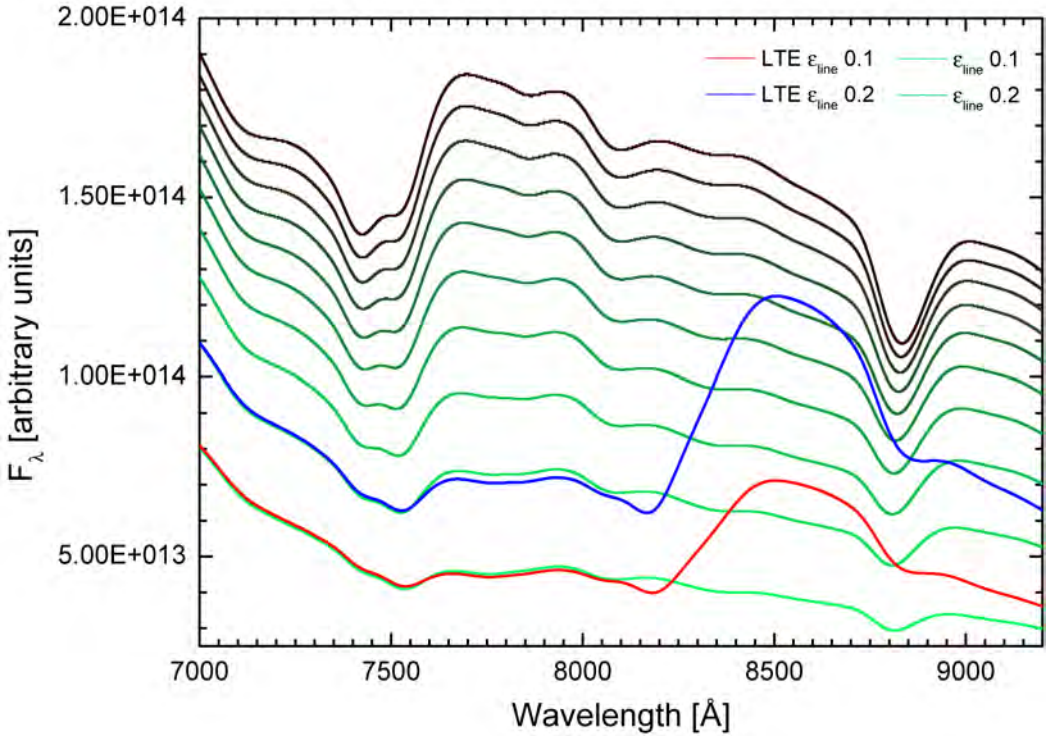

Figure 5.44: Synthetic NLTE spectra around the maximum brightness (for day 20 after the explosion) taking into account Ca I, Ca II, and Ca III. All other elements were treated in LTE with different $\varepsilon_{\text{line}}$. Plotted is the flux in arbitrary units as a function of the wavelength within the wavelength region of the I band $[7000, 9200]$ Å. The amount of $\varepsilon_{\text{line}}$ was changed in steps of 0.1 from 0.1 (green line) to 1 (black line). Additionally, LTE spectra with $\varepsilon_{\text{line}}^{LTE} = 0.1$ (red line) and $\varepsilon_{\text{line}}^{LTE} = 0.2$ (blue line) are shown. The differences in this region come from Ca II infrared triplet. See text for details.

[7] Taking into account H I, He I, He II, C I, Ne I, Na I, Na II, Mg I, Mg II, Mg III, Si I, Si II, Si III, S I, S II, S III, Ca I, Ca II, Ca III, Fe I, Fe II, Fe III, Co I, Co II, and Co III

Strong deviations arise in the lines of singly ionized calcium Ca II 3800 Å and 4000 Å and the intervening region. This shows very clearly the great influence of NLTE.
The corresponding light curves in the Johnson bands U, B, V, R, I, J, H, and K are shown in Figure 5.43. Additionally, light curves of the LTE models with $\varepsilon_{\text{line}}^{LTE} = 0.1$ (red dashed line) and $\varepsilon_{\text{line}}^{LTE} = 0.2$ (blue dotted line) are shown. Note that the scale of the ordinate is the same everywhere.
Good agreement between LTE and NLTE was found in the bands V, R, and H. The largest deviations were in the bands U, I, and K. In the ultra violet region and in the I band the deviation starts early. In particular, the blue part of the visible region the late days depart from the LTE calculations. The NLTE light curves have the same shape as the LTE light curves in the J band, but they are fainter. In the K band days around the maximum differ, as well as the later models. Even if the deviations of the NLTE models in the I band appear huge (in same places more than ≈ 1 mag), they are an improvement. Compared to the template light curves shown in Section 2.4, Figure 2.4 and the observed light curves of SN 2011fe (Section 2.4, Figure 2.3) the second maximum is significantly reduced. This second maximum is too strong in the modeling and has been never observed in that strength. The spectra within the wavelength region of the I band are shown in Figure 5.44. The differences in this region originate from Ca II. It is located in the region around 8500 Å. This is one of the points that show how important NLTE calculations are. Even if only one element is considered in NLTE it changes the entire light curve in the I band. Unfortunately, the effort to calculate NLTE models is enormous, despite the use of a converged LTE model structure. One of the points why the calculation of the NLTE models is much too expensive, is to increase the number of wavelength points several times. Despite everything, NLTE in modeling of supernovae is a very important aspect for more powerful computers and the future.

Chapter 6

Conclusions and outlook

Parameters of Type Ia supernova light curve simulations were systematically varied to test the model sensitivity due to parameter changes. A systematic study in this direction is indeed well worth the effort. However, the number of possible effects to investigate is truly astronomical. Therefore, the focus was placed on parameters that obviously have strong impact on the model sensitivity.
The results, to be able to exclude certain parameter ranges are important. For future projects, they can be accompanied as additional conditions in the parameter estimation problem (cf. Section 3, Eq. (3.13)).
While it is argued here from a theoretical point of view, parameter estimation problems include observational data of individual objects. This means that models are adjusted individually to each object to determine systematically the best parameters.
First, the content of the radioactive energy was changed. For this purpose, the initial ^{56}Ni mass of the $W7$ model ($m_{^{56}Ni} \equiv 0.568\,m_{\odot}$) was changed (cf. Section 5.1). The impact on the models are largely driven by temperature differences (up to $11 \cdot 10^3$ K), while the optical depth roughly remains the same.
The statistical analysis of the light curves shows no outliers in the bands U, B, and V (Johnson), u and g (SDSS), and Kp and D51 (Kepler). Because of outliers the models with 50 % ^{56}Ni and 60 % ^{56}Ni can be statistically excluded. In addition, the models which are outside the first and third quartile, even within the whiskers, have to be viewed critically. Although there is no rigid mathematical definition what an outlier is, the interquartile range is a trimmed estimator and the most significant basic robust measure of scale. It concerns the models with 70 % ^{56}Ni, 130 % ^{56}Ni, 140 % ^{56}Ni, and 150 % ^{56}Ni. The second maximum in the infrared shifts further back in time for models with higher ^{56}Ni content. This leads partially to an inversion in the brightness of the light curves. This distorts the statistical analysis in these bands. Therefore, with our models neither statistical evidence nor statements can be made about the abundance of ^{56}Ni for these bands within this inversion. These are the bands, J, H, and K (Johnson), J, H, and K (2MASS), Y, J, H, and K (UKIDSS), and i (SDSS). Other bands, such as I (Johnson), z (SDSS), and Z (UKIDSS) are less suitable to make statements about the abundance of ^{56}Ni. For day 30 after the explosion, the models are in these bands very close together. According to our models, the two bands D51 and Kp (Kepler) are particularly suitable for quantitative statements. Although Kp covers a wide wavelength range ($\simeq$ 6220 Å) in the visible and near infrared, the differences can be quite clearly seen in the respective models. The light curves of the models are clearly spread apart, there are no statistical outliers. D51, which surrounds only an infinitesimally narrow wavelength range ($\simeq$ 380 Å), shows the same behavior.

For future projects, it would be important to include optimum experimental design. Statements about the parts of the spectrum could be made, which are relevant to make quantitative statements about parameters.

Then, the initial v_{exp} ($v_{exp}^{max} \equiv 30 \cdot 10^3$ km s^{-1}) is varied (cf. Section 5.2), which is equivalent to the variation of the kinetic energy of the explosion. In this case, the total optical depths ($\Delta \log \tau \simeq 1.1$) change and a temperature difference of up to $33 \cdot 10^3$ K occurs. Accordingly, the changes in the spectra are stronger. By changing v_{exp}, therefore, the opacity changes, obviously a determining parameter in a problem concerned with the escape of radiation. An increase in v_{exp} means a decrease in opacity. The spectra for day 20 of the models with reduced v_{exp} are overall brighter. However, the maxima of the light curves are no longer around day 20. More energetic explosions peak earlier, are brighter, and decline more rapidly. Models with reduced v_{exp} are hotter and reach the maximum later. In the near infrared the two models with 50 % v_{exp} and 60 % v_{exp} reach no maximum. For day 50 their brightness increase continuously in the bands I, H, and K (Johnson).

Changing these two parameter simultaneously (cf. Section 5.3), they may amplify or compensate each other. This can be observed in the spectra. In the light curves, however, the effects are not always immediately apparent. This shows how difficult it is to evaluate the model response when parameters are varied simultaneously. Furthermore, the number of permutations increases significantly.

Although the assumption of homologous expansion seems to be appropriate, it is a limitation of the model. However, Pinto & Eastman (2000) noted that energy release by the radioactive decay and high velocity material at the surface, in which the density drops more rapidly, can influence the dynamics of the expansion. The additional source of energy will have a modest, but perhaps not completely negligible effect upon the velocity structure.

Then the ^{56}Ni mass and distribution was changed (cf. Section 5.4). Fe, which is at locations slower than $\lesssim 4440$ km s^{-1}, is successively replaced in the core by ^{56}Ni (cf. Section 5.4). This is a total increase of ^{56}Ni of 12.8 %. The effects are smaller than for the global increase of ^{56}Ni of 10 %. This means that it is not based only on the amount of ^{56}Ni, but also on the position, since the diffusion time of the energy is changed. Even with this small percentage of additional ^{56}Ni the Phillips relation can be reproduced differentially. It leads to a time shift of the second maximum, and thus an inversion of the brightness in the infrared light curves.

Jack et al. (2011, 2012) found that a change of the ratio of line scattering to absorption improves the fits to the I band light curves (in LTE). Therefore, we varied the value of the parametrized line scattering parameter, (ε_{line}) (cf. Section 5.5). The result of an improvement in the Johnson I band can not be confirmed. Although the light curves are fainter for small ε_{line}, i.e., more photons are scattered, however, this is due to the shift of the second maximum further back in time. From a physical point of view, the change of the line scattering fraction with time represents the simplifying assumption to simulate NLTE. Moreover, the model answer for time-dependent[1] $\varepsilon_{line}(t)$ should be taken into account in the other infrared bands, e.g., Johnson J, H, and K. However, the better fitting of theoretical models with time-dependent $\varepsilon_{line}(t)$ to the observational data seems to indicate that the column density of the model is too high. Roughly speaking, it is inversely proportional to ε_{line}.

[1] Jack et al. (2012) used for the line scattering factor $\epsilon = \epsilon_0 f(t)$, where $f(t)$ is a function of time

Therefore, NLTE calculations are essential, however, they are much more complex and computationally intensive. Considering the three ionization stages of calcium (Ca I, Ca II, and Ca III) under the assumption of NLTE (cf. Section 5.6), significant changes compared to the pure LTE calculations can be observed, both in the spectra and in the light curves. The largest deviations occur in the (Johnson) bands U, Ca II H and K and I, Ca II (8579 Å) infrared triplet. This result shows that an accurate treatment of NLTE effects and scattering are very important, especially in the infrared, where the position of the infrared photosphere is strongly influenced by scattering effects (cf. Section 5.5).
Although the model is limited by simplifying assumptions, it is adequate for demonstrating parameter sensitivity of synthetic spectra and light curves of Type Ia supernovae.
For the future, it seems clear what is needed. From a theoretical point of view, faster computers are urgently needed, with which the improved models can be calculated. Observational data would be desirable, so that the question of the progenitor star can be finally resolved. From an observational point of view, a relatively near supernova is urgently needed, which can be observed during the explosion in a known environment.

Bibliography

Allard, F. & Hauschildt, P. H. 1995, ApJ, 445, 433

Auer, L. H. 1987, Acceleration of Convergence, ed. W. Kalkofen (Cambridge: Cambridge University Press), 101–109

Baade, W. & Zwicky, F. 1938, ApJ, 88, 411

Bailer-Jones, C. A. L. 2002, in Automated Data Analysis in Astronomy, ed. R. Gupta, H. P. Singh, & C. A. L. Bailer-Jones, 83–98

Barbon, R., Ciatti, F., & Rosino, L. 1973, A&A, 25, 241

Baron, E., Bongard, S., Branch, D., & Hauschildt, P. H. 2006, ApJ, 645, 480

Baron, E., Hauschildt, P. H., Branch, D., Kirshner, R. P., & Filippenko, A. V. 1996, MNRAS, 279, 799

Baron, E., Höflich, P., Friesen, B., et al. forthcoming, ApJ

Baron, E., Höflich, P., Krisciunas, K., et al. 2012, ApJ, 753, 105

Baschek, B., Butler, K., Scholz, M., Ulmenschneider, P., & Wehrse, R. 1996, Physics of stellar atmospheres, ed. H. Voigt, Landolt-Börnstein: Numerical Data and Functional Relationships in Science and Technology, New Series, Group VI: Astronomy and Astrophysics Volume 3, Astronomy and Astrophysics. Extension and Supplement to Volume 2, Stars and Star Clusters (Berlin: Springer), 41–61

Baschek, B., Efimov, G. V., von Waldenfels, W., & Wehrse, R. 1997, A&A, 317, 630

Bertola, F. 1962, Mem. S.A.It., 33, 77 [=Asiago Contr., No. 128]

Bessell, M. S. 2005, ARA&A, 43, 293

Bloom, J. S., Kasen, D., Shen, K. J., et al. 2012, ApJ, 744, L17

Bock, H. G. 1981, in Springer Series in Chemical Physics, Vol. 18, Modelling of Chemical Reaction Systems, ed. K. Ebert, P. Deuflhard, & W. Jäger (Heidelberg: Springer), 102–125

Bock, H. G. 1987, Bonner Mathematische Schriften, Vol. 183, Randwertproblemmethoden zur Parameteridentifizierung in Systemen nichtlinearer Differentialgleichungen (Bonn: Universität Bonn), iv, 264 pp.

Borucki, W. J., Koch, D., Basri, G., et al. 2010, Science, 327, 977

Branch, D. 1977a, in Astrophysics and Space Science Library, Vol. 66, Supernovae, ed. D. N. Schramm, 21–28

Branch, D. 1977b, MNRAS, 179, 401

Branch, D. 1985a, in Lecture Notes in Physics, Vol. 224, Supernovae as Distance Indicators, ed. N. Bartel, 138–150

Branch, D. 1985b, in Nucleosynthesis: Challenges and New Developments, ed. W. D. Arnett & J. W. Truran, 261–271

Branch, D. 1987, ApJ, 316, L81

Branch, D. 1990, in Supernovae, ed. A. G. Petschek, 30–58

Branch, D. 2004, in Cosmic explosions in three dimensions, ed. P. Höflich, P. Kumar, & J. C. Wheeler, 132–141

Branch, D., Buta, R., Falk, S. W., et al. 1982, ApJ, 252, L61

Branch, D., Doggett, J. B., Nomoto, K., & Thielemann, F.-K. 1985, ApJ, 294, 619

Branch, D., Drucker, W., & Jeffery, D. J. 1988, ApJ, 330, L117

Branch, D., Fisher, A., & Nugent, P. 1993, AJ, 106, 2383

Branch, D., Livio, M., Yungelson, L. R., Boffi, F. R., & Baron, E. 1995, PASP, 107, 1019

Branch, D. & Patchett, B. 1972, in Bulletin of the American Astronomical Society, Vol. 4, Bulletin of the American Astronomical Society, 340

Branch, D. & Patchett, B. 1973, MNRAS, 161, 71

Branch, D. & Tammann, G. A. 1992, ARA&A, 30, 359

Brown, T. M., Latham, D. W., Everett, M. E., & Esquerdo, G. A. 2011, AJ, 142, 112

Cannon, C. J. 1973a, J. Quant. Spec. Radiat. Transf., 13, 627

Cannon, C. J. 1973b, ApJ, 185, 621

Cannon, C. J. 1985, The transfer of spectral line radiation (Cambridge: Cambridge University Press), x, 541 pp.

Cappellaro, E., Turatto, M., Tsvetkov, D. Y., et al. 1997, A&A, 322, 431

Castelli, F. & Kurucz, R. L. 2004, ArXiv Astrophysics e-prints

Chandrasekhar, S. 1931, ApJ, 74, 81

Chandrasekhar, S. 1939, An introduction to the study of stellar structure (Chicago: The University of Chicago press), ix, 509 pp.

Chandrasekhar, S. 1950, Radiative transfer, ed. R. H. Fowler, P. Kapitza, N. F. Mott, & E. C. Bullard, International series of monographs on physics (London: Oxford at the Clarendon Press), xiv, 393 pp.

Chandrasekhar, S. 1961, Hydrodynamic and hydromagnetic stability (London: Oxford at the Clarendon Press), xx, 652 pp.

Chomiuk, L., Soderberg, A. M., Moe, M., et al. 2012, ApJ, 750, 164

Clark, D. H. & Stephenson, F. R. 1977, The historical supernovae (Oxford: Pergamon Press), x, 233 pp.

Cohen-Tannoudji, C., Diu, B., & Laloe, F. 1999, Quantenmechanik/1, 2nd edn. (Berlin, New York: de Gruyter), xviii, 755 pp.

Colgate, S. A. & McKee, C. 1969, ApJ, 157, 623

Crawley, M. J. 2007, The R book (Chichester: John Wiley & Sons Ltd), viii, 942 pp.

da Silva, L. A. L. 1993, Ap&SS, 202, 215

Dittmann, O. J. 1997, J. Quant. Spec. Radiat. Transf., 58, 279

Dye, S., Warren, S. J., Hambly, N. C., et al. 2006, MNRAS, 372, 1227

Efimov, G. V., Kryzhevoi, N. V., von Waldenfels, W., & Wehrse, R. 2001, ArXiv Astrophysics e-prints

Efimov, G. V., von Waldenfels, W., & Wehrse, R. 1995, J. Quant. Spec. Radiat. Transf., 53, 59

Elias, J. H., Matthews, K., Neugebauer, G., & Persson, S. E. 1985, ApJ, 296, 379

Evans, R., McNaught, R. H., & Humphries, C. 1986, IAU Circ., 4208, 1

Feast, M. W., Hill, P. W., Stobie, R. S., et al. 1986, IAU Circ., 4210, 1

Filippenko, A. V. 1997, ARA&A, 35, 309

Filippenko, A. V., Richmond, M. W., Branch, D., et al. 1992a, AJ, 104, 1543

Filippenko, A. V., Richmond, M. W., Matheson, T., et al. 1992b, ApJ, 384, L15

Foley, R. J., Challis, P. J., Chornock, R., et al. 2013, ApJ, 767, 57

Frieman, J. A., Bassett, B., Becker, A., et al. 2008, AJ, 135, 338

Gaposchkin, C. P. 1936, ApJ, 83, 245

Gass, H., Wehrse, R., & Liebert, J. 1988, A&A, 189, 194

Goldhaber, G., Groom, D. E., Kim, A., et al. 2001, ApJ, 558, 359

Golub, G. H. & Van Loan, C. F. 1996, Matrix computations, third edition edn., Johns Hopkins series in the mathematical sciences (Baltimore: The Johns Hopkins University Press), xxvii, 694 pp.

Graur, O. & Maoz, D. 2013, MNRAS, 430, 1746

Green, D. A. & Stephenson, F. R. 2003, in Lecture Notes in Physics, Vol. 598, Supernovae and Gamma-Ray Bursters, ed. K. Weiler, 7–19

Hamann, W.-R. 1985, A&A, 148, 364

Hamann, W.-R. 1986, A&A, 160, 347

Hamann, W.-R. 1987, Line Formation in Expanding Atmospheres: Multi-Level Calculations using Approximate Lambda Operators, ed. W. Kalkofen (Cambridge: Cambridge University Press), 347–351

Hamuy, M., Maza, J., & Phillips, M. 2002, IAU Circ., 8028, 2

Hamuy, M., Maza, J., Phillips, M. M., et al. 1993, AJ, 106, 2392

Hamuy, M., Phillips, M., Suntzeff, N., & Maza, J. 2003a, IAU Circ., 8151, 2

Hamuy, M., Phillips, M. M., Maza, J., et al. 1995, AJ, 109, 1

Hamuy, M., Phillips, M. M., Suntzeff, N. B., et al. 2003b, Nature, 424, 651

Hamuy, M., Phillips, M. M., Suntzeff, N. B., et al. 1996a, AJ, 112, 2408

Hamuy, M., Phillips, M. M., Suntzeff, N. B., et al. 1996b, AJ, 112, 2391

Harkness, R. P. & Wheeler, J. C. 1990, in Supernovae, ed. A. G. Petschek, 1–29

Harkness, R. P., Wheeler, J. C., Margon, B., et al. 1987, ApJ, 317, 355

Hartwig, E. 1885, Astronomische Nachrichten, 112, 355

Hauschildt, P. H. 1992, J. Quant. Spec. Radiat. Transf., 47, 433

Hauschildt, P. H. 1993, J. Quant. Spec. Radiat. Transf., 50, 301

Hauschildt, P. H. & Baron, E. 1995, J. Quant. Spec. Radiat. Transf., 54, 987

Hauschildt, P. H. & Baron, E. 1999, Journal of Computational and Applied Mathematics, 109, 41

Hauschildt, P. H. & Baron, E. 2004, A&A, 417, 317

Hauschildt, P. H., Starrfield, S., Shore, S. N., Allard, F., & Baron, E. 1995, ApJ, 447, 829

Hewett, P. C., Warren, S. J., Leggett, S. K., & Hodgkin, S. T. 2006, MNRAS, 367, 454

Hoffleit, D. 1939, Harvard College Observatory Bulletin, 910, 1

Höflich, P., Khokhlov, A. M., & Wheeler, J. C. 1995, ApJ, 444, 831

Horesh, A., Kulkarni, S. R., Fox, D. B., et al. 2012, ApJ, 746, 21

Howell, D. A. 2001, ApJ, 554, L193

Hoyle, F. & Fowler, W. A. 1960, ApJ, 132, 565

Hoyle, F. & Fowler, W. A. 1961, ApJ, 134, 1028

Hubble, E. 1929, Proceedings of the National Academy of Science, 15, 168

Hubble, E. P. 1925, The Observatory, 48, 139

Hubble, E. P. 1936, The Realm of the Nebulae (London, Humphrey Milford: Oxford University Press), xiii, 207 pp.

Iben, Jr., I. & Tutukov, A. V. 1984, ApJS, 54, 335

Jack, D., Hauschildt, P. H., & Baron, E. 2009, A&A, 502, 1043

Jack, D., Hauschildt, P. H., & Baron, E. 2011, A&A, 528, A141

Jack, D., Hauschildt, P. H., & Baron, E. 2012, A&A, 538, A132

Jäger, W., Rannacher, R., & Warnatz, J. 2007, Reactive Flow, Diffusion and Transport: From Experiments Via Mathematical Modeling to Numerical Simulation and Optimization, Mathematics and Statistics (Berlin: Springer), x, 676 pp.

Jeffery, D. J. 1998, ArXiv Astrophysics e-prints

Jha, S., Branch, D., Chornock, R., et al. 2006, AJ, 132, 189

Jha, S., Riess, A. G., & Kirshner, R. P. 2007, ApJ, 659, 122

Johnson, H. L. 1966, ARA&A, 4, 193

Johnson, W. A. 1936, Harvard College Observatory Bulletin, 902, 11

Jones, D. O., Rodney, S. A., Riess, A. G., et al. 2013, ApJ, 768, 166

Junde, H., Su, H., & Dong, Y. 2011, Nuclear Data Sheets, 112, 1513

Kalkofen, W. & Wehrse, R. 1982, A&A, 108, 42

Kanschat, G., Meinköhn, E., Rannacher, R., & Wehrse, R. 2009, in Numerical Methods in Multidimensional Radiative Transfer, ed. G. Kanschat, E. Meinköhn, R. Rannacher, & R. Wehrse, 1–18

Karush, W. 1939, PhD thesis, Master's Thesis. Department of Mathematics, University of Chicago

Khokhlov, A., Mueller, E., & Hoeflich, P. 1993, A&A, 270, 223

Kirshner, R. P. 1990, in Supernovae, ed. A. G. Petschek, 59–75

Kirshner, R. P. & Kwan, J. 1974, ApJ, 193, 27

Kourganoff, V. 1952, Basic methods in transfer problems, The international series of monographs on physics (Oxford: Clarendon Press), xv, 281 pp.

Kowal, C. T. 1972, IAU Circ., 2405, 1

Kowalski, M., Rubin, D., Aldering, G., et al. 2008, ApJ, 686, 749

Krisciunas, K., Li, W., Matheson, T., et al. 2011, AJ, 142, 74

Kryzhevoi, N. V., Efimov, G. V., & Wehrse, R. 2001, A&A, 370, 707

Kuchner, M. J., Kirshner, R. P., Pinto, P. A., & Leibundgut, B. 1994, ApJ, 426, L89

Kuhn, H. W. & Tucker, A. W. 1951, in Proceedings of the Second Berkeley Symposium on Mathematical Statistics and Probability, ed. J. Neyman, Vol. 356, 481–492

Kurucz, R. & Bell, B. 1995, Atomic Line Data (R.L. Kurucz and B. Bell) Kurucz CD-ROM No. 23. Cambridge, Mass.: Smithsonian Astrophysical Observatory

Kurucz, R. L. 2010, Atomic line list, http://kurucz.harvard.edu/atoms.html

Landi Degl'Innocenti, E. 1996, Solar Phys., 164, 21

Law, N. M., Kulkarni, S. R., Dekany, R. G., et al. 2009, PASP, 121, 1395

Lawrence, A., Warren, S. J., Almaini, O., et al. 2007, MNRAS, 379, 1599

Leavitt, H. S. & Pickering, E. C. 1912, Harvard College Observatory Circular, 173, 1

Leibundgut, B. 1988, PhD thesis, Universität Basel

Leibundgut, B. 2000, A&A Rev., 10, 179

Leibundgut, B., Kirshner, R. P., Phillips, M. M., et al. 1993, AJ, 105, 301

Lentz, E. J., Baron, E., Branch, D., & Hauschildt, P. H. 2001a, ApJ, 557, 266

Lentz, E. J., Baron, E., Branch, D., & Hauschildt, P. H. 2001b, ApJ, 547, 402

Lentz, E. J., Baron, E., Branch, D., Hauschildt, P. H., & Nugent, P. E. 2000, ApJ, 530, 966

Li, W., Bloom, J. S., Podsiadlowski, P., et al. 2011, Nature, 480, 348

Li, W., Filippenko, A. V., Chornock, R., et al. 2003, PASP, 115, 453

Mandel, L. & Wolf, E. 1995, Optical coherence and quantum optics, 1st edn. (Cambridge: Cambridge University Press), xxvi, 1166 pp.

Maoz, D. & Mannucci, F. 2012, PASA, 29, 447

Marietta, E., Burrows, A., & Fryxell, B. 2000, ApJS, 128, 615

Marion, G. H., Höflich, P., Gerardy, C. L., et al. 2009, AJ, 138, 727

Marion, G. H., Höflich, P., Vacca, W. D., & Wheeler, J. C. 2003, ApJ, 591, 316

Maza, J. & van den Bergh, S. 1976, ApJ, 204, 519

Mazzali, P. A., Chugai, N., Turatto, M., et al. 1997, MNRAS, 284, 151

McMillan, R. J. & Ciardullo, R. 1996, ApJ, 473, 707

Mie, G. 1908, Annalen der Physik, 25, 377

Mihalas, D. 1978, Stellar atmospheres (San Francisco: W. H. Freeman and Co.), xvii, 632 pp.

Mihalas, D. 1980, ApJ, 237, 574

Mihalas, D., Kunasz, P. B., & Hummer, D. G. 1975, ApJ, 202, 465

Mihalas, D. & Weibel Mihalas, B. 1984, Foundations of radiation hydrodynamics, ed. Mihalas, D. & Weibel Mihalas, B. (New York: Oxford University Press), viii, 718 pp.

Minkowski, R. 1939, ApJ, 89, 156

Minkowski, R. 1941, PASP, 53, 224

Miyaji, S., Nomoto, K., Yokoi, K., & Sugimoto, D. 1980, PASJ, 32, 303

Nomoto, K. 1980, in Texas Workshop on Type I Supernovae, ed. J. C. Wheeler, 164–181

Nomoto, K. 1985, in Nucleosynthesis: Challenges and New Developments, ed. W. D. Arnett & J. W. Truran, 202–232

Nomoto, K., Thielemann, F.-K., & Yokoi, K. 1984, ApJ, 286, 644

Nomoto, K., Yamaoka, H., Shigeyama, T., & Iwamoto, K. 1996, in Supernovae and Supernova Remnants, ed. R. McCray & Z. Wang, 49–68

Norgaard-Nielsen, H. U., Hansen, L., Jorgensen, H. E., et al. 1989, Nature, 339, 523

Nugent, P., Baron, E., Branch, D., Fisher, A., & Hauschildt, P. H. 1997, ApJ, 485, 812

Nugent, P., Kim, A., & Perlmutter, S. 2002, PASP, 114, 803

Nugent, P. E. 1997, PhD thesis, The University of Oklahoma

Nugent, P. E., Sullivan, M., Cenko, S. B., et al. 2011, Nature, 480, 344

Olson, G. L. & Kunasz, P. B. 1987, J. Quant. Spec. Radiat. Transf., 38, 325

Osterbrock, D. E. 2001, in Bulletin of the American Astronomical Society, Vol. 33, American Astronomical Society Meeting Abstracts, 1330

Oxenius, J. 1986, Springer series in electrophysics, Vol. 20, Kinetic theory of particles and photons. Theoretical foundations of Non-LTE plasma spectroscopy (Berlin: Springer), xii, 356 pp.

Pain, R., Fabbro, S., Sullivan, M., et al. 2002, ApJ, 577, 120

Pain, R., Hook, I. M., Deustua, S., et al. 1996, ApJ, 473, 356

Panagia, N., Sandage, A., Saha, A., Tammann, G. A., & Macchetto, F. D. 1992, in European Southern Observatory Conference and Workshop Proceedings, Vol. 44, ST-ECF / STScI Workshop. Science with the Hubble Space Telescope. Chia Laguna, Sardinia, Italy 29 June - 7 July 1992, ed. P. Benvenuti & E. Schreier, 183

Parrent, J. T., Howell, D. A., Friesen, B., et al. 2012, ApJ, 752, L26

Peraiah, A. 1984, in Methods in radiative transfer, ed. W. Kalkofen (Cambridge: Cambridge University Press), 281–306

Peraiah, A. 2001, An Introduction to Radiative Transfer: Methods and Applications in Astrophysics (Cambridge: Cambridge University Press), xii, 492 pp.

Perlmutter, S. 1999, in Lepton and Photon Interactions at High Energies, ed. J. A. Janos & M. E. Peskin, 733–757

Perlmutter, S., Aldering, G., Goldhaber, G., et al. 1999, ApJ, 517, 565

Perlmutter, S., Gabi, S., Goldhaber, G., et al. 1997, ApJ, 483, 565

Phillips, M. M. 1993, ApJ, 413, L105

Phillips, M. M., Lira, P., Suntzeff, N. B., et al. 1999, AJ, 118, 1766

Phillips, M. M., Wells, L. A., Suntzeff, N. B., et al. 1992, AJ, 103, 1632

Pinto, P. A. & Eastman, R. G. 2000, ApJ, 530, 744

Popper, D. M. 1937, PASP, 49, 283

Porter, A. C. & Filippenko, A. V. 1987, AJ, 93, 1372

Pskovskii, Y. P. 1969, Soviet Ast., 12, 750

Pskovskii, Y. P. 1977, Soviet Ast., 21, 675

Pskovskii, Y. P. 1984, Soviet Ast., 28, 658

Rau, A., Kulkarni, S. R., Law, N. M., et al. 2009, PASP, 121, 1334

Riess, A. G., Filippenko, A. V., Challis, P., et al. 1998, AJ, 116, 1009

Riess, A. G., Press, W. H., & Kirshner, R. P. 1995, ApJ, 438, L17

Riess, A. G., Press, W. H., & Kirshner, R. P. 1996, ApJ, 473, 88

Rodgers, J. L. & Nicewander, W. A. 1988, The American Statistician, 42, 59

Sadakane, K. 1990, in Lecture Notes in Physics, Vol. 356, Accuracy of Element Abundances from Stellar Atmospheres, ed. R. Wehrse, 57–67

Saha, A., Sandage, A., Labhardt, L., et al. 1995, ApJ, 438, 8

Saha, A., Sandage, A., Labhardt, L., et al. 1996a, ApJ, 466, 55

Saha, A., Sandage, A., Labhardt, L., et al. 1996b, ApJS, 107, 693

Saha, A., Sandage, A., Labhardt, L., et al. 1997, ApJ, 486, 1

Saha, A., Sandage, A., Tammann, G. A., et al. 2001a, ApJ, 562, 314

Saha, A., Sandage, A., Tammann, G. A., et al. 1999, ApJ, 522, 802

Saha, A., Sandage, A., Thim, F., et al. 2001b, ApJ, 551, 973

Sako, M., Bassett, B., Becker, A., et al. 2008, AJ, 135, 348

Sandage, A., Saha, A., Tammann, G. A., et al. 1996, ApJ, 460, L15

Sandage, A., Saha, A., Tammann, G. A., et al. 1994, ApJ, 423, L13

Sandage, A., Saha, A., Tammann, G. A., Panagia, N., & Macchetto, D. 1992, ApJ, 401, L7

Sandage, A. R. 1956, The red-shift (San Francisco: W. H. Freeman and Company), 9 pp

Sapar, A. 1978, Publications of the Tartu Astrofizica Observatory, 46, 17

Scharmer, G. B. 1981, ApJ, 249, 720

Scharmer, G. B. 1984, Accurate solutions to non-LTE problems using approximate lambda operators, ed. W. Kalkofen (Cambridge: Cambridge University Press), 173–210

Schneider, D. P., Mould, J. R., Porter, A. C., et al. 1987, PASP, 99, 1167

Schuster, A. 1903, The Observatory, 26, 379

Schuster, A. 1905, ApJ, 21, 1

Schwarzschild, K. 1914, Sitzungsberichte der Königlich Preussischen Akademie der Wissenschaften, 1, 1183

Shappee, B. J. & Stanek, K. Z. 2011, ApJ, 733, 124

Sherman, O. T. 1885, Astronomische Nachrichten, 113, 45

Sherman, O. T. 1886, MNRAS, 47, 14

Skrutskie, M. F., Cutri, R. M., Stiening, R., et al. 2006, AJ, 131, 1163

Steiner, O. 1991, A&A, 242, 290

Steiner, O. 2003, in Astronomical Society of the Pacific Conference Series, Vol. 288, Stellar Atmosphere Modeling, ed. I. Hubeny, D. Mihalas, & K. Werner, 83

Stenflo, J. O. 1994, Solar magnetic fields, Astrophysics and space science library No. 189 (Dordrecht: Kluwer), xv, 385 pp.

Stephenson, F. R. & Green, D. A. 2005, in Astronomical Society of the Pacific Conference Series, Vol. 342, 1604-2004: Supernovae as Cosmological Lighthouses, ed. M. Turatto, S. Benetti, L. Zampieri, & W. Shea, 63–70

Stöcker, H. 1994, Taschenbuch der Physik, 2nd edn. (Frankfurt am Main: Verlag Harri Deutsch), xxv, 874 pp.

Strohmeier, W. 1938, Astronomische Nachrichten, 266, 225

Thielemann, F.-K., Nomoto, K., & Yokoi, K. 1986, A&A, 158, 17

Travaglio, C. & Hix, R. W. 2013, Frontiers of Physics, 8, 199

Truran, J. W., Arnett, W. D., & Cameron, A. G. W. 1967, Canadian Journal of Physics, 45, 2315

Turatto, M., Benetti, S., Cappellaro, E., et al. 1996, MNRAS, 283, 1

Unno, W. 1967, PASJ, 19, 140

Unsöld, A. 1938, Physik der Sternamosphären mit besonderer Berücksichtigung der Sonne (Berlin: Springer), viii, 500 pp.

Unsöld, A. 1942a, ZAp, 21, 1

Unsöld, A. 1942b, ZAp, 21, 22

Unsöld, A. 1942c, ZAp, 21, 229

Unsöld, A. 1944, ZAp, 23, 75

Unsöld, A. 1968, Physik der Sternatmosphären mit besonderer Berücksichtigung der Sonne. Berichtigter Nachdruck der zweiten Auflage (Heidelberg: Springer-Verlag), ix, 866 pp.

Vogel, W. & Welsch, D.-G. 2006, Quantum Optics, third, revised and extended edition edn. (Weinheim: Wiley-VCH Verlag GmbH & Co. KGaA), xii, 508 pp.

von Waldenfels, W. 2009, in Numerical Methods in Multidimensional Radiative Transfer, ed. G. Kanschat, E. Meinköhn, R. Rannacher, & R. Wehrse (Berlin: Springer), 19–25

von Waldenfels, W., Wehrse, R., & Baschek, B. 2011, A&A, 525, A70

Wang, L., Baade, D., Höflich, P., et al. 2004, ApJ, 604, L53

Ward, I. W. 1885, Astronomical register, 23, 242

Webbink, R. F. 1984, ApJ, 277, 355

Wehrse, R. 1991, in Nuclear Astrophysics, 6th Workshop, ed. W. Hillebrandt & E. Mueller, 62

Wehrse, R. & Kalkofen, W. 2006, A&A Rev., 13, 3

Wehrse, R. & Rosenau, P. 1997, in IAU Symposium, Vol. 189, IAU Symposium, ed. T. R. Bedding, A. J. Booth, & J. Davis, 235–238

Wheeler, J. C. & Benetti, S. 2000, Supernovae, 4th edn., ed. A. N. Cox (New York: Springer), 451–469

Wheeler, J. C. & Harkness, R. P. 1990, Reports on Progress in Physics, 53, 1467

Wheeler, J. C. & Levreault, R. 1985, ApJ, 294, L17

Whelan, J. & Iben, Jr., I. 1973, ApJ, 186, 1007

Wilson, O. C. 1939, ApJ, 90, 634

Wood-Vasey, W. M., Aldering, G., & Nugent, P. 2002a, IAU Circ., 8019, 2

Wood-Vasey, W. M., Aldering, G., Nugent, P., et al. 2002b, IAU Circ., 7902, 3

Wood-Vasey, W. M., Wang, L., & Aldering, G. 2004, ApJ, 616, 339

Woosley, S. E. & Weaver, T. A. 1986, ARA&A, 24, 205

Zwicky, F. 1938, Physical Review, 53, 1019

Zwicky, F. 1965, in Stellar Structure - Stars and Stellar Systems, ed. L. H. Aller & D. B. McLaughlin, 367

Danksagung

Ganz zu Anfang möchte ich Peter Hauschildt danken, für die Möglichkeit innerhalb dieses Bereichs zu forschen und meine in Heidelberg begonnene Arbeit in Hamburg fortzusetzen. Trotz zahlreicher Verpflichtungen hatte er ausnahmslos immer ein offenes Ohr für meine Fragen und Probleme und konnte stets wertvolle Tipps zur Lösungsfindung geben. Nochmal, ganz herzlichen Dank für die Betreuung und die Erstellung des Gutachtens.

Eddie Baron (University of Oklahoma, USA) danke ich besonders für die Betreuung auf dem Gebiet der Supernovae und auch sonst allen anstehenden Fragen. In vielen Gesprächen und Diskussionen entstanden bei mir zahlreiche neue Ideen und ein tieferes Verständnis des astrophysikalischen Problems. Der Aufenthalt in Norman mit dem Arbeitsplatz in David Branchs Büro wurde mir durch ihn ermöglicht. Schließlich möchte ich mich noch für die gemeinsame Kooperation in Raleigh (North Carolina) bedanken und die Erstellung des Zweitgutachtens.

Rainer Wehrse († 8 Dezember 2009) werde ich immer dankbar in Erinnerung behalten.

Stefan Körkel (Ruprecht-Karls-Universität Heidelberg), meinem mathematischen Betreuer, schulde ich großen Dank. In vielen Gesprächen und Diskussionen hat er mir beigebracht, was Parameterschätzung und Optimierung aus mathematischer Sicht bedeutet. Durch die Aufnahme in seine „BASF Junior Research Group Optimum Experimental Design“ gab er mir in Heidelberg nicht nur einen Arbeitsplatz, sondern auch eine wissenschaftliche Heimat und Perspektive.

Dennis Jack (Universidad de Guanajuato, Mexiko) danke ich für die gemeinsame Zusammenarbeit und das Korrekturlesen einzelner Kapitel meiner Arbeit.

Hans-Georg Bock (Ruprecht-Karls-Universität Heidelberg), möchte ich für die Aufnahme an das „Interdisziplinäre Zentrum für Wissenschaftliches Rechnen“, die „Heidelberg Graduate School of Mathematical and Computational Methods for the Sciences“ und in seine Gruppe „Simulation and Optimization“ danken. Er hat mich stets unterstützt und gefördert.

Andreas Schweizer, ein herzliches Dankeschön für das stetige Lächeln, das geduldige Zuhören, die Hilfe, die Tipps und das Korrekturlesen einzelner Kapitel meiner Arbeit.

Den Leuten an der Hamburger Sternwarte und ganz besonders der `PHOENIX`-Gruppe danke ich für zahlreiche Gespräche, Hilfe und Unterstützung. Das experimentelle Kochen zu den wöchentlichen group meetings wird mir immer im Gedächtnis bleiben.

Dem Collaborative Research Center, SFB 676, „Particles, Strings, and the Early Universe“ am Deutschen Elektronen-Synchrotron (DESY) danke ich für die Förderung dieser Arbeit und das Einbetten in das Teilprojekt C5 („Type Ia Supernovae and Dark Energy“).

Dem Norddeutschen Verbund für Hoch- und Höchstleistungsrechnen (HLRN) und dem National Energy Research Scientific Computing Center (NERSC) des US Department of Energy (USA) für die großzügige Zuteilung von Rechenzeit.

Meinen Eltern möchte ich für ihre Unterstützung besonders danken, sowie meinen Freunden und meiner Familie für das entgegengebrachte Verständnis.

Manuela, für so vieles und für den gemeinsam beschrittenen Weg.

Eidesstattliche Versicherung

Hiermit erkläre ich an Eides statt, dass ich die vorliegende Dissertationsschrift selbst verfasst und keine anderen als die angegebenen Quellen und Hilfsmittel benutzt habe.

Hamburg, den 27. Dezember 2013 Unterschrift